

UNIVERSIDAD DE GRANADA



*Atomic Information-Theoretic Measures
and
Quantum Entanglement of Many-Particle
Systems*

Tesis doctoral

por

Peter Alexander Bouvrie Morales

Programa de doctorado en Física y Matemáticas (FisyMat)

Departamento de Física Atómica, Molecular y Nuclear
Instituto Carlos I de Física Teórica y Computacional

3 de Septiembre, 2013

Editor: Editorial de la Universidad de Granada
Autor: Peter Alexander Bouvrie Morales
D.L.: GR 492-2014
ISBN: 978-84-9028-798-9

Tesis doctoral dirigida por:

Juan Carlos Angulo Ibáñez

y

Jesús Sánchez-Dehesa Moreno-Cid

Tribunal:

<i>Presidente:</i>	Juan LEON	-	C.S.I.C. (Madrid)
<i>Secretaria:</i>	Rosario GONZÁLEZ FÉREZ	-	Universidad de Granada
<i>Vocales:</i>	Susana HUELGA	-	Universidad de Ulm (Alemania)
	Rodolfo ESQUIVEL	-	Universidad Autónoma de México-Iztapalapa
	Enrique SOLANO	-	Universidad del País Vasco e Ikerbasque

D. Juan Carlos Angulo Ibáñez, Doctor en Ciencias Físicas y Profesor Titular del Departamento de Física Atómica, Molecular y Nuclear de la Universidad de Granada.

D. Jesús Sánchez-Dehesa Moreno-Cid, Doctor en Ciencias Físicas, Doctor en Matemáticas y Catedrático del Departamento de Física Atómica, Molecular y Nuclear de la Universidad de Granada.

MANIFIESTAN:

Que la presente Memoria titulada *Atomic Information-Theoretic Measures and Quantum Entanglement of Many-Particle Systems*, presentada por Don Peter Alexander Bouvrie Morales para optar al Grado de Doctor en Física, ha sido realizada bajo nuestra dirección en el Departamento de Física Atómica, Molecular y Nuclear de la Universidad de Granada y el Instituto Carlos I de Física Teórica y Computacional de la Universidad de Granada.

Granada, 25 de Junio de 2013

Fdo.: Juan Carlos Angulo Ibáñez

Fdo.: Jesús Sánchez-Dehesa Moreno-Cid

Memoria presentada por Don Peter Alexander Bouvrie Morales para optar al Grado de Doctor en Física por la Universidad de Granada.

Fdo.: Peter Alexander Bouvrie Morales

Compromiso de respeto de los derechos de autor

El doctorando D. Peter Alexander Bouvrie Morales y los directores de tesis Dr. Juan Carlos Angulo Ibáñez y Dr. Jesús Sánchez-Dehesa Moreno-Cid garantizan, al firmar esta tesis doctoral, que el trabajo ha sido realizado por el doctorando bajo la dirección de los directores de tesis y hasta donde nuestro conocimiento alcanza, en la realización del trabajo, se han respetado los derechos de otros autores a ser citados, cuando se han utilizado sus resultados o publicaciones.

Granada, 25 de Junio de 2013

Directores de la Tesis

Fdo.: Juan Carlos Angulo Ibáñez

Fdo.: Jesús Sánchez-Dehesa Moreno-Cid

Doctorando

Fdo.: Peter Alexander Bouvrie Morales

Título de Doctor con Mención Internacional

Con el fin de obtener la Mención Internacional en el Título de Doctor, se han cumplido, en lo que atañe a esta Tesis Doctoral y a su Defensa, los siguientes requisitos:

1. Esta Memoria ha sido escrita en inglés, con la introducción y las conclusiones además en español.
2. Esta Tesis ha sido evaluada por dos investigadores externos pertenecientes a centros no españoles.
3. Dos de los miembros del tribunal provienen de una universidad europea no española.
4. Una parte de la defensa de la Tesis se ha realizado en inglés.
5. Una parte de esta Tesis Doctoral se ha realizado en Dinamarca, en el Institut for Fysik og Astronomi, de la Universidad de Aarhus, Dinamarca.

*A mis padres
y especialmente a Elena*

Agradecimientos

Ante todo querría agradecer a Jesús la confianza que ha depositado en mí desde el primer día que entré por la puerta de su despacho hasta el día de hoy. Gracias por transmitirme tu ilimitado entusiasmo por la física, por enseñarme la constancia, el rigor, la imaginación y la valentía que requiere la investigación, pero sobre todo por haber sido para mí un gran maestro de la vida.

También quiero agradecer a Juan Carlos su apoyo incondicional durante estos años. Gracias por todo el tiempo y esfuerzo que has invertido en mi enseñanza, por todo lo que has hecho por mí tanto en lo profesional como en lo personal y especialmente por haber tenido conmigo una actitud positiva y comprensiva en todo momento.

Ana y Angel, vuestra amistad me hace pensar que los argentinos sos personas maravillosas. Gracias a vosotros no he aprendido tan solo acerca de la quintaesencia de la física cuántica, sino que la humildad es la parte más importante de la ciencia. Gracias por la infinidad de discusiones sobre el entrelazamiento en el Moshinsky, por las conversaciones y anécdotas de todo tipo y en definitiva, por vuestra entrañable amistad.

Many thanks Klaus Mølmer for giving me the opportunity, several times, to stay with your research group, and also for the fantastic discussions about possible cobosons experiments. Thanks to you I had the pleasure to share with all the people of the 6th floor, and Etienne of course, many great times in Aarhus.

Gracias Malte por tu incansable paciencia conmigo, por enseñarme física profundamente maravillosa y la forma de llegar a ella. Por los conciertos, los juegos de mesa, los paseos rodeados por vacas, las barbacoas y cervezas en los parques de Aarhus, pero sobre todo gracias por ser un gran amigo.

Quiero agradecer a Fernando Cornet por haber confiado en mí y con gran entusiasmo enseñarme los primeros pasos del apasillante mundo de la física de partículas.

La becarrera y aldeaños, ese lugar al que uno entra con timidez y del que luego nunca querría salir. Los sentimientos me abruman cuando intento expresar mi más sentido agradecimiento a todos vosotros y que no necesito nombrar. Gracias a vosotros el trabajo en un antro se transformó en una ilusión de palacio, la tarea rutinaria en la sorpresa del devenir, los momentos difíciles en consuelo y lo mejor de todo, las risas en carcajadas, ¡Gracias!

Querría agradecer también la valiosa amistad que me han brindado y que me siguen brindando toda mi gente del Albaicín, de la cueva, de mi infancia y del instituto. Con vosotros he vivido momentos inoventables, fiestas, conciertos, paseos por el campo, aventuras de las cuales algunas que no se han de contar, largas y tendidas conversaciones de todo tipo... He crecido a vuestro lado viviendo los mejores momentos y habéis sido el empuje para salir de los peores, por ello no estoy en deuda simplemente me tenéis para vosotros.

Quiero daros las gracias especialmente a Javi y a Richard porque habéis sido, sois y seréis mis hermanos, no de sangre pero sí de alma.

Alfredo, has sido como un padre para mí. Esta tesis ha sido la causa por la que te he tenido más abandonado, pero siempre estás presente en mi corazón. Contigo he aprendido

a vivir el deporte pero sobre todo a vivir de la ilusión honesta, y comprendí que es el valor más importante que puede tener el ser humano, gracias Alfredo. También quiero agradecer a todos mis compañeros de la Sierra, especialmente a Kike y a Reyes, por los innumerables retos, aventuras, glorias y fracasos, pues de todo ello hemos aprendido juntos el coraje de luchar por esa ilusión. El Naranja Team, las competiciones, los viajes, el waterjump de Tignes y de San Rafael, Push!!!, Utah, el Rainbow, ya sabemos que Quick Silver no es una marca de quesos. Gracias Cheli porque tengo todos esos recuerdos grabados a fuego en mi memoria. También quiero agradecer a mis niños del Monachil por devolverme la ilusión por el esquí que estaba pendiente de un hilo y que vuelve a avivarse con una fuerza temeraria.

Los profesores que realmente me motivaron para seguir estudiando en la universidad fueron los del I.E.S Hermenegildo Lanz, salvo alguna escasa excepción del I.E.S Albaicín; a todos ellos quiero agradecerles profundamente la educación y valores que recibí.

Gracias Cristo y Azufre por haber encendido en mí la llama que me hace pensar, sentir y expresar en plenitud.

Fruto del amor, me habéis dado más de lo que un hijo pueda necesitar. A mis padres es imposible expresar con palabras mi agradecimiento. Aún así gracias por vuestro apoyo y ánimo incondicional siempre presente.

No hay cabida en esta tesis para decir todo lo que siento por tí, Elena. Pero gracias por haberme apoyado en todos los vaivenes emocionales especialmente los últimos meses. Y sobre todo gracias por ser tan alegre y entusiasta, por tu espíritu aventurero e inconformista, por tu sentido de la justicia y la tolerancia, por tu valentía, por tu creatividad, por estos y muchísimos otros valores de los que aprendo cada día que comparto contigo.

Finalmente, querría agradecer también los proyectos de excelencia de la Junta de Andalucía con refs. P06-FQM-2445 y P11-FQM7276, y el proyecto del Ministerio de Ciencia e Innovación con ref. FIS2011-24540, ya que gracias a la financiación que de ellos he recibido, ha sido posible realizar esta tesis doctoral y formarme como investigador. Con ellos quisiera agradecer a todos los contribuyentes que honradamente han pagado sus impuestos correspondientes; gracias a ellos el desarrollo de la ciencia en España ha sido y será posible.

Contents

Foreword	1
Prefacio	5
Author's publications	9
I Information-theoretic measures with applications to atomic systems	11
Introduction	15
1 Information-theoretic measures: Basics	19
1.1 Information-theoretic description of a probability density	20
1.2 Uncertainty relations	22
1.3 Complexity measures	25
1.4 Comparative measures: Similarity and divergence	27
2 Entropy and complexity analysis of Dirac-delta-like quantum potentials	31
2.1 Information theory of a single-delta potential	32
2.2 Information theory of a twin-delta potential	35
2.3 Numerical analysis	41
2.3.1 Single-delta potential: lengths and complexities	41
2.3.2 Twin-delta potential: lengths	42
2.3.3 Twin-delta potential: complexities	45
Conclusions	46
3 Complexity quantification of Dirac effect	47
3.1 Complexity measures and Dirac hydrogenic densities	48
3.2 Complexity quantification of Dirac effects	51
3.2.1 Relativistic effects enhancement with nuclear charge.	51
3.2.2 Quantum numbers and Dirac effects.	55
3.3 Hydrogenic complexities, energy and Dirac quantum number	58
3.3.1 Complexity and Dirac energy	58
3.3.2 Dependence on the relativistic quantum number k	58
3.3.3 Information planes	59
Conclusions	59
4 Entropic uncertainty inequality and applications	61
4.1 Upper bounds on frequency moments in terms of radial expectation values .	62
4.2 Particular cases of physical interest	64
4.3 Numerical analysis with atomic one-particle densities	65

4.3.1	Disequilibrium or information energy	65
4.3.2	Thomas-Fermi kinetic energy	68
4.3.3	Dirac exchange energy	70
Conclusions	71
5	Generalized quantum similarity index	73
5.1	Generalized quantum similarity index	74
5.2	Numerical analysis with atomic one-particle densities	76
5.2.1	Pairs of neutral atoms	77
5.2.2	Ionization processes	80
Conclusions	82
6	Geometric Rényi divergence	83
6.1	Geometric Rényi divergence	84
6.2	Numerical analysis with atomic one-particle densities	86
6.2.1	Neutral atoms	86
6.2.2	Ionization processes	90
6.2.3	Atomic models	92
6.2.4	Discrimination of nuclear charges	93
Conclusions	94
7	Generalized relative complexity	97
7.1	Relative complexity: a two-folded generalization	98
7.2	Numerical analysis with atomic electron charge densities	100
Conclusions	106
II	Quantum entanglement in harmonic many-body systems	107
	Introduction	111
8	Quantum entanglement: Basics	113
8.1	Quantum correlations: The qubit	113
8.1.1	Correlations in two qubit systems	114
8.1.2	Mixed states and quantum correlations	115
8.2	Entangled and separable states	116
8.3	Schmidt decomposition	117
8.4	Entanglement quantification of pure states	118
8.4.1	Entanglement for identical fermions	119
9	The Moshinsky model with three electrons, and with two electrons in an uni- form magnetic field	121
9.1	Entanglement measure	121
9.2	The three-electron Moshinsky atom	123
9.2.1	Ground state	126

9.2.2	First excited states	126
9.2.3	Second excited states	127
9.3	Two-electron Moshinsky atom in a magnetic field	129
9.3.1	Ground state	133
9.3.2	First excited states	134
9.3.3	Confining effect of the magnetic field	137
9.4	Perturbative Approach	140
9.4.1	Moshinsky model with three electrons	142
9.4.2	Moshinsky model with two electrons in an uniform magnetic field	145
	Conclusions	146
10	Entanglement and Born-Oppenheimer approximation in an exactly solvable quantum many-body system	149
10.1	Preliminaries	150
10.1.1	Moshinsky-like many-particle model	150
10.1.2	Quantum entanglement	151
10.1.3	Born-Oppenheimer approximation	151
10.2	Exact solution of the many particle system	152
10.3	Entanglement of the three-particle model	156
10.3.1	Nucleus-electrons entanglement	157
10.3.2	Electron entanglement	159
10.4	Entanglement of the many-particle model	160
10.4.1	Nuclei-electrons entanglement	161
10.4.2	Single-particle entanglement: Nucleus and electron entanglement	163
10.5	Born-Oppenheimer approximation in the many-particle Moshinsky model	166
10.5.1	Helium-like atoms	168
10.5.2	N-particles system	169
	Conclusions	170
III	Entanglement and interference of composite bosons	173
	Introduction	177
11	Composite bosons: Foundations	179
11.1	Second quantization	179
11.2	Many-coboson states	180
11.2.1	Composite boson operator	180
11.2.2	Non-ideal behavior of many-coboson states	181
11.2.3	Normalization factor: Fermions and bosons	182
12	Bosonic behavior of entangled Fermions	185
12.1	Normalization factor of two-fermion composite bosons	185
12.1.1	Normalization and entanglement	185
12.1.2	Normalization ratio as a measure of bosonic behavior	187

12.2	Tight bounds on the normalization ratio	187
12.2.1	Extremal entangled states	188
12.2.2	Normalization ratio for extremal states	189
12.3	Illustration and interpretation of bounds	190
12.3.1	Upper and lower bounds	190
12.3.2	Limit of many particles	191
	Conclusions	193
13	Collective interference of composite two-fermion bosons	195
13.1	Beam splitter dynamics: Hong-Ou-Mandel (HOM) effect	196
13.1.1	Two particles interference	196
13.1.2	Many bosons interference	201
13.1.3	Bosons macroscopic approach	202
13.2	Physical model	203
13.3	Coboson state, preparation	204
13.4	Behavior of cobosons under beam-splitter dynamics	206
13.5	Evaluation of counting statistics	210
13.6	Many cobosons interference in the macroscopic approach	213
	Conclusions	214
	Appendix A Single-particle densities	217
	Appendix B Proof of bounds on the cobosons normalization ratio	219
B.1	Uniforming and peaking operations	219
B.2	Normalization ratio under operations	220
	Concluding remarks	225
	Conclusiones	229
	Bibliography	235

Foreword

The information theory of quantum systems gives a view of the physical world in which information is regarded as the primary entity from which physical reality is built. This theory is common among scientists who work on the foundations of quantum mechanics and quantum computation, as well as among physicists who deal with quantum information. It provides not merely a technical change in perspective with respect to the orthodox one, but a radical shift in world view, well captured by John Archivald Wheeler's pithy slogan "It from bit". In this view the laws of physics are informational statements: they tell us something about the way the physical world operates. Then, it is natural to ask ourselves about the different ways to describe, to quantify the information content of the quantum systems and the universe. After all, stretching things a bit, physics may be regarded as the science of everything that is quantifiable.

This Thesis is primarily intended as a contribution to the information-theoretical representation of the microscopic complex systems (atoms, molecules,...), which complements the familiar energy-representation provided by the density-functional and wave-function theories. In passing, let us just bring here the Peres and Zurek's comment that "there is nothing in quantum theory making it applicable to, say, three atoms and inapplicable to 10^{23} " [1]. The studies of microscopic complex systems that use information-theoretical ideas have exploited with the advent of this century, so that there is a need for much further work in this area. To date, approaches have been made to numerous systems and phenomena not only in atomic and molecular physics and quantum chemistry [2, 3, 4, 5] but also in quantum cryptography and teleportation [6, 7], quantum information and computation [8, 9, 10], quantum optics and quantum metrology [11, 12, 13, 14], quantum and cognitive biology [15], and quantum social science, psychology, evolution, brain sciences and life [16, 17, 18, 19], among many other fields.

The most important role in the treatment of the one- and many-particle quantum systems considered in this Thesis is played by the notions of information, complexity, divergence, similarity and entanglement of the characteristic probability density of the quantum-mechanical states of the systems under consideration.

The Thesis is structured in three self-contained Parts (each one with its own Introduction and Conclusions), and two Appendices. They may be read in arbitrary order, and correspond to six (**Part I**), two (**Part II**) and two (**Part III**) scientific publications done by the autor in collaboration with a variety of coworkers.

Let us now briefly outline the contents of the Thesis. A more detailed introduction and motivation can be found at the beginning of the respective parts and chapters.

Part I, entitled *Information-theoretic Measures with Applications to Atomic Systems* and conformed by **Chapters 1-7**, addresses various measures of the information content and the relative informational distance of some non-relativistic and relativistic atomic sys-

tems, their properties and their applications to some specific atomic quantities and processes. The basic variable is the electron distribution as a source and carrier of information in atomic systems.

In the opening **Chapter 1** the main information-theoretic measures which quantify a single facet of the internal disorder of the system (*e.g.*, entropic or frequency moments, disequilibrium, Rényi and Shannon entropies, Fisher information) are defined, and the uncertainty relations associated to them are pointed out. As well, the two-component complexity indices are also briefly discussed; they quantify two different facets of local-global (Fisher-Shannon, Fisher-Rényi, Crámer-Rao) and global-global (LMC or Disequilibrium-Shannon, Disequilibrium-Rényi or LMC-Rényi) character. These indices are usually understood as general indicators of pattern, structure and correlation in physical and chemical systems and processes, and their quantitative characterization is a very important subject of research that has received considerable attention over the past years. Finally, some relative similarity and Jensen's divergence indices, which measures the distance and/or similarity among different distribution densities, are described such as the quantum similarity index, the Jensen-Shannon and Jensen-Fisher divergences and the relative Kullback-Leibler and Rényi entropies.

In **Chapter 2** we calculate the previous entropy and complexity measures in position and momentum spaces for the bound-state wavefunctions of the one-dimensional hydrogen atom with a Dirac-delta-function interaction, which has been used to study different phenomena of bosonic, fermionic and anionic systems. As well, we compute the corresponding quantities for the wavefunctions of the single-particle systems with a twin-delta-function potential, which has been used to approximate the helium atom, the hydrogen molecular ion and some scattering and solid-state phenomena.

In **Chapter 3** a complexity analysis of the non-relativistic (Schrödinger) and relativistic (Dirac) hydrogen atom is carried out. This is done by studying the dependence on the nuclear charge and on quantum numbers of the ground and some excited states, and the quantification of the main dynamical Dirac effects (charge contraction towards the nucleus, nodal disappearance and gradient reduction near to and far from the nucleus) by means of the LMC and Fisher-Shannon complexity measures, and some related information planes.

In **Chapter 4** we find some universal upper bounds on the entropic moments of a quantum probability density in terms of the radial expectation values of the density in the conjugate space, by means of inequality relations of uncertainty type which involve position and momentum entropic moments. Then, they are applied to several macroscopic energies in many-electron systems of Thomas-Fermi and Dirac exchange types, and their accuracy for all the neutral atoms from hydrogen to lawrencium is numerically analyzed.

Chapters 5, 6 and 7 are devoted to extend and generalise the similarity and Jensen's divergence measures of electron distributions, what allow us to quantify the dissimilarity among two or more many-electron systems. We have introduced three new relative measures: the one-parameter generalised quantum similarity index (see **Chapter 5**), the one-parameter generalised divergence measure (called by geometric Rényi divergence; see **Chapter 6**) and the two-parameter generalised relative complexity (see **Chapter 7**). Their main theoretical features are also discussed in detail, including their advantages with respect to previous related quantities which turn out to be instances of them. As well,

they are applied to pairs of neutral and ionized atoms with nuclear charge from 1 to 103 in a non-relativistic Hartree-Fock setting. Keeping in mind the shell-filling patterns of the systems, we give answers to the following questions: (i) Can we grasp the difference between the physico-chemical properties of two atoms and/or ions by means of the relative measures of the corresponding position and/or momentum electron densities?, (ii) To what extent the ionization of a neutral atom modifies its electron densities in the two conjugate spaces?, (iii) Are these relative measures appropriate to quantify the modifications of the densities?, (iv) In an ionization process, how are connected the relative measures of the initial and final systems with the ionization potential?, how do the relative measures depend on the quantum numbers of the ejected or added electron during the process?, (v) Do these relative measures allow the atoms and ions to cluster somehow, and what are the common physico-chemical properties of the systems of a given cluster?,... and some related ones.

Part II, entitled *Quantum Entanglement in Harmonic Many-body Systems* and conformed by **Chapters 8, 9 and 10**, is devoted to investigate the entanglement-related features of the ground and excited states of the three following exactly solvable harmonic systems: the 3D two-electron Moshinsky system subject to an external uniform magnetic field, the 1D three-electron Moshinsky system, and the 1D many-body Moshinsky-like system consisting of N_n heavy particles (“nuclei”) and N_e light particles (“electrons”) which interact harmonically with each other and, moreover, they are assumed to be confined by an harmonic potential.

Beyond the opening **Chapter 8**, which collects some basic knowledge about the phenomenon of entanglement, the first two systems are considered in **Chapter 9**. Therein we discuss the dependence of the entanglement on the energy and the field strength, as well as its behaviour in the regime of vanishing interaction. For strong magnetic fields the entanglement approaches a finite asymptotic value that depends on the interaction strength. Then, we develop a perturbative approach in order to shed some light on the energy dependence of the entanglement, as well as to clarify the finite value of the entanglement exhibited by excited states in the limit of weak interactions.

In **Chapter 10** we analytically compute the entanglement of the eigenstates of the 1D many-body system. We investigate its dependence on the different system parameters, such as the relative strength between the two-particle interaction and the confining harmonic potential, and the number of particles; particular attention is paid to the dependence of the entanglement on the mass ratio of the constituent particles. We consider the entanglement of different bi-partitions of the system, beyond the particular situation in which the two subsystems have very different masses (where the electrons are known to be disentangled from the nuclei). It is found that entanglement takes its maximum value when the masses of the two subsystems are comparable. When these masses are very different from each other, the eigenstates of the system are well represented by the Born-Oppenheimer Ansatz, and our present study naturally leads to consider the connection between this approximation and entanglement. The Born-Oppenheimer approach turns out to provide a good description of the system even in cases where there is an appreciable amount of entanglement between the two subsystems under consideration.

Part III, entitled *Entanglement and Interference of Composite Bosons*, is conformed by **Chapters 11, 12** and **13**. It is devoted to a detailed treatment of the deviations from the ideal bosonic behavior of the cobosons (two-fermion bosons), which are shown to be observable in many coboson interferences. In the opening **Chapter 11** we briefly review the concepts and methods that are necessary for an accurate treatment of composite particles and for the understanding of its quantum statistics.

In **Chapter 12** we investigate the relationship between the compositeness character of cobosons and the entanglement, as characterized by the purity of the single-fermion states. We have improved the existing bounds and derived the explicit form of those quantum states that maximize and minimize the indicator of the bosonic behavior given by the ratio of normalizations constants of N -coboson states for a given purity P . Our bounds are optimal in the sense that they are saturated by the extremal states found. The tight upper bound comes close to the lower bound when $N \cdot P \ll 1$, so that in this regime, not only the deviation from perfectly bosonic behavior is small, but it can also be bounded very tightly via the purity.

In **Chapter 13** we provide a general formalism of the interference process for many composite bosons, we characterize the physical interference model of cobosons by a Fermi-Hubbard lattice model, and we show how the cobosons state describing the behavior of cobosons under beam-splitter dynamics is imitated exactly by a superposition of states with a different number of perfect bosons and fermions. Finally, let us point out that this superposition allows to understand the partially fermionic behavior of cobosons, and ultimately leads to simple expressions for the interference of Bose-Einstein condensates (BEC) and molecular Bose-Einstein condensates (mBEC).

Prefacio

La teoría de información de los sistemas cuánticos proporciona una descripción del mundo físico donde la información es el elemento primario de construcción de la realidad física. Esta teoría se usa por los científicos que trabajan en los fundamentos de la mecánica cuántica y la computación cuántica, así como por los físicos que trabajan en información cuántica. No es meramente una modificación técnica de la perspectiva ortodoxa, sino un cambio radical de la visión del mundo, que está bien recogida por el eslogan breve de John Archivald Wheeler : “It from bit”. En esta forma de ver e interpretar las cosas, las leyes de la física son declaraciones o afirmaciones informacionales: nos dicen algo acerca de la forma de funcionamiento del mundo físico. Parece entonces natural preguntarse sobre las diferentes maneras de describir y cuantificar el contenido informacional de los sistemas cuánticos en particular, y del universo en general. Al fin y al cabo, exagerando un poco las cosas, la física puede considerarse como la ciencia de todo lo que puede cuantificarse.

Esta Tesis constituye una contribución a la representación teórico-informacional de los sistemas complejos microscópicos (átomos, moléculas,...), que complementa la representación energética familiar que proporcionan las teorías basadas en la función de onda y en los funcionales de la densidad. Vale la pena mencionar aquí entre paréntesis el comentario de Peres y Zurek “There is nothing in quantum theory making it applicable to, say, three atoms and inapplicable to 10^{23} ” [1]. Los estudios de los sistemas complejos microscópicos que usan las ideas y técnicas teórico-informacionales han experimentado una pujanza impresionante en las dos últimas décadas, de forma que hay mucho trabajo que hacer próximamente en este área. En efecto, no solo se han podido explicar teórico-informacionalmente con éxito muchos fenómenos y sistemas cuánticos en física atómica y molecular y química cuántica [2, 3, 4, 5], sino también en criptografía y teleportación cuánticas [6, 7], información y computación cuántica [8, 9, 10], óptica cuántica y metrología cuántica [11, 12, 13, 14], biología cognitiva, ciencias sociales cuánticas y otros aspectos de la evolución, la psicología, las ciencias del cerebro y la vida [16, 17, 18, 19], entre otros campos.

El papel más relevante en el tratamiento de los sistemas de una y de muchas partículas que se consideran en esta Tesis lo juegan las nociones de información, complejidad, divergencia, similitud y entrelazamiento de la densidad de probabilidad característica de los estados cuánticos de tales sistemas.

La Tesis está estructurada en tres Partes auto-contenidas (cada una con su Introducción y Conclusiones propias) y dos apéndices, de forma que pueden leerse en orden arbitrario. Su contenido corresponde a seis (**Parte I**), dos (**Parte II**) y dos (**Parte III**) publicaciones científicas realizadas por el autor en colaboración con varios colegas.

A continuación se describen brevemente los contenidos de esta Tesis. Una introducción y motivación más detalladas puede encontrarse al inicio de las partes y capítulos respectivos.

La **Parte I**, titulada *Information-theoretic Measures with Applications to Atomic Systems*, está compuesta por los **Capítulos 1-7**. En ella se analizan varias medidas del contenido informacional y de la distancia teórico-informacional relativa de varios sistemas atómicos no-relativistas y relativistas, sus propiedades y sus aplicaciones a algunos fenómenos y procesos atómicos específicos. La variable básica es la distribución mono-electrónica como fuente y mensajero de información en los sistemas atómicos. En el **Capítulo 1** se definen las medidas teórico-informacionales principales que cuantifican una faceta concreta del desorden interno del sistema (*e.g.*, el desequilibrio, los momentos entrópicos, las entropías de Rényi y Shannon, la información de Fisher), y se analizan las relaciones de incertidumbre asociadas a ellas. Asimismo, también se discuten brevemente los índices de complejidad de dos componentes recientemente introducidos, que cuantifican dos facetas diferentes de tipo local- global (Fisher-Shanon, Fisher-Rényi, Crámer-Rao) y global-global (LMC o desequilibrio-Shannon, Desequilibrio-Rényi o LMC-Rényi). Estos índices son interpretados usualmente como indicadores generales de patrones, estructura y correlación en sistemas y procesos físicos y químicos. Su caracterización cuantitativa es un tópico de investigación que ha recibido una considerable atención en los últimos años. Finalmente, se describen algunos índices relativos de similitud y de divergencia de tipo Jensen-Shannon y Jensen-Fisher, así como las entropías relativas de Kullback-Leibler y Rényi.

En el **Capítulo 2** se calculan las medidas entrópicas y de complejidad antes mencionadas en los espacios de posiciones y momento para los estados ligados del átomo de hidrógeno mono-dimensional con una interacción de tipo delta de Dirac, que ha sido usada para aproximar numerosos fenómenos en sistemas bosónicos, fermiónicos y aniónicos. Asimismo, se determinan las magnitudes correspondientes a las funciones de onda de los sistemas mono-particulares con un potencial de Dirac gemelo, que ha sido usado para aproximar el átomo de helio, el ion molecular de hidrógeno y algunos fenómenos de estado sólido.

En el **Chapter 3** se lleva a cabo un análisis de complejidad del átomo de hidrógeno tridimensional no-relativista (Schrödinger) y relativista (Dirac). Se estudia la dependencia en la carga nuclear y en los números cuánticos de los estados fundamental y estados excitados, y la cuantificación de los efectos de Dirac principales (*i.e.*, contracción de la carga, desaparición de los nodos, y reducción del gradiente) por medio de las medidas de complejidad LMC y Fisher-Shannon y de algunos planos de información asociados.

En el **Chapter 4** se obtienen algunas cotas superiores universales a los momentos entrópicos de la densidad de probabilidad cuántica en un espacio, en términos de los valores esperados radiales de la densidad en el espacio conjugado. Para ello se utiliza una metodología basada en las relaciones de incertidumbre que involucran a momentos entrópicos de posiciones y momentos. Luego, estos resultados son aplicados a varias energías macroscópicas en los sistemas multi-electrónicos de tipo Thomas-Fermi y de intercambio de Dirac, y su precisión es investigada numéricamente en todos los átomos neutros desde el hidrógeno al lawrencio.

En los **Capítulos 5, 6 y 7** se generalizan las medidas de similitud o semejanza, se extiende las medidas de divergencia de Jensen, que cuantifican la disimilaridad entre dos o mas sistemas de muchos cuerpos y mejora mediante una generalización el concepto de complejidad relativa. Hemos introducido tres nuevas medidas comparativas: el índice

de similitud cuántica generalizada mono-paramétrico (ver **Capítulo 5**), la medida de divergencia geométrica mono-paramétrica (ver **Capítulo 6**) y la complejidad relativa generalizada bi-paramétrica (ver **Capítulo 7**). Se discuten sus propiedades principales y sus ventajas con respecto a las correspondientes medidas comparativas conocidas con anterioridad en la literatura, las cuales resultan ser casos particulares de las introducidas en esta memoria. Después se aplican las nuevas medidas a pares de átomos neutros y átomos singularmente ionizados con carga nuclear desde 1 a 103 en un marco Hartree-Fock no-relativista. Habida cuenta de los patrones de llenado de capas de estos sistemas, abordamos y respondemos a cuestiones tales como: (i) ¿Puede cuantificarse la diferencia entre propiedades físico-químicas de dos átomos y/o dos iones por medio de las medidas comparativas antes mencionadas en los espacios de posiciones y/o de momentos?. (ii) ¿Hasta qué punto la ionización de un átomo neutro modifica sus densidades electrónicas en los dos espacios conjugados?, (iii) ¿Son estas medidas comparativas adecuadas para cuantificar las modificaciones de las densidades?, (iv) En un proceso de ionización, ¿cómo están conectadas las medidas comparativas de los sistemas inicial y final?, (v) ¿Permiten estas medidas agrupar de alguna manera a los átomos e iones?, y ¿qué propiedades comunes poseen los átomos de un grupo dado?,... y otras cuestiones relacionadas.

La **Parte II**, titulada *Quantum Entanglement in Harmonic Many-body Systems*, está compuesta por los **Capítulos 8, 9 y 10**. En ella se investigan las características de entrelazamiento de los estados fundamental y de los estados excitados de los tres sistemas armónicos exactamente resolubles siguientes: el sistema de Moshinsky tri-dimensional de dos electrones en presencia de un campo magnético externo, el sistema de Moshinsky mono-dimensional de tres electrones, y el sistema de tipo Moshinsky de muchos cuerpos que consta de N_n partículas de masa grande (“núcleos”) y N_e partículas de masa pequeña (“electrones”) que interactúan armónicamente entre sí y, además, están confinados en un potencial armónico. En el **Capítulo 8** se recogen algunos conocimientos básicos acerca del entrelazamiento.

En el **Capítulo 9** se analiza el entrelazamiento del primer sistema armónico, su dependencia con la energía y la intensidad del campo, así como su comportamiento cuando la interacción tiende a cero. Se observa que para campos fuertes, el entrelazamiento tiende a un valor asintótico finito, que depende de la intensidad del campo. Asimismo, se desarrolla un método perturbativo para lograr una mayor introspección en la dependencia energética del entrelazamiento, así como para explicar más claramente la finitud del entrelazamiento que presentan los estados excitados en el límite de interacción débil.

En el **Capítulo 10** se determina el entrelazamiento de los estados propios del sistema de muchos cuerpos de Moshinsky mono-dimensional. Se investiga su dependencia con los diversos parámetros del sistema, tales como la intensidad relativa entre la interacción a dos cuerpos y el potencial de confinamiento, y el número de partículas; se presta una atención especial a la dependencia del entrelazamiento con respecto a la ratio de las masas de las partículas constituyentes. Se considera el entrelazamiento de diferentes bi-particiones del sistema, más allá del caso particular en que los dos subsistemas tienen masas muy distintas (donde se sabe que los electrones no están entrelazados con los núcleos). Se encuentra que el entrelazamiento toma su máximo valor cuando las masas de los dos subsistemas

son comparables. Cuando estas masas son muy diferentes entre sí, los autoestados del sistema están bien representados en la aproximación de Born-Oppenheimer, de forma que ello nos da la oportunidad de observar el entrelazamiento en este marco. Resulta que la aproximación de Born-Oppenheimer proporciona una buena descripción del sistema incluso en los casos en que existe una diferencia apreciable entre los dos subsistemas involucrados.

La **Parte III**, titulada *Entanglement and Interference of Composite Bosons*, está compuesta por los **Capítulos 11, 12 and 13**. En ella se hace un tratamiento detallado del comportamiento bosónico ideal de los cobosones (bosons formados por dos fermiones), que se dejan observar en interferencias cobosónicas. En el **Capítulo 11** revisamos brevemente los conceptos y métodos necesarios para un tratamiento preciso de las partículas compuestas y para la comprensión de su estadística cuántica.

En el **Capítulo 12** se investiga la relación entre el carácter compuesto de los cobosones y el entrelazamiento (descrito por la pureza de los estados mono-fermiónicos). Se encuentra una mejora sustancial de las cotas existentes en la literatura, y se obtiene la forma explícita de los estados cuánticos que optimizan el indicador del carácter bosónico dado por la ratio de las constantes de normalización de los estados de N -cobosones para una pureza P dada. Las cotas obtenidas son óptimas en el sentido de que saturan para los estados extremos encontrados. La cota superior precisa obtenida cae cerca de la cota inferior cuando el producto $N \cdot P$ es mucho menor que la unidad, de forma que en este régimen no solo la desviación del comportamiento perfectamente bosónico es pequeña sino que puede estar también acotada de manera muy precisa por la pureza.

En el **Capítulo 13** se da un formalismo general del proceso de interferencia de muchos bosones compuestos, usándose el modelo de Fermi-Hubbard para su interpretación, y mostrándose de qué forma el estado de los cobosones describe el comportamiento cobosónico en una dinámica de tipo beam-splitter es descrito por una superposición de estados con un número diferente de bosones y fermiones perfectos. Finalmente, cabe señalar que esta superposición permite entender el comportamiento parcialmente fermiónico de los cobosones, y finalmente dar lugar a expresiones sencillas para la interferencia de los condensados Bose-Einstein (BEC) y de BEC moleculares (mBEC).

Author's publications

Publications upon which this Thesis is based. The numbers in brackets at the end of each reference indicate the Chapters where they have been used.

- *Entropy and complexity analysis of Dirac-delta-like quantum potentials.*
P.A. Bouvrie, J.C. Angulo, J.S. Dehesa.
Physica A: Statistical Mechanics and its Applications **390**, 2215 (2011).
[Chapter 2]
- *Generalized Quantum Similarity Index: Applications in atoms.*
P.A. Bouvrie, J. Antolín, J.C. Angulo.
Chemical Physics Letters **506**, 326–331 (2011).
[Chapter 5]
- *Geometric Rényi divergence: A comparative measure with applications to atomic densities.*
J. Antolín, P.A. Bouvrie, J.C. Angulo.
Physical Review A **84**, 032504 (2011).
[Chapter 6]
- *Quantum entanglement in exactly soluble atomic models: the Moshinsky model with three electrons, and with two electrons in a uniform magnetic field.*
P.A. Bouvrie, A.P. Majtey, A.R. Plastino, P. Sánchez-Moreno, J.S. Dehesa.
European Physical Journal D **66**, 15 (2012).
[Chapter 9]
- *Uncertainty inequalities among frequency moments and radial expectation values: applications to atomic systems.*
J.C. Angulo, P.A. Bouvrie, J. Antolín.
Journal of Mathematical Physics **53**, 043512 (2012).
Selected for the *Virtual Journal of Quantum Information*, Vol. 12, issue 5, May 2012.
[Chapter 4]
- *A generalized relative complexity: application to atomic one-particle densities.*
J.C. Angulo, P.A. Bouvrie, J. Antolín.
Chemical Physics Letters **539**–**540**, 191 (2012).
[Chapter 7]
- *Quantifying Dirac hydrogenic effects via complexity measures.*
P.A. Bouvrie, S. López-Rosa, J.S. Dehesa.
Physical Review A **86**, 012507 (2012).
[Chapter 3]

- *Bosonic behavior of entangled fermions.*
M.C. Tichy, P.A. Bouvrie, K. Mølmer.
Physical Review A **86**, 042317 (2012).
[Chapter 12]
- *Collective interference of composite two-fermion bosons.*
M.C. Tichy, P.A. Bouvrie, K. Mølmer.
Physical Review Letters **109**, 260403 (2012).
[Chapter 13]
- *Entanglement and Born-Oppenheimer approximation in an exactly solvable quantum many-body system.*
P.A. Bouvrie, A.P. Majtey, M.C. Tichy, A.R. Plastino, J.S. Dehesa.
Preprint (2013)
[Chapter 10]

Part I

Information-theoretic measures with applications to atomic systems

Table of Contents

Introduction	15
1 Information-theoretic measures: Basics	19
1.1 Information-theoretic description of a probability density	20
1.2 Uncertainty relations	22
1.3 Complexity measures	25
1.4 Comparative measures: Similarity and divergence	27
2 Entropy and complexity analysis of Dirac-delta-like quantum potentials	31
2.1 Information theory of a single-delta potential	32
2.2 Information theory of a twin-delta potential	35
2.3 Numerical analysis	41
2.3.1 Single-delta potential: lengths and complexities	41
2.3.2 Twin-delta potential: lengths	42
2.3.3 Twin-delta potential: complexities	45
Conclusions	46
3 Complexity quantification of Dirac effect	47
3.1 Complexity measures and Dirac hydrogenic densities	48
3.2 Complexity quantification of Dirac effects	51
3.2.1 Relativistic effects enhancement with nuclear charge.	51
3.2.2 Quantum numbers and Dirac effects.	55
3.3 Hydrogenic complexities, energy and Dirac quantum number	58
3.3.1 Complexity and Dirac energy	58
3.3.2 Dependence on the relativistic quantum number k	58
3.3.3 Information planes	59
Conclusions	59

4	Entropic uncertainty inequality and applications	61
4.1	Upper bounds on frequency moments in terms of radial expectation values .	62
4.2	Particular cases of physical interest	64
4.3	Numerical analysis with atomic one-particle densities	65
4.3.1	Disequilibrium or information energy	65
4.3.2	Thomas-Fermi kinetic energy	68
4.3.3	Dirac exchange energy	70
	Conclusions	71
5	Generalized quantum similarity index	73
5.1	Generalized quantum similarity index	74
5.2	Numerical analysis with atomic one-particle densities	76
5.2.1	Pairs of neutral atoms	77
5.2.2	Ionization processes	80
	Conclusions	82
6	Geometric Rényi divergence	83
6.1	Geometric Rényi divergence	84
6.2	Numerical analysis with atomic one-particle densities	86
6.2.1	Neutral atoms	86
6.2.2	Ionization processes	90
6.2.3	Atomic models	92
6.2.4	Discrimination of nuclear charges	93
	Conclusions	94
7	Generalized relative complexity	97
7.1	Relative complexity: a two-folded generalization	98
7.2	Numerical analysis with atomic electron charge densities	100
	Conclusions	106

Introduction

Quantum Information Theory (QIT) [8] and the study of entanglement [20, 21] are examples of the versatility of information theory techniques applied in new fields of scientific or technological interest [22]. In particular there has been a tremendous interest in the literature to apply information theory to quantum mechanical systems [5, 23, 24, 25, 26, 27], to study the electronic structure of atoms and molecules [28, 29, 30], to explore some chemical processes such as ionization or chemical reactions [31, 32] or even to study the controversial homochirality of amino acids [19], building blocks of the biological systems.

The concepts of uncertainty, randomness, correlation, organization, complexity, information, disorder or delocalization are basic ingredients in the study of relevant properties for many probability distributions appearing as descriptors of chemical or physical systems or processes. These concepts concerning probability distributions are quantified by means of closely related and well known density functionals, such as Shannon entropy, Fisher information or disequilibrium. Other relevant quantities, dependent on two (or more) different densities, have been also defined, studied and applied to detect similarity or discrepancy, as comparative measures among them.

In Chapter 1 we discuss in a non-exhaustive way the best known information-theoretic measures, of continuous probability densities, which we shall use throughout this part of the thesis. We provide their definitions and interpretation, as well as their most relevant mathematical properties and relationships among them. These measures, when applied to the basic variable of the Hohenberg-Kohn Density Functional Theory (DFT) [33, 34, 35, 36] of many-electron systems (*i.e.*, the electron density in position and momentum spaces), are closely related to the density functionals which characterize the main macroscopic quantities of atoms and molecules.

The interpretation of the information-theoretic measures outlined in Chapter 1 becomes more clear and understandable in analytically solvable quantum models, since therein one can control all the parameters of the system or model. Dirac-delta-like quantum-mechanical potentials are frequently used to describe and interpret numerous phenomena in many scientific fields including atomic and molecular physics, condensed matter and quantum computation. In Chapter 2, the entropy and complexity properties of potentials with one and two Dirac delta functions are analytically calculated and numerically discussed in both position and momentum spaces. We have studied the information-theoretic lengths of Fisher, Rényi and Shannon types as well as the Crámer-Rao, Fisher-Shannon and LMC shape complexities of the lowest-lying stationary states of one delta and twin-delta. They allow us to grasp and quantify different facets of the spreading of the charge and momentum of the system far beyond the celebrated standard deviation.

In Chapter 3 we characterize by means of single-density information measure computed analytically, the relativistic (Dirac equation) and non-relativistic (Schrödinger equation) hydrogen atom. The primary dynamical Dirac relativistic effects can only be seen in hydrogenic systems without the complications introduced by electron-electron interactions in many-electron systems. They are known to be the contraction towards the origin of the

electronic charge in hydrogenic systems and the nodal disappearance (because of the raising of all the non-relativistic minima) in the electron density of the excited states of these systems. In addition we point out the (largely ignored) gradient reduction of the charge density near to and far from the nucleus. In this work we quantify these effects by means of single (Fisher information) and composite (Fisher-Shannon complexity and plane, LMC complexity) information-theoretic measures. While the Fisher information measures the gradient content of the density, the (dimensionless) composite information-theoretic quantities grasp two-fold facets of the electronic distribution: The Fisher-Shannon complexity measures the combined balance of the gradient content and the total extent of the electronic charge, and the LMC complexity quantifies the disequilibrium jointly with the spreading of the density in the configuration space. Opposite to other complexity notions (e.g., computational and algorithmic complexities), these two quantities describe intrinsic properties of the system because they do not depend on the context but they are functionals of the electron density.

Rigorous and universal bounds on frequency moments of one-particle densities in terms of radial expectation values in the conjugate space are obtained in Chapter 4. The results, valid for any d -dimensional quantum-mechanical system, are derived by using Rényi-like position-momentum inequalities in an information-theoretical framework. Especially interesting are the upper bounds on the Dirac exchange and Thomas-Fermi kinetic energies, as well as the disequilibrium or self-similarity of both position and momentum distributions. A variety of bounds for these functionals in a given space are known, but most usually in terms of quantities defined within the same space. Very few results including a density functional on one space, and expectation values on the conjugate one, are found in the literature. In Chapter 4, a pioneering bound on the disequilibrium in terms of the kinetic energy is improved. A numerical study of the aforementioned relationships is carried out for atomic systems in their ground state. Some results are given in terms of relevant physical quantities, including the kinetic and electron-nucleus attraction energies, the diamagnetic susceptibility and the height of the peak of the Compton profile, among others.

In the following chapters of this part of the thesis, we propose three novel comparative measures within the framework of the information theory.

In Chapter 5, a generalized quantum similarity index is defined, quantifying the similarity among density functions. The generalization includes, as new features (i) comparison among an arbitrary number of functions, (ii) its ability to modify the relative contribution of different regions within the domain of the densities, and (iii) the possibility of assigning different weights to each function according to its relevance on the comparative procedure. The similarity among atomic one-particle densities in both conjugated spaces, and neutral-cation similarity in ionization processes are analyzed. The results are interpreted attending to shell-filling patterns, and also in terms of experimentally accessible quantities of relevance in ionization processes.

A new one-parameter measure of divergence is proposed in Chapter 6, quantifying the discrepancy among general probability densities. Its main mathematical properties include the features above described. The main difference with the measures of divergence in the literature, is that it is a functional of the geometric mean of the densities to compare instead of the arithmetic mean. Applications to the study of atomic density functions, in

both conjugated spaces, show the versatility and universality of this divergence.

Finally, in Chapter 7, the search of an appropriate measure of relative complexity among density functions is afforded. In doing so, the main properties required for complexity functionals of a given distribution, as well as those for discrimination measures among two or more distributions are considered. A proposal for a generalized relative complexity is provided, which includes a pioneering definition as a limiting case. A theoretical analysis of the generalized measure for arbitrary distributions is carried out. The applications regard the electron charge densities of neutral atoms, and the results are interpreted on the basis of the main physical properties of the systems considered.

In this part of the thesis we use atomic units (a.u.) except in Chapter 2 and Chapter 3.

Information-theoretic measures: Basics

A major goal of the information theory of the atomic and molecular systems is the quantification of the multiple facets of their internal disorder which is manifest in the electron density of the system, as recently reviewed [4, 37, 38].

First, various single (one-component) information-theoretic measures were used to grasp single facets of the rich variety of complex three-dimensional geometries of these systems in a non-relativistic framework, such as the spread of the electronic distribution all over the configuration space (Shannon, Rényi and Tsallis entropies), the gradient content (Fisher information) and other manifestations of the non-uniformity of the electron density (disequilibrium). Later, composite (two-component) measures have been proposed to jointly grasp various facets of the electron density. They are called complexity measures because they are minimum for the two extreme distributions of perfect order and maximum disorder (so, approaching the intuitive notion of complexity), such as the Crámer-Rao, Fisher-Shannon and LMC (López-Ruiz, Mancini and Calbet) complexity measures. Opposite to the single-component measures, they are dimensionless (what lets them be mutually compared) and moreover they fulfil a number of invariance properties under replication, translation and rescaling transformations. Throughout the development of the probability, statistics and information theories, comparative measures have also emerged in order to quantify the “distance” or similarity among different systems, each one with its own properties and characteristics, which makes these measures to be more or less useful according to the kind of problem, system or process as well as the interpretation we are dealing with. Different approaches have dealt with the aim of establishing quantitative measures of similarity or dissimilarity (or divergence), among two or more probability distributions, giving rise to various measures such as the Kullback-Leibler, Jensen-Shannon and Jensen-Rényi divergences or the Quantum Similarity Index among other.

In this chapter we describe the best known information-theoretic measures for continuous probability densities which we shall use in the first part of this thesis. We provide their definitions, their most relevant properties and relationships among them as well as the uncertainty relations that they satisfy. Moreover, we present some relevant applications existing in the literature for these measures within the context of this thesis. The structure of the chapter is the following. In Section 1.1 we deal with the basic spreading measures of a single probability distribution. Uncertainty relations among different information measures are shown in Section 1.2 and two-component composite information-theoretic measures, *i.e.* complexity measures, in Section 1.3. Finally, in Section 1.4, we turn to deal with information theory measures of two or more probability distributions.

1.1 Information-theoretic description of a probability density

The application of the information theory for a probability distribution $\rho(\vec{r})$ (see Appendix A to know in detail how these densities are derived) corresponding to some d -dimensional continuous random variable \vec{r} (e.g. position, momentum, phase,...) have provided a wide range of measures to quantify the spread (or uncertainty) of \vec{r} over a domain $\Delta \subseteq \mathbb{R}^d$ [39, 40] far beyond the statistical root-mean-square or standard deviation

$$\Delta\vec{r} = \langle |\vec{r} - \langle \vec{r} \rangle|^2 \rangle^{1/2} \quad (1.1)$$

where the expectation value $\langle f(\vec{r}) \rangle$ is given by

$$\langle f(\vec{r}) \rangle = \int_{\Delta} f(\vec{r}) \rho(\vec{r}) d\vec{r}. \quad (1.2)$$

The choice $f(\vec{r}) = |\vec{r}|^a = r^a$ (i.e., $\langle \vec{r}^a \rangle$) provides the moment of order a of the probability distribution $\rho(\vec{r})$:

$$\langle r^a \rangle = \int_{\Delta} r^a \rho(\vec{r}) d\vec{r} \quad (1.3)$$

In this part of the thesis we will deal with some of the most relevant information-theory-based spreading measures of $\rho(\vec{r})$, namely the Shannon and Rényi entropies and the Fisher information. In the nineteen forties Claude E. Shannon proposed a set of reasonable assumptions that should satisfy a candidate for being an appropriate measure of average uncertainty contained in a discrete probability distribution of a finite set of observational events; i.e. the outcomes of a measurement or a detection of a signal in a communication channel. Shannon entropy was introduced as the uncertainty on the outcome of an experiment based on a given probability distribution. Then, it is a measure of ignorance or lack of information concerning the outcome of the experiment. The original definition was generalized to a continuous probability density as proposed by Shannon himself [41, 39], in the form

$$S[\rho] = - \int_{\Delta} \rho(\vec{r}) \ln \rho(\vec{r}) d\vec{r}, \quad (1.4)$$

where it is assumed that $\rho(\vec{r}) \ln \rho(\vec{r}) = 0$ for those values \vec{r} for which $\rho(\vec{r}) = 0$. See also [42].

Although Shannon entropy for continuous variables has some properties which are quite different from those of its discrete counterpart (e.g., it may take negative values), retains enough properties, such as the Schur concavity [40] (i.e., it is non decreasing under a doubly stochastic transformation), to make of this entropy a very useful information-theoretic tool.

The Rényi entropy of order q , $R_q[\rho]$ [43, 39], of the normalized to unity (i.e. $\langle 1 \rangle = 1$) probability density $\rho(\vec{r})$ is defined by

$$R_q[\rho] = \frac{1}{1-q} \ln \omega_q[\rho] \quad \text{for } q > 0, \text{ and } q \neq 1 \quad (1.5)$$

where the quantity

$$\omega_q[\rho] = \int_{\Delta} [\rho(\vec{r})]^q d\vec{r} \quad (1.6)$$

denotes the q -th order frequency, or entropic, moment of the distribution $\rho(\vec{r})$ [44]. In spite of their names, the mathematical definition of the frequency moments (expectation values of powers of the density $\rho(\vec{r})$) strongly differs from that of the “usual” moments given in Eq. (1.3) (expectation values of powers of the independent variable \vec{r}). Frequency moments of a (d -dimensional) probability density are essentially a class of quantities whose key property is Schur concavity [40], see also [8, 45, 46]. Frequency moment of order two [47] is particularly relevant because quantifies the departure of the probability density from uniformity or equiprobability situation (equilibrium). It is known as disequilibrium (also known as self-similarity [48] or information energy [49])

$$D[\rho] = \omega_2[\rho] = \int \rho^2(\vec{r}) d\vec{r} = \langle \rho(\vec{r}) \rangle, \quad (1.7)$$

which is basically the expected value of the own density $\rho(\vec{r})$. The interpretation as a measure of departure from equiprobability arised in the framework of discrete and finite probability distributions [49]. Later on, this interpretation was generalized for the case of infinite and continuous probability distributions [50]. In spite of the nonexistence of uniform distributions in those cases, uniformity can be arbitrarily approached by means of sequences of distributions. The disequilibrium plays a relevant role, also, in what concerns the concept of “shape complexity” [51, 52] and its physical interpretation for atomic [53] and molecular [54] systems as will be shown in Section 1.3.

Rényi entropy is also a measure of uncertainty that can be viewed as a generalization of Shannon’s entropy. In the limiting value $q \rightarrow 1$, taking into account the normalization condition $\omega_1[\rho] = 1$, yields the Shannon entropy

$$S[\rho] = \lim_{q \rightarrow 1} R_q[\rho]. \quad (1.8)$$

The allowed range of values for the characteristic order parameter q of the Rényi entropy in the continuous case is determined by the convergence conditions on the integral definition of the frequency moment, Eq. (1.6), being imposed by the probability distribution $\rho(\vec{r})$. The order parameter q of the frequency moments and the Rényi entropy, Eqs. (1.6) and (1.5) respectively, allows to enhance or diminish, by increasing or decreasing its value, the contribution of the probability distribution over different regions. The higher the value of q the more concentrated is the function $[\rho(\vec{r})]^q$ around the local maxima of the distribution, while the lower values have the effect of smoothing that function over its whole domain.

The quantities previously defined are global measures of spreading. In contrast, Ronald A. Fisher introduced the Fisher information that could be able to detect local changes of the probability distribution besides giving us the notion of information concerning to statistical inference. The Fisher information of a probability distribution $\rho(\vec{r})$ is defined as [55, 56]

$$F[\rho] = \int_{\Delta} \frac{[\vec{\nabla} \rho(\vec{r})]^2}{\rho(\vec{r})} d\vec{r}. \quad (1.9)$$

One of the most relevant features of this magnitude is that fulfils the consequence of the Cauchy-Schwartz inequality known as the Cramér-Rao inequality [39],

$$(\Delta \vec{r})^2 \cdot F[\rho(\vec{r})] \geq d^2 \quad (1.10)$$

allowing us to measure the ability to estimate the value of the random variable \vec{r} . Fisher information gives the minimum error in estimating \vec{r} from the given probability distribution.

Fisher information has a property of locality because of its gradient-functional form. It measures the narrowness of the distribution as a property of locality, then, it is very sensitive to the fluctuations of $\rho(\vec{r})$. In contrast, the Rényi and Shannon entropies are global measures of spreading, as well as the standard deviation, because they are power and logarithmic functionals of $\rho(\vec{r})$, respectively. Let us highlight that while the standard deviation quantifies the separation of the region(s) of the probability concentration with respect to the mean value or centroid $\langle \vec{r} \rangle$, the Rényi and Shannon entropies do not depend on any specific point of the domain Δ , so they are (global) measures of the extent to which the density is in fact concentrated anywhere. On the other hand, the Fisher information measures the pointwise concentration of the probability density over its domain.

Shannon and Rényi entropies and the Fisher information have, however, a disadvantage: each one has its own units which differ among each other, what bears a difficulty for their mutual comparison. To overcome this difficulty, sometimes, it is more convenient to use instead the Rényi and Shannon lengths [46, 40] defined by

$$L_q^R[\rho] = \exp(R_q[\rho]) = \{\omega_q[\rho]\}^{\frac{1}{1-q}} \quad (1.11)$$

and

$$N[\rho] = \lim_{q \rightarrow 1} L_q^R[\rho] = \exp(S[\rho]) \quad (1.12)$$

respectively, and the Fisher length [57, 58] given by

$$\delta \vec{r} = \frac{1}{\sqrt{F[\rho]}}. \quad (1.13)$$

The standard deviation and these three information-theoretic lengths are *direct* spreading measures of $\rho(\vec{r})$ in the sense that they have the same units as \vec{r} . Moreover, all four quantities share the following relevant properties: translation and reflection invariance, linear scaling with \vec{r} (e.g., $\Delta \vec{R} = \alpha \Delta \vec{r}$ for $\vec{R} = \alpha \vec{r}$ in the case of standard deviation) and vanishing in the limit for which the random variable has some definite value, that is when $\rho(\vec{r})$ approaches a Dirac-delta function. These four direct spreading measures are complementary in the sense that they grasp different facets of the distribution of the probability density $\rho(\vec{r})$ all over its support interval. Moreover, all of them enjoy an uncertainty property as will be shown in the next section.

1.2 Uncertainty relations

Different expectation values and density functionals have been considered in order to characterize or to estimate the main physical properties of quantum systems. A relevant concept for the interpretation of different quantum-mechanical phenomena is that of “uncertainty”, in the Heisenberg sense, regarding the accuracy in the knowledge of the particle’s position and momentum simultaneously. Here we give the uncertainty relations corresponding to the moments, frequency moments together with those associated to the

Rényi and Shannon entropies and the Fisher information of general d -dimensional quantum systems. These relations constitute different mathematical formulations of the quantum-mechanical uncertainty principle which describes a characteristic feature of quantum mechanics and states the limitations to perform measurements on a system without disturbing it. Moreover, since the two canonically conjugate observables involved in the uncertainty relations here considered -position and momentum- do not commute, both observables cannot be precisely simultaneously determined in any quantum state of the system.

The original Heisenberg uncertainty relation was extended by using information-theoretic methods, to a product of both position \vec{r} and momentum \vec{p} , radial expectation values of arbitrary order in [59], and to d -dimensional spaces in [60] where is provided the position-momentum Heisenberg-like uncertainty relation

$$\langle r^{d/\alpha} \rangle^\alpha \langle p^{d/\beta} \rangle^\beta \geq \alpha^\alpha \beta^\beta \frac{[\Gamma(1 + \frac{d}{2})]^2}{\Gamma(1 + \alpha)\Gamma(1 + \beta)} e^{d-\alpha-\beta}; \quad \alpha, \beta > 0 \quad (1.14)$$

which is given in terms of the radial expectation values, Eq. (1.2) with $f(\vec{r}) = r^a$,

$$\langle r^a \rangle = \int r^a \rho(\vec{r}) d\vec{r} \quad (1.15)$$

with $r = |\vec{r}|$, and similarly for $\langle p^a \rangle$. The real exponent a will be referred to as the ‘‘order’’ of the radial expectation value, whose range of allowed values will be imposed by the convergence conditions of the involved integrals. For densities with finite value at the origin, the condition $a > -d$ has to be taken into account, according to the expression of the volume element $d\vec{r} = r^{d-1} dr d\Omega$ where Ω is the d -dimensional solid angle.

The quantity $\langle r^a \rangle$ does not depend on the angular variables of the distribution $\rho(\vec{r})$. This means that we can determine them from the spherically averaged density $\rho(\vec{r})$, whose moments over the interval $r \in [0, \infty)$

$$\mu_a = \int_0^\infty r^a \rho(r) dr \quad (1.16)$$

are related to the aforementioned radial expectation values as $\langle r^a \rangle = \Omega_{d-1} \mu_{a+d-1}$, where $\Omega_D = 2\pi^{D/2}/\Gamma(D/2)$ the volume of the D -dimensional sphere. From a mathematical point of view, we can deal in similar ways with the quantities $\langle r^a \rangle$ or μ_a . In the present work, the radial expectation values $\langle r^a \rangle$ will be considered, because of their physical meaning.

For $\alpha = \beta = d/2$, Eq. (1.15) simplifies to the familiar d -dimensional form of the Heisenberg inequality [61, 62, 63]

$$\langle r^2 \rangle \langle p^2 \rangle \geq \frac{d^2}{4} \quad (1.17)$$

which shows that the more accurately the position is known, the less accurately is the momentum determined, and conversely. See [64, 65] for recent improvements of this relation.

Similar relationships were obtained drawing upon the concept of ‘‘Shannon entropy’’, Eq. (1.4), which is a measure of ‘‘spreading/delocalization’’ of the probability distribution.

As suggested by the notion of uncertainty previously discussed, the Shannon entropies in position and momentum spaces, namely $S(\rho)$ and $S(\gamma)$, fulfil the uncertainty relation given in Ref. [66]

$$S(\rho) + S(\gamma) \geq d(1 + \ln \pi), \quad (1.18)$$

what implies that it is not possible to deal, simultaneously, with arbitrary low values of both entropies or, in other words, with extremely accurate values of the position and momentum variables. The above inequality will be denoted as BBM, paying homage to its pioneering authors Bialynicki-Birula and Mycielski. This inequality has been recently improved for central potentials by Rudnicki et al [67].

Other entropic inequalities are also known [45, 68] with a variety of applications in a quantum framework [69]. A generalization of the (power-moments-based) Heisenberg-like uncertainty relation was obtained by Rajagopal [70] using the entropic moments, Eq. (1.6), in position and momentum spaces. He extended to d dimensions and improved the one-dimensional results of Maassen-Uffink [45], obtaining the following entropic-moment-based uncertainty relation:

$$(\omega_{\mu+1}[\rho])^{-\frac{1}{\mu}} (\omega_{\nu+1}[\gamma])^{-\frac{1}{\nu}} \geq \left(\frac{\pi(1 + 2\mu)^{1+\frac{1}{2\mu}}}{1 + \nu} \right)^d \quad (1.19)$$

which is valid for $\mu > -\frac{1}{2}$ and $\nu = -\frac{\mu}{1+2\mu}$ whenever both entropic moments converge. The BBM uncertainty relation (1.18) is recovered as a limiting case for $\mu = \nu = 0$.

A very recent improvement of the BBM inequality on radial uncertainty products has been achieved [71] by considering a Rényi-like inequality instead of the Shannon-like BBM one, giving rise to a lower bound with a new parameter q , providing the original bound as $q = 1$. The optimization of this new bound with respect to the parameter q improves the well-known results with the particular value $q = 1$. Similarly to the uncertainty inequality for frequency moments, Eq.(1.19), there exists a Rényi-like one given by [72]

$$R_q(\rho) + R_t(\gamma) \geq \ln \left[(2\pi)(2q)^{\frac{1}{2(q-1)}} (2t)^{\frac{1}{2(t-1)}} \right]^d, \quad (1.20)$$

with $\frac{1}{q} + \frac{1}{t} = 2$. The BBM inequality is recovered for the particular case $q = t = 1$. Apart from the above mentioned case, it is clear that one of the orders must be above unity while the other is below unity. In what follows, let us choose the parameters in such a way that $q \geq 1 \geq t$. The opposite order can be considered by exchanging the distributions ρ and γ .

Let us now discuss the uncertainty relations which involve the Fisher informations. Since the nineteen fifties the Stam inequalities [73] are known to be

$$F[\rho] \leq 4 \langle p^2 \rangle \quad \text{and} \quad F[\gamma] \leq 4 \langle r^2 \rangle, \quad (1.21)$$

which link the position (momentum) Fisher information and the momentum (position) radial expectation value $\langle p^2 \rangle$ (respectively $\langle r^2 \rangle$). See also Ref. [74] where generalized uncertainty-like relationships to arbitrary dimensions are found and some of its applications to finite many-electron systems are provided. Recently, a Fisher-information-based uncertainty relation has been found [75] as

$$F[\rho] \cdot F[\gamma] \leq 4d^2, \quad (1.22)$$

which is valid not only for one-dimensional [27] but also for d -dimensional [76] real-valued wavefunctions.

Finally, let us point out that for further relevant information about uncertainty relations, particularly the ones of entropic character, see the recent publications [77, 78, 79].

1.3 Complexity measures

Another relevant concept within Information Theory is complexity [4, 80, 81, 82], strongly related, in some cases, to the aforementioned magnitudes. Indeed some of the recent definitions of complexity consist of the product of two factors measuring respectively order and disorder on the given system or process, or equivalently localization and delocalization [50]. It is important to note here that there is not a unique and universal definition of complexity and therefore many mathematical quantifications exist to explore pattern, structure or uncertainty as complexity ingredients or indicators. Complexity is used in very different fields including, for instance, molecular and DNA (deoxyribonucleic acid) analyses, dynamical systems, time series, spatial patterns or analysis of atomic models [83, 84] and multielectronic systems [81, 85, 54, 86, 53, 87], the last two being the focus of interest in this work. For further properties of these statistical complexities see the recent monograph of K.D. Sen [4].

The product complexity measures were criticized and consequently modified, leading to powerful estimators applied in a wide variety of fields [88, 89, 85]. Following the pioneering product measure of López-Ruiz, Mancini and Calbet (LMC shape complexity) [50] some other related and generalized complexity measures were defined and successfully applied [85, 90, 91, 86].

Here we collect three two-component composite information-theoretic measures which have been recently shown to be very useful to quantify the complexity of a probability distribution $\rho(\vec{r})$ of a continuous variable \vec{r} define over the d -dimensional domain $\Delta \subset \mathbb{R}^d$. In this context, the term ‘‘complexity’’ refers to the difficulty of modeling the distribution, according to the number and intricacy of functions needed to do it. This will be clearly illustrated in the discussion of the numerical results in Section 4.3. Below, we present the LMC, Fisher-Shannon and Cramér-Rao complexities which seems to be, up to now, the main two-component measures of complexity for a probability distribution $\rho(\vec{r})$.

The LMC or shape complexity [50, 92]

$$C_{LMC} = D[\rho] \cdot N[\rho] \quad (1.23)$$

involves the product of two important information-theoretic quantities, namely the disequilibrium, $D[\rho]$ given in Eq. (1.7) which quantifies the departure of the probability density from uniformity, and the Shannon entropy $S[\rho]$ defined in Eq. (1.4), which is a general measure of randomness or uncertainty of the probability density. Then, this composite information-theoretic quantity measures the complexity of the system by means of a combined balance of the average of the probability density $\rho(\vec{r})$, as given by $D[\rho]$, and its total bulk extent, as given by Shannon entropy power or Shannon length $N[\rho]$ given by

Eq. (1.12). As both quantities D and S possess a global character, the C_{LMC} complexity is a global measure of complexity.

The Fisher-Shannon complexity [87, 93],

$$C_{FS}[\rho] = F[\rho] \cdot J[\rho] \quad (1.24)$$

is built up as the product of a global information measure given by the "normalized" Shannon entropy power

$$J[\rho] = \frac{1}{2\pi e} e^{\frac{2}{d} S[\rho]} \quad (1.25)$$

and a local one, the Fisher information, Eq. (1.9). Then, the Fisher-Shannon complexity measures the gradient content or oscillatory degree of $\rho(\vec{r})$ (given by the Fisher information, $F[\rho]$) combined with its total extent (Shannon entropy power, $J[\rho]$). The properties of the Fisher information make this measure to be an appropriate candidate to define a complexity measure in terms of complementary global and local factors. The definition of $J[\rho]$ has been chosen in order to preserve the general properties of complexity, in particular the scaling invariance, including a constant factor in order to simplify the expression of its universal lower bound, $I[\rho] \cdot J[\rho] \geq d$, see [39, 94].

From the Cramér-Rao bound [39, 94] we can consider a complexity measure given by the Cramér-Rao product as [53]

$$C_{CR}[\rho] = F[\rho] \cdot (\Delta\vec{r})^2 \quad (1.26)$$

where the connection between both the local and global levels of uncertainty is manifested again. The Cramér-Rao complexity quantifies the gradient content of $\rho(\vec{r})$ together with the spreading of the probability distribution respect to its mean value (centroid).

According to the units in which each individual component is measured, it is straightforwardly observed that the above complexities are dimensionless quantities. It is also worthy to mention that the three complexities are known to be bounded from below for d -dimensional distributions [94, 73, 95, 96]. In addition, and contrary to other notions of complexity encountered and used also in the scientific literature [97, 98, 99, 100], such as the computational and logarithmic complexities which depend on the context, these three complexity measures are intrinsic properties of the system since they are described by density-dependent functionals.

Finally, we define a one-parameter generalization of the two-component LMC shape complexity, namely the Shape-Rényi complexity [90]

$$C_{SR}^{(q)}[\rho] = D[\rho] \cdot e^{R_q[\rho]}, \quad (1.27)$$

defined as the product of the disequilibrium, Eq. (1.7), and the the exponential of the Rényi entropy, Eq. (1.5). The power q of the distribution allows us to enhance or diminish, by increasing or decreasing its value, the relative contribution to the complexity measure of the Rényi entropy power integrand over different regions. In the limit case $q \rightarrow 1$, the LMC complexity is recovered, $C_{LMC}[\rho] = C_{SR}^{(1)}[\rho]$.

1.4 Comparative measures: Similarity and divergence

In Part I of the Thesis we will place particular emphasis on the concepts of similarity and dissimilarity (or divergence) among two or more distributions $\rho_1(\vec{r}), \rho_2(\vec{r}), \dots, \rho_n(\vec{r})$, all of them defined over the same d -dimensional domain $\Delta \subset \mathbb{R}^d$. It is of general interest to have at our disposal other density functionals which enable us to measure the "distance" and/or similarity among different distributions to compare them.

Many information-theoretic similarity and divergence measures between two probability distributions have been introduced and extensively studied regarding their mathematical properties [101, 39, 102, 103, 104]. The wide variety of applications of these measures can be found in the analysis of contingency tables [105], as well as in approximation of probability distributions [106], in signal processing [107], inference problems [108], pattern recognition [109], biodiversity [110], classification [111], homology [112], neural networks [113], computational linguistics [114], study of electronic densities [29, 30, 115, 31, 116], molecular similarity [117, 118], texture and image registration [119, 120, 121], sequence analysis [122], machine learning [123], artificial intelligence [124], fuzzy set theory [125] and more recently in quantum information theory [25], in particular as a measure of entanglement [23].

The recent development in knowledge-based chemical research has created a surge of interest in chemical similarity or divergence. Molecular modelling, molecular similarity [48, 117] and quantitative structure activity relationship (QSAR) are simple examples of such an interest [126]. More recently the molecular quantum similarity framework has been used to provide a new set of quantum quantitative structure-properties relationship procedures (QQSPR) [127].

Among the proposed measures, the pioneering and best known one is the Kullback-Leibler divergence or relative entropy [128] based on Shannon entropy [41]. It is defined as

$$KL[\rho_1, \rho_2] = \int_{\Delta} \rho_1(\vec{r}) \ln \frac{\rho_1(\vec{r})}{\rho_2(\vec{r})} d\vec{r}. \quad (1.28)$$

The main properties of this quantity are: (i) it is always non-negative if the normalization of both distributions are identical, i.e. $\int_{\Delta} \rho_1(\vec{r}) d\vec{r} = \int_{\Delta} \rho_2(\vec{r}) d\vec{r}$, (ii) the minimum value $KL[\rho_1, \rho_2] = 0$ is reached only for $\rho_1(\vec{r}) = \rho_2(\vec{r})$, (iii) the Shannon entropy, $S[\rho]$, can be obtained except for a sign by taking $\rho_2(\vec{r}) = 1$ in Eq. (1.28), so, we can give a new interpretation for the Shannon entropy, as the relative entropy of $\rho_1(\vec{r})$ with respect to the uniform distribution. This quantity can be considered as a measure of how different the two distributions are attending to their global spreading. The absence of symmetry of the KL divergence induces its symmetrization

$$KLS[\rho_1, \rho_2] = \frac{1}{2} (KL[\rho_1, \rho_2] + KL[\rho_2, \rho_1]), \quad (1.29)$$

in order to get an appropriate interpretation of this quantity as an information distance.

The divergence measure $KL[\rho_1, \rho_2]$, has been extensively used in Bayesian updating through the minimum-cross-entropy principle [129]. Another recent and important application belongs to the field of QIT, where the relative entropy can be used as a measure

of distinguishability between quantum systems and therefore as a quantum entanglement measure [24]. Kullback-Leibler divergences have been also widely employed in a huge variety of applications in atomic and molecular systems [130, 116, 131].

Since then many other measures of divergence have been proposed, studied and applied, in particular by considering theoretic-information magnitudes with both local character (using Fisher information, [132]), or global character (using Shannon entropy, [133, 134]), on which we inquire. Jensen-Shannon divergence ($JSD[\rho_1, \rho_2]$) is directly related to both the Shannon entropy (1.4) and the Kullback-Leibler relative entropy (1.28) as [133, 134]

$$\begin{aligned} JSD[\rho_1, \rho_2] &= S\left[\frac{\rho_1 + \rho_2}{2}\right] - \frac{1}{2}(S[\rho_1] + S[\rho_2]) = \\ &= \frac{1}{2}\left(KL\left[\rho_1, \frac{\rho_1 + \rho_2}{2}\right] + KL\left[\rho_2, \frac{\rho_1 + \rho_2}{2}\right]\right). \end{aligned} \quad (1.30)$$

It is characterized for quantifying the Shannon "entropy excess" of the mean density with respect to the mean entropy of the involved distributions. Last equality provides an additional interpretation of the $JSD[\rho_1, \rho_2]$ as the mean "distance", in terms of $KL[\rho_1, \rho_2]$ of each density to the mean one. Jensen-Shannon divergence possesses the main properties required for a measure to be interpreted as an informational distance, namely non-negativity (as a consequence of the convexity of the $S[\rho]$ functional), symmetry and the minimum value zero being reached only when $\rho_1 = \rho_2$.

The Jensen-Shannon divergence can be generalized to a measure of the mean distance among an arbitrary number n of distributions, $\rho_i(\vec{r})$, each one weighted by a factor λ_i (with $i = 1, \dots, n$) as follows:

$$JSD[\lambda_i, \rho_i] = S[\bar{\rho}] - \sum_{i=1}^n \lambda_i S[\rho_i], \quad (1.31)$$

where

$$\bar{\rho} = \sum_{i=1}^n \lambda_i \rho_i; \quad \sum_{i=1}^n \lambda_i = 1. \quad (1.32)$$

This definition reduces to the initial one in Eq. (1.30) by considering the particular case $n = 2$ and $\lambda_1 = \lambda_2 = 1/2$. Recently, Lamberti and Majtey have investigated and generalized the properties of JSD in the framework of non-extensive Tsallis statistics [135, 25], and J. Antolín and J.C. Angulo found several applications of this generalized divergence to atomic systems [136].

Some generalized entropies such as the Rényi one, Eq. (1.5), have also been used to formulate one-parameter generalized measures of divergence, discrepancy or distinguishability [137]. The "Jensen-Rényi divergence", to be denoted as $JRD^{(q)}$, was conceived at a first step [138] as a measure of dissimilarity/divergence between two distribution density functions, say $\rho_1(\vec{r})$ and $\rho_2(\vec{r})$. In this way, the deviation from linearity allows to define the Jensen-Rényi divergence between two distributions as [138]

$$JRD^{(q)}[\rho_1, \rho_2] = R_q\left[\frac{\rho_1 + \rho_2}{2}\right] - \frac{1}{2}(R_q[\rho_1] + R_q[\rho_2]), \quad (1.33)$$

which constitutes the difference between the Rényi entropy of the arithmetic mean and the arithmetic mean of the respective Rényi entropies of $\rho_1(\vec{r})$ and $\rho_2(\vec{r})$. Generalizations of this divergence have been provided very recently [137], by considering mean values for arbitrary number of distributions and their associated weights, as previously done for *JSD*:

$$JRD^{(q)}[\lambda_i, \rho_i] = R_q[\bar{\rho}] - \sum_{i=1}^n \lambda_i R_q(\rho_i). \quad (1.34)$$

This divergence generalizes the previously introduced which is reached in the limit $JSD = \lim_{q \rightarrow 1} JRD^{(q)}$. The non-negativity of $JRD^{(q)}$ is guaranteed only for $0 < q < 1$, constraint which arises from the convex/concave character of the frequency moments ω_q , Eq. (1.6), according to the value of q . So, $JRD^{(q)}$ allows us to establish a comparison among densities, with weights λ_i , emphasizing their similarity within specific regions of their common domain.

Another straightforward one-parameter relative measure, now in terms of the Rényi entropy is that given by the relative Rényi entropy [39]

$$R_q[\rho_1, \rho_2] = \frac{1}{q-1} \ln \int_{\Delta} \frac{\rho_1(\vec{r})^q}{\rho_2(\vec{r})^{q-1}} d\vec{r}, \quad (1.35)$$

which constitutes a generalization of the Kullback-Leibler relative entropy, Eq. (1.28), found in the limit $KL[\rho_1, \rho_2] = \lim_{q \rightarrow 1} R_q[\rho_1, \rho_2]$. Like the *KL* relative entropy, the relative Rényi entropy is non-negative for any $q > 0$ whenever the involved integral converge, and the original Rényi entropy, Eq. (1.5) is obtained for the uniform distribution $\rho_2(\vec{r}) = 1$.

In contrast to the above measures, which have an entropic origin, there exists a measure for comparing two probability distributions within information theory. Quantum similarity, introduced in the early eighties, attempts to provide a quantitative measure of the degree of similarity between two quantum objects, having its grounds on the comparison of their one-particle densities with later applications to other quantities, such as *e.g.* Fukui functions [139]. To quantify the similarity between quantum systems under comparison, a general Quantum Similarity Measure (*QSM*) [118] can be defined by means of an integrated measure enclosing the density functions attached to the quantum systems. For the case of molecules or atoms this kind of similarity measures can be defined as the scalar product between the first order density functions weighted with a bielectronic definite positive operator [140]. The simplest choice, the Dirac delta operator, leads to the well-known Quantum Similarity Index (*QSI*) [48]

$$QSI[\rho_1, \rho_2] = \frac{\int \rho_1(\vec{r})\rho_2(\vec{r})d\vec{r}}{\sqrt{\int \rho_1^2(\vec{r})d\vec{r} \int \rho_2^2(\vec{r})d\vec{r}}}, \quad (1.36)$$

which is basically the overlap integral of the density distributions. The numerator is referred as the *QSM* of $\rho_1(\vec{r})$ and $\rho_2(\vec{r})$, while the denominator normalizes the *QSM* in terms of the respective disequilibria defined in Eq. (1.7). The main properties of this measure are: (i) symmetry under exchange of distributions, (ii) it is bounded within the interval (0, 1]

and (iii) the maximum value 1 is only reached for $\rho_1(\vec{r}) = \rho_2(\vec{r})$. There is an important mathematical connection between the *QSI* measure, Eq. (1.36), and Hölder's inequality [141] as will be described in more detail in Chapter 5.

The definition of *QSI* arises from the molecular research field [118, 142, 117], but later has been widely applied in many different problems related to atomic systems in order to establish a comparative measure as indicator of similarity between two atomic one-particle probability distributions [115, 143, 144, 139, 145, 146].

So far, we have reviewed some of the most relevant measures used to characterize different facets and properties of probability distributions from a statistical standpoint. These probability distributions can represent both classical and quantum systems. In the first part of the thesis we perform an information-theoretic study, of probability density functions of quantum systems or models, from a classical statistics point of view.

Entropy and complexity analysis of Dirac-delta-like quantum potentials

The elementary one-dimensional potentials $V(x)$ are interesting *per se* because they provide approximate models for the physically exact three-dimensional quantum-mechanical potentials of physical systems. Moreover, they are very useful for the interpretation of numerous microscopic and macroscopic properties of natural systems, mainly because their associated quantum-mechanical equation of motion can be exactly solved, so that their physical solutions (wavefunctions) are known to be expressed in terms of special functions of applied mathematics and mathematical physics [147, 148]. This is the case for the piecewise-constant potentials (finite and infinite wells), harmonic oscillator ($V \sim x^2$), Coulomb potential ($V \sim 1/|x|$) and delta-function potential ($V \sim \delta(x)$), to mention just a few although they do not abound.

Recently the emerging information theory of quantum systems, which is at the basis of the modern quantum information and quantum computation, has provided the best methodology to quantify the various facets of the position (usually associated with the charge distribution in atomic systems) and momentum spreading all over the confinement region of the system, far beyond the well-known standard deviation or Heisenberg measure. This quantification is carried out by means of various information-theoretic functionals (such as the Fisher information, the Rényi and Shannon entropies, and the associated information-theoretic lengths) and complexity measures (such as the Cramér-Rao, Fisher-Shannon and LMC ones) previously defined in Chapter 1. Such a work has been partially done for the infinite well [149, 150, 27, 151], finite well [152], the harmonic-oscillator [153, 154], Coulomb potential [153, 154] and other potentials [155, 156], but the Dirac-delta-like ones still remain to be explored within that framework, to the best of our knowledge. Here we want to contribute to fill this lacuna.

The one-dimensional Dirac-delta-function potential $\delta(x)$, where x is the cartesian coordinate, $-\infty < x < \infty$, has been shown to be very useful to describe a number of properties not only for the three-dimensional hydrogen atom and molecular ion [157, 158, 159, 160] but also in d -dimensional physics [161, 162]. Moreover, this function has been proved to describe short-range potentials such as the interaction between the electrons and fixed ions in a lattice crystal. The use of potentials composed by an array of N delta functions is very frequent in atomic and molecular physics [163, 164, 157, 160, 159], condensed matter [165, 166, 167] and quantum computation [168]. Let us just mention the useful Kronig-Penney model to study the physical and chemical properties of solids (see e.g. [165]) and the numerous works done to describe the behaviour of impurities in solid state systems, particularly quantum wires (see e.g. [169, 166, 170] and references therein) and to char-

acterize the instantaneous interaction between flying and static qubits (see e.g. [168] and references therein).

In this chapter we will first calculate the position and momentum entropy and complexity measures of the bound-state wavefunctions of the one-dimensional hydrogen atom with a delta-function interaction, which has been used to study different phenomena of bosonic [171, 172], fermionic [163, 159, 160, 157] and anionic [162] systems. In addition, we will compute these quantities for the wavefunctions of the single-particle systems with a twin delta-function potential, which has been used to approximate the helium atom [164, 157], the hydrogen molecular ion [159, 157, 160] and some scattering [173] and solid-state [167] phenomena.

In Section 2.1, we obtain the direct spreading and complexity measures of the one-dimensional hydrogen atom with a single-delta potential, including, the standard deviation and the Fisher, Rényi and Shannon information-theoretic lengths in the two reciprocal spaces. In Section 2.2, we carry out a similar study for a single-particle system with a twin-delta interaction. The previous analytical results are numerically analyzed in Section 2.3. Finally we give some conclusions and open problems.

2.1 Information theory of a single-delta potential

The time-dependent Schrödinger equation of a particle with mass m moving under the action of a single attractive singular potential of Dirac-delta type, $V(x) = -g\delta(x)$ with $g > 0$ a real constant, is given by

$$\left[-\frac{\hbar^2}{2m} \frac{d^2}{dx^2} - g\delta(x) \right] \Psi(x, t) = i\hbar \frac{\partial}{\partial t} \Psi(x, t) \quad (2.1)$$

When the particle is an electron and $g = Ze^2/4\pi\epsilon_0$, this system may be considered as the one-dimensional hydrogenic atom (in particular $Z = 1$ for neutral hydrogen) with δ -function interaction. It is well-known that this system has a unique bound state with energy $E = -|E| < 0$ and a continuum of unbound states for $E > 0$. Moreover, the wavefunction of the bound state is given [159, 158, 174] by

$$\Psi(x, t) = \psi(x) e^{-\frac{i}{\hbar}Et} \quad (2.2)$$

with the expressions

$$E = -\frac{mg^2}{2\hbar^2} \quad \text{and} \quad \psi(x) = \sqrt{k} e^{-k|x|} \quad ; \quad k \equiv \frac{mg}{\hbar^2} \quad (2.3)$$

for its energy and normalized-to-unity eigenfunction, respectively. Notice that $k = a_0^{-1}$ in the hydrogen case, where $a_0 = 4\pi\epsilon_0\hbar^2/me^2$ is the Bohr radius.

The momentum-space wavefunction $\Phi(p, t) = \phi(p) e^{-\frac{i}{\hbar}Et}$, where the momentum eigenfunction $\phi(p)$ is given [159] by the Fourier transform of the position eigenfunction $\psi(x)$ so that

$$\phi(p) = \frac{1}{\sqrt{2\pi\hbar}} \int_{-\infty}^{\infty} \psi(x) e^{-\frac{i}{\hbar}px} dx = \sqrt{\frac{2p_0}{\pi}} \frac{p_0}{p^2 + p_0^2}, \quad (2.4)$$

with $p_0 \equiv \hbar k$, has a Lorentzian form.

In this section we will compute the information-theoretic measures of the position and momentum spreading of this system, which are characterized by the position and momentum probability densities

$$\rho(x) = ke^{-2k|x|} \quad (2.5)$$

and

$$\Pi(p) = \frac{2p_0^3/\pi}{(p^2 + p_0^2)^2}, \quad (2.6)$$

respectively. Emphasis will be made on the direct spreading measures in both position and momentum spaces which include the standard deviation and the Fisher, Rényi and Shannon lengths.

(a) In position space we obtain from Eqs. (1.1), (1.2) and (2.5) the value

$$\Delta x = \frac{\sqrt{2}}{2k} \quad (2.7)$$

for the standard deviation in a straightforward manner, because $\langle x \rangle = 0$ and $\langle x^2 \rangle = 1/(2k^2)$. Moreover, from Eqs. (1.5)-(1.9) and (2.5), the values

$$\omega_q[\rho] = \frac{1}{q}k^{q-1} \quad ; \quad R_q[\rho] = - \left(\ln k + \frac{\ln q}{1-q} \right) \quad (2.8)$$

$$S[\rho] = 1 - \ln k \quad \text{and} \quad F[\rho] = 4k^2 \quad (2.9)$$

are obtained for the entropic moments, the Rényi and Shannon entropies and the Fisher information, respectively. Then, from Eqs. (1.11)-(1.13), (2.8) and (2.9) we obtain the values

$$L_q^R[\rho] = \frac{1}{kq} \quad , \quad N[\rho] = \frac{e}{k} \quad \text{and} \quad \delta x = \frac{1}{2k} \quad (2.10)$$

for their respective lengths. The mutual comparison of Eqs. (2.7) and (2.10) indicates that $\delta x = \Delta x/\sqrt{2} \cong 0.7071\Delta x$ and $N[\rho] = 2e\delta x$, so that

$$\delta x < \Delta x < N[\rho] \quad (2.11)$$

In addition, it is useful to calculate, in order to quantify the complexity of the distribution, the two-component composite measures of Cramér-Rao, Fisher-Shannon and LMC types defined by Eqs. (1.26), (1.24) and (1.23) respectively. From those expressions and Eq. (2.10), we have the values

$$C_{CR}[\rho] = 2 \quad , \quad C_{FS}[\rho] = \frac{2e}{\pi} \quad \text{and} \quad C_{LMC}[\rho] = \frac{e}{2} \quad (2.12)$$

for the corresponding complexities. It is worthy to remark that, in spite of the dependence of the individual components on the potential strength g , the above complexity values do not depend on such a parameter. It is worth noting that the same phenomenon holds for homogeneous potentials [156]. Additionally, all of them are above unity as should be expected [94, 95].

(b) In momentum space we observe that the moments $\langle p^a \rangle$ of the momentum density in Eq. (2.6) diverge for $a \geq 3$ due to the long-range behavior of the density $\Pi(p)$. The only finite moments of integer order are $\langle p^0 \rangle = 1$, $\langle p \rangle = 0$ and $\langle p^2 \rangle = p_0^2$. Then, the momentum standard deviation is given by

$$\Delta p = (\langle p^2 \rangle - \langle p \rangle^2)^{\frac{1}{2}} = p_0. \quad (2.13)$$

The entropic moments have the values

$$\omega_q[\Pi] = \left(\frac{2}{\pi p_0} \right)^q p_0 \frac{\Gamma(2q - \frac{1}{2})\sqrt{\pi}}{\Gamma(2q)} \quad (2.14)$$

with $q > \frac{1}{4}$ as imposed by the convergence of the integral defining $\omega_q[\Pi]$, and the Rényi entropies

$$R_q[\Pi] = \frac{1}{1-q} \ln \omega_q[\Pi] = \frac{1}{1-q} \ln \left(p_0 \sqrt{\pi} \left(\frac{2}{\pi p_0} \right)^q \frac{\Gamma(2q - \frac{1}{2})}{\Gamma(2q)} \right), \quad (2.15)$$

also with $q > \frac{1}{4}$. Moreover, taking into account Eqs. (2.6) and (2.14) one has that the momentum Shannon entropy is given by

$$S[\Pi] = - \left. \frac{d}{dq} \ln \omega_q[\Pi] \right|_{q=1} = \ln \frac{8\pi p_0}{e^2} \quad (2.16)$$

and the momentum Fisher information by

$$F[\Pi] = \frac{2}{p_0^2}. \quad (2.17)$$

Therefore, the Rényi, Shannon and Fisher information-theoretic lengths (1.11)-(1.13) are

$$L_q^R[\Pi] = \left[p_0 \sqrt{\pi} \left(\frac{2}{\pi p_0} \right)^q \frac{\Gamma(2q - \frac{1}{2})}{\Gamma(2q)} \right]^{\frac{1}{1-q}}, \quad q > \frac{1}{4}, \quad (2.18)$$

$$N[\Pi] = \frac{8\pi p_0}{e^2}, \quad (2.19)$$

and

$$\delta p = \frac{\sqrt{2}}{2} p_0, \quad (2.20)$$

respectively. The mutual comparison of Eqs. (2.13), (2.19) and (2.20) shows that $\delta p = \Delta p / \sqrt{2} \cong 0.7071 \Delta p$ and $N[\Pi] = \frac{8\pi}{e^2} \Delta p$, so that

$$\delta p < \Delta p < N[\Pi], \quad (2.21)$$

as also occurs for the position density $\rho(x)$, see Eq. (2.11), showing the hierarchy of the different spreading measures for a single-delta potential.

In addition, we obtain the values

$$C_{CR}[\Pi] = 2 \quad , \quad C_{FS}[\Pi] = \frac{64\pi}{e^5} \quad \text{and} \quad C_{LMC}[\Pi] = \frac{10}{e^2} \quad (2.22)$$

for the Cramér-Rao, Fisher-Shannon and LMC complexities of the system in momentum space, where we have taken into account Eqs. (1.26)-(1.23) together with Eq. (2.14) for $q = 2$, and Eqs (2.13), (2.17) and (2.19). It is important to note that: (i) the Cramér-Rao complexities in position and momentum spaces are equal; this is because when the wavefunction is real and its moment of order 1 vanishes, the relationships $F[\rho] = \frac{4}{\hbar^2} V[\Pi]$ and $F[\Pi] = \frac{4}{\hbar^2} V[\rho]$ between Fisher information and variance are fulfilled; and (ii) these three complexity measures are independent of the parameter k , highlighting that the difficulty of modeling the distributions $\rho(x)$ and $\Pi(p)$ is determined by the presence of a unique parameter, but not by its specific value.

- (c) Finally, the expressions given by Eqs. (2.7), (2.10), (2.13), (2.19) and (2.20) yield the following uncertainty products:

$$\Delta x \cdot \Delta p = \frac{\hbar}{\sqrt{2}} = 0.7071\hbar \quad (2.23)$$

$$\delta x \cdot \delta p = \frac{\sqrt{2}}{4}\hbar = 0.3536\hbar \quad (2.24)$$

$$N[\rho] \cdot N[\Pi] = \frac{8\pi}{e}\hbar = 9.2458\hbar \quad (2.25)$$

respectively. The above products do not depend on the g parameter value, and also they certainly fulfil the Heisenberg [175], Fisher-information-based [27, 75] and Shannon-entropy-based or entropic [66, 176, 177] uncertainty relations given by

$$\Delta x \cdot \Delta p \geq \frac{\hbar}{2} \quad (2.26)$$

$$\delta x \cdot \delta p \leq \frac{\hbar}{2} \quad (2.27)$$

$$N[\rho] \cdot N[\Pi] \geq e\pi\hbar \quad (2.28)$$

respectively.

2.2 Information theory of a twin-delta potential

Let us here consider the non-relativistic motion of a particle with mass m in a potential having not only one (as in the previous section) but two attractive centers separated by a distance $2a$, i.e. in the twin- δ -function potential defined as

$$V(x) = -g[\delta(x+a) + \delta(x-a)]$$

This potential with $g = e^2/4\pi\epsilon_0$ not only describes the one-dimensional hydrogen molecule with δ -function interactions (see [159, 157, 160] and references therein) and approximates the helium atom [164, 157], but also it has been used to interpret some scattering [173] and solid-state phenomena [167]. Because of its symmetry, this potential has two types of solutions which correspond to even and odd eigenfunctions [159, 158].

The even bound-state solution has the eigenfunction

$$\psi_+(x) = \begin{cases} Ae^{kx} & , x < -a \\ B \cosh(kx) & , -a < x < a \\ Ae^{-kx} & , x > a \end{cases} \quad (2.29)$$

and the energy E is given by the eigenvalue condition

$$\gamma(1 + \tanh \gamma) = \frac{2a}{a_0} \quad (2.30)$$

with $\gamma = ka$, $k = \frac{\sqrt{2m|E|}}{\hbar}$ and $a_0 = \frac{\hbar^2}{mg}$. The parameters A and B are given by

$$A = Be^\gamma \cosh \gamma \quad \text{and} \quad B = \left(\frac{2\gamma}{a}\right)^{1/2} (e^{2\gamma} + 2\gamma + 1)^{-1/2}, \quad (2.31)$$

as imposed by the continuity and the normalization conditions.

The odd solution has the eigenfunction

$$\psi_-(x) = \begin{cases} Ce^{kx} & , x < -a \\ D \sinh(kx) & , -a < x < a \\ -Ce^{-kx} & , x > a \end{cases} \quad (2.32)$$

where

$$C = -De^\gamma \sinh \gamma \quad \text{and} \quad D = \left(\frac{2\gamma}{a}\right)^{1/2} (e^{2\gamma} - 2\gamma - 1)^{-1/2}, \quad (2.33)$$

and the corresponding eigenvalue equation being

$$\gamma(1 + \coth \gamma) = \frac{2a}{a_0}. \quad (2.34)$$

A detailed analysis of the energy eigenvalue conditions (2.30) and (2.34) shows [158] that (i) for $a \gg a_0/2$ (i.e., in the limit of large separation) there are two degenerated eigenfunctions, one even and the other odd, at the energy given by Eq. (2.3) of the single-delta case, (ii) for $a < a_0/2$ there are no odd solutions and, most important, (iii) the odd solution, whenever exists, lies energetically above the corresponding even solution, see Fig 2.1; *i.e.* it is less bounded. So, we will restrict ourselves to the even bound-state eigenstate given by Eqs. (2.29) and (2.31) in position space. The corresponding Fourier transformation provides the expression

$$\phi_+(p) = \frac{1}{\sqrt{2\pi\hbar}} \int_{-\infty}^{\infty} \psi_+(x) e^{-\frac{i}{\hbar}px} dx = B \sqrt{\frac{2\hbar}{\pi}} \frac{p_0 e^{\frac{p_0 a}{\hbar}} \cos \frac{pa}{\hbar}}{p^2 + p_0^2}, \quad (2.35)$$

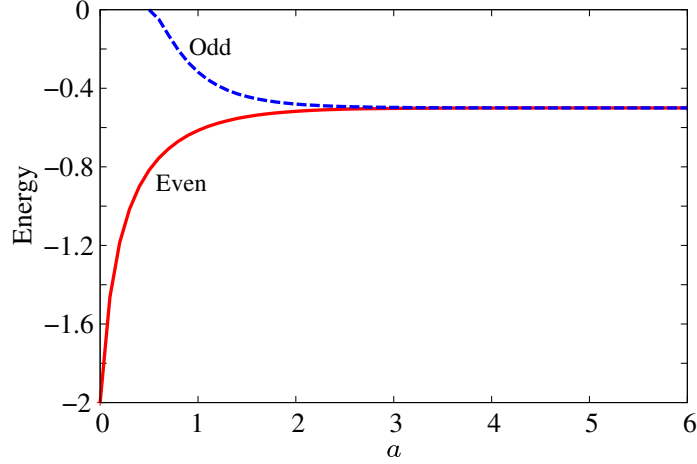


Figure 2.1: Even (red) and odd (blue) eigenenergies as a function of the distance ($2a$) between delta function. Atomic units are used.

where $p_0 \equiv \hbar k$. In this section we will quantify the position and momentum spreading of this system in its ground state as described by the eigenfunctions (2.29) and (2.35), respectively. This will be done not only by means of the standard deviation (already done by Lapidus [159]) but also by the following information-theoretic measures: Rényi and Shannon entropies and Fisher information and, most appropriately, their corresponding lengths. To do that, and according to the procedure used in Section 2.1, we start with the expressions $\rho_+(x) = |\psi_+(x)|^2$ and $\Pi_+(p) = |\Phi_+(p)|^2$ for the position and momentum space quantum-mechanical probability densities of this state, respectively.

- (a) In position space, we first check that $\langle x^0 \rangle_+ = 1$ so that the density $\rho_+(x)$ is normalized to unity. Then, since $\langle x \rangle_+ = 0$ (all odd-order moments vanish because of symmetry), one obtains that the standard deviation $(\Delta x)_+$ is given by

$$(\Delta x)_+^2 = \langle x^2 \rangle_+ = \frac{a^2}{2\gamma^2} + a^2 \frac{e^{2\gamma} + \frac{2}{3}\gamma + 1}{e^{2\gamma} + 2\gamma + 1} \quad (2.36)$$

which provides the Heisenberg uncertainty measure of the system. Moreover, one can also obtain the even-order moments of $\rho_+(x)$ as

$$\begin{aligned} \langle x^{2n} \rangle_+ &= \frac{a^{2n}}{(2\gamma)^{2n}(e^{2\gamma} + 2\gamma + 1)} \times \\ &\times \left[\left(\frac{e^{4\gamma}}{2} + e^{2\gamma} \right) \Gamma(2n+1, 2\gamma) + \frac{\Gamma(2n+1, -2\gamma)}{2} + \frac{(2\gamma)^{2n+1}}{2n+1} \right] \end{aligned} \quad (2.37)$$

for $n = 0, 1, 2, \dots$, where the symbol $\Gamma(\alpha, \beta)$ denotes the incomplete gamma function. In addition, the Fisher information (1.9) of the system is computed as

$$F[\rho_+] = \frac{4B^2}{a} \gamma [e^\gamma \cosh \gamma - \gamma] = \frac{4\gamma^2}{a^2} \cdot \frac{e^{2\gamma} - 2\gamma + 1}{e^{2\gamma} + 2\gamma + 1} \quad (2.38)$$

so that the Fisher length $(\delta x)_+$ of the system, as defined by Eq (1.13), is given by

$$(\delta x)_+ = \frac{1}{\sqrt{F[\rho_+]}} = \frac{a}{2\gamma} \left(\frac{e^{2\gamma} + 2\gamma + 1}{e^{2\gamma} - 2\gamma + 1} \right)^{1/2}. \quad (2.39)$$

Working similarly, one can calculate the frequency or entropic moments

$$\omega_q[\rho_+] = 2 \left\{ B^{2q} \int_0^a [\cosh(kx)]^{2q} dx + A^{2q} \int_a^\infty e^{-2kqx} dx \right\}. \quad (2.40)$$

According to the integral expressions

$$\int_a^\infty e^{-2kqx} dx = \frac{ae^{-2q\gamma}}{2q\gamma}$$

and

$$\int_0^a [\cosh(kx)]^{2n} dx = \frac{a}{2^{2n}\gamma} \left[\binom{2n}{n} \gamma + \sum_{m=1}^n \binom{2n}{n-m} \frac{\sinh(2m\gamma)}{m} \right]$$

for any non-negative integer n , one has that the entropic moments $\omega_q[\rho_+]$ with integer order $q = n$ have the values

$$\omega_n[\rho_+] = \frac{2\gamma^{n-1}}{(2a)^{n-1}(e^{2\gamma} + 2\gamma + 1)^n} \times \left\{ \binom{2n}{n} \left(2\gamma + \frac{1}{n} \right) + \sum_{\substack{l=-n \\ l \neq 0}}^n \binom{2n}{n-l} \left(\frac{1}{n} + \frac{1}{l} \right) e^{2l\gamma} \right\}. \quad (2.41)$$

For the lowest n 's we have that $\omega_1[\rho_+] = 1$ and

$$\omega_2[\rho_+] = \frac{\gamma}{4a} \cdot \frac{e^{4\gamma} + 6e^{2\gamma} - 2e^{-2\gamma} + 12\gamma + 3}{(e^{2\gamma} + 2\gamma + 1)^2}, \quad (2.42)$$

which gives the "disequilibrium", Eq. 1.7, of the system. It is also worth noting that in the limit $a \rightarrow 0$ we obtain the single-delta-potential value k^{n-1}/n as given by Eq. (2.8). From the expressions (1.11) and (2.41) we obtain the Rényi uncertainty measure as given by the Rényi lengths

$$L_n^R[\rho_+] = (\omega_n[\rho_+])^{\frac{1}{1-n}}.$$

For $n = 2$ we have the Onicescu-Heller measure [49]

$$L_2^R[\rho_+] = \frac{4a}{\gamma} \cdot \frac{(e^{2\gamma} + 2\gamma + 1)^2}{e^{4\gamma} + 6e^{2\gamma} - 2e^{-2\gamma} + 12\gamma + 3}$$

Let us now compute the position Shannon entropy of the ground-state density $\rho_+(x)$. According to its definition (1.4), one has

$$\begin{aligned} S[\rho_+] &= -2 \left\{ \int_0^a \rho_+(x) \ln \rho_+(x) dx + \int_a^\infty \rho_+(x) \ln \rho_+(x) dx \right\} = \\ &= \frac{e^{2\gamma} - 2\gamma + 1}{e^{2\gamma} + 2\gamma + 1} - \ln \left(\frac{2\gamma/a}{e^{2\gamma} + 2\gamma + 1} \right) + \\ &+ 2 \left[\frac{\gamma^2 - \frac{\pi^2}{12} + 2\gamma \ln(1 + e^{2\gamma})}{e^{2\gamma} + 2\gamma + 1} - \frac{Li_2(-e^{-2\gamma})}{e^{2\gamma} + 2\gamma + 1} - \ln \cosh \gamma \right] \end{aligned} \quad (2.43)$$

where $Li_s(x) = \sum_{k=1}^{\infty} \frac{x^k}{k^s}$ is the polylogarithm function.

- (b) In momentum space we first observe that the density $\Pi_+(p) = |\phi_+(p)|^2$ has null odd moments $\langle p^{2n+1} \rangle_+ = 0$ for $n = 0, 1, 2, \dots$) because of symmetry. Moreover, all the even moments $\langle p^{2n} \rangle_+$ diverge except for $n = 0$ and 1: $\langle p^0 \rangle_+ = 1$ and

$$\langle p^2 \rangle_+ = \frac{\hbar^2 \gamma^2}{a^2} \cdot \frac{e^{2\gamma} - 2\gamma + 1}{e^{2\gamma} + 2\gamma + 1}. \quad (2.44)$$

So, the Heisenberg uncertainty measure of the system in momentum space is given by the standard deviation

$$(\Delta p)_+ = \langle p^2 \rangle_+^{1/2} = \frac{\hbar \gamma}{a} \left(\frac{e^{2\gamma} - 2\gamma + 1}{e^{2\gamma} + 2\gamma + 1} \right)^{1/2}. \quad (2.45)$$

Since the momentum wavefunction $\phi_+(p)$ is a real function, the Fisher information (1.9) of the ground state momentum density $\Pi_+(p)$ is related to the second order moment $\langle x^2 \rangle$ as we have already mention in page 35, *i.e.*

$$\begin{aligned} F[\Pi_+] &= \int_{-\infty}^{\infty} \frac{[\Pi'_+(p)]^2}{\Pi_+(p)} dp = 4 \int_{-\infty}^{\infty} [\phi'_+(p)]^2 dp = \\ &= -4 \int_{-\infty}^{\infty} \phi_+(p) \phi''_+(p) dp = \frac{4}{\hbar^2} \langle x^2 \rangle_+, \end{aligned} \quad (2.46)$$

which was calculated in Eq. (2.36). Then, the Fisher uncertainty measure $(\delta p)_+$ has, according to Eq. (1.13), the value

$$(\delta p)_+ = \frac{1}{\sqrt{F[\gamma_+]}} = \frac{\hbar}{2} \langle x^2 \rangle_+^{-1/2}. \quad (2.47)$$

Working similary, the frequency or entropic moments $\omega_n[\Pi_+]$ with integer n of the momentum density $\Pi_+(p)$ are given by

$$\omega_n[\Pi_+] = \frac{n}{(4\pi p_0)^{n-1}} \frac{e^{2n\gamma}}{(e^{2\gamma} + 2\gamma + 1)^n} \times$$

$$\times \left[\frac{(4n-3)!!}{(n!)^2} + 2^{2-2n} \sum_{l=1}^n \frac{e^{-2l\gamma}}{(n-l)!(n+l)!} \cdot \sum_{j=0}^{2n-1} \frac{(4n-j-2)!(4l\gamma)^j}{j!(2n-j-1)!} \right] \quad (2.48)$$

with $p_0 = \hbar k = \frac{\hbar\gamma}{a}$. It is interesting to check the normalization condition $\omega_1[\Pi_+] = 1$, and to compute the second order entropic moment or disequilibrium:

$$\omega_2[\Pi_+] = \frac{a}{8\pi\hbar\gamma(e^{2\gamma} + 2\gamma + 1)} \times \left\{ 15e^{4\gamma} + 4e^{2\gamma} \left(\frac{8}{3}\gamma^3 + 8\gamma^2 + 10\gamma + 5 \right) + \frac{64}{3}\gamma^3 + 32\gamma^2 + 20\gamma + 5 \right\}. \quad (2.49)$$

From Eqs. (1.5), (1.11) and (2.48) the Rényi entropies and lengths of the system are obtained in a straightforward manner. Moreover, from Eq. (1.4) and the expression of $\Pi_+(p)$ one obtains that the momentum Shannon entropy of the twin-delta potential can be expressed as

$$S[\Pi_+] = -2M \times \left\{ \frac{\pi(\ln M - 4 \ln p_0)}{8p_0^3} [1 + e^{-2\gamma}(1 + 2\gamma)] + J_1(a, p_0) - 2J_2(a, p_0) \right\} \quad (2.50)$$

with

$$M = \frac{4p_0^3}{\pi} \frac{e^{2\gamma}}{e^{2\gamma} + 2\gamma + 1}$$

and the integrals

$$J_1(a, p_0) = \int_0^\infty \frac{\cos^2\left(\frac{pa}{\hbar}\right) \ln \cos^2\left(\frac{pa}{\hbar}\right)}{(p^2 + p_0^2)^2} dp$$

$$J_2(a, p_0) = \int_0^\infty \frac{\cos^2\left(\frac{pa}{\hbar}\right) \ln(p^2 + p_0^2)}{(p^2 + p_0^2)^2} dp$$

which have not been solved analytically up to now. The corresponding Shannon length is given by Eq. (1.12). We can go forward by calculating the momentum two-component complexities of Cramér-Rao, Fisher-Shannon and LMC types by use of Eqs. (1.23)-(1.26) together with Eqs. (2.45), (2.49), (2.50) and (1.12). From the information-theoretic quantities previously considered in this section, plenty of results can be derived. Let us here only point out the Heisenberg-Fisher uncertainty products defined as

$$(\Delta x)_+(\delta p)_+ = (\delta x)_+(\Delta p)_+ = \frac{\hbar}{2} \quad (2.51)$$

and the connection between the Cramér-Rao complexity and the Heisenberg product given by

$$\begin{aligned} C_{CR}[\rho_+] &= C_{CR}[\Pi_+] = \frac{4}{\hbar^2} [(\Delta x)_+(\Delta p)_+]^2 = \\ &= 4\gamma^2 \frac{e^{2\gamma} - 2\gamma + 1}{e^{2\gamma} + 2\gamma + 1} \left(\frac{1}{2\gamma^2} + \frac{e^{2\gamma} + \frac{2}{3}\gamma + 1}{e^{2\gamma} + 2\gamma + 1} \right) \end{aligned} \quad (2.52)$$

The reason for these two complexity measures to be equal in both conjugated spaces is the same as described in the previous section. Note that in this case, however, the three complexity measures depend on the parameters k and a through $\gamma = ka$. It is worthy remarking that the complexity measures obtained for the even solution tend to the complexity values of the single-delta when the distance a approaches zero. We continue with a more detailed description of this phenomenon in the next section.

2.3 Numerical analysis

In this section the information-theoretic measures (lengths and complexities) of the stationary states of the single- and twin-delta potentials (even solution), previously obtained in an analytical way, are numerically analyzed and discussed in terms of their characteristic parameters in both position and momentum space. We use here atomic units (a.u.), that is $\hbar = m = e = a_0 = 1$.

2.3.1 Single-delta potential: lengths and complexities

Each of the densities given in Eqs. (2.5) and (2.6), corresponding to position and momentum spaces respectively, is characterized by a parameter which is determined, in fact, by the energy of the bounded state. The characteristic parameter is k in position space and p_0 in the momentum one.

Let us analyze the Shannon and Fisher-type information measures, as well as the standard deviation, by means of their corresponding lengths. In doing so, different values of k and p_0 will be considered. Those values are given in Table 2.1, in terms of the aforementioned parameters and lengths.

POSITION SPACE			
k	$(\Delta x) \times 10^{-2}$	$N[\rho] \times 10^{-2}$	$(\delta x) \times 10^{-2}$
1	70.711	271.828	49.991
20	3.536	13.591	2.491
50	1.414	5.437	0.991
90	0.786	3.020	0.556

MOMENTUM SPACE			
p_0	$(\Delta p) \times 10^{-2}$	$N[\Pi] \times 10^{-2}$	$(\delta p) \times 10^{-2}$
1	0.730	2.482	0.516
20	14.595	49.642	10.320
50	36.487	124.104	25.800
90	65.676	223.387	46.440

Table 2.1: Standard deviation, Shannon length and Fisher length for different values of the parameter k (position space) and p_0 (momentum space) for the single-delta position and momentum space densities, $\rho(x)$ and $\Pi(p)$ respectively.

Some comments are in order. It is firstly observed the decreasing trend of all spreading measures, in position space, as the parameter k increases. In fact, and according to Eqs. (2.10), (2.18) with $q = 2$, (2.19) and (2.20), the three measures are essentially the inverse of k in position space and proportional to p_0 in momentum space. Let us remind the functional expression of $\rho(x)$, an exponential on each of the half-axes with a decreasing rate determined by k . Consequently, increasing the value of k provokes a higher concentration of the density around the origin, where its value becomes higher as far as k increases. On the other hand, diminishing the k value makes the density to progressively spread over the whole real line. This means that, as k decreases, (i) the variance, a measure of the mean deviation from the centroid at the origin, increases because the density enhances its contribution in regions far from the origin, (ii) the Shannon length, a measure of spread over the whole real line, also increases because of its progressive approach to a uniform distribution, and (iii) the Fisher information, a measure of the 'content of gradient', decreases notably with a consequent increase of its inverse, the square of the Fisher length; the reason is that the density approaches a Dirac delta for extremely large k , with a very high value of the derivative (its absolute value) around the origin.

In what concerns the momentum density, similar interpretations can be done, according to the value of p_0 , the parameter which determines the structural characteristics of the momentum density $\Pi(p)$. An increasing trend of each measure as functions of p_0 (notice that $p_0 = \hbar k$) is now displayed. The functional dependence of $\Pi(p)$ on p_0 , as shown in Eq. (2.6), makes the density to spread over its domain and to reduce its content of gradient as far as p_0 increases. This behavior appears opposite to that of the position space density, and consequently the same occurs with the information measures considered, namely standard deviation and Shannon and Fisher lengths, as clearly observed in Table 2.1.

2.3.2 Twin-delta potential: lengths

The interpretation of the different information lengths in the twin delta problem is based on identical arguments for both the symmetric and antisymmetric solutions. For the sake of simplicity and briefly, we will restrict the discussion to the symmetric solution, keeping in mind that similar conclusions in opposite spaces are obtained from the analysis of the antisymmetric wavefunction. The densities $\rho_+(x)$ and $\Pi_+(p)$ will be denoted by $\rho(x)$ and $\Pi(p)$ in what follows.

In position space, we observe that the density $\rho(x)$ has two different components: (i) an hyperbolic function within the interval $(-a, a)$ determined by the location of the two attractive centers, and (ii) a decreasing exponential out of the aforementioned interval.

The parameter k , which determines the decreasing rate of the exponential component as well as the curvature of the hyperbolic one, is determined by the half width a of the interval through the eigenvalue equation (2.30). The analysis of their mutual relationship allows to assert that the parameter k is a decreasing function of a . Consequently, considering wider intervals $(-a, a)$ implies to deal with lower values of k .

In Figure 2.2a, the standard deviation Δx and the Shannon, Fisher and second-order Rényi lengths (denoted by $N[\rho]$, δx and $R_2[\rho]$, respectively) are displayed for different values of the interval half-width a . It is remarkable that the curves for the three lengths

display an unimodal shape: they increase until reaching their absolute maximum, and then slowly decrease towards an asymptotic value for large a . Opposite behaviour is observed in momentum space (Figure 2.2b): the curves first decrease and then tend to a constant long-range limit.

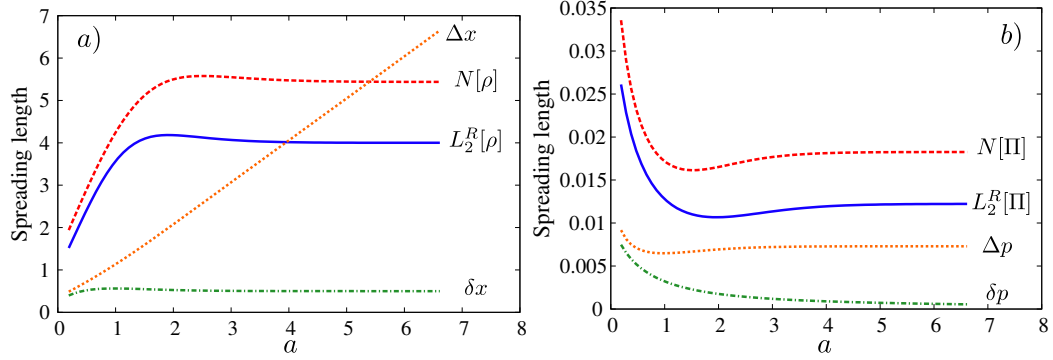


Figure 2.2: Standard deviation and Shannon, Fisher and second-order Rényi lengths for the symmetric solution of the twin-potential problem, in (a) position and (b) momentum spaces.

Let us interpret the above comments according to the structural properties of the densities $\rho(x)$ and $\Pi(p)$, as displayed in Figure 2.3 for different values of their characteristic parameters. In what concerns the position space density (Figure 2.3a) and starting with a very narrow interval, amplifying the small-sized hyperbolic interval increases the global spreading, not only due to the lower curvature and exponential decreasing rate as determined by k , but also because the contribution of the exponential component diminishes as compared to the hyperbolic one. On the other hand, the extremely high gradient at the points $x = \pm a$ decreases as far as a increases, what justifies the enhancement of the Fisher length.

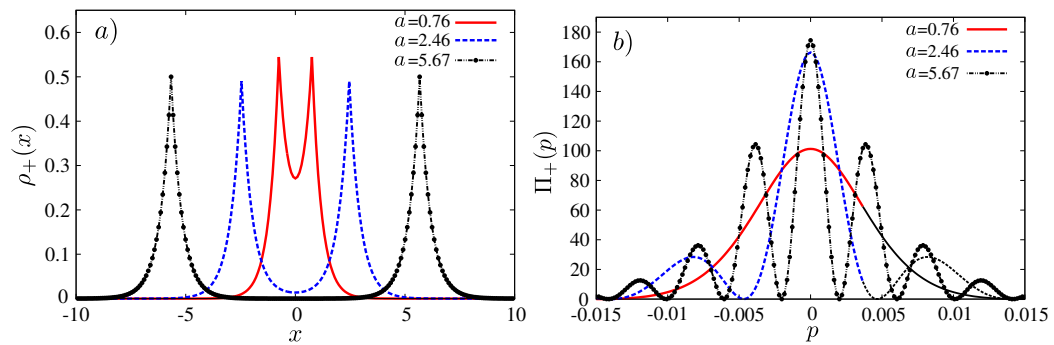


Figure 2.3: Density function for the symmetric solution of the twin-potential problem, in (a) position and (b) momentum spaces.

However, after reaching the interval a large enough width, the aforementioned lengths display a decreasing trend. The reason is that the hyperbolic component mainly governs the length values as compared to the exponential contribution. In this sense, the global

spread as measured by the variance and the Shannon, Rényi and Fisher lengths remains almost constant, because the density approaches a unique-component distribution, namely the hyperbolic one with very low curvature.

Concerning the momentum space density, we firstly observe that its analytical expression in Eq. (2.35) consists of an (oscillatory) cosine-like numerator and a decreasing factor as given by the denominator. The behaviour of both factors is determined by the parameter p_0 : the numerator becomes increasingly oscillatory as far as p_0 increases, while the complementary factor (denominator) governs the rate of global decrease. In this sense, higher values of p_0 give rise to highly oscillatory momentum densities but also with a higher global spreading. Again we observe a counterbalance of both contributions for large enough p_0 , as displayed in Figure 2.3b for the momentum density and Figure 2.2b for the momentum space lengths.

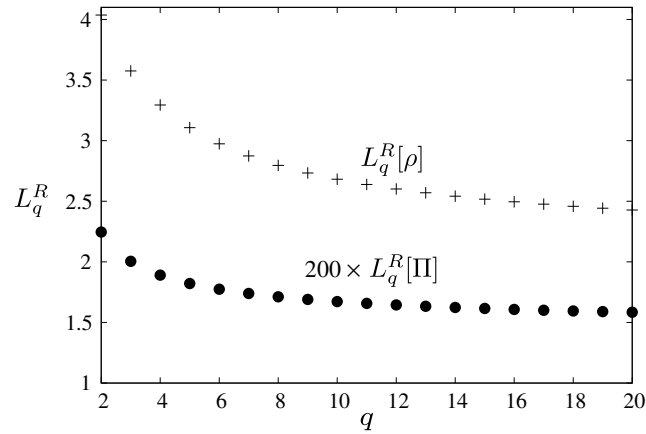


Figure 2.4: Rényi length, as a function of its order q , for the symmetric solution of the twin-potential problem with a fixed value $a = 1.4$ in position and momentum spaces.

It is also interesting to analyze the dependence of the Rényi lengths on the order parameter q . This will be done attending to the curves displayed in Figure 2.4 for a fixed interval extremum a . The decreasing behaviour observed for the symmetric solution, as also occurs with the antisymmetric one, independently of dealing with position or momentum space densities, can be justified as follows. The effect of increasing q translates into a 'more concentrated' integrand within the expression (1.5) defining the frequency moments and their corresponding Rényi lengths in position space. So, increasing q makes the relative contribution from the exponential component in position space to become almost negligible as compared to the hyperbolic one, as corresponds to a density highly concentrated around the origin and, consequently, less sparse. Concerning the momentum density, an enhancement of both the strength of oscillations as well as a global concentration around the origin arises as q increases. The consequence is the same as in position space, that is, lower values of the Rényi length, indicating a higher level of concentration, especially around the origin but also at the extrema of the oscillatory curve.

2.3.3 Twin-delta potential: complexities

According to the general interpretation of the 'complexity' concept, as a measure of the difficulty of modeling the distribution, it is clear that the distance between the locations of the delta functions or, equivalently, the width of the interval $(-a, a)$, will be essential in determining the level of complexity. This is shown in Figure 2.5, where the LMC, Fisher-Shannon and Cramér-Rao complexities are displayed as functions of the half-distance a between delta attractors. Let us analyze the results in position (Fig. 2.5a) and momentum (Fig. 2.5b) spaces.

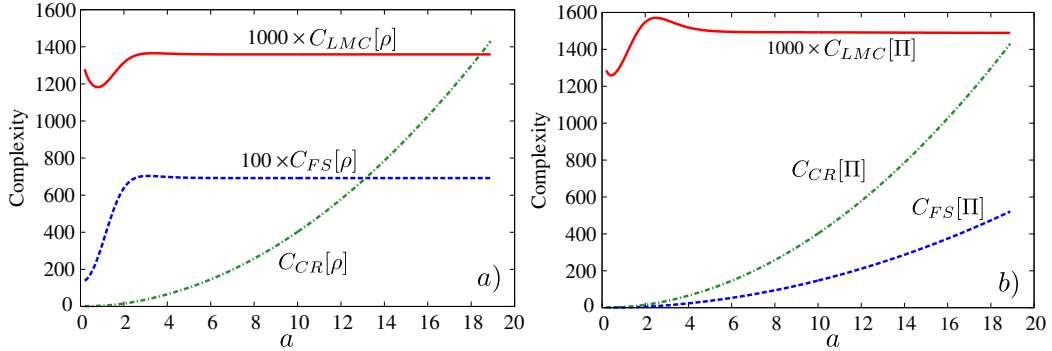


Figure 2.5: Complexities LMC, Fisher-Shannon (FS) and Cramér-Rao (CR) for the symmetric solution of the twin-potential problem, in (a) position and (b) momentum spaces.

In doing so, let us firstly think on the process of 'separation of deltas' (increase of a). For large enough separation, the quantum-mechanical problem can be approximated by an 'overlap' of two independent single-delta equations, dealt in detail in Section 2.1. For the single-delta case we obtained constant values of all complexities; in our case we observe that the LMC and Fisher-Shannon complexities displayed in Figure 2.5a are constant unless dealing with very small values of a . This is a consequence of the behavior of the factors composing those complexities, as observed in Fig. 2.3a. Increasing a makes the Shannon, Fisher and second-order Rényi lengths to become almost constant, because each of the single-delta components corresponding to potentials centered at $x = \pm a$ gives rise to a density approaching uniformity as far as a increases. The situation is very different, however, regarding the variance or the standard deviation, which monotonically increases because the centers of the delta potentials separate between themselves. The key point here is the definition of variance as a measure of spreading with respect to the centroid, the origin in the present problem. So, location of the highest values of the density, which occur around the attractive centers, are progressively more distant from the centroid at the origin. This makes the variance to increase because of its reference with respect to the origin, contrary to the other information measures and lengths which have no reference points, being determined instead according to the behavior of the density over its whole domain.

Concerning the momentum space complexities (Figure 2.5b), the essential difference among themselves is the presence or not of the Fisher information factor, which appears in the Fisher-Shannon and Cramér-Rao cases but not in the LMC one. It is observed that (i) the LMC complexity in momentum space displays a very similar shape to the corre-

sponding one in position space, and (ii) the Fisher-Shannon and Cramér-Rao momentum complexities are increasing functions, in a similar fashion as the Crámer-Rao one in position space. It is worthy remembering the presence of an oscillatory factor in the momentum density, the frequency of the oscillations being determined by the half-distance a . Such an oscillatory behavior mainly affects the Fisher information factor, whose increase with a translates into that of the associated complexities. Such is not the case of the LMC complexity, for which a “counterbalance effect” of each factor constrains the LMC complexity value for arbitrary a to a much narrower interval.

Conclusions

In this chapter we have studied both analytically and numerically the single information-theoretic lengths (Fisher, Shannon and Rényi) and complexity measures (Cramér-Rao, Fisher-Shannon and LMC) of the lowest-lying stationary state of the single-delta and twin-delta potentials in terms of their energies and characteristic parameters. These quantities are analyzed in both position and momentum spaces. They grasp various individual and combined spreading facets of the charge and momentum of the particle far beyond that described by the celebrated standard deviation.

Finally, we point out some open problems. First, to study the information and complexity properties of the bound states of the one-dimensional hydrogen atom as well as the helium and hydrogen molecular ion with a single and twin delta potential, respectively, confined in a box [178, 179] or with an external electric and/or magnetic fields. Second, to extend the results of this work to N -delta one-dimensional arrays because of their use to approximate and describe numerous scientific and technological properties of quantum wires and other semiconductor nanostructures. Third, to study the related information-theoretic complexity measures of higher dimensionality delta potentials, which do not have the same properties as those in one dimension. Delta potentials in more than one dimension do not allow bound states and scattering but, nevertheless, once regularized they are very instructive for illustrating basic concepts of quantum field theory [180]. Fourth, to investigate the relativistic effects in the aforementioned information-theoretic properties of delta-like potentials. It is planned the inclusion, in all of the above points, of information lengths based on a so relevant information quantifier as the Tsallis entropy [citeTsallis1988](#), a non-extensive measure which characteristic parameter measures the departure from extensivity. Numerous applications of this entropy in nonextensive thermodynamics or statistical mechanics and many other scientific fields have been carried out [181].

Complexity quantification of Dirac effect

Single and composite information-theoretic quantities reviewed in this Thesis have been numerically determined in position space for a great deal of atomic and molecular systems in a Hartree-Fock-like framework (see [4, 37, 38] and references therein). On the contrary, the information theory of relativistic quantum systems is a widely open field [182, 183, 184]; indeed, only a few recent works have been done for single-particle systems [185, 83, 182] and neutral atoms [186, 187, 188, 189] in various relativistic settings. Let us here mention that the comparison of some Hartree-Fock and Dirac-Fock ground-state results in neutral atoms shows that Shannon entropy is able to characterize the atomic shell structure but it hardly grasps any relativistic effects [186], while the disequilibrium and the LMC complexity measure [186], as well as the Fisher information [4], strongly exhibits them. Moreover, it has been recently shown that these quantities are good relativistic indicators for ground-state hydrogenic systems in a Dirac setting [182] and for ground and excited states of pionic systems in a Klein-Gordon setting [185, 83].

In this chapter we use the Fisher information and the Fisher-Shannon and LMC complexity measures to characterize and quantify some fundamental features [190, 191] of the stationary solutions of the Dirac equation of hydrogenic systems; namely, the well established charge contraction towards the nucleus in both ground and excited states, the raising of all the non-relativistic minima and the (largely ignored) gradient reduction near to and far from the nucleus of the electron density of any excited state of the system.

This work extends the information-theoretic study of the hydrogenic systems recently done in the Schrödinger [84] and relativistic Klein-Gordon [185, 83] and Dirac [182] frameworks. Indeed, previous efforts have analyzed not only the single and composite information-theoretic measures of both ground and excited states in the Schrödinger [192, 84] and Klein-Gordon [185, 83] settings, but also the single entropic measures of the ground state in the Dirac setting [182].

The structure of the Chapter is the following. First, in Section 3.1, we briefly discuss the two information-theoretic quantities needed for that aim, and we give the known relativistic (Dirac) and non-relativistic (Schrödinger) electron densities of a hydrogenic system. Later, in Section 3.2, we carry out a detailed study of the dependence of the previous complexity measures on the nuclear charge in the ground state and some excited states, as well as the quantification of the main dynamical relativistic effects (charge contraction towards the nucleus, minima raising or nodal disappearance, and gradient reduction near to and far from the nucleus) by means of the Dirac-Schrödinger complexity ratios of LMC and Fisher-Shannon types. In Section 3.3, we analyse the dependence of the complexity measures on

the energy and the relativistic quantum number as well as the associated information planes for the ground and various excited states. Finally, some conclusions are drawn.

3.1 Complexity measures and Dirac hydrogenic densities

Here we briefly review the concepts of LMC shape complexity and Fisher-Shannon complexity of a general probability density $\rho(\vec{r})$ used in this Chapter, which turn to be good indicators of the Dirac relativistic effects in hydrogenic systems and in neutral atoms [186]. Then, we collect here the known Dirac wave functions of the hydrogenic bound states, and their associated probability densities together with their non-relativistic limit (Schrödinger densities).

The LMC shape complexity, Eq. (1.23), is defined by the product of the disequilibrium $D[\rho]$ (which quantifies the departure of the probability density from uniformity, see Eq. (1.7)) and the exponential of the Shannon entropy $S[\rho]$ (a general measure of the uncertainty of the density, see Eq. (1.4)):

$$C_{\text{LMC}}[\rho] = D[\rho] \times e^{S[\rho]}, \quad (3.1)$$

where

$$D[\rho] = \int [\rho(\vec{r})]^2 d\vec{r}; \quad S[\rho] = - \int \rho(\vec{r}) \ln \rho(\vec{r}) d\vec{r}. \quad (3.2)$$

The Fisher-Shannon complexity, Eq. (1.24), is given by

$$C_{\text{FS}}[\rho] = F[\rho] \times J[\rho], \quad (3.3)$$

where

$$F[\rho] = \int \frac{|\vec{\nabla} \rho(\vec{r})|^2}{\rho(\vec{r})} d\vec{r}; \quad J[\rho] = \frac{1}{2\pi e} e^{\frac{2}{3}S[\rho]} \quad (3.4)$$

are the (translationally invariant) Fisher information, Eq. (1.9), and the Shannon entropic power, Eq. (1.25), of the probability density, respectively. The latter quantity, which is an exponential function of the Shannon entropy, measures the total extent to which the single-particle distribution is in fact concentrated [39]. The Fisher information, $F[\rho]$, which is closely related to the kinetic energy [193], is a local information-theoretic quantity; *i.e.*, it is very sensitive to strong changes on the distribution over a small-sized region of its domain.

On the other hand, the Dirac wavefunctions of the stationary states of a hydrogenic system with nuclear charge Z are described by the eigensolutions (E, ψ^D) of the Dirac equation of an electron moving in the Coulomb potential $V(r) = -\frac{Ze^2}{4\pi\epsilon_0 r}$, namely

$$\left(E + i\hbar c \vec{\alpha} \cdot \vec{\nabla} - \beta m_0 c^2 - V(r) \right) \psi^D = 0. \quad (3.5)$$

where m_0 denotes the mass of the electron at rest. The Dirac matrices $\vec{\alpha} = (\alpha_1, \alpha_2, \alpha_3)$ and β are given in terms of the Pauli matrices and the identity as follows:

$$\beta = \begin{pmatrix} \mathbb{I} & 0 \\ 0 & -\mathbb{I} \end{pmatrix} \quad \alpha_j = \begin{pmatrix} 0 & \sigma_j \\ \sigma_j & 0 \end{pmatrix},$$

where

$$\sigma_1 = \begin{pmatrix} 0 & 1 \\ 1 & 0 \end{pmatrix} \quad \sigma_2 = \begin{pmatrix} 0 & -i \\ i & 0 \end{pmatrix} \quad \sigma_3 = \begin{pmatrix} 1 & 0 \\ 0 & -1 \end{pmatrix}.$$

The stationary eigensolutions are most naturally obtained by working in spherical polar coordinates (r, θ, ϕ) and taking into account that the Dirac hamiltonian commutes with the operators $\{\vec{J}^2, J_z, \vec{K}\}$. The total angular momentum operator is given by the coupling $\vec{J} = \vec{L} + \vec{S}$ and the Dirac operator by $\vec{K} = \beta(\vec{\Sigma} \cdot \vec{L} + \hbar)$, being \vec{L} and $\vec{S} \equiv \frac{\hbar}{2}\vec{\Sigma}$ the orbital and spin angular momenta, respectively, and $\vec{\Sigma} = (\sigma_1, \sigma_2, \sigma_3)$. So, the stationary states are to be characterized by the quantum numbers (n, k, m_j) , where $n \in \mathbb{N}$, the Dirac or relativistic quantum number

$$k = \pm 1, \pm 2, \dots, \pm(n-1), -n$$

and

$$-j \leq m_j \leq j \quad \text{with} \quad j = \frac{1}{2}, \frac{3}{2}, \dots, n - \frac{1}{2}.$$

Besides, let us remark that $k = \mp(j + \frac{1}{2})$ for $j = l \pm \frac{1}{2}$, so that

$$k = \begin{cases} -(l+1) & \text{if } j = l + \frac{1}{2} \\ l & \text{if } j = l - \frac{1}{2} \end{cases};$$

in other terms, $k = \pm(j + \frac{1}{2})$, to which there corresponds (upper component) angular momentum $l = j \pm \frac{1}{2}$ and (lower component) $l' = j = \mp \frac{1}{2}$. The energy eigenvalues are known (see e.g. [190, 194, 195, 196]) to be

$$E = M \left(1 + \frac{(\alpha Z)^2}{\left(n - |k| + \sqrt{k^2 - (\alpha Z)^2} \right)^2} \right)^{-1/2}, \quad (3.6)$$

where α denotes the fine structure constant, $M = m_0 c^2$ and $Z \leq 137$. For $Z > 137$ the Klein paradox [197] comes into play and the eigenenergies become complex beyond that point; the resolution of this paradox is known to be related with the creation of electron-positron pairs from the Dirac-Fermi sea [198]. Note that, because of the smallness of the binding energies, E is only slightly less than $m_0 c^2$. The corresponding eigensolutions of the bound relativistic hydrogenic states are given by the four-component spinors

$$\psi_{nk m_j}^D(\vec{r}) = \begin{pmatrix} g_{nk}(r) \Omega_{k m_j}(\theta, \phi) \\ i f_{nk}(r) \Omega_{-k m_j}(\theta, \phi) \end{pmatrix}, \quad (3.7)$$

where the symbol $\Omega_{k, m_j}(\theta, \phi)$ denotes the (two-component) spin-orbital harmonics

$$\Omega_{k m_j} = \begin{pmatrix} -\frac{k}{|k|} \sqrt{\frac{k + \frac{1}{2} - m_j}{2k+1}} Y_{|k + \frac{1}{2}| - \frac{1}{2}, m_j - \frac{1}{2}}(\theta, \phi) \\ \sqrt{\frac{k + \frac{1}{2} + m_j}{2k+1}} Y_{|k + \frac{1}{2}| - \frac{1}{2}, m_j + \frac{1}{2}}(\theta, \phi) \end{pmatrix}, \quad (3.8)$$

and the so-called large (g) and small (f) radial components with the normalization $\int_0^\infty (g^2 + f^2)r^2 dr = 1$, are known to be

$$\left. \begin{array}{l} g_{nk}(r) \\ f_{nk}(r) \end{array} \right\} = \frac{\pm(2\lambda)^{3/2}}{\Gamma(2\gamma+1)} \sqrt{\frac{(M \pm E)\Gamma(2\gamma+n'+1)}{4M \frac{(n'+\gamma)M}{E} \left(\frac{(n'+\gamma)M}{E} - k\right) n'!}} (2\lambda r)^{\gamma-1} e^{-\lambda r} \times \\ \times \left[\left(\frac{(n'+\gamma)M}{E} - k \right) F(-n', 2\gamma+1; 2\lambda r) s \mp n' F(1-n', 2\gamma+1; 2\lambda r) \right] \quad (3.9)$$

where $n' = n - |k|$, $\gamma = \sqrt{k^2 - (\alpha Z)^2}$, $\lambda = \frac{1}{\hbar c}(M^2 - E^2)^{1/2}$, and $F(a, b; z)$ denotes the Kummer confluent hypergeometric function. Notice that the lower and the upper components of the Dirac wavefunction have an opposite parity. Moreover, the binding energy $B = |E_{n,|k}|^D = m_0 c^2 - E$ depends on the principal quantum number n and on the absolute value of the Dirac quantum number k , but not on its sign. This means that states with the same angular momentum quantum number j which belongs to different pairs of orbital quantum numbers (l, l') are degenerated in energy. In addition we should point out that we will often identify $\psi_{nljm_j}^D$ with $\psi_{nkm_j}^D$ although the Dirac relativistic states are no longer eigenfunctions of the orbital angular momentum because the Dirac hamiltonian does not commute with \vec{L} ; so, the orbital quantum number is not an appropriate quantum number. Indeed, each relativistic state contains two values: l and $l' = l \pm 1$. However, since the component with the radial function $g_{nk}(r)$ is large as compared to its partner $f_{nk}(r)$, the value l pertaining to the large component may be used to denote the state. So, although we use the non-relativistic notation $|n, l, j, m_j\rangle$ we should keep in mind that it stands for $|n, k, m_j\rangle$.

Then, the Dirac probability density $\rho_{nljm_j}^D(\vec{r}) = |\psi_{nljm_j}^D(\vec{r})|^2$ of the hydrogenic state $|n, l, j, m_j\rangle$ can be written down in the following separable form:

$$\rho_{nljm_j}^D(\vec{r}) = \rho_{\text{radial}}^D(r) \rho_{\text{angular}}(\theta), \quad (3.10)$$

where the radial and angular parts are given by

$$\rho_{\text{radial}}^D(r) = |g_{nk}(r)|^2 + |f_{nk}(r)|^2 \quad (3.11)$$

and

$$\rho_{\text{angular}}(\theta) = \langle l, m_j - \frac{1}{2}; \frac{1}{2}, +\frac{1}{2} | j, m_j \rangle^2 |Y_{l, m_j - \frac{1}{2}}(\theta, \phi)|^2 + \\ + \langle l, m_j + \frac{1}{2}; \frac{1}{2}, -\frac{1}{2} | j, m_j \rangle^2 |Y_{l, m_j + \frac{1}{2}}(\theta, \phi)|^2, \quad (3.12)$$

respectively.

Finally, it is well known that in the non-relativistic limit of the hydrogenic system the large component $g_{nk}(r)$ tends to the corresponding radial function of the Schrödinger equation, while the small component $f_{nk}(r)$ tends to zero. So, the Schrödinger probability density $\rho_{nljm_j}^S(\vec{r})$ which describes the state $|nljm_j\rangle$ of the system is

$$\rho_{nljm_j}^S(r, \theta) = |\psi_{nljm_j}^S(r, \theta, \phi)|^2 = \rho_{\text{radial}}^S(r) \rho_{\text{angular}}(\theta), \quad (3.13)$$

where

$$\rho_{\text{radial}}^S(r) = \frac{\Gamma(n-l)}{2n\Gamma(n+l+1)} \left(\frac{2Z}{a_0 n}\right)^{2l+3} \times e^{-\frac{2Z}{a_0 n} r} r^{2l} \left| L_{n-l-1}^{2l+1} \left(\frac{2Z}{a_0 n} r\right) \right|^2 \quad (3.14)$$

gives the radial part of the wavefunction, and $\rho_{\text{angular}}(\theta)$ is the same angular part as in Dirac case, given by Eq. (3.12). The corresponding energy of the non-relativistic system is known to be $E_n^S = -\frac{\hbar^2 Z^2}{2a_0^2 n^2}$.

3.2 Complexity quantification of Dirac effects

In this Section we quantify the two main dynamical Dirac relativistic effects (charge contraction towards the origin and raising of all non-relativistic minima), as well as the gradient reduction near to and far from the origin, in hydrogenic systems by means of the LMC and Fisher-Shannon complexity measures. This is done by studying the comparison between the Schrödinger and Dirac values of the LMC and Fisher-Shannon complexities for the ground and excited states of hydrogenic systems. Specifically we show the dependence of these quantities, as well as the Fisher-Shannon information plane, on the nuclear charge Z and the principal quantum number n . For convenience we will use atomic units hereafter.

3.2.1 Relativistic effects enhancement with nuclear charge.

First, let us present and discuss the dependence on the nuclear charge Z of the LMC (see Fig. 3.1-left) and Fisher-Shannon (see Fig. 3.1-right) complexity measures in the ground state of the hydrogenic system in the Schrödinger and Dirac settings described in the previous section. We find that for both complexity measures (i) the Schrödinger values remain constant for all Z (as recently proved in an analytical way [95, 84]), and (ii) the Dirac values enhance when the nuclear charge increases, in accordance with the corresponding Klein-Gordon results found in pionic systems [83].

This enhancement is provoked by the contraction of the electron density towards the origin, a phenomenon similar to that observed for Klein-Gordon single-particle systems [185, 83]. To quantify it we have defined the relative ratios $\zeta_{\text{LMC}} = 1 - \frac{C_{\text{LMC}}^S}{C_{\text{LMC}}^D}$ and $\zeta_{\text{FS}} = 1 - \frac{C_{\text{FS}}^S}{C_{\text{FS}}^D}$. They are shown in the inner windows of Figs. 3.1-left-and-right in terms of Z . We observe that both complexity ratios behave similarly in the ground state. This is not, however, the case for other states as it is illustrated in Fig. 3.2-left for the LMC measure in three circular states with $n \leq 3$, and in Fig. 3.2-right for the Fisher-Shannon complexity in the ground state and two excited states. Therein we observe that while the LMC ratio is always positive and has an increasing behavior as a function of Z , this is not the case for the Fisher-Shannon ratio. Indeed, the latter ratio can reach negative values for the excited states, indicating that the Dirac value of the Fisher-Shannon complexity is lower than the Schrödinger one.

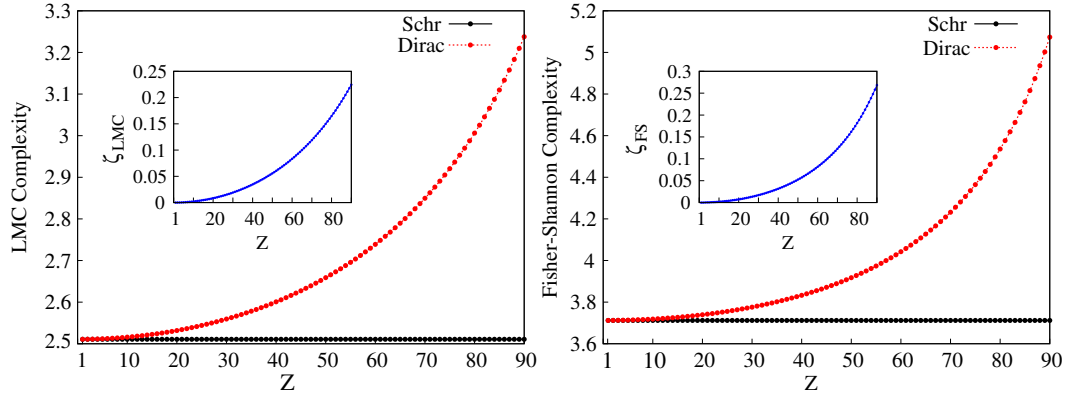


Figure 3.1: Dependence of the ground-state hydrogenic LMC (left) and Fisher-Shannon (right) complexity measures on the nuclear charge Z

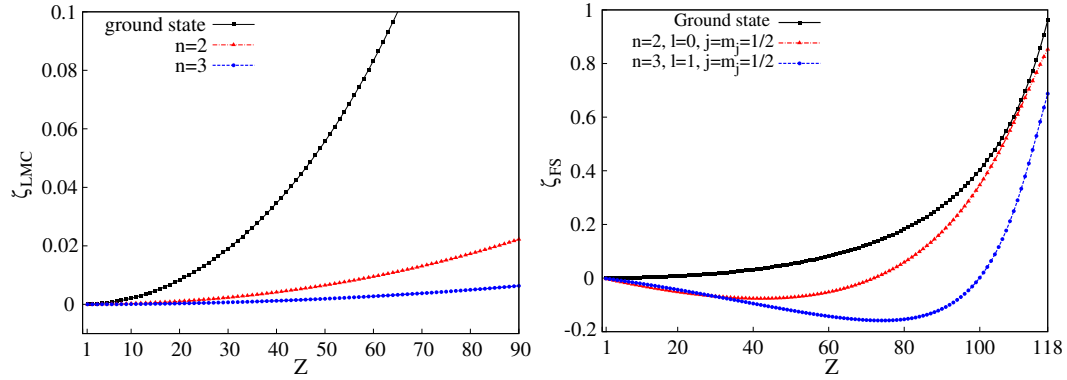


Figure 3.2: LMC relative ratio, ζ_{LMC} , for circular states with $n \leq 3$ (left) and Fisher-Shannon relative ratio, ζ_{FS} , for the ground state and the excited states $(n, l, j, m_j) = (2, 0, \frac{1}{2}, \frac{1}{2})$ and $(3, 1, \frac{1}{2}, \frac{1}{2})$ (right).

The positivity of the LMC ratio can be understood because it measures the charge contraction towards the nucleus by means of two global concentration (or spreading) information-theoretic quantities, the disequilibrium and the Shannon entropy. We observe that although these two factors work in the same sense, the contribution of the disequilibrium turns out to be much greater than that of the Shannon entropy. The negativity of the Fisher-Shannon ratio is more difficult to explain, because it quantifies the combined balance of the spreading (via the Shannon entropy) and the gradient content (via the Fisher information) of the charge distribution of the hydrogenic system. To understand this phenomenon we analyze the behavior of the two components of the Fisher-Shannon complexity, Eq. (3.3). Keeping in mind that the Shannon entropy is not very sensitive to the relativistic effects, the former analysis boils down to a careful determination of the Fisher

information which can be written down as

$$F[\rho] = F_{\text{radial}} + \langle r^{-2} \rangle \times F_{\text{angular}}, \quad (3.15)$$

where F_{radial} denotes the Fisher information of the radial probability function $\rho_{\text{radial}}^i(r)$ ($i = D$ or S for the Dirac and Schrödinger cases, respectively), and F_{angular} the Fisher quantity associated to the angular probability function, $\rho_{\text{angular}}(\theta)$. Let us point out that the Fisher information presents a singularity at $Z = 118.68$, as pointed out by Katriel and Sen [182], what explains why we do not approach to the extreme relativistic limit. Since the angular density is the same function in both relativistic and non-relativistic descriptions and $\langle r^{-2} \rangle$ is slightly higher in the relativistic case, the main reason for the negativity of the Fisher-Shannon complexity ratio arises from the difference between the Dirac and Schrödinger radial probability densities. This is clearly shown in Fig. 3.3, where we have plotted the Dirac and Schrödinger radial densities, $D^i(r) \equiv \rho_{\text{radial}}^i(r)r^2$, and the corresponding Fisher kernels, $F_{\text{kernel}}^i(r) \equiv \frac{1}{\rho_{\text{radial}}^i(r)} \left(\frac{\partial \rho_{\text{radial}}^i(r)}{\partial r} \right)^2 r^2$, for the excited states $(n, l, m_j) = (5, 2, 3/2)$ and $(6, 1, 3/2)$ of the hydrogenic atom with nuclear charge $Z = 50$ in Fig. 3.3-left and -right, respectively.

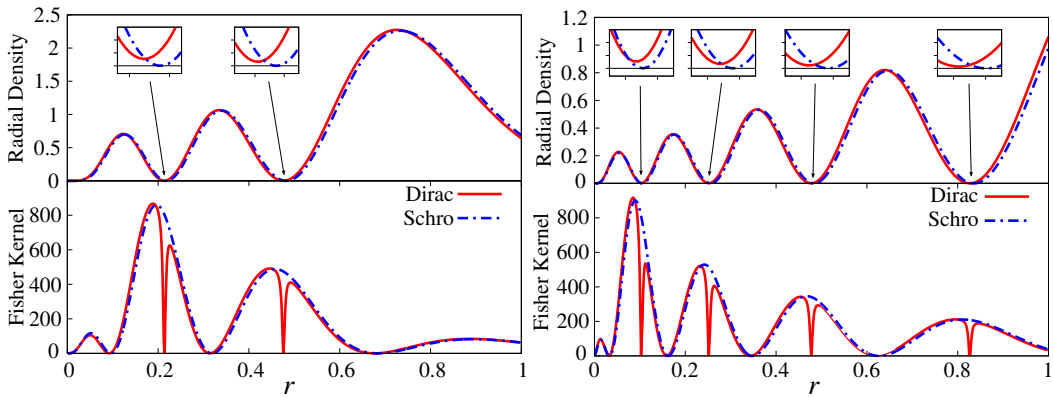


Figure 3.3: Radial density, $D^i(r)$, and radial Fisher information kernel, $F_{\text{kernel}}^i(r)$, in the Dirac ($i = D$) and Schrödinger ($i = S$) settings for the hydrogenic states $n = 5, l = 2, j = \frac{1}{2}$ (left) and $n = 6, l = 1, j = \frac{1}{2}$ (right) with nuclear charge $Z = 50$. Atomic units (a.u.) are used.

Therein we notice that while the Schrödinger radial density, $D^S(r)$, vanishes at various points (nodes), the Dirac radial density, $D^D(r)$, only vanishes at the origin and the infinity. This means that the Dirac density has finite values also at the radial positions of the non-relativistic nodes (this is the relativistic minima-raising effect). Hence, the Fisher information kernel is zero at these points because although the radial density does not vanish, its derivative does (see Fig. 3.3); and this is the reason for the high negative values of ζ_{FS} detected in Fig. 3.2.

This relativistic effect of nodal disappearance (or existence of non-nodal minima) in the Dirac density, firstly pointed out by Burke and Grant [190, 191], is indeed due to the different behavior of the two components $g(r)$ and $f(r)$ of the Dirac wave function.

Both functions vanish at different values of r as we can observe in Fig. 3.4, where the contribution of g and f to the total probability density for the state $n = 5, l = 2, j = 2.5$ of the system with $Z = 90$ have been plotted for illustrative purposes. As we can see in Fig. 3.4, the largest contribution to the total probability density is indeed due to the component $g(r)$ of the Dirac spinor, Eq (3.7). The contribution of the f -component, although very small, is sufficiently significant as to make the Dirac density not to vanish for any radial value except for $r = 0$ and ∞ .

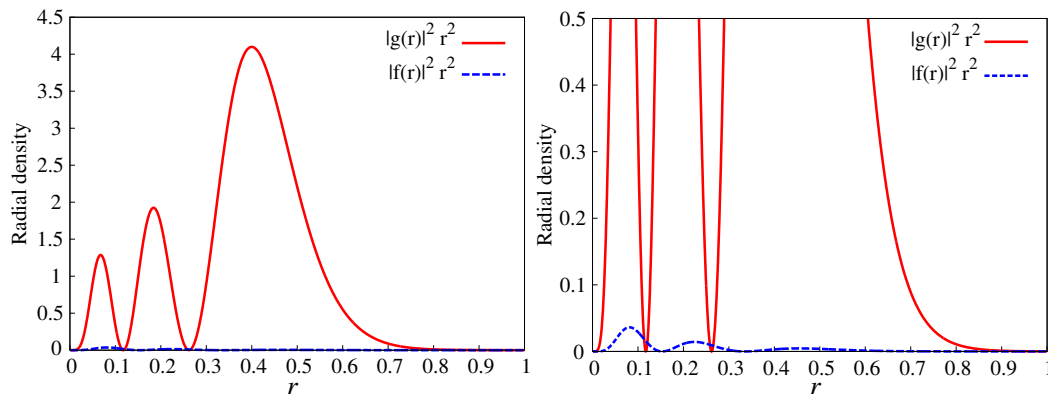


Figure 3.4: Contribution of the $g(r)$ and $f(r)$ component to the total probability density for the hydrogenic state $n = 5, l = 2, j = 2.5$ with nuclear charge $Z = 90$. Atomic units (a.u.) are used.

For illustrative purposes we show in Fig. 3.5 the Dirac and Schrödinger radial distributions and the Fisher information kernels of the ground state and the circular state with $n = 5$ of the hydrogenic system with $Z = 50$. Therein it is observed that (i) in the two states the Dirac radial density (solid red) is always above the Schrödinger curve (dashed blue) when r is lower than the radial expectation value (centroid), and below otherwise, and (ii) the behavior of the Fisher kernel in the excited state is different from that of the ground state: the Dirac values are smaller than the Schrödinger ones not only when r is larger than the radial expectation value, but also in the neighborhood of the nucleus.

We have observed that the latter effect (to be called gradient reduction effect heretoforth) is present in all bound states other than the ground state, although in excited non-circular states this effect is hidden by the nodal disappearance or minima-raising effect. In circular states other than the ground state, this effect gives rise to the small negativity of the Fisher-Shannon ratio, as we can also observe in the next Fig. 3.7 discussed in Section 3.2.2.

Finally let us emphasize that while the LMC ratio quantifies the charge contraction towards the nucleus (mainly by means of its disequilibrium ingredient), the Fisher-Shannon ratio quantifies the combined balance of this charge concentration, the gradient reduction in the regions near to and far from the origin, and the minima raising or nodal disappearance of the charge distribution. This balance is very delicate, so that the latter ratio is positive in all ground-state systems and in all excited states of heavy hydrogenic states. However, the Fisher-Shannon ratio is negative for all excited states of hydrogenic systems with nuclear charge lower than a critical state-dependent value; in these cases the relativistic minima-

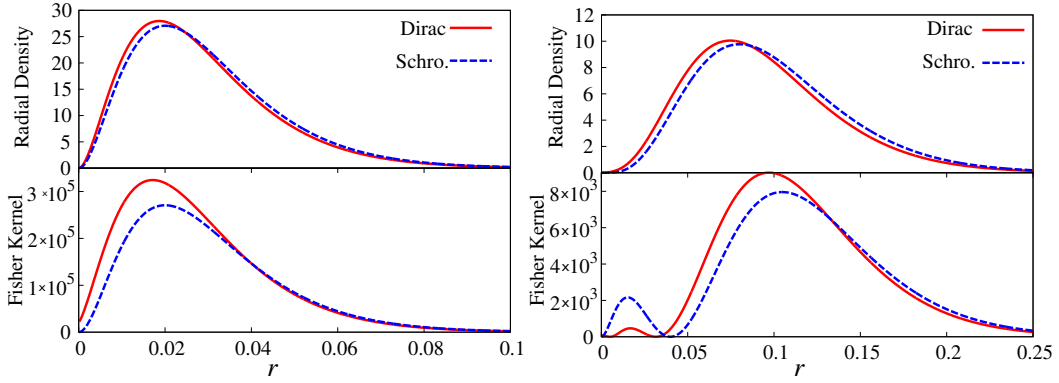


Figure 3.5: Radial density, $D^i(r)$, and radial Fisher information kernel, $F_{kernel}^i(r)$, in the Dirac ($i = D$) and Schrödinger ($i = S$) settings for the ground state (left) and the circular state $n = 5$ (right) with nuclear charge $Z = 50$. Atomic units (a.u.) are used.

raising and gradient reduction joint effects are greater than the charge-contraction effect.

All in all, the Fisher-Shannon ratio quantifies (a) the charge contraction towards the nucleus in the ground state, (b) the charge contraction together with the gradient reduction effect for circular states other than the ground state, and (c) the combined effect due to the charge contraction, the gradient reduction and the minima raising for the remaining excited states.

3.2.2 Quantum numbers and Dirac effects.

The quantification of the Dirac effects for all excited states with $n \leq 6$ in hydrogenic systems with $Z = 19$ and $Z = 90$ is examined by means of the LMC (see Figs. 3.6) and Fisher-Shannon (see Figs. 3.7) complexity ratios. In Fig. 3.6-left for $Z = 19$ and Fig. 3.6-right for $Z = 90$, the LMC ratio displays a common general structure. For given quantum numbers (n, l) the ratio has higher values for states with $j = l - \frac{1}{2}$ than for states with $j = l + \frac{1}{2}$. Moreover, it does not depend on the magnetic quantum number m_j , what can be theoretically understood from Eqs. (3.1), (3.2), (3.10) and (3.13) which allow us to factorize the LMC complexity as a product of a radial complexity (associated to the radial density) and an angular complexity (associated to the angular density, which is the same in both Dirac and Schrödinger frameworks); then, the LMC ratio has no dependence on any angular property. In addition, the LMC ratio (i) decreases when the orbital quantum number l increases for fixed n and (ii) increases with the principal quantum number n for fixed values of (j, l) . As already pointed out in Section 3.2.1, for large values of Z , the bigger the nuclear charge is, the higher the ratio due to the common electronic charge contraction.

The Fisher-Shannon ratio displays a different behavior regarding its dependence on the quantum numbers than the LMC one, as we show in Fig. 3.7-left for $Z = 19$ and in Fig. 3.7-right for $Z = 90$. Indeed, it has negative values except in a few s ($l = 0$) and p ($l = 1$) states. Moreover, although the relativistic effects are stronger in the system with nuclear charge $Z = 90$, the qualitative dependence of the ratio on the quantum numbers is similar

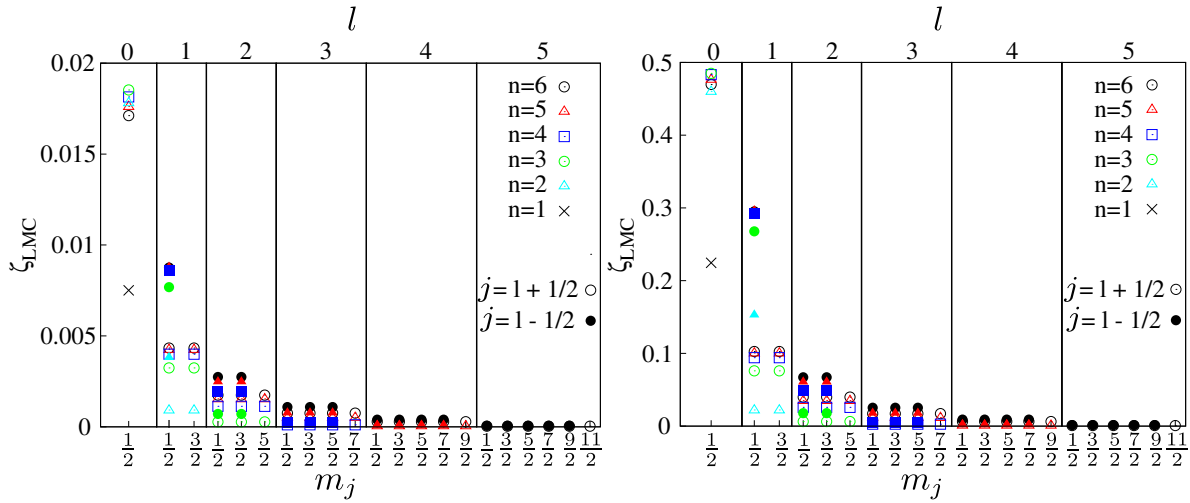


Figure 3.6: Dependence of the LMC complexity on m_j for $Z = 19$ (left) and $Z = 90$ (right).

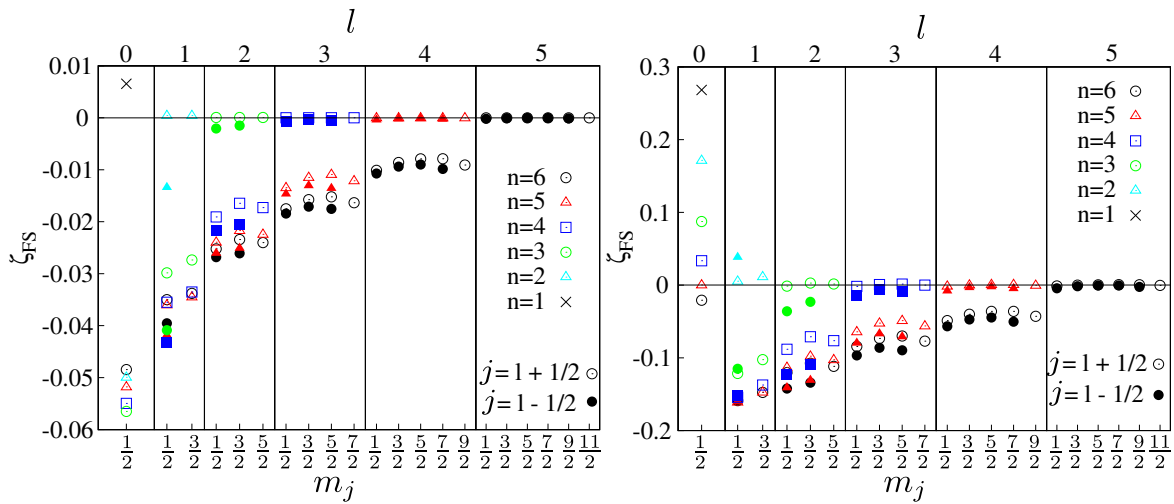


Figure 3.7: Dependence of the Fisher-Shannon complexity on m_j for $Z = 19$ (left) and $Z = 90$ (right).

in the two systems: it has higher values for states with $j = l + \frac{1}{2}$ than for states with $j = l - \frac{1}{2}$ for fixed (n, l) . For states with $l < n - 1$ the ratio severely decreases because of the minima raising, as previously discussed. Moreover, for penetrating states (mainly states s) the charge contraction effect counterbalances the minima-raising effect and makes the ratio to become positive. Besides, the ratio hardly depends on the magnetic quantum number m_j because the Fisher-Shannon complexity, opposite to the LMC quantity, cannot be factorized into radial and angular parts.

The gradient reduction effect is increasingly higher for states with $j = l - \frac{1}{2}$ than for states with $j = l + \frac{1}{2}$ when the nuclear charge increases. For excited states with $l < n - 1$, the minima-raising effect (which grows with Z) decreases the ratio. For large values of Z , the charge-contraction effect is so powerful that makes negligible the gradient reduction and minima-raising effects, producing a global positive Fisher-Shannon ratio.

We have done a similar analysis for states ns , which all have $j = l + \frac{1}{2} = \frac{1}{2}$, as shown in Figs. 3.8 for the hydrogenic system with $Z = 55$. Contrary to the other excited states wherein the LMC (Fisher-Shannon) ratio decreases (increases) asymptotically to a constant value, the LMC ratio grows up to a maximum at $n = 3$, and then slowly decreases towards a constant asymptotic value as shown in Fig. 3.8-left. On the other hand, the Fisher-Shannon ratio (see Fig. 3.8-right) shows an opposite behavior as a function of n ; that is, initially it decreases down to a minimum at $n = 4$ and then it slowly increases towards a constant asymptotic value. For large values of Z , both LMC and Fisher-Shannon ratios of ns -states behave like in the other states. Notice, in addition, that LMC and Fisher-Shannon complexities of states ns have different behavior: while the LMC one remains roughly constant, the Fisher-Shannon one increases monotonically. The latter is because the charge density oscillates more and more when the principal quantum number n increases, what makes the Fisher-information factor of the Fisher-Shannon complexity to grow in a monotonic way.

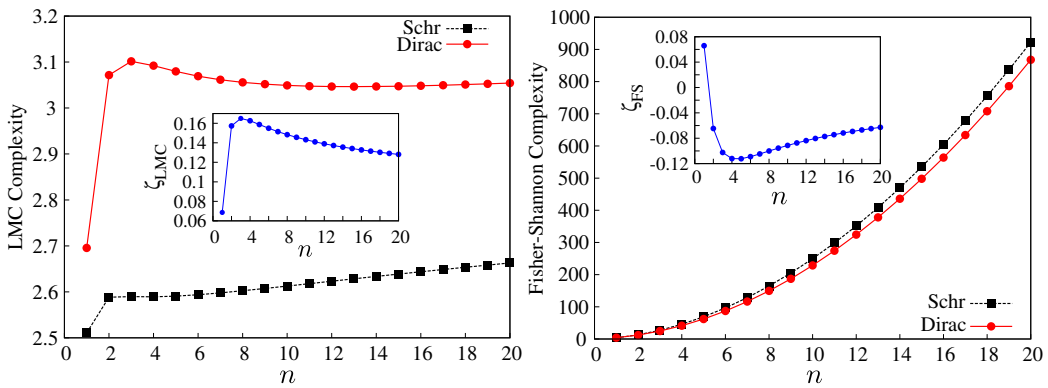


Figure 3.8: LMC (left) and Fisher-Shannon (right) complexities for excited s -states versus n with $Z = 55$.

3.3 Hydrogenic complexities, energy and Dirac quantum number

In this section we study the dependence of the LMC and Fisher-Shannon complexities on both the binding energy B and the Dirac or relativistic quantum number k for various excited states of the hydrogenic system with nuclear charge $Z = 90$, and also we discuss the associated Fisher-Shannon ($F - J$) and disequilibrium-Shannon ($D - e^S$) information planes.

3.3.1 Complexity and Dirac energy

In Fig. 3.9 we show the values of LMC (Fig. 3.9-left) and Fisher-Shannon (Fig. 3.9-right) complexities for several excited states ($n \leq 6, m_j = j$) of the hydrogenic system with nuclear charge $Z = 90$. Therein we observe that when the energy increases, the LMC complexity (a) decreases for states with the same quantum number j , and (b) increases parabolically for states with $l = n - i$ and fixed i ($i = 1, \dots, n$). Moreover, the LMC complexity of the states ns have significantly larger values, mainly because of the relativistic sensitivity previously discussed of the disequilibrium ingredient.

Furthermore, the behavior of the Fisher-Shannon complexity as a function of the energy is similar to the LMC complexity for states with the same j , but it varies slightly within a narrow interval for states with $l = n - i$ and fixed i ($i = 1, \dots, n$).

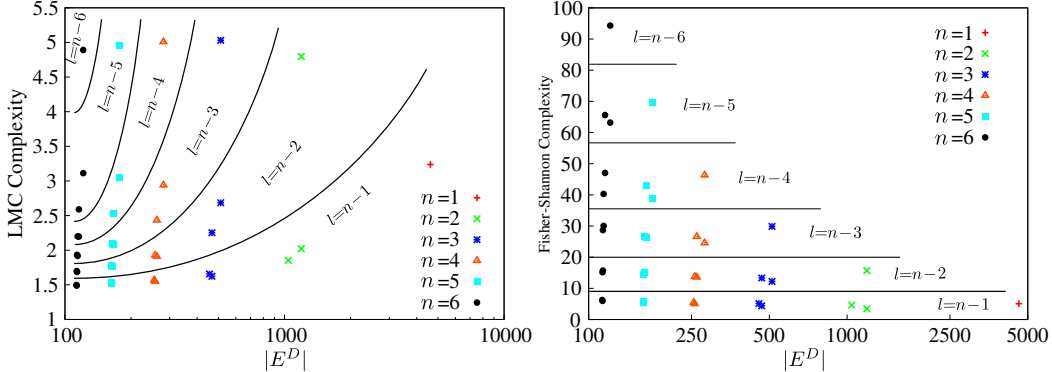


Figure 3.9: LMC (left) and Fisher-Shannon (right) complexities for some excited states in n and l with $Z = 90$ and $m_j = j$ as a function of the energy. Atomic units (a.u.) are used.

3.3.2 Dependence on the relativistic quantum number k

In Fig. 3.10 we show the dependence of the LMC (left) and Fisher-Shannon (right) complexity measures on the relativistic quantum number k for the ground state and several excited states ($n \leq 6, l, j, m_j = j$) of the hydrogenic system with nuclear charge $Z = 90$.

We observe that the LMC complexity (a) has a global maximum for states ns (i.e., $k = -1$), and (b) presents a quasi-symmetric decreasing behavior around the line with $k = -1$ (i.e., for states ns). On the other hand, the Fisher-Shannon complexity has not a

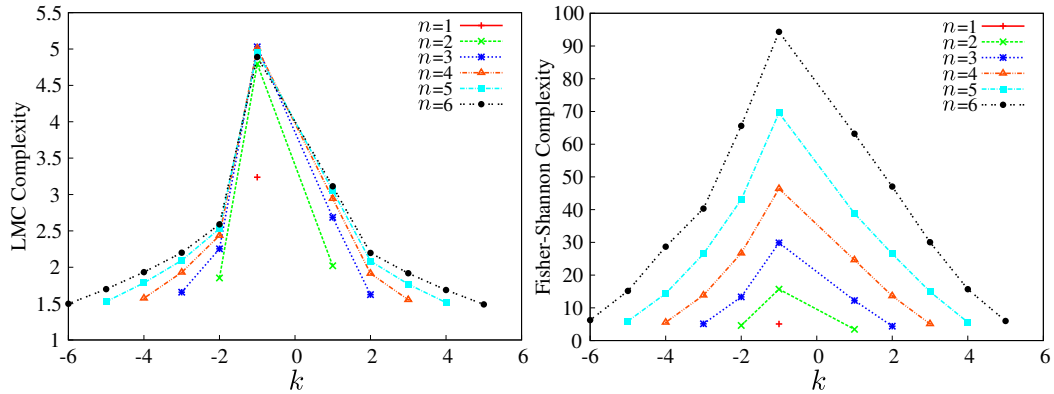


Figure 3.10:) LMC (left) and Fisher-Shannon (right) complexities for some excited states in n and k with $Z = 90$ and $m_j = j$ as a function of the relativistic quantum number k .

global maximum at ns states but it shows up a monotonically decreasing behavior for the l -manifold states with a given principal quantum number n , mainly because of the decreased number $(n - l)$ of maxima of the density.

3.3.3 Information planes

The previous behaviors can be studied by means of the associated relativistic information-theoretic planes. In Fig. 3.11 we show the disequilibrium-Shannon (left) and Fisher-Shannon (right) information planes which include the same states as above ($n \leq 6, l, j = l + \frac{1}{2}, m_j = j$) of the hydrogenic system with nuclear charge $Z = 90$. Notice that the scale in both axes is logarithmic.

First of all, we observe that in both cases all the complexity values lie down the allowed region; that is, they are in the right side of the rigorous frontier (see continuous line in the two graphs) defined by the known analytic LMC and Fisher-Shannon lower bounds [95, 73, 96]: $C_{\text{LMC}}[\rho] \geq 1$ and $C_{\text{FS}}[\rho] \geq 3$. Moreover while the LMC values remain closer to the borderline, the Fisher-Shannon ones move away from this bound when the principal quantum number increases. This is a clear indication that the Fisher-Shannon values of a given state (a) are higher than the corresponding LMC ones and (b) this enhancement is greater when the principal quantum number increases, mainly because the gradient content (so, the Fisher-information ingredient) raises faster than the disequilibrium.

Conclusions

We have studied the LMC and Fisher-Shannon complexities of both ground and several excited states of hydrogenic systems by means of the Dirac relativistic wavefunctions. First we have shown the enhancement of these composite measures when the nuclear charge increases and we have compared these values with the corresponding non-relativistic (Schrödinger) ones, what has allowed us (i) to illustrate that these complexity measures are good indicators of the Dirac relativistic effects, and (ii) to quantify the three

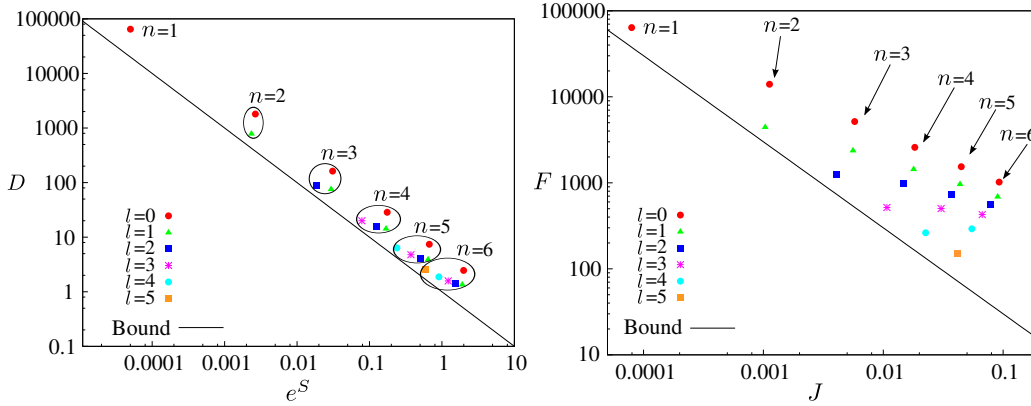


Figure 3.11: LMC or disequilibrium-Shannon (left) and Fisher-Shannon (right) information planes of hydrogenic states with $n \leq 6$, $m_j = j = l + \frac{1}{2}$ and $Z = 90$. Atomic units (a.u.) are used.

primary dynamical Dirac effects (electronic charge contraction, minima-raising and gradient reduction) by means of a Schrödinger-Dirac ratio. We have observed that while the LMC ratio is always positive and it has an increasing behavior as a function of Z (mainly because its disequilibrium ingredient enhances when Z increases), the Fisher-Shannon ratio can reach negative values for the excited states although finally enhances when Z increases. Moreover, the global enhancement phenomenon of the two complexities is mainly due to the electronic charge contraction, and the Fisher-Shannon negativity in the excited states is associated to the raising of the non-relativistic minima. The latter phenomenon is mainly due to the Fisher-information ingredient of the Fisher-Shannon complexity, because it is the only factor which is very sensitive to the fact that the Dirac relativistic radial density cannot vanish except at the origin and infinity, keeping in mind that it is a gradient functional of the density. The (largely ignored) gradient reduction effect is present in all excited states although it is, at times, hidden by the minima-raising effect.

Furthermore, we have shown in large- Z hydrogenic systems the dependence of the two previous statistical complexities as a function of the following parameters of the Dirac states: the energy, the principal quantum number (n) and the relativistic quantum number (k). We have observed that for the l -manifold states of a given quantum number n , the LMC complexity enhances parabolically and the Fisher-Shannon complexity varies within the same interval when energy is increasing; this is mainly because of the delicate balance of the charge contraction and the minima raising effects. Besides, beyond the ground state, we have observed that for $j = m_j$ the behavior of the two complexity measures of the l -manifold states in terms of the relativistic quantum number k is quasi-symmetric around the line with $k = -1$ (i.e., states s).

Entropic uncertainty inequality and applications

The entropic, or frequency, moments of a one-particle density function $\rho(\vec{r})$, defined in Eq. (1.6), play a relevant role within a Density Functional Theory framework [35, 34]. Much effort has been made to obtain a similar formulation of the DFT theory in the conjugate space, *i.e.* in terms of the momentum one-particle density $\gamma(\vec{p})$, with many successful results [199, 200, 201, 202].

Different studies based on the simultaneous use of quantities in the position and momentum spaces have been carried out. Most of them aim to provide uncertainty-like relationships. For instance, the well-known Heisenberg uncertainty principle [61, 62, 63] involves variances (defined by means of radial expectation values) in conjugate spaces. Since the formulation of the Heisenberg principle, many other uncertainty relations have been obtained, with a diversity of expectation values and/or density functionals. It is worth mentioning the lower bounds on products of radial expectation values $\langle r^\alpha \rangle$ and $\langle p^\beta \rangle$ [60] emphasizing the particular case $\alpha = \beta = 2$. Bounds on the disequilibrium of the charge density [203], the product of logarithmic uncertainties [60] and the sum of Shannon [66] or Rényi [72] entropies are also known. Although these relationships are usually applied in three-dimensional systems (*i.e.* with vectors of three components \vec{r} and \vec{p}), all of them are valid for arbitrary dimensionality [59, 176].

Such uncertainty relations are physically relevant, not only because of their importance in a theoretical quantum-mechanical framework [204, 205, 206], but also in the development of quantum information and computation [8, 207]. In this sense, the studies of entropic uncertainty relations [68] and their connection with entanglement [69] are also remarkable.

The aim of this study is to present uncertainty inequalities, in the form of bounds on a frequency moment (quantity defined in Section 1.1) in a given space (position or momentum) in terms of two radial expectation values in the conjugate space. Such inequalities can handle radial expectation values of positive or negative orders. The bounds provided here are of universal validity (*i.e.* for any d -dimensional quantum mechanical system). By way of example, we carry out a numerical study for selected inequalities of physical interest in atomic systems, and the results are interpreted taking into account that some radial expectation values for atomic densities, in both position and momentum spaces, are physically relevant and/or experimentally accessible.

The term “frequency moments“ is usually employed in probability and statistics. Sichel [208, 209] employed them for the fitting of certain frequency curves. It happens that estimators based on frequency moments are, at times, much better than the ordinary moment

estimates. Moreover, the frequency moments are fairly efficient in the range where the ordinary moments are very inefficient. This is so in some cases where the range is unlimited and the density is poorly known [44].

The quantities ω_q are called also "entropic moments" of the density function, because they are closely connected to the so-called Rényi and Tsallis entropies [43, 135]. The entropic adjective and the frequency term allow us to identify more appropriately the moments ω_q from the other type of moments [44]: moments around the origin, central moments, factorial moments, absolute moments,... of a distribution.

The frequency moments play a central role in the description of many-fermion systems in terms of the one-particle density. In this sense, it is worth remarking the relevance of those with orders $q = 4/3$ and $5/3$, within a DFT framework. They correspond, essentially, to the exchange and kinetic energy terms of the energy functional [36]. The frequency moment of order 2 is the disequilibrium of the probability distribution as we have shown in previous chapters. In addition, the problem of fully characterizing the distribution by frequency moments was also addressed by considering the so-called Hausdorff entropic moment problem [210].

This chapter is structured as follows: In Section 4.1, the uncertainty relations associated to the main quantities we will deal with (frequency moments) are provided, as universal bounds on frequency moments in terms of radial expectation values in the conjugate space. Particular cases of physical interest are detailed in Section 4.2, by providing rigorous inequalities whose accuracy is numerically analyzed in Section 4.3 for atomic one-particle densities. Some concluding remarks are finally given.

4.1 Upper bounds on frequency moments in terms of radial expectation values

Using Eq. (1.5), the Rényi uncertainty relation (1.20) can be expressed in terms of frequency moments as follows:

$$\omega_q[\rho] \leq \left(\frac{(q/\pi)^{q-1}}{(2q-1)^{\frac{2q-1}{2}}} \right)^d \omega_t^{\frac{1}{2t-1}}[\gamma], \quad \text{for } q \geq 1 \geq t \quad \text{with } \frac{1}{q} + \frac{1}{t} = 2, \quad (4.1)$$

and the opposite inequality holds for $q \leq 1 \leq t$.

Many expectation values are well-known relevant quantities which can be accessed or estimated from experiments (diamagnetic susceptibility, electron-nucleus attraction energy, height of the peak of the Compton profile, kinetic energy and its relativistic correction due to mass variation,...) [211]. That is not the case of frequency moments, in spite of their physical significance, especially in a Density Functional Theory (DFT) framework. Let us mention the relevant role played by the exchange and kinetic terms in the expansion of the functional for the total energy [36], the Shannon entropy [41] (as a limiting case having its roots in information theory, statistical mechanics and thermodynamics), or the disequilibrium [49] in the study of organization patterns in statistical mechanics, to mention a few of them. Additionally, let us remark that some of the previous functionals are essential

4.1. Upper bounds on frequency moments in terms of radial expectation values 63

ingredients in defining a variety of further information-theoretic concepts (e.g. complexity [50], similarity [48], divergence [137, 212, 213]).

The key point here, from a physical point of view, is that the radial expectation values of the one-particle densities (in position or momentum spaces) are physical observables, while the density functionals do not. It appears consequently of high interest to have at our disposal useful tools to get relevant information from density functionals by using the information we could get at the laboratory, or through alternative ways (theoretical, computational,..).

Due to the physical interest of the frequency moments, the variational procedure has been also employed in order to bound them in terms of physical observables. In Ref. [214], lower (upper) bounds on the d -dimensional frequency moments of order above (below) unity are given in terms of two radial expectation values, not necessarily of positive order. Regarding Eq. (4.1), let us take into account the upper bound $\omega_t^*[\gamma]$ to the frequency moment $\omega_t[\gamma]$ with order below unity, as provided in Ref. [214] in terms of two radial expectation values:

$$\omega_t[\gamma] \leq \omega_t^*[\gamma] \equiv G(\alpha, \beta, t, d) \left[\langle p^\alpha \rangle^{-t(\beta+d)+d} \langle p^\beta \rangle^{t(\alpha+d)-d} \right]^{1/(\alpha-\beta)} \quad (4.2)$$

where

$$\alpha > d \frac{1-t}{t} > \beta$$

This bound is given in the aforementioned work, together with similar lower ones for order $t > 1$. Their analytical expressions, as well as that of the function $G(\alpha, \beta, t, d)$ can be found there.

The joint use of Eq. (4.1) and its 'opposite version' for $q \leq 1$, together with the above mentioned variational upper and lower bounds on frequency moments [214], provide us with a variety of bounds (upper or lower) on $\omega_q[\rho]$ in terms of $\langle p^\alpha \rangle$ and $\langle p^\beta \rangle$. The symbol $B(x, y)$, in the equations below, stands for the beta function.

(a) Upper bounds for $q > 1$ with $\alpha > d \frac{q-1}{q} > \beta$:

$$\begin{aligned} \omega_q[\rho] \leq & (\alpha - \beta) \left(\frac{\pi}{q} \right)^{d(1-q)} q^q (2q-1)^{d \frac{1-2q}{2}} \left[\Omega_d B \left(\frac{d+q(\alpha-d)}{(q-1)(\alpha-\beta)}, \frac{q(d-\beta)-d}{(q-1)(\alpha-\beta)} \right) \right]^{q-1} \times \\ & \times \left\{ \left[\frac{\langle p^\beta \rangle}{d+q(\alpha-d)} \right]^{d+q(\alpha-d)} \left[\frac{\langle p^\alpha \rangle}{q(d-\beta)-d} \right]^{q(d-\beta)-d} \right\}^{\frac{1}{\alpha-\beta}}, \end{aligned} \quad (4.3)$$

where $\Omega_d = 2\pi^{d/2}/\Gamma(d/2)$ and $\alpha > 0$, while β can be either positive or negative.

(b) Lower bounds for $q < 1$ with $\alpha > \beta > -d \frac{1-q}{q}$:

$$\begin{aligned} \omega_q[\rho] \geq & (\alpha - \beta) \left(\frac{\pi}{q} \right)^{d(1-q)} q^q (2q-1)^{d \frac{1-2q}{2}} \left[\Omega_d B \left(\frac{q(\beta-d)+d}{(\alpha-\beta)(1-q)}, \frac{1}{1-q} \right) \right]^{q-1} \times \\ & \times \left\{ \left[\frac{\langle p^\beta \rangle}{d-q(d-\alpha)} \right]^{d-q(d-\alpha)} \left[\frac{q(\beta-d)+d}{\langle p^\alpha \rangle} \right]^{q(\beta-d)+d} \right\}^{\frac{1}{\alpha-\beta}} \end{aligned} \quad (4.4)$$

In this case, each order α and β can be either positive or negative.

(c) Lower bounds for $q < 1$ with $\beta < \alpha < -d\frac{1-q}{q}$:

$$\begin{aligned} \omega_q[\rho] \geq & (\alpha - \beta) \left(\frac{\pi}{q}\right)^{d(1-q)} q^q (2q - 1)^{d\frac{1-2q}{2}} \left[\Omega_d B \left(\frac{q(d-\alpha)-d}{(\alpha-\beta)(1-q)}, \frac{1}{1-q} \right) \right]^{q-1} \times \\ & \times \left\{ \left[\frac{\langle p^\alpha \rangle}{q(d-\beta)-d} \right]^{q(d-\beta)-d} \left[\frac{q(d-\alpha)-d}{\langle p^\beta \rangle} \right]^{q(d-\alpha)-d} \right\}^{\frac{1}{\alpha-\beta}} \end{aligned} \quad (4.5)$$

Now, both orders α and β of the radial expectation values are negative necessarily.

The same inequalities apply after exchanging the conjugated variables and densities, giving rise to bounds on frequency moments $\omega_q[\gamma]$ in momentum space in terms of radial expectation values in the position one.

4.2 Particular cases of physical interest

For atomic systems, the expectation values $\langle r^n \rangle$ and $\langle p^n \rangle$ have been extensively used to bound and/or estimate other global quantities [215, 214] and the density itself [216]. Among those quantities, let us remark the frequency moments of both $\rho(\vec{r})$ and $\gamma(\vec{p})$. Additionally, different uncertainty-like inequalities, in terms of radial expectation values, have been derived by using information-theoretical tools [71, 217].

It is worth mentioning that some of these expectation values are physically relevant and/or experimentally accessible in three-dimensional N -electron atoms. Some examples are the following [211]:

- (a) The kinetic energy T , given by $T = N\frac{\langle p^2 \rangle}{2}$, with its relativistic correction being proportional to $\langle p^4 \rangle$.
- (b) The height of the peak of the Compton profile $J(q)$, experimentally accessible from electron scattering experiments, is $J(0) = N\frac{\langle p^{-1} \rangle}{2}$.
- (c) The diamagnetic susceptibility χ , proportional to $\langle r^2 \rangle$.
- (d) The electron-nucleus attraction energy (absolute value) $E_{eN} = NZ\langle r^{-1} \rangle$, with Z being the nuclear charge.

Concerning the frequency moments, Eq. (1.6), and their corresponding Rényi entropies, Eq. (1.5), they have been considered as essential tools in a wide variety of fields, including the study of three-dimensional ($d = 3$) many-electron systems and physical processes. Many of those studies have emphasized the role played by the order ' q ' of the aforementioned density functionals, as also done in more recent applications based on the concepts of Jensen-Rényi [137], Jensen-Tsallis [212] and Kullback-Leibler [30] divergences, the quantum similarity index [118, 143] and its generalization [218] or the generalized shape complexity [86], among others. In most of these applications, considering low enough values (usually below unity) of the order q appears very important in order to get non-trivial

information, based on the features of the one-particle density in position space, regarding a variety of relevant properties of e.g. atomic systems.

However, the main applications in the present chapter deal with frequency moments of order above unity. For N-fermion systems, it is known [36] that the frequency moments $\omega_{4/3}[\rho]$ and $\omega_{5/3}[\rho]$ are related to the local density approximations to the exchange and kinetic energies, K_0 and T_0 respectively, as

$$K_0 = \frac{(3N)^{4/3}}{4\pi^{1/3}} \omega_{4/3}[\rho], \quad (4.6)$$

$$T_0 = \frac{(3N)^{5/3} \pi^{4/3}}{10} \omega_{5/3}[\rho], \quad (4.7)$$

It is worth mentioning the upper bound

$$\langle \rho \rangle \leq (8/3\pi^2)(2/3)^{1/2}(T/N)^{3/2} \approx 0.2206(T/N)^{3/2}, \quad (4.8)$$

due to Gadre and Chakravorty [203], and derived within a DFT framework by considering the relationship between the total kinetic energy functional T and its Weizsäcker term T_W . Moreover, T is proportional to the radial expectation value $\langle p^2 \rangle$.

4.3 Numerical analysis with atomic one-particle densities

The accuracy of the universal bounds on frequency moments and, in particular, to relevant physical quantities expressed in terms of them (shown in Section 4.2), will be analyzed in this section for ground-state neutral atoms throughout the whole Periodic Table (nuclear charge $Z = 1 - 103$). In doing so, accurate near-Hartree-Fock wavefunctions [219, 220] will be employed, from which the one-particle densities in position and momentum spaces are built up, see also Appendix A

Let us remind the normalization to unity of both densities, a condition expressed as $\omega_1[\rho] = \omega_1[\gamma] = 1$ or, equivalently, $\langle r^0 \rangle = \langle p^0 \rangle = 1$. The systems considered in this numerical applications are three-dimensional ones, so that $d = 3$ and $\Omega_3 = 4\pi$.

4.3.1 Disequilibrium or information energy

The disequilibrium D of a probability distribution [49] is defined as its mean value or, equivalently, the second-order frequency moment as given by Eq. (1.7). In order to bound from above the disequilibrium in terms of radial expectation values in the conjugate space, we must choose $q = 2$ in Eq. (4.3). Due to the validity of these bounds in both conjugate spaces, we will deal with equations for the disequilibrium $D[\rho]$ of the position space density $\rho(\vec{r})$. Similar inequalities are obtained for $D[\gamma]$ after exchanging the conjugate variables and their corresponding distributions.

We consider first the general inequality

$$D[\rho] \leq D_\rho(\alpha, \beta) = \frac{128(\alpha - \beta)}{3^{9/2}\pi^2} \Gamma\left(\frac{2\alpha - 3}{\alpha - \beta}\right) \Gamma\left(\frac{3 - 2\beta}{\alpha - \beta}\right) \times \left\{ \left[\frac{\langle p^\alpha \rangle}{3 - 2\beta} \right]^{3-2\beta} \left[\frac{\langle p^\beta \rangle}{2\alpha - 3} \right]^{2\alpha-3} \right\}^{\frac{1}{\alpha-\beta}}, \quad (4.9)$$

providing an upper bound, denoted as $D_\rho(\alpha, \beta)$, in terms of any two moments $\langle p^\alpha \rangle$ and $\langle p^\beta \rangle$ with orders constrained as $\alpha > \frac{3}{2} > \beta$. We observe that the order α is positive necessarily, while β can be positive, negative or zero. The notation of the bound as $D_\rho(\alpha) \equiv D_\rho(\alpha, 0)$ is employed for the particular choice $\beta = 0$, namely

$$D[\rho] \leq \frac{128\alpha}{(2\alpha - 3)^{2 - \frac{3}{\alpha}} 3^{\frac{9}{2} + \frac{3}{\alpha}} \pi^2} \Gamma\left(2 - \frac{3}{\alpha}\right) \Gamma\left(\frac{3}{\alpha}\right) \langle p^\alpha \rangle^{3/\alpha} \equiv D_\rho(\alpha) \quad (4.10)$$

Apart from normalization, the bound $D(\alpha)$ is defined in terms of a unique expectation value $\langle p^\alpha \rangle$ with $\alpha > 3/2$. Especially interesting are the cases $\alpha = 2$ and $\alpha = 4$, with the corresponding bounds determined, respectively, by the kinetic energy (proportional to $\langle p^2 \rangle$) and its relativistic correction (essentially $\langle p^4 \rangle$) due to mass variation.

In Figure 4.1a, the disequilibrium $D[\rho]$ for the charge density of neutral atoms is displayed, together with the aforementioned two upper bounds, namely $D_\rho(2)$ and $D_\rho(4)$. These bounds are given by

$$D_\rho(2) = \frac{128}{729\pi} \langle p^2 \rangle^{3/2} \approx 0.05589 \langle p^2 \rangle^{3/2} \quad (4.11)$$

and

$$D_\rho(4) = \frac{2^{15/2}}{3^{21/4} 5^5 \pi} \langle p^4 \rangle^{3/4}. \quad (4.12)$$

It is worth remarking that our bound $D_\rho(2)$ improves Gadre's one [63] in Eq. (4.8), rewritten as

$$D[\rho] \leq \frac{4}{3^{3/2} \pi^2} \langle p^2 \rangle^{3/2} \approx 0.07800 \langle p^2 \rangle^{3/2}, \quad (4.13)$$

after taking into account that $\langle \rho \rangle = D[\rho]$ and $T = N \langle p^2 \rangle / 2$. The improvement is quantified by a factor of 72% of Gadre's one.

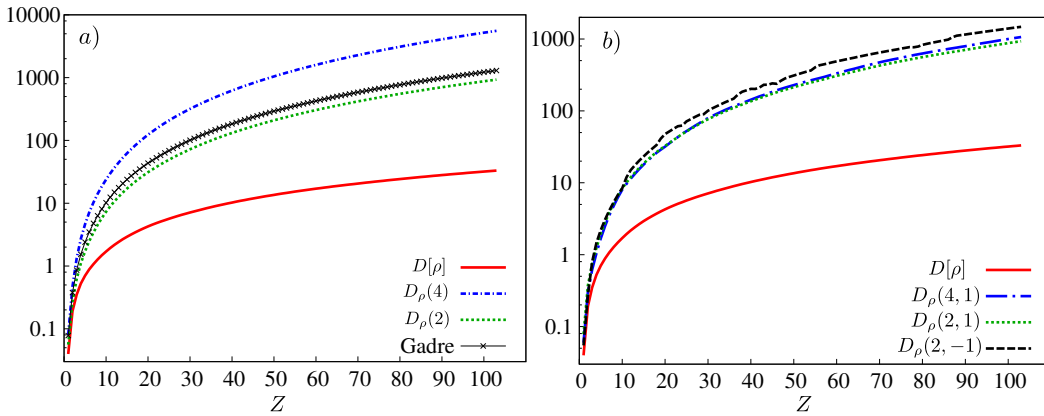


Figure 4.1: Upper bounds on the disequilibrium $D[\rho]$ in position space (neutral atoms with nuclear charge $Z = 1 - 103$), in terms of (a) one, and (b) two radial expectation values in momentum space.

It should be noticed also the functional dependence on the nuclear charge Z of the disequilibrium and the above discussed upper bounds of the systems under study. Such a

dependence is (roughly) a power-like one as Z^c , with c a constant. An approximate value $c = 1.3$ is induced numerically for the disequilibrium $D[\rho]$, and $c = 2.1$ and $c = 2.4$ for the upper bounds $D_\rho(2)$ and $D_\rho(4)$, respectively. Those values of the power c imply a higher accuracy of the upper bounds for light atomic systems as compared to the heavier ones.

Considering non-zero orders α and β in Eq. (4.9) provides us with upper bounds on $D[\rho]$ in terms of two radial expectation values, constrained by the inequality $\alpha > 3/2 > \beta$. Consequently the order β can be either positive or negative. Some examples are displayed in Figure 4.1b, corresponding to the analytical expressions given below:

$$D_\rho(2, 1) = \frac{128}{3^{9/2}\pi^2} \langle p \rangle \langle p^2 \rangle, \quad (4.14)$$

$$D_\rho(2, -1) = \frac{512}{3^5 5^{5/3} \pi} \langle p^{-1} \rangle^{1/3} \langle p^2 \rangle^{5/3}, \quad (4.15)$$

$$D_\rho(4, 1) = \frac{32\Gamma^2(1/4)}{3^{7/2} 5^{5/3} \pi^2} \langle p \rangle^{5/3} \langle p^4 \rangle^{1/3} \quad (4.16)$$

It is observed in Figure 4.1b the similar behavior of the three bounds above mentioned, as also that of the own disequilibrium. To have an idea of the dependence on the nuclear charge Z of all bounds, the power-like dependence corresponds roughly to the constant $c = 2.1$. Attending to the value $c = 1.3$ for $D[\rho]$ as observed in Figure 4.1a, similar comments apply in what concerns the accuracy of these bounds for light, medium or heavy systems.

We now consider the study of the momentum-space disequilibrium $D[\gamma]$, with upper bounds expressed in terms of radial expectation values, now in position space. As done above regarding the numerical analysis of the bounds on $D[\rho]$, we study also the corresponding ones $D_\gamma(\alpha)$ and $D_\gamma(\alpha, \beta)$ for the momentum space one-particle distribution $\gamma(\vec{p})$.

The analytical expressions of these bounds, denoted as $D_\gamma(\alpha)$ and $D_\gamma(\alpha, \beta)$, are straightforwardly obtained from the previous ones, by only exchanging the conjugate variables \vec{r} and \vec{p} , as well as the one-particle densities $\rho(\vec{r})$ and $\gamma(\vec{p})$. One- and two-moment upper bounds are considered, with the orders of the involved moment(s) constrained as discussed previously.

The disequilibrium $D[\gamma]$ of the atomic momentum density, together with the one-moment bounds $D_\gamma(2)$ and $D_\gamma(4)$, are displayed in Figure 4.2a, and two-moment bounds are shown in Figure 4.2b. As compared to the position-space case (Figs. 4.1a and 4.1b), a very rich structure is observed for both the disequilibrium and its bounds, regarding their dependence on the atomic nuclear charge Z . The presence of local extrema (maxima or minima) is very apparent in the figures. On a physical basis, the reason for finding a so rich structure is the enhancement, in the evaluation of the expectation values, of the contribution arising from the outermost (valence) region. The absolute maximum of the momentum densities occur (most usually) at the origin $p = 0$, or in its surrounding. The low-speed electrons (i.e. those with $p \approx 0$) correspond to the valence ones. Let us remark that the shell-filling pattern constitutes one of the main characteristics in atomic systems, determining most of their physical and chemical properties.

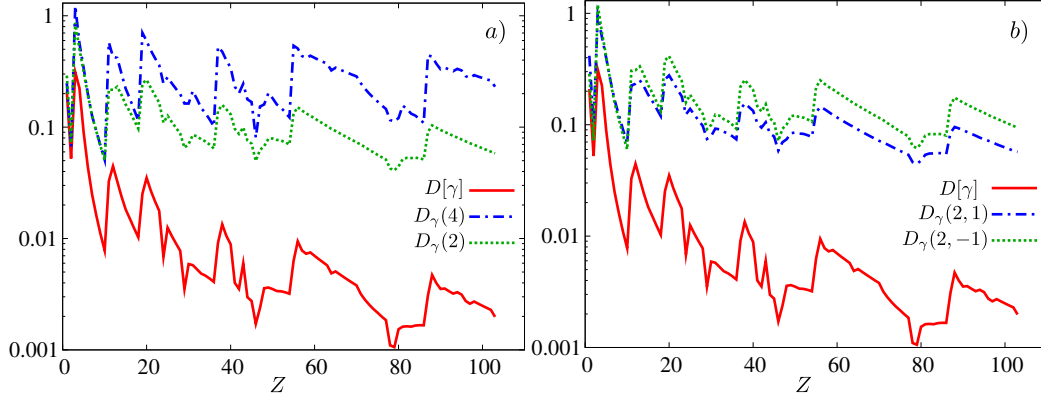


Figure 4.2: Upper bounds on the disequilibrium $D[\gamma]$ in momentum space (neutral atoms with nuclear charge $Z = 1 - 103$), in terms of (a) one, and (b) two radial expectation values in position space.

In this sense, it is worth pointing out that the local minima of $D[\gamma]$ correspond to systems $Z = 2, 10, 18, 24, 29, 36, 42, 46, 54, 58, 64, 79, 86, 90, 93, 97$, which can be classified as follows: (i) noble gases ($Z = 2, 10, 18, 36, 54, 86$), and (ii) systems suffering from the so-called 'anomalous shell filling' ($Z = 24, 29, 42, 46, 58, 64, 79, 90, 93, 97$). Similar sets of extrema and their classification are also found for the one- and two-moment upper bounds. Additionally, let us mention the systematic presence of local maxima for most alkaline earths ($Z = 12, 20, 38, 56, 88$).

4.3.2 Thomas-Fermi kinetic energy

One of the earliest tractable schemes for solving the many-electron problem was proposed by Thomas [221] and Fermi [222]. In this model the electron density $\rho(\vec{r})$ is the central variable rather than the wavefunction, and the total energy of a system is a functional of the density. The Thomas-Fermi energy functional is composed of three terms, one of them the electronic kinetic energy T_0 associated with a system of non-interacting electrons in a homogeneous electron gas. Its form, as provided in Eq. (4.7), is obtained by integrating the kinetic energy density of a homogeneous electron gas.

The expression of T_0 in terms of the frequency moment $\omega_{5/3}[\rho]$ allows to perform a bounding procedure as done in previous sections. In this way we obtain a variety of upper bounds in terms of radial expectation values in momentum space, as follows:

$$T_0 \leq N^{5/3} \frac{(\alpha-\beta)2^{5/3}3^{5/2}5^{8/3}}{7^{7/2}\pi^{1/3}} \left[\Gamma\left(\frac{5\alpha-6}{2(\alpha-\beta)}\right) \Gamma\left(\frac{6-5\beta}{2(\alpha-\beta)}\right) \right]^{2/3} \times \\ \times \left\{ \left[\frac{\langle p^\alpha \rangle}{6-5\beta} \right]^{6-5\beta} \left[\frac{\langle p^\beta \rangle}{5\alpha-6} \right]^{5\alpha-6} \right\}^{\frac{1}{3(\alpha-\beta)}} \equiv T_0(\alpha, \beta), \quad (4.17)$$

for any $\alpha > \frac{6}{5} > \beta$.

Choosing $\beta = 0$ gives rise to one-moment bounds,

$$T_0 \leq N^{5/3} \frac{\alpha 2^{\frac{5}{3}-\frac{2}{\alpha}} 3^{\frac{5}{2}-\frac{2}{\alpha}} 5^{8/3}}{7^{7/2} (5\alpha - 6)^{\frac{5}{3}-\frac{2}{\alpha}} \pi^{1/3}} \left[\Gamma\left(\frac{5}{2} - \frac{3}{\alpha}\right) \Gamma\left(\frac{3}{\alpha}\right) \right]^{2/3} \langle p^\alpha \rangle^{2/\alpha} \equiv T_0(\alpha), \quad (4.18)$$

for any $\alpha > \frac{6}{5}$. Figure 4.3a displays the value of the functional T_0 , together with the one-moment upper bounds $T_0(\alpha)$ for $\alpha = 2$ and $\alpha = 4$, namely in terms of $\langle p^2 \rangle$ and $\langle p^4 \rangle$, respectively:

$$T_0(2) = N^{5/3} \frac{3^{3/2} 5^{8/3}}{2^{1/3} 7^{7/2}} \langle p^2 \rangle \approx 0.3322 N^{5/3} \langle p^2 \rangle \quad (4.19)$$

and

$$T_0(4) = N^{5/3} \frac{2^{2/3} 5^{8/3} \Gamma^{4/3}(3/4)}{3^{8/3} 7^{14/3} \pi^{1/3}} \langle p^4 \rangle^{1/2} \approx 0.0139556 N^{5/3} \langle p^4 \rangle^{1/2} \quad (4.20)$$

As one should expect, the bound $T_0(2)$ is more accurate because of its dependence on $\langle p^2 \rangle$, a quantity proportional to the exact kinetic energy.

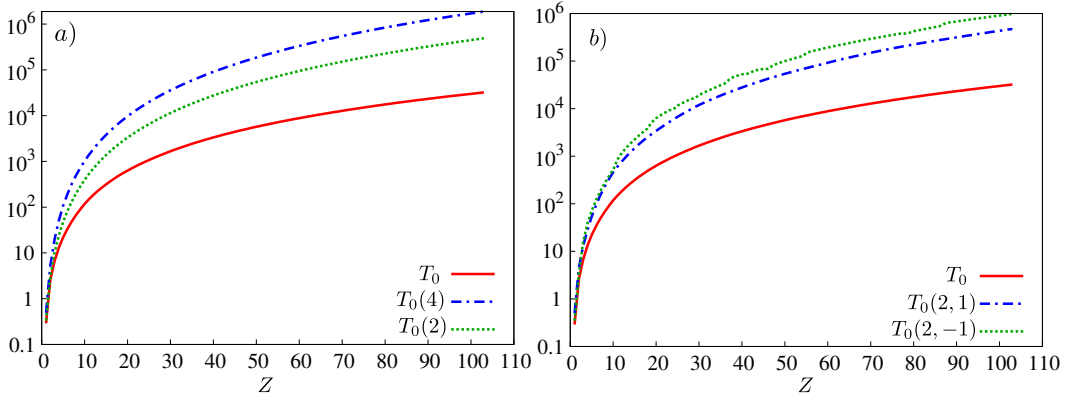


Figure 4.3: Upper bounds on the Thomas-Fermi kinetic energy T_0 (neutral atoms with nuclear charge $Z = 1 - 103$), in terms of (a) one, and (b) two radial expectation values in momentum space.

Similar comments to those provided in the discussion of results for disequilibrium in position space (Fig. 4.1a) apply for the results on T_0 , regarding the power-like functional dependence Z^c on the nuclear charge Z . While T_0 possesses a fit with $c = 4.1$, the corresponding values are $c = 4.7$ for $T_0(2)$ and $c = 5.0$ for $T_0(4)$. These values justify (i) the higher accuracy of $T_0(2)$ as compared to $T_0(4)$, and (ii) the higher accuracy of both bounds for light systems as compared to heavy ones.

A similar behavior is observed in Figure 4.3b, where two-moment bounds are considered, in particular

$$T_0(2,1) = N^{5/3} \frac{3^{5/2} 5^{8/3}}{2 \cdot 7^{7/2}} \langle p \rangle^{4/3} \langle p^2 \rangle^{1/3} \quad (4.21)$$

and

$$T_0(2, -1) = N^{5/3} \frac{2^{7/9} 3^{7/2} 5^{8/3}}{7^{7/2} 11^{11/9} \pi^{1/3}} [\Gamma(2/3)\Gamma(11/6)]^{2/3} \langle p^{-1} \rangle^{4/9} \langle p^2 \rangle^{11/9}, \quad (4.22)$$

both including the kinetic energy via $\langle p^2 \rangle$. The exponent of the nuclear charge have the values $c = 4.7$ and $c = 4.9$ for the respective fits.

4.3.3 Dirac exchange energy

Shortly after the introduction of Thomas-Fermi theory, Dirac [223] developed an approximation for the exchange interaction K_0 based on the homogeneous electron gas. The resulting formula is simple, and is also a local functional of the density, as given by Eq. (4.6).

The bounds on the frequency moment $\omega_{4/3}[\rho]$ translate into upper bounds on K_0 :

$$K_0 \leq N^{4/3} \frac{8(\alpha-\beta)^{3^{5/2}}}{5^{5/2}\pi} \left[\Gamma\left(\frac{4\alpha-3}{\alpha-\beta}\right) \Gamma\left(\frac{3-4\beta}{\alpha-\beta}\right) \right]^{1/3} \times \left\{ \left[\frac{\langle p^\alpha \rangle}{3-4\beta} \right]^{3-4\beta} \left[\frac{\langle p^\beta \rangle}{4\alpha-3} \right]^{4\alpha-3} \right\}^{\frac{1}{3(\alpha-\beta)}} \equiv K_0(\alpha, \beta), \quad (4.23)$$

for any $\alpha > \frac{3}{4} > \beta$. The one-moment bounds, obtained with the choice $\beta = 0$, are given by

$$K_0 \leq N^{4/3} \frac{8\alpha 3^{\frac{5}{2}-\frac{1}{\alpha}}}{5^{5/2}(4\alpha-3)^{\frac{4}{3}-\frac{1}{\alpha}}\pi} \left[\Gamma\left(4-\frac{3}{\alpha}\right) \Gamma\left(\frac{3}{\alpha}\right) \right]^{1/3} \langle p^\alpha \rangle^{1/\alpha} \equiv K_0(\alpha), \quad (4.24)$$

for any $\alpha > \frac{3}{4}$. Interesting particular cases are

$$K_0(2) = N^{4/3} \frac{8 \cdot 3^{7/3}}{5^{10/3} \pi^{2/3}} \langle p^2 \rangle^{1/2} \approx 0.2265 N^{5/3} \langle p^2 \rangle^{1/2} \quad (4.25)$$

and

$$K_0(4) = N^{4/3} \frac{32 \cdot 3^{9/4}}{5^{5/2} 13^{13/12} \pi} [\Gamma(13/4)\Gamma(3/4)]^{1/3} \langle p^4 \rangle^{1/4}, \quad (4.26)$$

displayed in Figure 4.4, together with the bound

$$K_0(1, -1) = N^{4/3} \frac{8 \cdot 3^{17/6}}{5^{13/6} 7^{7/6} \pi^{2/3}} \langle p^{-1} \rangle^{1/6} \langle p \rangle^{7/6} \quad (4.27)$$

as an illustrative example of the two-moment ones. In this figure, the power-like dependence on Z is emphasized, by using a logarithmic scale in both axes. These bounds behave as Z^c with $c = 3.4, 3.5, 3.3$ for $K_0(2)$, $K_0(4)$ and $K_0(1, -1)$ respectively, values to be compared with that for K_0 , namely $c = 3.0$. Similar comments to those given in discussing results for T_0 apply now, also.

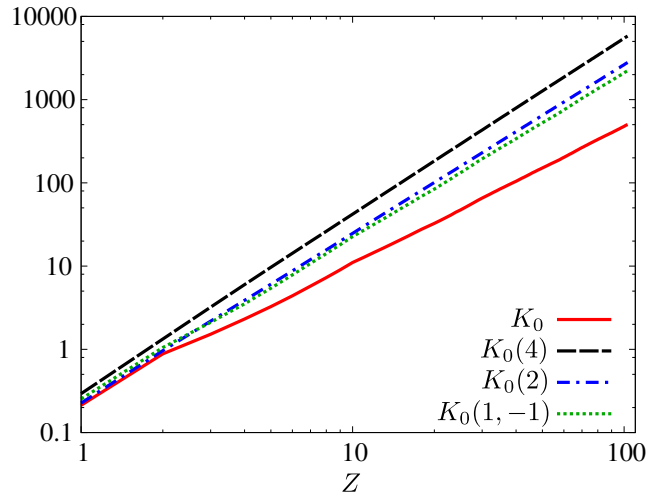


Figure 4.4: Upper bounds on the Dirac exchange energy K_0 (neutral atoms with nuclear charge $Z = 1 - 103$), in terms of one and two radial expectation values in momentum space.

Conclusions

The uncertainty inequality for Rényi entropies of conjugate distributions allowed us to perform a bounding procedure, whose main achievement is to provide upper and lower bounds on q -th order frequency moments in terms of radial expectation values in the conjugate space. The procedure here employed provides results of universal validity, in the sense of being applicable to arbitrary one-particle densities arising from wavefunctions related through a Fourier transform.

We apply the above procedure to the study of physically relevant density functionals, defined in terms of the position and momentum one-particle densities of neutral atoms throughout the Periodic Table. Emphasis is laid on the one- and two-moment upper bounds on the position and momentum disequilibria, the Thomas-Fermi kinetic energy and the Dirac exchange energy. These bounds are expressed also in terms of physically meaningful and/or experimentally accessible expectation values. The power-like dependence of the position-space functionals and their upper bounds has been observed, and analyzed numerically in detail. On the other hand, the results for the momentum-space disequilibrium are interpreted according to shell-filling patterns, a feature shared by the corresponding upper bounds in terms of radial expectation values in position space.

Further applications are planned to be carried out in a near future. In this sense, we will take into account that the frequency moments and the Rényi and Tsallis entropies, including the Shannon one as a particular case, have been shown to play a fundamental role in the definition and applications of information-theoretical concepts such as complexity, similarity and divergence. Additionally, other extensions of the present study will concern more sophisticated atomic models (e.g. configuration interaction), many-fermion systems (e.g. molecules) and physico-chemical processes (ionization, excitation, reaction).

Generalized quantum similarity index

Recently, different divergence measures have been used in the framework of quantum information theory. In particular, the Jensen-Shannon divergence [102] was applied as a measure of entanglement [24, 25], and also together with other similarity measures in the study of multielectronic systems [115, 145, 116, 30]. Chemical similarity is often described as an inverse of a measure of distance or divergence in the appropriate space.

Quantifying the dissimilarity among two or more many-electron systems by means of their one-particle densities is also a hot topic within the physical applications of the information theory. Some fundamental measures of information have been used with this aim: Shannon (1.4), Rényi (1.5) and Tsallis [224] entropies and Fisher information (1.9), as well as their associated divergences [31, 212, 137, 29]. Among those divergence measures, susceptible of being employed to study atomic or molecular systems, especially relevant are the “Kullback-Leibler or relative entropy” (1.28), and the quantum similarity index (*QSI*) [118, 144, 139, 115] defined in Eq. (1.36).

The aim of this work is to present a new general similarity measure. Its definition, as compared to the pioneering *QSI*, constitutes a generalization modifying the number of functions to be compared and the weights of each of them in different regions of their domain of definition. The usefulness of the new comparative quantifier is illustrated with applications for one-particle densities in position and momentum spaces. These densities are used as a benchmark to study a known but extremely hierarchical and complex [53] set of quantum objects: atoms, but the universality and versatility of this technique allows its application to other more complex or less known molecular or nuclear systems.

The quantum similarity index constitutes a particular case of a one-parameter “generalized quantum similarity index” $QSI^{(q)}$. The analysis of the $QSI^{(q)}$ here provided generalizes and improves some previous results on the *QSI* of atomic systems. Such an improvement mainly arises from the capability of $QSI^{(q)}$ to modify, by means of its characteristic parameter, the relative contribution of relevant specific regions of the atomic densities in both conjugated spaces. The $QSI^{(q)}$ allows a deep introspection within the structure of the atomic one-particle densities, capturing relevant differences in any of the conjugated spaces. This is not the case of other measures of divergence or similarity employed with multielectronic systems as, for instance, the own *QSI*.

The structure of this Chapter is the following. Section 5.1 is devoted to define the generalized quantum similarity index, and to analyze its main theoretical features, including its advantages with respect to the original similarity index *QSI*. In Section 5.2, applications to the similarity-based study of atomic one-particle densities are carried out, dealing with

neutral (Section 5.2.1) and ionized species (Section 5.2.2). Concluding remarks and open problems are given.

5.1 Generalized quantum similarity index

Let us consider a couple of functions, $f(\vec{r})$ and $g(\vec{r})$, with identical domain Δ in the d -dimensional space \mathbb{R}^d . In what follows, all integrations are understood to be performed over the common domain Δ . The Hölder's inequality [141] establishes the relationship

$$\int f g d\vec{r} \leq \left(\int f^p d\vec{r} \right)^{1/p} \left(\int g^q d\vec{r} \right)^{1/q} \quad (5.1)$$

for any $p, q > 1$ verifying $\frac{1}{p} + \frac{1}{q} = 1$. Equality in the above expression is reached if and only if $f(\vec{r}) = g(\vec{r})$.

The definition of the quantum similarity index $QSI[f, g]$, given by Eq. (1.36), together with Hölder's inequality for the particular case $p = q = 2$, allows to assert that $QSI[f, g] \in [0, 1]$, with $QSI[f, g] = 1$ if and only if $f(\vec{r}) = g(\vec{r})$.

The Hölder's inequality in Eq. (5.1) constitutes a particular case of the "generalized Hölder's inequality" [141], given by

$$\left[\int (fg)^m d\vec{r} \right]^{1/m} \leq \left(\int f^p d\vec{r} \right)^{1/p} \left(\int g^q d\vec{r} \right)^{1/q}, \quad (5.2)$$

with $p, q > m > 0$ verifying $\frac{1}{p} + \frac{1}{q} = \frac{1}{m}$. The particular case $m = 1$ provides Hölder's inequality, namely Eq. (5.1).

An iterative use of the above expression allows to generalize the inequality for an arbitrary number $n \geq 2$ of functions $\{f_1, f_2, \dots, f_n\}$:

$$\left[\int (f_1 \cdots f_n)^m d\vec{r} \right]^{1/m} \leq \left(\int f_1^{p_1} d\vec{r} \right)^{1/p_1} \cdots \left(\int f_n^{p_n} d\vec{r} \right)^{1/p_n}, \quad (5.3)$$

with $\frac{1}{p_1} + \dots + \frac{1}{p_n} = \frac{1}{m}$. Raising to 'm' and defining $\lambda_i \equiv m/p_i$ the inequality reads as

$$\int (f_1 \cdots f_n)^m d\vec{r} \leq \left(\int f_1^{p_1} d\vec{r} \right)^{\lambda_1} \cdots \left(\int f_n^{p_n} d\vec{r} \right)^{\lambda_n}, \quad (5.4)$$

with $\sum_{i=1}^n \lambda_i = 1$. We now define new functions $g_i(\vec{r})$ through the identity $f_i = g_i^{q/p_i}$ for an arbitrary $q > 0$, so that

$$\int (g_1^{\lambda_1} \cdots g_n^{\lambda_n})^q d\vec{r} \leq \left(\int g_1^q d\vec{r} \right)^{\lambda_1} \cdots \left(\int g_n^q d\vec{r} \right)^{\lambda_n}. \quad (5.5)$$

The left- and right-hand-side terms in the last inequality give rise to a quotient not greater than 1, as also occurred when defining QSI . This is the essential ingredient that allows to define the ' q th order generalized quantum similarity index':

$$QSI^{(q)}[\{g_i, \lambda_i\}_{i=1}^n] \equiv \frac{\int (g_1^{\lambda_1} \cdots g_n^{\lambda_n})^q d\vec{r}}{(\int g_1^q d\vec{r})^{\lambda_1} \cdots (\int g_n^q d\vec{r})^{\lambda_n}} \quad \text{with} \quad \sum_{i=1}^n \lambda_i = 1, \quad (5.6)$$

and $0 < \lambda_i < 1$ for all $i = 1, \dots, n$. It is worthy to remark that (i) $QSI^{(q)} \in [0, 1]$ for any $q > 0$, and (ii) the quantity $QSI^{(q)}$ does not depend on the normalization of the chosen functions $g_i(\vec{r})$, as also happens with the usual QSI . The last point implies that the similarity index constitutes a measure of how similar the distributions are according to their shapes rather than to their absolute values or sizes, contrary to the aforementioned divergences.

The definition of the above similarity index, as compared to the original QSI measure, constitutes a generalization in three different ways, namely:

- The number ' n ' of functions $g_i(\vec{r})$ under comparison, not necessarily $n = 2$ as for the QSI which constitutes a measure of overlap between two densities, while its generalization quantifies the total overlap among an arbitrary number of them.
- The order q , which allows to enhance or diminish the contribution of the 'tails' and, in general, the surroundings of the local extrema of each function, by considering higher or lower values of q .
- The 'weights' λ_i , a set of parameters which control the relative importance of each function in performing the comparison among themselves by means of the generalized similarity index.

For the sake of simplicity in notation, the weights λ_i will be omitted as arguments of $QSI^{(q)}$ unless necessary. Relevant particular cases of the generalized similarity index $QSI^{(q)}$ are detailed below:

(a) Similarity between two densities.

The usual QSI in Eq. (1.36) is obtained from the general expression in Eq. (5.6) by choosing a number of densities $n = 2$, the second order $q = 2$, and equal weights $\lambda_1 = \lambda_2 = 1/2$. That is,

$$QSI^{(2)}[g_1, g_2] = QSI[g_1, g_2] \quad (5.7)$$

For arbitrary order and weights, the generalized similarity index reads as

$$QSI^{(q)}[g_1, g_2] = \frac{\int (g_1^\lambda g_2^{1-\lambda})^q d\vec{r}}{(\int g_1^q d\vec{r})^\lambda (\int g_2^q d\vec{r})^{1-\lambda}} \quad (5.8)$$

for any $0 < \lambda < 1$.

(b) Uniformly weighted similarity.

Choosing uniform weights $\lambda_i = 1/n$ in Eq. (5.6) gives rise to

$$QSI^{(q)}[g_1, \dots, g_n] = \frac{\int (g_1 \cdots g_n)^{q/n} d\vec{r}}{\sqrt[n]{\int g_1^q d\vec{r} \cdots \int g_n^q d\vec{r}}}, \quad (5.9)$$

in particular

$$QSI^{(q)}[g_1, g_2] = \frac{\int (g_1 g_2)^{q/2} d\vec{r}}{\sqrt{\int g_1^q d\vec{r} \int g_2^q d\vec{r}}} \quad (5.10)$$

(c) Relationship among generalized $QSI^{(q)}$ of different order.

From the definition in Eq. (5.6), we check that

$$QSI^{(q)}[g_1, \dots, g_n] = QSI^{(t)}[g_1^{q/t}, \dots, g_n^{q/t}] \quad (5.11)$$

for arbitrary orders q and t . The particular case $t = 2$ provides, in the right-hand-side, the usual QSI , and consequently

$$QSI^{(q)}[g_1, \dots, g_n] = QSI[g_1^{q/2}, \dots, g_n^{q/2}] \quad (5.12)$$

This means that, in what concerns the dependence on the order q , considering the generalization $QSI^{(q)}$ is equivalent to evaluate QSI not among the considered functions, but instead among them raised, each one, to the power $q/2$. It is in that way that we better understand the role played by the order q : considering different values of the order implies to carry out a comparative study based on a higher or lower similarity in the short- and long-range domains, in a similar fashion as done in divergence-based previous studies [212, 137, 225].

5.2 Numerical analysis with atomic one-particle densities

In this section we analyze the similarity among atomic one-particle densities, in both position and momentum spaces. In doing so, accurate near-Hartree-Fock wavefunctions [219, 220] are employed as a benchmark, for both neutral and ionized species with a number of electrons up to 103 and 54, respectively. Atomic units (a.u.) will be used throughout the section.

For the sake of brevity, we will restrict the analysis of the results according to the dependence of the generalized similarity on its order q , dealing with uniformly weighted couples of functions. This description corresponds to the functional

$$QSI^{(q)}[g_1, g_2] = \frac{\int (g_1 g_2)^{q/2} d\vec{r}}{\sqrt{\int g_1^q d\vec{r} \int g_2^q d\vec{r}}} \quad (5.13)$$

in order to go far beyond the well-known results provided by QSI as obtained for the particular case $q = 2$ [115, 145].

5.2.1 Pairs of neutral atoms

Let us consider two neutral atoms, A and B, with respective nuclear charges Z_A and Z_B and electron charge densities $\rho_A(\vec{r})$ and $\rho_B(\vec{r})$. In previous studies, the problem of checking the extent to which the *similarity* between the one-particle densities of systems A and B implies a *similarity* among their physico-chemical properties, and conversely, was afforded by quantifying the similarity between ρ_A and ρ_B according to the QSI measure given by Eq. (1.36). The pioneering and very successful results obtained in comparing molecular densities [48] appeared to be very poor when dealing with atomic densities [115]. The main conclusion was that similarity between atoms A and B is roughly determined by the difference $|Z_A - Z_B|$ among their nuclear charges. So, the quantity $QSI(Z, Z') = QSI[\rho_Z, \rho_{Z'}]$ as function of Z for fixed Z' displays an unimodal shape, firstly increasing until reaching the extremal value 1 for $Z = Z'$ and decreasing hereinafter. This kind of information regarding similarity is very far from the physical one, where one should expect the presence of properties such as periodicity or shell-filling patterns, among others. A relevant improvement was provided in Ref. [144], where periodicity patterns are displayed by means of QSI with respect to closed-shell systems.

A complete displayment of periodicity patterns was achieved for arbitrary systems A and B throughout the Periodic Table by considering the atomic momentum densities $\gamma_A(\vec{p})$ and $\gamma_B(\vec{p})$, instead of the position space ones [115]. Within this context, the results obtained were extremely rich, in the sense discussed above: similarity between A and B was strongly determined by the atomic shell-filling patterns, and periodicity was clearly displayed.

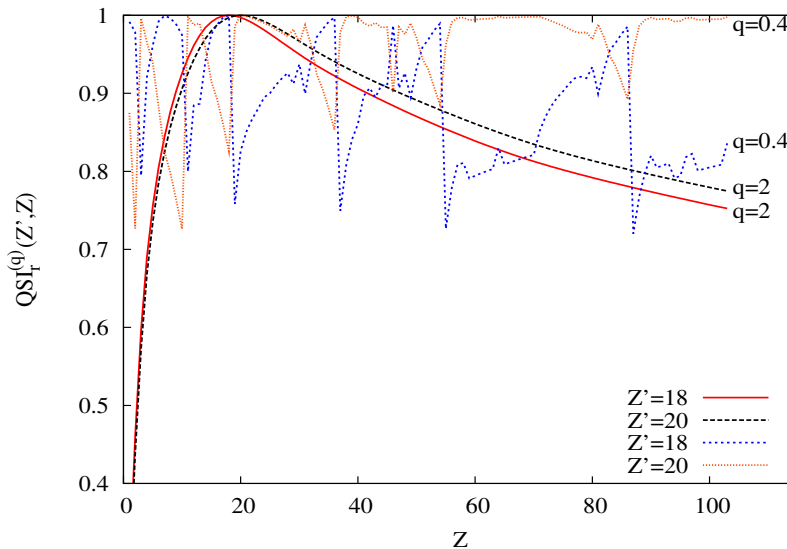


Figure 5.1: Generalized quantum similarity index $QSI_r^{(q)}(Z', Z)$ (for $q = 0.4$ and 2.0) in position space among each of Argon ($Z' = 18$) and Calcium ($Z' = 20$) with respect to all neutral atoms with nuclear charge $Z = 1 - 103$.

In this section, however, we show that the position-space generalized quantum simi-

larity index $QSI^{(q)}$ makes possible to get similar information as that provided by $QSI = QSI^{(2)}$ in momentum space, by dealing with appropriate values of q other than $q = 2$. For illustration, the $QSI(Z', Z)$ and $QSI^{(q)}(Z', Z)$ measures in position space (with $q = 0.4$) among each of $Z' = 18, 20$ (Ar and Ca) and all other atoms throughout the Periodic Table ($Z = 1 - 103$) are displayed in Fig. 5.1.

As previously mentioned, both curves for QSI behave in an unimodal way, almost overlapping one with each other because of the closeness of the nuclear charges $Z' = 18, 20$. Such a similarity between curves disappears progressively as far as q becomes smaller. Changes are dramatic for a value as low as $q = 0.4$, not only attending to the different paths followed by each curve, but also because of their higher level of structure, displaying numerous local extrema which location is determined by shell-filling patterns. Let us have in mind that $Z = 18$ corresponds to a noble gas (Argon) while $Z = 20$ to an alkaline-earth (Calcium), groups of the Periodic Table characterized by extremely different physical properties. In this sense, it is worthy to remark that the main maxima of $QSI_r^{(0.4)}(Ar, Z)$ occur for noble gases while those of $QSI_r^{(0.4)}(Ca, Z)$ for alkaline-earths. In both cases, additional minor extrema are usually associated to comparisons with systems suffering from an anomalous shell-filling. Similar effects are observed for systems other than $Z' = 18, 20$.

In order to test the usefulness of the generalized index $QSI^{(q)}$ as compared to the usual one QSI , let us observe Fig. 5.2 where the generalized $QSI^{(q)}(Kr, Z)$ for Krypton ($Z' = 36$) is displayed for different values of q , in position (Fig. 5.2a) and momentum (Fig. 5.2b) spaces. The fundamental reason for QSI_r (i.e. $q = 2$) to display a so unstructured curve arises from the exponential long-range behaviour of the charge density $\rho(\vec{r})$. This fact makes the three integrals included in the definition of QSI to be mainly determined by the values of the densities in the surrounding of the origin, the contribution from outermost regions being almost negligible. Such a quick decrease can be attenuated by raising the density to a low power, as controlled by the parameter q in the definition of $QSI^{(q)}$. Consequently, decreasing q makes the relative contribution of the outermost regions ('tails') in the evaluation of similarity to increase. Let us keep in mind that the main physical and chemical properties of atomic systems, including the shell-filling pattern, are determined by the structure of the density in the valence region, most usually the outermost one. This effect is clearly observed in Fig. 5.2a, with a very apparent increase in the number of local extrema within the curves with $q \leq 1$ as compared to the $q = 2$ one. Such an increase is progressive, especially in going from $q = 2$ to $q = 1$, but also for $q < 1$.

Let us notice the main features of systems for which $QSI_r^{(q)}(Kr, Z)$ with $q \leq 1$ displays local maxima: (i) other noble gases (e.g. $Z = 54, 86$ systematically, the rest occasionally), (ii) closed-subshell atoms ($Z = 12, 30, 48, 70, 80$), (iii) half-filled-subshells ($Z = 7, 15, 43, 75$), and (iv) systems with anomalous shell-filling ($Z = 24, 41, 42, 44, 46, 58, 64, 78, 90, 93, 96, 97$).

Concerning momentum space (Fig. 2b), highly structured curves were obtained in the recent past by using QSI . A detailed analysis of the number and location of local maxima allows to assert that: (i) a similar structure is obtained for values of the order within the interval $1.5 \leq q \leq 3$, which includes QSI as $q = 2$; these maxima correspond to the same

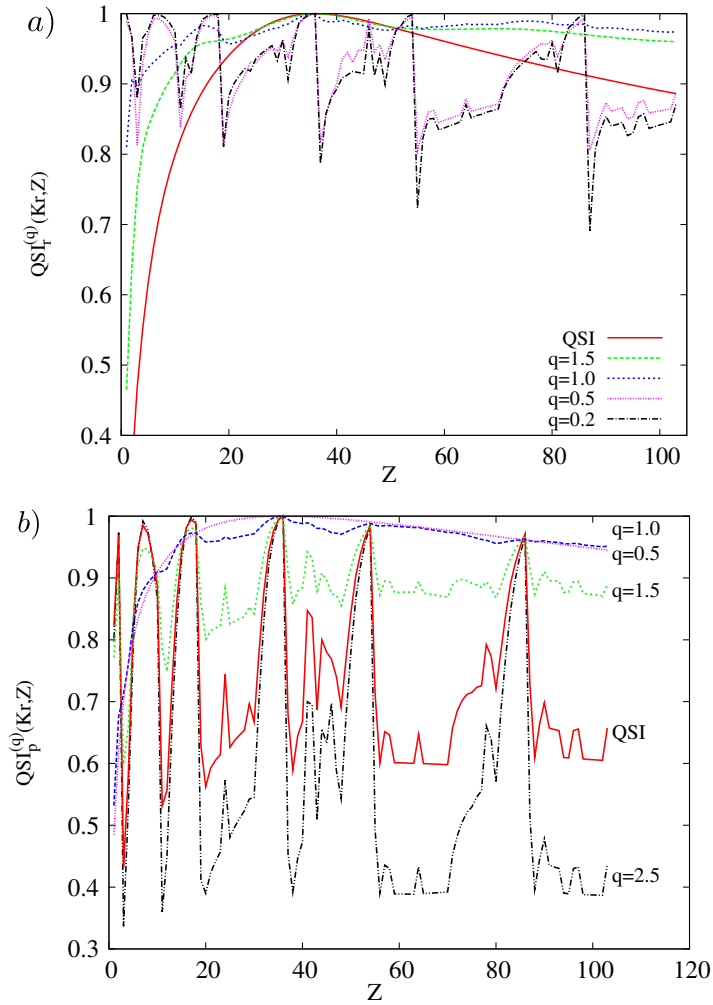


Figure 5.2: Generalized quantum similarity index $QSI^{(q)}(Kr, Z)$ between Krypton ($Z' = 36$) and all neutral atoms with nuclear charge $Z = 1 - 103$ for different orders q , in *a*) position and *b*) momentum spaces.

systems as in the position case, (ii) in going below such a range, a number of local extrema disappears progressively, as e.g. $Z = 2, 7, 29, 78$ (systems characterized in the previous position-space analysis) for the value $q = 1$, and (iii) an order as low as $q = 0.5$ provides an unimodal curve with the unique maximum at $Z = 36$.

Fig. 5.3 shows $QSI_r^{(0.4)}$, a position space index displaying extremely structured curves for all noble gases. The location of local extrema in each curve is determined according to similar patterns to those just discussed. All curves appear (roughly) ordered according to the nuclear charges of the reference systems. This behavior was emphasized in previous works dealing with the momentum space similarity QSI , instead of the position one as in the present figure. Specially remarkable are (i) the closeness to unity of the main maxima of $QSI_r^{(0.4)}$ when comparing a couple of noble gases, and (ii) the very apparent minima when a noble gas is compared with an alkaline system.

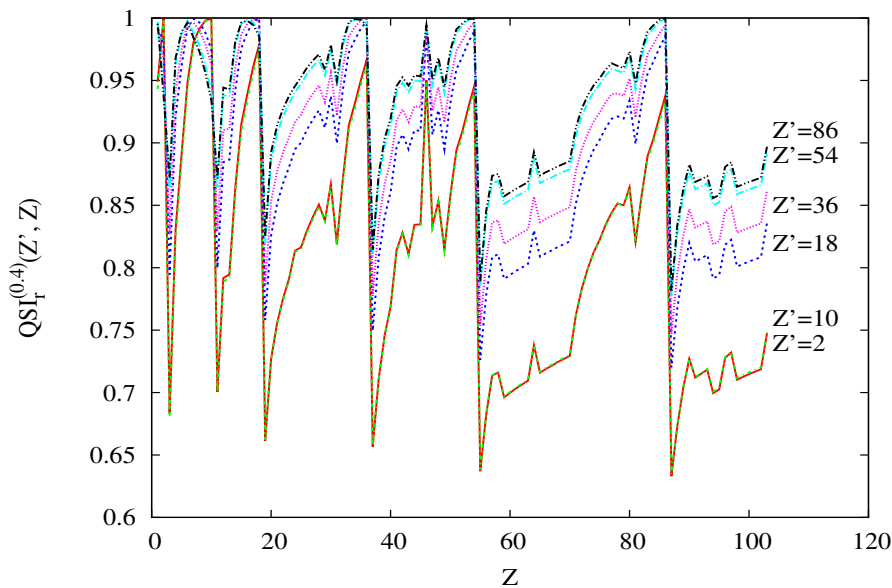


Figure 5.3: Generalized quantum similarity index $QSI_r^{(q)}(Z', Z)$, for $q = 0.4$, in position space of each noble gas with respect to all neutral atoms with nuclear charge $Z = 1 - 103$.

5.2.2 Ionization processes

The results obtained by means of the similarity indexes and their physical interpretation motivated us to ask ourselves about the following questions: to which extent the ionization of a neutral atom modifies its one-particle densities, in both conjugated spaces? Is the similarity measure an appropriate tool to quantify the modifications in the densities? Is there a connection between neutral-ion similarity and relevant physical properties in describing ionization processes?

All those questions are afforded here, employing the generalized measure $QSI^{(q)}(N, C)$ for different values of the order q . In doing so, a number of neutral atoms and their singly-charged cations are considered in order to compare the respective one-particle densities of the neutral system (N) and its cation (C). The results are interpreted according to shell-filling patterns (in particular the subshell from which the electron is ejected) as well as in terms of the first atomic ionization potential. Such a study is performed in both conjugated spaces. Previous works [145] employing the quantum similarity index $QSI(N, C)$ provided more limited results.

We first analyze Fig. 5.4, corresponding to the position space index $QSI_r^{(q)}(N, C)$ for different values of q , together with the atomic ionization potential (AIP) of the neutral system. The most remarkable feature is the increase of structure, according to the number and enhancement of local extrema, as the parameter q becomes smaller. In some cases, most local minima of $QSI_r^{(q)}(N, C)$ correspond to systems displaying local minima in the AIP curve. Such a resemblance does not occur for the position space QSI .

Restricting ourselves to $0.4 \leq q \leq 1$, the following comments are in order:

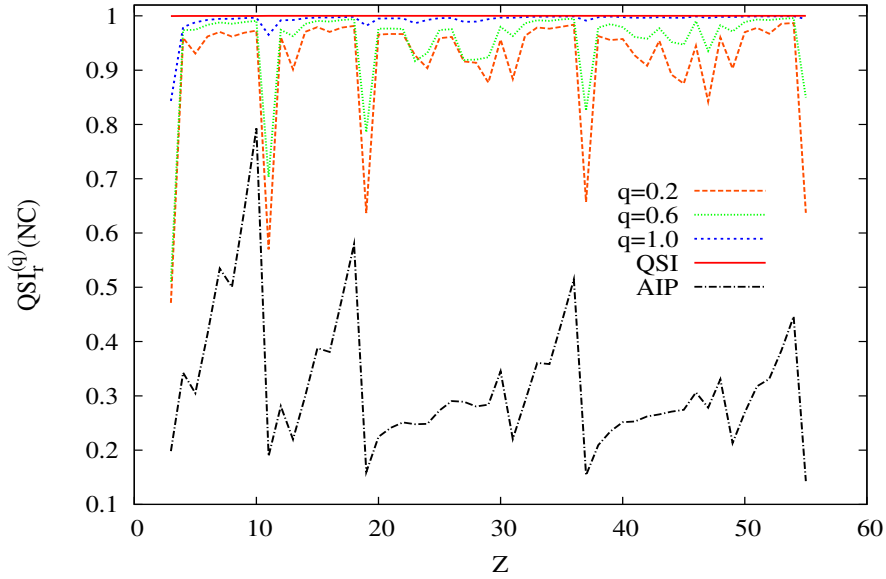


Figure 5.4: Generalized quantum similarity index $QSI_r^{(q)}(N, C)$ in position space for neutral-cation pairs (nuclear charge $Z = 3 - 55$) with different orders q , and atomic ionization potential AIP.

1. The systematic appearance of minima in q -similarity for systems $Z = 3, 8, 11, 19, (23 - 24), 31, 37, 42, 45, 47, 49$ is associated to ionization processes provoking the disappearance of a 's' one, except for $Z = 31$, or a 'p' subshell which becomes half-filled ($Z = 8$).
2. The closeness of the above list with that of AIP minima: $Z = 3, 5, 8, 11, 13, 16, 19, 23, 28, 31, 34, 37, 47, 49$. Values included in this list but not in the previous one are $Z = 5, 13, 16, 28, 34$, corresponding again to the disappearance of subshells ($Z = 5, 13, 28$) or half-filled 'p' ones in the cation ($Z = 16, 34$).
3. Nevertheless, most of the just mentioned 'additional systems' are detected by low enough values of q (0.8 for $Z = 13, 16, 34$ and 0.4 for $Z = 5$). Such a detection occurs also for $Z = 52$ (half-filled 'p' subshell in cation) with $q = 0.8$, in spite of not displaying a minimum of AIP.
4. Most usually, the steepest peaks in the curves are associated to ionization ejecting a s-subshell electron, as compared to the 'p' or 'd' ones. This means that the s-like ionization produces stronger changes in the electron charge density, appreciably more relevant than those produced by removing electrons from other types of subshells.

Conclusions from the analysis in momentum space are roughly the same as those arising from the position space study. A few additional comments are in order: (i) a strong resemblance among lists of minima in generalized similarity for different q 's is observed, even for an interval as wide as $0.5 \leq q \leq 3.0$, and (ii) those lists share many systems

enclosed in the lists of minima of both position-space generalized similarity for low q and the atomic ionization potential. The interpretation of the physical properties characterizing the systems displaying a minimum in momentum space can be done in a similar fashion as in the position one.

Conclusions

The capability of a generalization of the pioneering quantum similarity index to gain physical insight within the structural properties of many-electron systems has been shown. In doing so, we have taken advantage of its characteristic parameter in order to enhance or diminish the short- and long-range contributions in a similarity-based analysis. The generalized index allows to deal with a set of an arbitrary number of density functions, assigning different weights to each one in accordance with their role within the comparative purpose considered.

For atomic systems, a study based on one-particle densities in position space provides clearly an interpretation in terms of shell structure. The generalization introduced in this work allows to deal with densities of any of the conjugated spaces by choosing appropriately the value of its characteristic parameter.

A detailed numerical analysis has been presented, from which it is clearly established the relationship between valence subshell properties of the systems under comparison and the generalized similarity values, as well as the detection of the presence of systems suffering from anomalous shell-filling.

The usefulness of the tool here defined has been shown in the study of ionized systems, by considering the analysis of atomic pairs neutral-cation. It appears a strong resemblance among the extrema of similarity and those of the atomic ionization potential, mostly determined by occupancy numbers of the outermost subshell in neutral and cationic systems. In fact, it is observed that the angular momentum quantum number ' l ' of the electron ejected plays a relevant role in terms of similarity.

Further applications of the generalized index, arising from its rigorous mathematical properties here described, are planned to be carried out in a near future, including studies (i) on the ability in comparing different quantum models (e.g. configuration interactions, relativistic effects), (ii) comparing more than two functions, e.g. sequence anion-neutral-cation, groups/periods of the Periodic Table, isoelectronic series, 'parts' of a given composite system, (iii) assigning appropriate weights to each system according to relevant physical/chemical properties, such as mass, number of electrons, volume. Additional studies of quantum systems (e.g. molecules) and processes (reaction, excitation) will be provided elsewhere.

Geometric Rényi divergence

The aim of this chapter is to propose, study and apply a new one-parameter generalized divergence measure, the “geometric Rényi divergence” $GRD^{(q)}$, which has important advantages over other studied divergences. Particularly, we can not assert that the one-parameter Jensen-Rényi divergence, Eq. (1.34), is always positive as required for a measure of distance, fact that meets the $GRD^{(q)}$. Such improvement mainly arises from the capability of $GRD^{(q)}$ to modify, by means of its characteristic parameter, q , the relative contribution of relevant specific regions of the probability densities. The mathematical definition and properties of $GRD^{(q)}$ allows to deal with arbitrary probability distributions, independently of their meaning or the specific fields of research, including all those previously mentioned.

We show the main mathematical properties as well as the physical properties of this divergence by comparing and studying a simple but highly hierarchical and organized set of quantum systems. We study the one-particle densities of atomic systems, in both conjugated spaces, which contain all the physical and chemical information through Density Functional Theory [36].

In this sense, especially remarkable are the applications carried out in this chapter by means of $GRD^{(q)}$, namely (i) comparison among neutral atoms and interpretation in terms of shell-filling-patterns, (ii) study of ionization processes by analyzing the geometric divergence between the initial and final systems (neutral and cation) and its connection with the value of the ionization potential, (iii) divergence among densities, for a given system, computed within different models, and (iv) to discriminate if an atom belongs or not to a set of systems with identical nuclear charges. The results here provided improve some of the aforementioned applications performed by using other measures, such as e.g. the quantum similarity index [115] or the Jensen-Shannon divergence [136]. Further applications to other systems and/or processes of physico-chemical relevance (e.g. molecules, reactions) will be provided elsewhere.

In Section 6.1 of this chapter we define the geometric Rényi divergence, showing its main mathematical properties. Section 6.2 is devoted to the application of $GRD^{(q)}$ to the study of one-particle densities of atomic systems. Finally we summarize the main results of this chapter.

6.1 Geometric Rényi divergence

Regarding the definition of $JRD^{(q)}$, Eq. (1.34), any order $0 < q \neq 1$ can be considered, as far as the involved frequency moments converge. The limiting case $q \rightarrow 1$ provides the so-called “Jensen-Shannon divergence” [134, 133], $JSD = JRD^{(1)}$, Eq. (1.30), defined as $JRD^{(q)}$ but in terms of the Shannon entropy $S[\rho]$ in Eq. (1.4), instead of the Rényi one. This is due to the limiting equality $S[\rho] = R_1[\rho]$ among entropies.

However, an essential constraint in performing studies by means of $JRD^{(q)}$ has been the necessary condition of considering the order q not above unity. The reason is that non-negativity of $JRD^{(q)}$ is guaranteed only for $q \leq 1$, while for $q > 1$ it does not have a definite sign. According to the interpretation of $JRD^{(q)}$ as a measure of ‘distance/divergence’ among distributions, we must avoid values below zero, as usually done for arbitrary metrics in a given space.

Let us recall Eqs. (1.5) and (1.34): we can express the generalized $JRD^{(q)}$, for a set of densities $\rho_1(\vec{r}), \dots, \rho_n(\vec{r})$, in terms of frequency moments as

$$JRD^{(q)}[\rho_1, \dots, \rho_n] = \frac{1}{1-q} \ln \frac{\omega_q [\sum_{k=1}^n \alpha_k \rho_k]}{(\omega_q[\rho_1])^{\alpha_1} \cdots (\omega_q[\rho_n])^{\alpha_n}} \quad (6.1)$$

The nonnegativity of $JRD^{(q)}$ for $q < 1$ arises from the value above unity of the fraction within the logarithm. The same property of $JRD^{(q)}$ for $q > 1$ would be verified in case of the fraction being below unity, what is not necessarily true. We will deal with $\{\rho_i(\vec{r})\}_{i=1}^n$ d -dimensional normalized-to-unity distributions, a condition which can be expressed as $\omega_1[\rho_i] = 1$.

In order to get a Rényi-like divergence measure, nonnegative for arbitrary order, we apply the procedure shown in the previous chapter, Section 5.1. The inequality given in Eq. (5.5), coming from the “generalized Hölder’s inequality” [141], provide a quotient above unity, for arbitrary $q > 0$. This quotient has been defined in Eq. (1.36) as the “generalized quantum similarity index” $QSI^{(q)}$, and extensively characterized throughout previous Chapter 5. Applying logarithms to both sides of the inequality (5.5) we get, in terms of frequency moments,

$$\lambda_1 \ln \omega_q[\rho_1] + \cdots + \lambda_n \ln \omega_q[\rho_n] - \ln \omega_q[\rho_1^{\lambda_1} \cdots \rho_n^{\lambda_n}] \geq 0 \quad (6.2)$$

where $\sum_{i=1}^n \lambda_i = 1$. We can now define a novel measure of divergence in terms of the Rényi entropies, Eq. (1.5), as

$$GRD^{(q)}[\rho_1, \dots, \rho_n] \equiv (q-1) \left(R_q[\rho_1^{\lambda_1} \cdots \rho_n^{\lambda_n}] - \sum_{i=1}^n \lambda_i R_q[\rho_i] \right) \geq 0. \quad (6.3)$$

The quantity $GRD^{(q)}$ will be referred as “geometric Rényi divergence” of order q for the set of distributions $\{\rho_i\}$ with weights $\{\lambda_i\}$. Given the relationship between this new measure $GRD^{(q)}$ and the $QSI^{(q)}$, just through a logarithm $GRD^{(q)} = -\ln QSI^{(q)}$, one could interpret the Geometric Rényi Divergence as a “logarithmic similarity”.

Some comments are in order:

1. Let us notice the strong resemblance between the terms within parenthesis in Eq. (6.3) and those of the definition of the Jensen-Rényi divergence $JRD^{(q)}$ in Eq. (1.34). In fact, all terms associated to individual distributions are identical, the difference between both expressions being determined by the multicomponent term. That term corresponds to the frequency moment of the arithmetic mean $(\lambda_1\rho_1 + \dots + \lambda_n\rho_n)$ of the distributions in the $JRD^{(q)}$ case, while to the geometric mean $(\rho_1^{\lambda_1} \cdots \rho_n^{\lambda_n})$, instead, in $GRD^{(q)}$.
2. The additional factor $(q - 1)$ guarantees the nonnegativity of $GRD^{(q)}$ for any $q > 0$, including the non-zero and finite-valued limiting case $q = 1$. Adding the same factor in the definition of $JRD^{(q)}$ would not solve the problem of the undefiniteness of sign for $q > 1$, as will be shown in Section 6.2.1
3. A particular case, of physical relevance, is obtained for $q = 2$:

$$GRD^{(2)}[\rho_1, \dots, \rho_n] = \ln \frac{(D[\rho_1])^{\lambda_1} \cdots (D[\rho_n])^{\lambda_n}}{D[\rho_1^{\lambda_1} \cdots \rho_n^{\lambda_n}]} \quad (6.4)$$

where the functional $D[\rho]$ is the disequilibrium, Eq. (1.7). So, $GRD^{(2)}$ for a set of distributions is expressed in terms of the quotient between the geometric mean of their respective disequilibria and the disequilibrium of the geometric mean of the distributions.

4. For the sake of clarity, we give below the simplest case of two densities with uniform weights, namely

$$GRD^{(q)}[\rho_1, \rho_2] = (q - 1) \left\{ R_q[\sqrt{\rho_1\rho_2}] - \frac{1}{2} (R_q[\rho_1] + R_q[\rho_2]) \right\}, \quad (6.5)$$

to be compared with Eq. (1.33). The arithmetic mean is replaced by the geometric one, obtaining a nonnegative divergence measure once including the factor $(q - 1)$.

5. $GRD^{(q)}$ keeps other relevant properties of $JRD^{(q)}$, including (i) invariance under exchange of distributions, (ii) additivity, and (iii) they reach the minimal value zero if and only if all distributions are identical.
6. Nevertheless, $GRD^{(q)}$ possesses an additional property not shared with $JRD^{(q)}$. The geometric divergence of a set of distributions is independent of the normalization of each one within the set. Such an invariance under changes of normalization also holds for $JRD^{(q)}$ as far as those changes be identical for all distributions. In this sense, the comparison among distributions established by means of $GRD^{(q)}$ is based on a dissimilarity according to the shapes of the distributions, rather than on sizes, masses, charges or any other quantity for which normalization is relevant. This means that, in what concerns the measure $GRD^{(q)}$ it is not necessary to consider normalized-to-unity functions, contrary to the $JRD^{(q)}$ case as pointed out after Eq. (6.1).

7. The main usefulness of the geometric Rényi divergence arises from its ability to modify the relative contribution of specific regions within the domain of definition in obtaining the divergence value, by varying appropriately the order q . This is a fundamental feature in the applications to atomic systems, as will be discussed in the numerical analysis performed in next section.

An illustrative example will allow us to understand better the role played by the order q of GRD . Let us consider two one-dimensional gaussians, one of them centered at the origin, $f(x) = e^{-x^2}$, and the other one with center at an arbitrary point, $g(x) = e^{-(x-a)^2}$. Both them have identical long-range behavior, but short-range dissimilarity will be determined by the length of the shift a . Computing straightforwardly $GRD^{(q)}(f, g) = a^2q/4$, we can notice that, for fixed $a \neq 0$, the geometric divergence increases as q does, because of the “emphasis” in the comparison based on short-range values. For any fixed q , the saturation $GRD^{(q)}(f, g) = 0$ occurs for $a = 0$, that is $f = g$.

6.2 Numerical analysis with atomic one-particle densities

The geometric divergence introduced in this work possesses useful features, especially relevant when compared to previous measures of divergence. Let us remark, on one hand, the characteristic parameter q (“order”) which enables us to modify the relative contribution of specific regions for the comparative process among densities. On the other hand, its nonnegativity makes possible the interpretation as a “mean distance” (not in a strict mathematical sense) among the distributions under comparison. The latter is true for any $q > 0$. Such is not the case of the pioneering measure of divergence built up by means of the Rényi entropy, namely the Jensen-Rényi divergence $JRD^{(q)}$. In Section 6.1 we mentioned that its nonnegativity (necessary to be interpreted as a divergence) is guaranteed only for $q \leq 1$.

For illustration, both the Jensen-Rényi and the geometric-Rényi divergences between the one-particle densities of neutral atoms He and Fr ($Z = 2$ and $Z = 87$, respectively) are displayed in Figure 6.1 for $0 < q \leq 6$, in both position and momentum spaces. The procedure for calculating the one-particle densities of these N -electron systems is described in Appendix A. Atomic units (a.u.) will be used.

It is observed in Figure 6.1 that, as we should expect, $GRD^{(q)}(He, Fr)$ remains positive (in both spaces) within the whole interval, in fact for any $q > 0$. However, $JRD^{(q)}(He, Fr)$ becomes negative for q above unity. In this example, negativity of the Jensen-Rényi divergence is observed for $q \geq 1.26$ in position space, and $1.08 \leq q \leq 3.00$ in the momentum one. Let us notice the existence of values of q for which $JRD^{(q)}(He, Fr) = 0$, in spite of dealing with two different distributions. So, the requirement of having null divergence if and only if the distributions under comparisons are identical is violated.

6.2.1 Neutral atoms

At a first stage, we consider two significantly different atoms, such as Argon (noble gas, nuclear charge $Z = 18$) and Calcium (alkaline-earth, $Z = 20$). We compare, in Figure

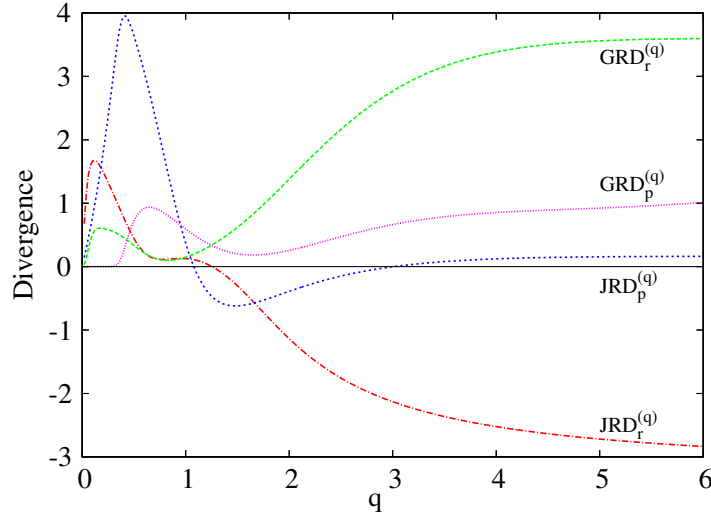


Figure 6.1: Jensen-Rényi, $JRD^{(q)}$, and Geometric Rényi, $GRD^{(q)}$, divergences between densities of He and Fr ($Z = 2$ and $Z = 87$, respectively) neutral atoms in position and momentum spaces, for $q = 0.4$ and $q = 2$.

6.2, each one of their charge densities $\rho(\vec{r})$ with all those of neutral atoms throughout the whole Periodic Table ($Z = 1 - 103$), and similarly with momentum densities $\gamma(\vec{p})$. In doing so, the uniformly weighted Geometric Rényi Divergence $GRD^{(q)}$ in Eq. (6.5) is employed for orders $q = 0.4$ and $q = 2$. Differences among the results obtained for each value of q are apparent: very “soft” and almost identical curves for both Ar and Ca are obtained with $q = 2$, while numerous local extrema appear for $q = 0.4$ with the structure of the curves being extremely different one from each other.

In order to justify these results from a physical point of view, it is worthy to remark that the main atomic physical and chemical properties are determined by the shell structure and, in particular, by the characteristics (quantum numbers, occupancy,...) of the outermost subshell (valence region). The computation of $GRD^{(q)}$ requires that of the q th order frequency moments of each density and also of their geometric mean. Due to the exponential long-range behavior of the atomic charge densities, the relative contribution of the outermost region to the evaluation of the integrals involved is very small as compared to that of the core. Such a contribution can be enhanced by raising the density to a relatively small power, as done when considering frequency moments of lower orders. Diminishing the value of $q = 2$ up to $q = 0.4$ allows to gain enough information regarding valence features, so that $GRD^{(q)}$ reveals in most cases if the systems under comparison share or not the above mentioned features (e.g. if they belong to the same group of the Periodic Table). However, the closeness between both curves for $q = 2$ is due to the similar values of their nuclear charges (18 and 20), together with the enhancement, for the computation of integrals, of the surround of the nuclei, where the attractive potential governed by the nuclear charge Z determines (roughly) the shape and magnitude of the electronic cloud. A detailed analysis on the patterns for the appearance of extrema is carried out in the discussion of next Figure 6.3.

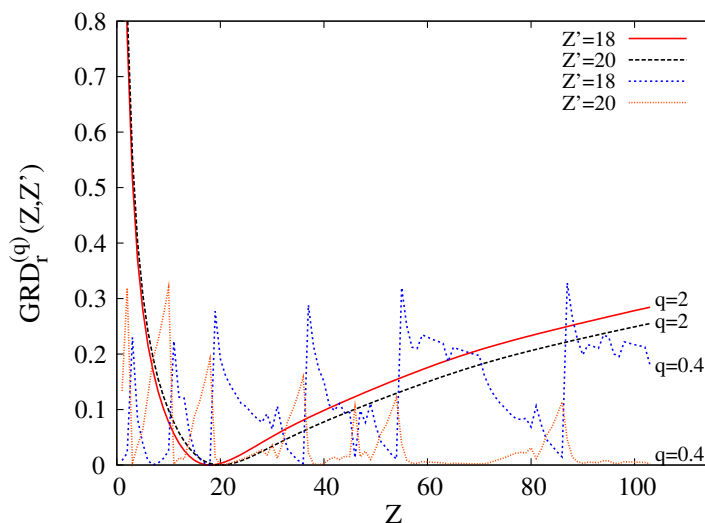


Figure 6.2: Geometric Rényi divergences $GRD_r^{(q)}(Ar, Z)$ and $GRD_r^{(q)}(Ca, Z)$ in position space, for $q = 0.4$ and $q = 2$ of both Argon and Calcium with respect to all neutral atoms $1 \leq Z \leq 103$.

Six curves are displayed in Figure 6.3, corresponding to the position-space $GRD_r^{(q)}$ with $q = 0.4$ between each alkaline metal (group IA) and all neutral atoms with $1 \leq Z \leq 103$. It is clearly observed the similar structure of all curves, appearing almost perfectly embedded. A detailed analysis of the location of maxima and minima brings on the following observations:

- Almost systematic appearance of local minima when comparing any of the above mentioned systems with another one belonging to its own group ($Z = 3, 11, 19, 37, 55, 87$). These minimum values should be interpreted as a low divergence among systems with share the fundamental features at the valence region and, consequently, with similar physico-chemical properties. Those minima correspond to the main ones observed in Figure 6.3.
- The opposite occurs when comparing alkalines with noble gases, with higher values (local maxima) of divergence. Let us remind the prediposition for reactivity of alkalines, while noble gases ($Z = 2, 10, 18, 36, 54, 86$) are conformed so as to keep their closed shell structure. According to the meaning of the divergence measure here considered, it should be expected a high divergence, based on the one-particle densities, when comparing a pair of so different systems from a physical point of view. The appearance of local maxima when comparing alkaline-noble atoms is absolutely systematic now.
- A number of additional extrema, not so apparent as compared to the above discussed, appear in each curve. The systems corresponding to minima can be classified, roughly, in two different groups: (i) non-alkaline systems with a unique electron at the valence subshell ($Z = 13, 31, 49, 81$), and (ii) systems suffering from anoma-

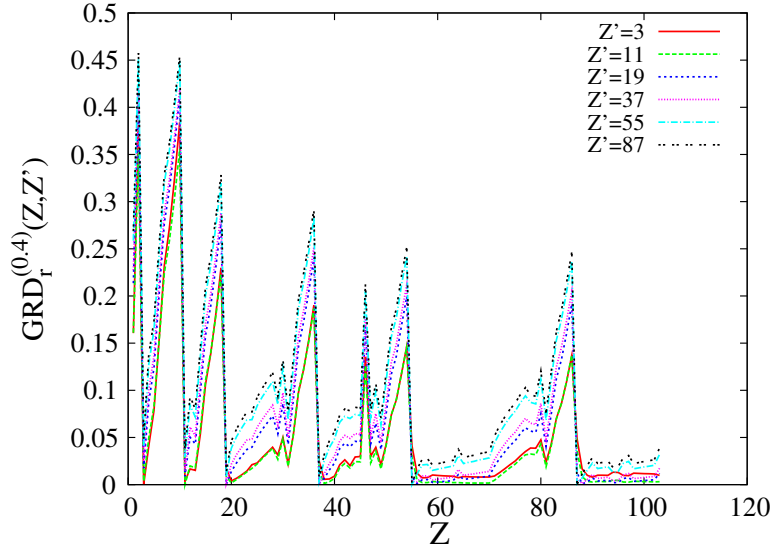


Figure 6.3: Geometric Rényi divergence $GRD_r^{(q)}(Z, Z')$ of order $q = 0.4$, in position space, between each alkaline ($Z' = 3, 11, 19, 37, 55, 87$) and all neutral atoms $1 \leq Z \leq 103$.

lous shell-filling ($Z = 29, 79, 93$). Similarly occurs for maxima, most of them corresponding to: (i) closed-subshell systems ($Z = 12, 30, 48, 80$) and (ii) anomalous shell-filling again ($Z = 42, 44, 46, 58, 64, 90, 97$).

The display (or not) of local extrema when comparing a density for a given neutral atom with the rest of them depends on the order q considered. This fact has been emphasized when discussing Figure 6.2 which includes two different orders: $q = 2$ (curves with no extrema at all) and $q = 0.4$ (with numerous extrema). The appearance of extrema is progressive in going from $q = 2$ to $q = 0.4$.

This fact is clearly observed in Figure 6.4, where divergence among the charge densities of Krypton ($Z = 36$) and each of the systems $1 \leq Z \leq 103$ are provided by means of $GRD_r^{(q)}$ for different values of q . The structural features of the curves, in what concerns number and enhancement of extrema, is very apparent as far as q decreases from 2.5 to 1. There exists a group of atoms for which a extremum appears in all the four curves, while other systems compared with Kr require a low enough value of q in order to be displayed as a extremum.

The opposite trend is observed in the momentum-space comparison (not shown here), in the sense of having curves with a higher structure as far as q becomes higher. The reason for those trends in opposite spaces requires again to consider the enhancement of the relative contributions of the valence and core regions. While increasing q provokes the enhancement of the core for the comparison of densities in position space, due to their maximal values at the origin, the enhancement in momentum space occurs for low-speed electrons (surround of $p = 0$), that is those of the outermost spatial region. Consequently, similar conclusions are obtained from the analysis in position and momentum space. This comment applies also to all other figures discussed in this subsection.

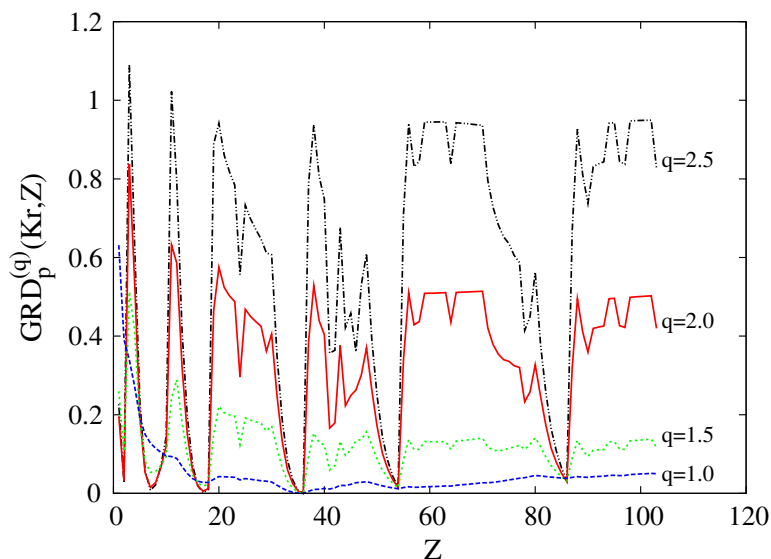


Figure 6.4: Geometric Rényi divergence in momentum space $GRD_p^{(q)}(Kr, Z)$ between Krypton ($Z = 36$) and all neutral atoms $1 \leq Z \leq 103$, for orders $q = 1.0, 1.5, 2.0, 2.5$.

6.2.2 Ionization processes

Our next purpose is to analyze the effects arising from the physical process of atomic ionization, attending to the changes experienced by the one-particle densities of the system considered. In doing so, we employ the geometric Rényi divergence in order to compare the respective densities of the 'initial and final products' (that is, the neutral atom and the singly-charged cation) involved in this physical process. Within this context, we employ the notation $GRD^{(q)}(NC)$ for the neutral-cation comparison in a given space.

For illustration, we consider the analysis in position space, i.e. for the quantity $GRD_r^{(q)}(NC)$, with NC pairs of nuclear charges $3 \leq Z \leq 55$, and consequently each system containing a number of electrons up to 54. This quantity is displayed in Figure 6.5 for different values of q , together with an algebraic function of the atomic ionization potential (AIP). This function of AIP is considered, instead of the own AIP, in order to make easier the interpretation of the correlation observed among the divergence and AIP values.

In what concerns $GRD_r^{(q)}(NC)$ for the considered q 's, some comments are in order:

1. Systems displaying (in Figure 6.5) higher values (local maxima) of divergence between the neutral and ionized species can be classified as follows:
 - $Z = 3, 11, 19, 37, 55$ (alkalines) for which the ionization left empty the valence 's' subshell of the neutral atom, and the resulting cation possesses a closed-shell structure. These maxima occur in all curves with the exception $q = 2$, a value too high in order to avoid the masking effect arising from the relatively small information on the valence features, as compared to the core ones.
 - Similarly for $Z = 5, 13, 31, 49$, now disappearing a 'p' subshell. Previous comment regarding the exception $q = 2$ applies also for these systems. Ad-

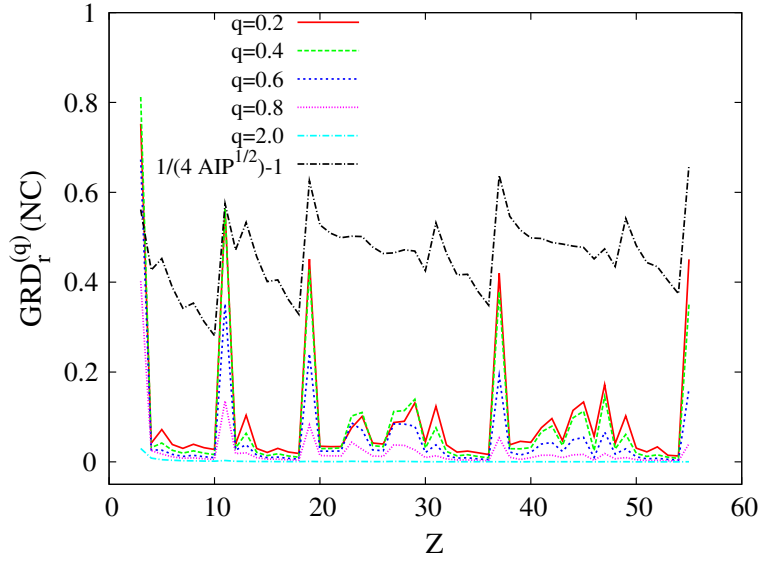


Figure 6.5: Geometric Rényi divergence in position space $GRD_r^{(q)}(NC)$ between a neutral atom (N) and its singly-charged cation (C) with $3 \leq Z \leq 55$, and phenomenological correspondence with the atomic ionization potential AIP of the neutral system.

ditionally, a 'd' subshell becomes empty for $Z = 39$, but a value as low as $q = 0.2$ is needed in order to “detect it” as a local maximum. Each of these systems provides (or not) a maximum according to the value of q .

- $Z = 8, 16, 34, 52$ correspond to systems for which the outermost 'p' subshell becomes half-filled. In this sense, we should emphasize the capability of $GRD_r^{(q)}(NC)$ to 'discrimate' systems with half-filled valence subshell from others with a number of electrons (there) different from half the occupation number. These systems are displayed as maxima for all $q < 1$, while no one for $q = 2$.
- Additional maxima are found for $Z = (23 \text{ or } 24)$, (one of 27, 28, 29), 42, 45, 47, depending on the curve. All these systems are characterized by an ionization process with the ejection of an electron from an inner 's' subshell, instead of the outermost one (3d or 4d). The only ones associated to maxima for $q = 2$ are $Z = 23, 27, 42$. The other ones require values of q below unity.

2. Display of low divergence (some local minima) in Figure 6.5 corresponds to closed-shell and closed-subshell systems ($Z = 4, 10, 12, 18, 30, 36, 48, 54$), the range of q for which they appear as minima depending on the specific systems considered. The subshell from which the electron is ejected remains occupied in the cation and, consequently, changes in one-particle densities, arising from the ionization, are not so strong because of the presence of exactly the same occupied orbitals in the neutral atom and its cation.

3. There exists a clear resemblance between the divergence of pairs NC and the

value of the AIP of the neutral system. The complete list of the 15 local minima of AIP for the systems here considered (displayed in Figure 6.5 as maxima in the corresponding curve, due to the functional of the AIP employed), is: $Z = 3, 5, 8, 13, 16, 19, 23, 28, 31, 34, 37, 47, 49, 55$. Let us notice that all these systems are included in the whole list of large divergence pairs.

To justify these results, let us notice that most systems with low AIP possess a valence subshell (independently of being or not the outermost one) containing a unique electron. Their ionization provokes the disappearance of that subshell, what translates, in terms of changes experienced by the one-particle densities, to a large value of the neutral-cation divergence.

Regarding the ionization analysis, we finally mention that similar conclusions to those here discussed, on the basis of the position-space densities, are obtained from the same analysis in momentum space.

6.2.3 Atomic models

In this subsection, we study to which extent the use of more simplified/sophisticated models for computing the wavefunction provokes more or less significant differences among the corresponding one-particle densities. In order to give a well-posed answer, it is firstly necessary to establish a quantitative measure of difference among densities. The $GRD^{(q)}$ divergence has been employed, both theoretically and numerically through this work, with the aim of quantifying how different two (or more) densities are.

In this sense, we could assert with a quantitative basis if, for instance, to take into account relativistic effects or correlations is worth or not for the study of multielectronic systems in terms of one-particle densities. Perhaps differences could be relevant when comparing wavefunctions, but not so important dealing with densities. Similar analyses would be useful also for a comparative study of relevant distributions in physical systems (e.g. molecules, clusters), arising from different theoretical and/or numerical frameworks.

The aim of the application here discussed is to analyze the effect of the interelectronic repulsion in the structural properties of the atomic charge and momentum densities. In doing so, we compute the densities using different models: the accurate near-Hartre-Fock (HF) one employed for previous applications in this work, and the bare Coulomb field (BCF) one [226], in which the interelectronic repulsive term of the Hamiltonian is neglected. This simplification provides a description of the multielectronic system as a superposition of hydrogen-like orbitals, in both spaces. The BCF system consists of a number of electrons within the attractive nuclear attraction, but not interacting among themselves via repulsive forces.

Neglecting the interelectronic repulsion will provoke more or less significant changes in going from the HF situation to the BCF one. The extent of these changes are quantified by means of the momentum space $GRD_p^{(q)}(HF, BCF)$, displayed in Figure 6.6 for different values of q . According to the previous description of these models, one should expect a more significant divergence among the HF and BCF densities as the number of electrons

N increases (with $N = Z$ for neutral atoms, that is, those here considered). This would be due to the much higher neglect of interelectronic repulsive forces occurring for high N .

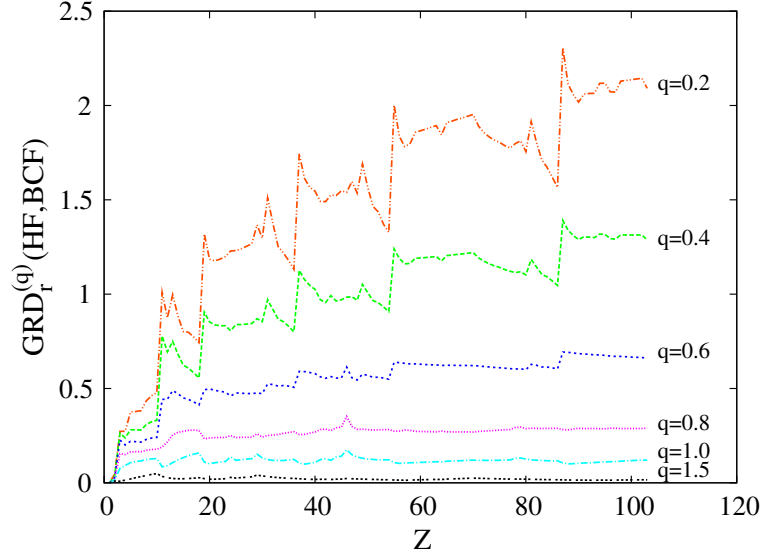


Figure 6.6: Geometric Rényi divergence $GRD_r^{(q)}(HF, BCF)$ between the Hartree-Fock (HF) and bare Coulomb field (BCF) charge densities of neutral atoms with $1 \leq Z \leq 103$.

Certainly an increasing trend is observed, for all curves of HF-BCF divergence in Figure 6.6. However, no one is strictly increasing, but local extrema appear with their number an enhancement depending on the order q considered. Location of maxima and minima are determined by the shell structure, as also observed in the two previous applications. Similar results are obtained when performing the same study in momentum space.

The main conclusion, regarding the present comparison among densities computed within the HF and BCF models, is that the effects of the interelectronic repulsion on the atomic one-particle densities depends not only on the total number of electrons, but also on shell-filling features of the systems considered.

6.2.4 Discrimination of nuclear charges

It is worthy to remember the capability of the geometric Rényi divergence to quantify the divergence of a number of functions higher than two. The interpretation as a 'mean distance' among two or more functions remains, independently of the number of densities considered. For the sake of simplicity, we have restricted all previous applications in this chapter to one-to-one comparisons.

Nevertheless, there exists additional applications of $GRD^{(q)}$ among a set of distributions. We find interesting to show one of them in the present work, but additional applications will be provided elsewhere.

Let us consider a number of atomic one-particle densities corresponding to systems sharing an specific property. Now we include in that set an additional distribution. A new question appears appropriate within this context: could we assert, attending to the $GRD^{(q)}$

values, if the system added to the initial set shares or not the specific feature(s) which characterize(s) the initial set?

We provide here an example for which $GRD^{(q)}$ appears able to discriminate if the system added belongs or not to the initial set according to the features which characterize the set.

Consider a pair of cations with identical nuclear charge Z , one of them singly-charged and the other doubly-charged. We denote them as Z^{+1} and Z^{+2} , where the superscripts correspond to the respective global charges. Let us notice that a pair of systems as chosen above share the property of having the same nuclear charge Z . Now we add to this two-element set a third system: a neutral atom (global charge zero) with nuclear charge Z' . To perform the study of the uniformly-weighted three-density divergence $GRD_r^{(q)}(Z^{+1}, Z^{+2}, Z')$, we choose $q = 2$ for illustration. For the doubly-charged ion, the near-Hartree-Fock wavefunctions of Ref. [227] for isoelectronic series with a number of electrons $N = 2 - 10$ are considered. They allow us to consider, for the present comparative purpose, values of the nuclear charges in the range $Z = 3 - 12$ for the systems conforming the initial set.

In Figure 6.7, each curve corresponds to the election of Z for the initial two cations. Consequently, ten curves are displayed ($Z = 3 - 12$), each one as a function of the nuclear charge of the neutral atom added to the previous set ($1 \leq Z' \leq 103$). The first observation from Figure 6.7 is the unimodal shape of all curves, decreasing quickly as Z' increases, until reaching a minimum value (which appears amplified in the framebox inserted), and increasing hereinafter. It is observed that the absolute minima occurs when $Z' = Z$ in each curve. The horizontal line establishes a threshold in the following sense: values of $GRD_r^{(2)}(Z^{+1}, Z^{+2}, Z')$ above the aforementioned threshold allows to assert that the neutral system added does not share the nuclear charge of the first two cations, that is $Z' \neq Z$. However, any value below the line corresponds, necessarily, to the comparison of three systems with the same nuclear charge, what means that $Z' = Z$.

Summarizing this application, it has been shown the usefulness of $GRD^{(q)}$ as a tool to discriminate atomic systems, in the sense of its ability to determine if a system added to a set of atoms characterized by some physical property(ies) belongs or not to that set. Or, in other words, if the new atom included shares or not the aforementioned property(ies), common to all initial systems.

Further applications will be provided elsewhere. They should include (i) the use of different values of q , (ii) employment of weights other than the uniform ones, and (iii) a study based on properties (e.g. long range behaviors) associated to the outermost regions, instead of the inner ones as done here.

Conclusions

A new measure of dissimilarity among probability distributions, the geometric Rényi divergence GRD, has been introduced in the present work. It is expressed in terms of the Rényi entropy, as also happens with the well-known Jensen-Rényi divergence JRD. Both them include a characteristic parameter in their definitions. The interpretation of JRD as a

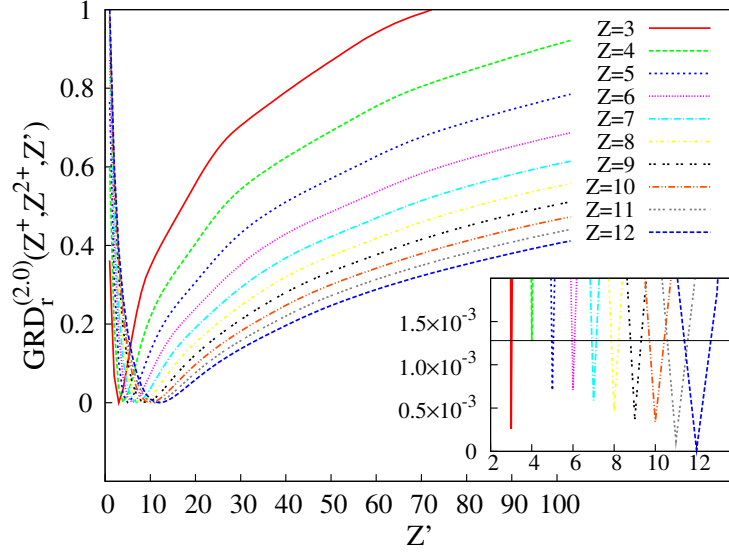


Figure 6.7: Geometric Rényi divergence in position space $GRD_r^{(2,0)}(Z^+, Z^{2+}, Z')$ among singly and doubly charged cations with nuclear charge $3 \leq Z \leq 12$, together with a neutral system of nuclear charge $1 \leq Z' \leq 103$. A threshold of GRD values appears amplified.

divergence measure constraints the parameter to values below unity, but such a constraint is not a requirement for GRD.

The GRD statistical measure of divergence is used to compare atomic one-particle densities. The capability of GRD to gain physical insight within the structural properties of many-electron systems has been shown. In doing so, we have taken advantage of its characteristic parameter in order to enhance or diminish the short- and long-range contributions in a divergence-based analysis. The geometric Rényi divergence allows to deal with a set of an arbitrary number of density functions, assigning different weights to each one in accordance, *e.g.* with their role within the comparative purpose considered. For atomic systems, a study based on one-particle densities in both position and momentum spaces provides clearly an interpretation in terms of shell structure.

From a detailed numerical analysis, it is clearly established the relationship between valence subshell properties of the systems under comparison and the GRD values, as well as the detection of the presence of systems suffering from anomalous shell-filling. The usefulness of the tool here defined has been shown in the study of ionized systems, by considering the analysis of atomic pairs neutral-cation. It appears a strong resemblance among the extrema of divergence and those of the atomic ionization potential, mostly determined by occupancy numbers of the outermost subshell in neutral and cationic systems. Further applications of the generalized index, arising from its rigorous mathematical properties here described, have been carried out in this work, including studies on (i) the ability in comparing different quantum models, and (ii) the detection of systems which not share specific physical properties with their partners within an atomic set.

Additional studies are planned to be performed in a near future: (i) use of more sophisticated atomic models including relativistic effects and/or correlations, (ii) comparing

more than two functions, *e.g.* sequences anion-neutral-cation, groups/periods of the Periodic Table, isoelectronic series, subsystems of a given composite system, (iii) assigning appropriate weights to each system according to relevant physical/chemical properties, such as mass, number of electrons, volume, and (iv) to consider other quantum systems (*e.g.* molecules) and processes (reaction, excitation). It is worthy to remark that the universality of GRD, in what concerns its definition and mathematical properties, allows its use in a wide variety of fields, systems and processes, far beyond atoms, molecules or reactions.

Generalized relative complexity

A thorough discussion on the meaning and properties of atomic and molecular complexities can be found in Refs. [54, 86, 53, 228] and Chapter 6 of Ref. [4] where relevant results were obtained. In the atomic case, it is clearly established the connection between the complexity values of the electron densities and physically relevant properties. It has been paid particular attention to the interpretation in terms of the organization of electrons into shells and subshells, for both neutral and ionized systems. Additionally, the complexity analysis of atomic ionization processes provides further connections with the value of the ionization potential, as well as with the quantum numbers of the electron(s) ejected or added. In all these studies, a more complete information is achieved when dealing simultaneously with the one-particle densities in both conjugate spaces, namely position and momentum.

Complementary with the just mentioned numerical studies, rigorous bounds on the complexity in terms of physical observables are also known [86]. Specially relevant are those expressed in terms of radial expectation values of both the position and momentum electron densities. Some of these observables are related to relevant physical quantities, such as e.g. the kinetic energy and its relativistic correction, the electron-nucleus attraction energy or the diamagnetic susceptibility, among others.

Very recently new statistical relative complexities have been defined [229, 230], and the pioneering LMC-like one has been applied to atomic densities [229]. This is an intrinsic measure that compares more efficiently the complexity of two electronic distributions, rather than merely the difference of their absolute complexities. Important properties have been also shown for this relative complexity, but the numerical tests are limited to some selected cases.

In this chapter we define a two-parameter generalized relative complexity, which contains the above mentioned relative complexity in Ref. [229] as a particular case and fulfils the most important properties for a measure of relative complexity. Furthermore this relative complexity is extended and applied to more than two densities, their relative weights can be modulated if desired, and also allows, by using appropriate values of its parameters, to enhance more or less different regions of the densities according to specific properties of the distributions. Some numerical difficulties of the original relative complexity are also marked.

The chapter is organized as follows. In Section 7.1 the generalized relative complexity is defined and its main properties are shown. In Section 7.2 numerical tests are carried out for atomic electron densities. Finally, conclusions and open questions are presented.

7.1 Relative complexity: a two-folded generalization

The recently introduced [229] LMC-like relative complexity of system A with respect to system B ,

$$C(A, B) = D(A, B) \cdot H(A, B) \quad (7.1)$$

is based on the definition of the pioneering LMC complexity for a unique system [50], namely

$$C(A) = D(A) \cdot H(A). \quad (7.2)$$

For the most general definition of a product-like complexity, the factor $H(A)$ is a measure of disorder or delocalization of the representative probability distribution $\rho_A(\vec{r})$ (of a random d -dimensional variable \vec{r}) of the system A , while the factor $D(A)$ constitutes a measure of its “disequilibrium”. In the case of the LMC complexity defined in Eq. (1.23), the delocalization factor is the Shannon length, Eq. (1.12),

$$H(A) \equiv N[\rho_A] = \exp\{S[\rho_A]\}, \quad (7.3)$$

and the disequilibrium $D(A) = D[\rho_A]$ is that given by Eq. (1.7). Normalized to unity distributions will be considered throughout this chapter.

The complexity $C(A)$ given by Eq. (7.2) constitutes a measure of pattern, structure and correlation in systems and processes. Its relative version $C(A, B)$ quantifies the complexity of system A with respect to that of an a priori or reference system B . An appropriate symmetrization of the composing factors will allow us to consider the relative complexity among A and B , avoiding the use of an a priori reference in order to deal with a “distance in complexity”, in some sense. To define $C(A, B)$ in this way, let us consider the two factors of the complexity itself $C(A)$, building up then the relative complexity $C(A, B)$ in terms of the relative functionals $D(A, B)$ and $H(A, B)$, in a similar way as done in Ref. [229]:

$$D(A, B) \equiv \frac{D[\sqrt{\rho_A \rho_B}]}{\sqrt{D[\rho_A]D[\rho_B]}} = \frac{\int \rho_A \rho_B d\vec{r}}{\sqrt{\int \rho_A^2 d\vec{r} \int \rho_B^2 d\vec{r}}} \quad (7.4)$$

is the relative disequilibrium of A with respect to B , and

$$H(A, B) \equiv \exp \left\{ \frac{1}{2} (KL[\rho_A, \rho_B] + KL[\rho_B, \rho_A]) \right\} \quad (7.5)$$

is the relative exponential entropy, given in terms of the symmetrized Kullback-Leibler entropy, Eq. (1.29). This definition of $D(A, B)$ in Eq. (7.4) provides a symmetric functional per se, being identical to the quantum similarity index $QSI[\rho_A, \rho_B]$ defined in Eq. (1.36). Its main properties allow to be considered as a measure of distance among probability distributions. Let us remark that the QSI values are restricted to the finite interval $[0, 1]$, with $QSI[\rho_A, \rho_B] = 1$ only for $\rho_A = \rho_B$.

A straightforward definition of the factor $H(A, B)$ from that of $H(A)$ is proposed in Ref. [229] by replacing the Shannon entropy in Eq. (7.3) by the relative entropy $KL[\rho_A, \rho_B]$. This is done, there, in such a way because the Shannon entropy $S[\rho_A]$ is,

except for a sign, the relative entropy of system A with respect to an uniform distribution for system B .

However, such a definition does not provide a symmetric factor, because $KL[\rho_A, \rho_B] \neq KL[\rho_B, \rho_A]$ in general. This fact justifies the symmetrization carried out in Eq. (7.5), in order to consider $H(A, B)$ as an unbiased measure of relative disorder between systems A and B , and then preserving in the relative complexity $C(A, B)$ the symmetry just achieved for $D(A, B)$.

The main purpose in this section is to provide a generalization of the relative complexity functional $C(A, B) = QSI[\rho_A, \rho_B] \cdot H(A, B)$, by taking advantage of monoparametric generalizations for each of the composing factors QSI and H . In our recent work [218], reviewed in Chapter 5, the definition of the quantum similarity index $QSI[\rho_A, \rho_B]$ given by Eq. (1.36) has been generalized by means of the q th order generalized quantum similarity index, Eq. 5.6:

$$D_q(\{\rho_i, \lambda_i\}_{i=1}^N) \equiv QSI^{(q)}[\{\rho_i, \lambda_i\}_{i=1}^N] = \frac{\int (\rho_1^{\lambda_1} \cdots \rho_N^{\lambda_N})^q d\vec{r}}{(\int \rho_1^q d\vec{r})^{\lambda_1} \cdots (\int \rho_N^q d\vec{r})^{\lambda_N}}, \quad (7.6)$$

with the sum of positive numbers $\sum_{i=1}^N \lambda_i = 1$.

For the case of two distributions ($N = 2$) with identical weights ($\lambda_1 = \lambda_2 = 1/2$), the generalized similarity index reads as Eq. (5.10)

$$D_q(A, B) = \frac{\int (\rho_A \rho_B)^{q/2} d\vec{r}}{\sqrt{\int \rho_A^q d\vec{r} \int \rho_B^q d\vec{r}}}, \quad (7.7)$$

which includes the similarity $QSI = D$ in Eq. (7.4) for the particular case $q = 2$. The generalized $QSI^{(q)} = D_q$ preserves, for arbitrary q , the relevant properties of QSI .

Let us now focus on the disorder/uncertainty factor $H(A, B)$, expressed in Eq. (7.5) in terms of Kullback-Leibler entropies KL . The KL functional is a limiting case of the “relative Rényi entropy” [231] of order t defined in Eq. (1.35) as

$$R_t[\rho_A, \rho_B] = \frac{1}{t-1} \ln \int \frac{\rho_A^t}{\rho_B^{t-1}} d\vec{r}, \quad (7.8)$$

so that $KL[\rho_A, \rho_B] = R_1[\rho_A, \rho_B]$. Then, the $H(A, B)$ symmetrized factor admits the generalization

$$H_t(A, B) \equiv \exp \left\{ \frac{1}{2} (R_t[\rho_A, \rho_B] + R_t[\rho_B, \rho_A]) \right\} \quad (7.9)$$

verifying $H_1(A, B) = H(A, B)$. A further generalized measure $H_t(\{\rho_i, \lambda_i\}_{i=1}^N)$ of weighted relative uncertainty can be defined from an appropriate combination of relative Rényi entropies.

Now we are ready to define a two-parametric relative complexity from the joint use of the two generalized factors described above:

$$C_{q,t}(A, B) \equiv D_q(A, B)H_t(A, B), \quad (7.10)$$

for any $q, t > 0$ whenever the involved integrals converge. Attending to the descriptions provided below, the quantity $C_{q,t}(A, B)$ constitutes a generalized measure of complexity among distributions. Some comments are in order:

- (i) The identity $C_{q,t}(A, A) = 1$ holds for any orders q, t . This means that the relative complexity among a given system and itself is 1.
- (ii) The particular case $C_{2,1}(A, B)$ corresponds to the LMC-like relative complexity, with QSI as the first factor and the exponential of the mean KL as the second one. Relevant properties verified by $C_{2,1}(A, B)$ (e.g. invariance under translation and rescaling transformations) are preserved in $C_{q,t}(A, B)$.
- (iii) The generalization can be straightforwardly extended by considering a number of functions higher than two, as well as by including arbitrary weights for each of them.

The just introduced definition can be applied to the study of complexity for arbitrary probability distributions. Let us keep in mind that the methodology employed throughout this section is universal, having its grounds in the use of well-known mathematical techniques and information-theoretical functionals.

Next section is devoted to the analysis of the generalized relative complexity among the probability distributions arising from the electron charge density of neutral atoms, through the whole Periodic Table. This kind of study has been already carried out by using both the complexity itself [53, 232, 82, 186, 228], and more recently by means of the relative complexity [229]. In those cases, as also in next section, computations are carried out within a Hartree-Fock framework [219, 220]. Atomic units (a.u.) are used throughout.

7.2 Numerical analysis with atomic electron charge densities

Accordingly with the interpretation of the complexity and the relative complexity as measures of structure, we wonder about the possible connection among their values for atomic systems and their main physical properties. Let us mention that recent studies were carried out, by using the LMC complexity and a variety of other complexities as well [53, 232, 82, 186, 228, 90, 85, 91, 86] (e.g. Fisher-Shannon, Cramér-Rao or Rényi-like ones). A clear evidence of the aforementioned connection is provided, mainly in terms of the atomic shell-filling patterns, for both neutral and ionized atomic species.

More recently, a similar interpretation has been provided for the LMC-like relative complexity measure $C(A, B)$ proposed in Ref. [229]. The numerical study was performed there as follows: first the system A is chosen as the initial element when filling a given subshell (of 'p', 'd' or 'f' type), and then system B runs over the subshell, starting with $B = A$, until the subshell is completely filled, that is, when B becomes a closed-subshell system.

We give here a summary of the main conclusions derived from that work: (i) for each subshell, characterized by the reference system A , the initial value is $C(A, B = A) = 1$,

(ii) the relative complexity $C(A, B)$ increases monotonically as far as B runs over the subshell, and (iii) the rate of such an increase becomes progressively smaller for subshells with heavier atoms, as compared to that of lighter ones.

Consequently, the only evidence of periodicity, as displayed in the figures enclosed in Ref. [229], arises from the choice ad hoc of the reference systems, namely, just those enclosing a new subshell as compared to the previous element, throughout the whole Periodic Table for neutral atoms with nuclear charges $Z = 1 - 103$.

We have extended the previous study, at a first step, by choosing one of the aforementioned reference systems, namely Boron (system A with $Z_A = 5$, the initial one as filling the $2p$ subshell), but considering B running all over the Periodic Table ($Z_B = 1 - 103$), instead of constraining A and B to the same subshell. The results obtained in this way for $C_{q,t}(A, B)$ are displayed in Figs. 7.1a and 7.1b, as curves in red for the values $(q, t) = (2, 1)$.

Some comments are in order: (i) the results are roughly the same independently of using for $C(A, B)$ the unsymmetrized definition of Ref. [229] or the symmetrized one $C_{2,1}(A, B)$ as in the present work, (ii) the aforementioned monotonic behavior is clearly observed when both A and B have the same valence subshell ($Z_B = 5 - 10$), and (iii) for most systems with different valence subshell, the relative complexity falls below unity.

Last comment is extremely important, in order to consider $C(A, B)$ as an appropriate measure of relative complexity. For a pair of systems A and B with relative complexity lower than 1, and keeping in mind that $C(A, A) = 1$, we get the inequality $C(A, B) < C(A, A)$ for many elements B . This inequality holds not only for the illustrative example $Z_A = 5$, but for any other Z_A also.

Considering complexity, in this context, as a measure of structure and organization of the underlying distribution, the inequality $C(A, B) < C(A, A)$ introduces a strong difficulty from a conceptual point of view, as clarified by the following comment: 'the relative complexity of A with respect to B is lower than that of A with respect to itself'. This reading of the above inequality forbids to consider $C(A, B)$ as a measure of structure in B as compared to that of A . In this sense, one should expect to obtain, for fixed A , the minimizer of the relative complexity $C(A, B)$ for $B = A$ or, in other words, the inequality $C(A, A) \leq C(A, B)$, with the equality being reached if and only if $A = B$.

This interpretation is used, in fact, within the comments on the results obtained in Ref. [229] for systems belonging to the same subshell, then interpreting $C(A, B)$, in some sense, as a measure of 'distance in complexity' of A from B . The results displayed in Fig. 7.1 provide us with the evidence that such an interpretation fails, in general, when dealing with systems from different subshells.

We consider now the generalization $C_{q,t}(A, B)$ of the relative complexity. All previous discussions on the behavior of the red lines for $C(A, B)$ regard, in fact, the particular case $q = 2$ and $t = 1$. The difficulties arising from this choice of (q, t) have been corroborated, unless restricting the analysis to systems with identical valence subshell. We wonder now about the existence of (q, t) values, different from $(2, 1)$, allowing us to avoid the previous difficulties. The answer regarding their existence is affirmative, as shown by the blue and gray lines in Figs. 7.1a and 7.1b. The generalized relative complexity $C_{1,1}(A, B)$ is considered in Fig. 7.1a, enclosing the similarity factor QSI_1 instead of the QSI one. It

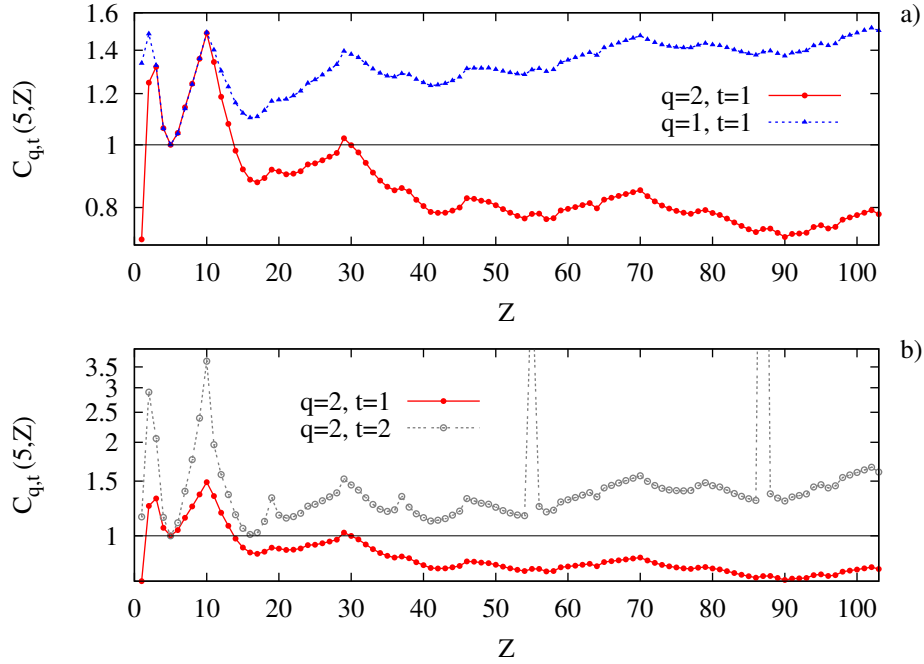


Figure 7.1: Comparison among the electron charge density of Boron (nuclear charge $Z' = 5$) and those of all neutral atoms with $Z = 1 - 103$, by means of the generalized relative complexities $C_{q,t}(Z, Z')$ with $(q, t) = (2, 1)$ and (in red) and (a) $(q, t) = (1, 1)$ (in blue) and (b) $(q, t) = (1, 2)$ (in gray).

is observed that the measure $C_{1,1}(A, B)$ never crosses the unity frontier for the illustrative example here considered, as also occurs for the rest of systems in the Periodic Table. The same conclusion arises from the analysis of $C_{2,2}(A, B)$ in Fig. 7.1b, where the exponential of the symmetrized relative Rényi entropy of order $t = 2$ replaces the limiting factor KL corresponding to $t = 1$.

Consequently, it is numerically observed that the generalized comparative functionals $C_{1,1}(A, B)$ and $C_{2,2}(A, B)$ comply with the desirable properties for a measure of relative complexity, contrary to the pioneering $C(A, B) \sim C_{2,1}(A, B)$ one. In addition, the display of numerous local extrema in all curves is related to the atomic shell structure of the systems under comparison, as will be discussed later.

And, what about other arbitrary (q, t) values? For several pair of systems, with nuclear charges Z_A and Z_B , a plane subtended by q and t has been drawn, according to the condition $C_{q,t}(A, B) \geq 1$. The condition divides the plane into two regions, the 'allowed' and 'forbidden' ones. An illustrative example is provided in Fig. 7.2 for systems $Z = 5, 17$. The upper area, in colour, is the allowed region when dealing with the (q, t) -generalized relative complexity. Let us notice the star in the white forbidden area, located at $(q = 2, t = 1)$, i.e. just the values corresponding to the particular case $C(A, B)$ as defined in Ref. [229].

Other planes for different pairs of atomic systems have been also analyzed. The main

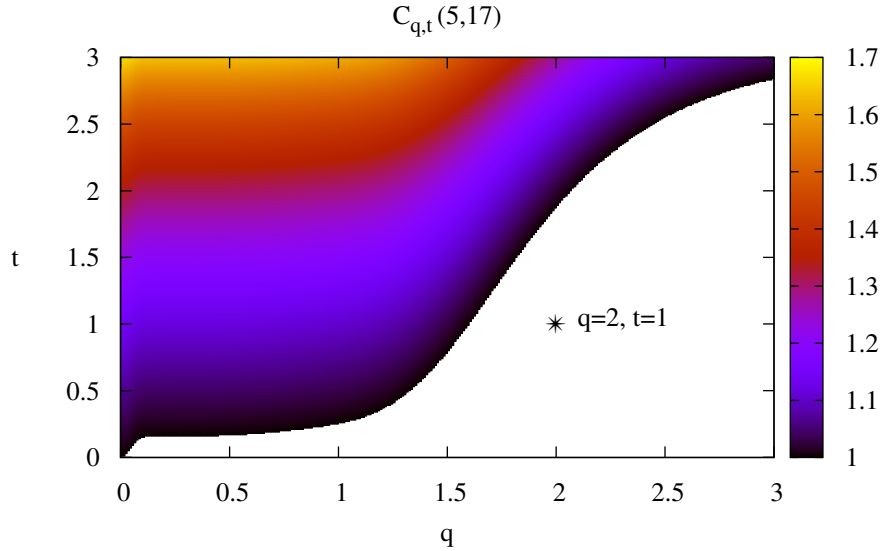


Figure 7.2: Region (coloured) in the (q, t) plane where the generalized relative complexity between Boron ($Z = 5$) and Chlorine ($Z = 17$) verifies $C_{q,t}(5, 17) \geq 1$.

comments regarding all those planes are: (i) the shape of the frontier between the aforementioned regions strongly depends on the choice of systems, most usually because of their shell structure, and (ii) in spite of the different shapes, a common feature is the existence of thresholds, which translate into the condition $t > t_{min}(q)$ for a given q .

It still remains the problem of determining a rigorous (and desirable) analytical condition on the parameters (q, t) in order to guarantee that the value of the relative complexity between two arbitrary distributions is not below 1. Nevertheless, some achievements are noteworthy:

- for the particular case $q = 1$, the inequality $C_{1,t}(f, g) \geq 1$ holds with arbitrary probability distributions f, g for any $t \geq 1/2$ (as far as the integrals involved converge); in particular, we have proven the existence of a value $0 < t_{min} \leq 1/2$ so that the condition reads as $t \geq t_{min}$,
- for ground-state d -dimensional hydrogenic atoms (one-electron systems), with respective nuclear charges Z_A and Z_B , the above inequality is fulfilled for arbitrary $q > 0$ and $1/4 \leq t \leq \max\{Z_A, Z_B\}/|Z_A - Z_B|$. Let us remark that this condition (i) depends upon the nuclear charges through their quotient Z_A/Z_B , and (ii) does not depend on the dimensionality d .

Continuing with the numerical analysis of the atomic relative complexity, we compare now two curves of $C_{1,1}(Z', Z)$ throughout the Periodic Table ($Z = 1 - 103$), for Z' corresponding to extremely similar (Fig.7.3a) or different (Fig. 7.3b) systems from

physical and chemical points of view. As an illustrative example, two noble gases are chosen in Fig. 7.3a: Helium ($Z' = 2$) and Neon ($Z' = 10$). In spite of the differences based on their absolute values, the curves $C_{1,1}(2, Z)$ and $C_{1,1}(10, Z)$ display a very similar structure, accordingly with the fact that both Helium and Neon belong to the same group of the Periodic Table. In this sense, it is worthy to mention that they share most local minima, at $Z = 2, 10, 18, 24, 29, 36, 42, 46, 54$, as well as the close ones $Z = 78 - 79$ for Helium and Neon respectively. Let us notice that the list encloses (i) the noble gases $Z = 2, 10, 18, 36, 54$, and (ii) systems suffering from the anomalous shell-filling: $Z = 24, 29, 42, 46, 78 - 79$. So, the value of the relative complexity provides information on relevant features regarding the shell-structure of the systems compared.

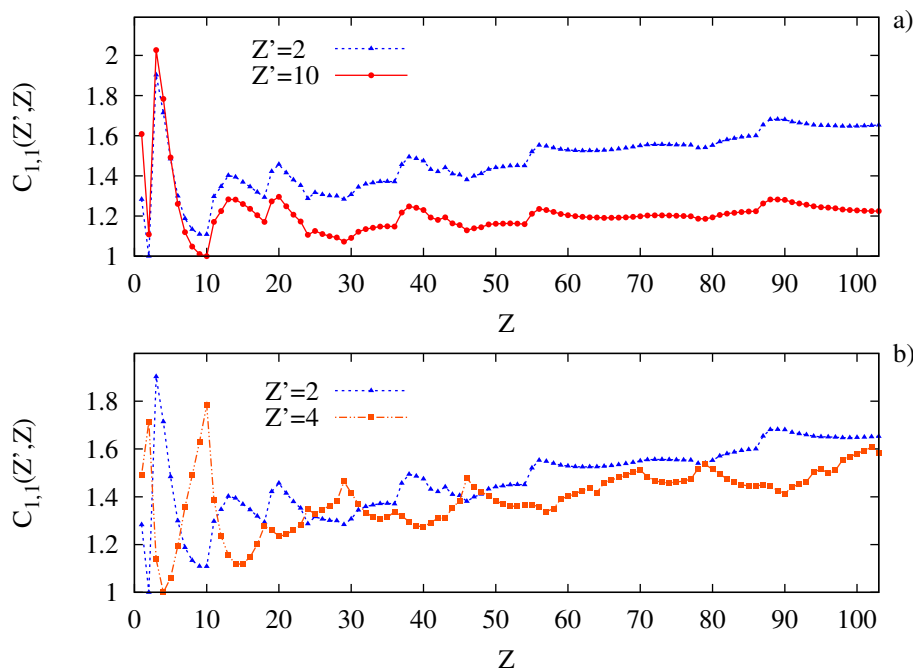


Figure 7.3: Generalized relative complexity $C_{1,1}(Z, Z')$, for $Z = 1 - 103$, and (a) two noble gases (Helium and Neon, $Z' = 2, 10$), and (b) a noble gas (Helium, $Z' = 2$) and an alkaline-earth (Beryllium, $Z' = 4$).

We find just the opposite behavior when dealing with two systems as different as Helium (noble gas, $Z' = 2$) and Beryllium (alkaline-earth, $Z' = 4$), shown in Fig. 7.3b. While different minima of Helium's curve occurs for the comparison with other noble gases, the same comment applies for alkaline-earths with respect to Beryllium. In fact, most minima for one system corresponds to maxima of the other, and conversely. For instance, systems $Z = 2, 10, 18, 24, 29, 36, 42, 46$ are minima of Helium and maxima of Beryllium. Additionally, the same occurs for the close ones $Z = 54 - 55, 62 - 63, 78 - 79$. As discussed previously, most of them are either noble gases or systems with anomalous shell-filling. But now, they are displayed as minima or maxima depending on the performance of a comparison with a noble gas or an alkaline-earth.

Similar comments to those here provide apply also for the numerical study by choosing

other elements belonging to different groups of the Periodic Table. The shell-filling patterns are clearly displayed, as provided by the location of local maxima or minima for the curves considered.

To conclude the numerical study, we provide here an application of the relative complexity among a set of systems. In doing so, we consider the filling process of the different atomic subshells. In Ref. [229], this kind of analysis is carried out in terms of the 'one-to-one' relative complexity, by fixing a reference system as the initial one of a given subshell, the second one running over such a subshell. Here, instead, we consider the relative complexity among all systems belonging to the same subshell. For illustration, uniform weights are chosen for both factors of the relative complexity, namely $QSI^{(q)}$ and the exponential of relative Rényi entropies between each density within the set and their arithmetic mean (the mean obtained by employing uniform weights also). Nevertheless, different criteria could be considered in order to establish the weights, such as e.g. relative number of electrons, masses or sizes.

The results obtained are shown in Table 7.1. It is observed a rough decreasing trend of the values, as far as heavier systems are considered. This comment is in accordance with those regarding the aforementioned analysis in Ref. [229], where the relative complexity with respect to the initial system increases through the subshell, but at a progressively slower rate. This means that differences in terms of relative complexity become smaller for heavy systems as compared to the lighter ones, as induced from the results on that work and the present one.

Subshell n,l	$C_{2,1}(nl)$
2p	1.448005
3p	1.192296
3d	1.152400
4p	1.046343
4d	1.102025
5p	1.024107
4f	1.065817
5d	1.028909
6p	1.010805
5f	1.045200

Table 7.1: Generalized relative complexity $C_{2,1}(nl)$ among the electron densities of all neutral atoms filling the subshell characterized by the quantum numbers (n, l) .

Deviations from the decreasing trend occur for subshell 3d, 4f and 5f. These subshells contain a relevant number of elements with anomalous shell-filling. Their high values of relative complexity are interpreted according to a mix of elements with relevant differences regarding their shell-structure. This fact is clearly revealed in the values of Table 1. Let us point out that these comments, regarding relative complexities of whole subshells, also hold for other values of the parameters q and/or t .

Conclusions

In order to define an appropriate measure of relative complexity among two or more distributions, it is essential to take into account the desirable properties which should be verified. This is so because of the aim of dealing with a physically meaningful measure. Such is not the case of the pionnering definition, which leads to a contradictory interpretation from a conceptual point of view.

Those difficulties can be avoided by dealing with the generalized relative complexity defined in the present work. Furthermore, this generalization allows to introduce the concept of relative complexity among an arbitrary number of functions, with the option of considering different weights for each of them.

The numerical analysis for the comparison of two neutral atoms, located anywhere at the Periodic Table, has allowed us to provide a clear interpretation in terms of a so relevant feature of atomic systems as their shell structure is. This kind of interpretation is even more efficient when expressed in terms of the different groups which the systems belong to. In this sense, it is worthy to remark that these groups are characterized by the main physical and chemical atomic properties.

There are several open problems regarding both the definition and applications here considered. Let us remark the following: (i) the determination of rigorous conditions on the characteristics parameters in order to guarantee values of the relative complexity not below unity, and (ii) the application to more sophisticated systems (e.g. molecules), physical processes (ionization, excitation), distributions (e.g. momentum space) or models (relativistic effects, configuration interactions).

Part II

Quantum entanglement in harmonic many-body systems

Table of Contents

Introduction	111
8 Quantum entanglement: Basics	113
8.1 Quantum correlations: The qubit	113
8.1.1 Correlations in two qubit systems	114
8.1.2 Mixed states and quantum correlations	115
8.2 Entangled and separable states	116
8.3 Schmidt decomposition	117
8.4 Entanglement quantification of pure states	118
8.4.1 Entanglement for identical fermions	119
9 The Moshinsky model with three electrons, and with two electrons in an uniform magnetic field	121
9.1 Entanglement measure	121
9.2 The three-electron Moshinsky atom	123
9.2.1 Ground state	126
9.2.2 First excited states	126
9.2.3 Second excited states	127
9.3 Two-electron Moshinsky atom in a magnetic field	129
9.3.1 Ground state	133
9.3.2 First excited states	134
9.3.3 Confining effect of the magnetic field	137
9.4 Perturbative Approach	140
9.4.1 Moshinsky model with three electrons	142
9.4.2 Moshinsky model with two electrons in an uniform magnetic field	145
Conclusions	146

10 Entanglement and Born-Oppenheimer approximation in an exactly solvable quantum many-body system	149
10.1 Preliminaries	150
10.1.1 Moshinsky-like many-particle model	150
10.1.2 Quantum entanglement	151
10.1.3 Born-Oppenheimer approximation	151
10.2 Exact solution of the many particle system	152
10.3 Entanglement of the three-particle model	156
10.3.1 Nucleus-electrons entanglement	157
10.3.2 Electron entanglement	159
10.4 Entanglement of the many-particle model	160
10.4.1 Nuclei-electrons entanglement	161
10.4.2 Single-particle entanglement: Nucleus and electron entanglement	163
10.5 Born-Oppenheimer approximation in the many-particle Moshinsky model	166
10.5.1 Helium-like atoms	168
10.5.2 N-particles system	169
Conclusions	170

Introduction

Coined by Einstein as “spukhafte Fernwirkung” (“spooky action at a distance”), entanglement describes an inherently nonlocal correlation between detached quantum systems that is predicted by quantum theory, and which cannot be adequately described or explained in the language of classical physics, at least without making assumptions about hidden variables [21]. Entanglement is an essential ingredient of the quantum mechanical description of Nature [233, 5, 234]. Besides its central role for the basic understanding of the quantum world, entanglement constitutes a physical resource admitting numerous technological applications. The study of entanglement sheds new light on the mechanisms behind the quantum-to-classical transition [235] as well as on the foundations of statistical mechanics [236]. On the other hand, the controlled manipulation of entangled states of multipartite systems is fundamental for the implementation of quantum information processes, such as quantum computation [8, 237].

Quantum entanglement is also relevant in connection with the physical characterization of atoms and molecules. The exploration of the entanglement features exhibited by atoms and molecules is a captivating field of enquiry because these composite quantum objects play a central role in our understanding of both Nature and technology. In point of fact, the entanglement properties of atomic systems have been the subject of considerable research activity in recent years [5, 238, 239, 240, 241, 242, 243, 244, 245, 246, 247, 248, 249]. This line of research is contained within the more general one aimed at the application of information-theoretic concepts and methods to the study of atomic and molecular systems [250, 251, 31, 252, 253, 76, 254, 228, 255, 256, 257, 258, 259].

Some of the most detailed results on the entanglement properties of atomic systems, particularly in the case of excited states, have been obtained from analytical investigations of soluble two-electron models [238, 245]. Partial results were also obtained numerically for the eigenstates of helium-like systems [245], employing high quality wave functions [248] or configuration-interaction variational methods [249]. Some general trends are beginning to emerge from these investigations. It is observed that the entanglement increases with the strength of the interaction among the constituent particles. The amount of entanglement of the atomic eigenstates also tends to increase with the concomitant energy. For example, in the case of Helium it was observed that the entanglement increases with the energy of the singlet-states, but not in the case of triplet-states [248] which is still an open question. On the other hand, the entanglement of excited states shows an apparent discontinuous behavior: it does not necessarily vanish in the limit of very small interactions [238]. This has been shown to be closely related to the degeneracy of the energy levels of the associated independent particle model obtained in the limit of vanishing interaction [260].

An analytically solvable model that can be carried to virtually any number of particles is the Moshinsky atom [261, 262] (sometimes referred to as “harmonium” [263]), for which all appearing potentials are set to be harmonic. This model admits exact analytical solution and constitutes a valuable “testing bench” for the study of diverse aspects of atomic

and molecular physics. Indeed, it has been used for assessing the quality of the Hartree-Fock approximation [261], for investigating low-order density matrix descriptions of the ground state of atomic systems [264] and for exploring the entanglement-related features [241, 244, 263, 238, 265] and other manifestations of quantum correlations [259] in atomic systems. The application of harmonium as a tractable model for elucidating some aspects of the behavior of more realistic systems has a long history, that goes back almost to the very beginning of quantum mechanics [266]. This model has also been found useful for the study of other subjects beyond atomic physics, such as the thermodynamics of black holes [267].

It would be desirable to extend the above studies to more general scenarios, particularly to models consisting of more than two electrons, or involving magnetic fields. The aim of the Chapter 9 is to investigate the entanglement properties of the eigenstates of the exactly soluble Moshinsky model [261], extending previous works to the cases of a three-electron system and a three-dimensional two-electron system in an uniform external magnetic field.

Quantum entanglement renders efficient simulations of many-particle systems impossible and entails the breakdown of efficient numerical treatments. With the help of analytically solvable models, one can use entanglement to assess the validity and scope of approximation techniques. In Chapter 10, we show that the entanglement, present in many-particle systems, can be understood to wide range from purely kinematic considerations, which permit to assess the validity of the Born-Oppenheimer approximation. For this purpose, we choose the many-electron many-nuclei Moshinsky atom (or molecule) in an external harmonic potential. We also investigate the entanglement properties of the eigenstates of this many-particle Moshinsky-like model, for different bipartitions of the system, through the parameters that characterize it, namely the strengths interaction between particles the number of particles and their corresponding masses.

First of all, let us review in Chapter 8 the basic concepts of quantum correlation emphasizing aspects concerning to entanglement and the measures we use for its quantification.

Quantum entanglement: Basics

In this chapter, we review some elementary concepts from the theory of quantum entanglement and quantum information. This is by no means a comprehensive overview, but rather a selection of those aspects that will be of particular importance in this thesis. For a comprehensive and recent review of quantum entanglement, it is suggested to consult the monographs [8, 10].

Quantum systems exhibit properties that are unknown in the classical theories. Superposition of states, interference or tunneling are some of such one-particle quantum effects, but there are also further differences that manifest themselves in composite systems, *i.e.* in the correlations among the different subsystems which compose the whole system. Whereas the classical correlations can always be described in terms of classical probabilities, for quantum systems is not true.

Entanglement is the quintessential quantum phenomenon according to which quantum states of bipartite systems are correlated in such a way that the states of one of the subsystems can not be completely determined (in the sense of being describable by a pure state) even if the state of the total system is. Such a non-classical correlations gave rise to the celebrated EPR (Einstein, Podolsky and Rosen) paradoxes [21] which is the argument for incompleteness of the quantum mechanics. For them, entanglement was a *spooky action at distance* and a Local Hidden Variables Model (LHVM) is needed. In defense of quantum mechanics, Schrödinger emphasized the key role of the entanglement in this theory [20, 268] which coined the term for such correlations. Thirty years later, in 1965, John S. Bell showed that no LHVM can reproduce the non local nature of entangled states [269]. He also proposed a test that was experimentally verified by Alain Aspect *et al* [270]. This is, therefore, one of the pillars supporting quantum theory as a non-classical theory.

The recipe of this chapter is the following. In Section 8.1, we use systems of one and two qubits, which are the simplest systems that display this essential feature of quantum mechanical systems, for easy understanding of the quantum correlation of pure and mixed states. The concept of separable and entangled quantum states are drawn in Section 8.2, and its essential decomposition Schmidt theorem in Section 8.3. Finally, in Section 8.4 we present the measure of entanglement we use as well as their main features and implications for pure states and many identical fermions.

8.1 Quantum correlations: The qubit

In classical information theory the *bit* represents the natural elementary unit for storing information, corresponding to a classical variable that takes two possible values: 0 or 1. Quantum systems can also be used to codify information, usually in systems with two

possible and well defined states *i.e.* the *qubit*. The qualitative difference among classically and quantum-mechanically correlated states can be appreciated upon these system with two spatially well-separated constituents (*i.e.* a bipartite system), which carry a two-dimensional (qubit) internal degree of freedom each, such as spin or polarization.

The main difference between bit and qubit is that while a bit has only two possible values $\{0, 1\}$, a qubit can be in a state different to $|0\rangle$ or $|1\rangle$. It can be in a more general state $|\Psi\rangle$ which is a linear combination of the two previous states:

$$|\Psi\rangle = \alpha |0\rangle + \beta |1\rangle \quad (8.1)$$

where α and β are complex numbers. The state $|\Psi\rangle$ is said to be in a *superposition* of the two states that together form a single-particle basis. When we measure the state of the qubit, it will be in the state $|0\rangle$ with probability $|\alpha|^2$, or the state $|1\rangle$ with probability $|\beta|^2$ whenever the normalization condition $|\alpha|^2 + |\beta|^2 = 1$ is fulfilled.

8.1.1 Correlations in two qubit systems

The simplest example of a composite quantum system is given by a coupling of two qubits A and B . The Hilbert space of such a system is then $\mathcal{H}_{A,B} = \mathcal{H}_A \otimes \mathcal{H}_B$, where \mathcal{H}_A and \mathcal{H}_B denote the Hilbert space describing each qubit. Considering that the systems A and B are qubits, *i.e.* the pairs of states $\{|0\rangle_A, |1\rangle_A\}$ and $\{|0\rangle_B, |1\rangle_B\}$ are two orthogonal bases, the general state of the two qubit system is given by a coherent superposition of all tensorial products $|\Phi\rangle_A \otimes |\Phi\rangle_B = |A, B\rangle$ that is

$$|\Psi\rangle = a |0, 0\rangle + b |1, 1\rangle + c |0, 1\rangle + d |1, 0\rangle \quad (8.2)$$

where now $|a|^2 + |b|^2 + |c|^2 + |d|^2 = 1$.

If we perform a projective measurement of a non-degenerate observable associated with one of the qubits *e.g.* A , the outcome will give us full information about the state of the other qubit if it is satisfied that

$$c = d = 0 \quad \rightarrow \quad |\Psi_1\rangle = a |0, 0\rangle + b |1, 1\rangle \quad (8.3)$$

or

$$a = b = 0 \quad \rightarrow \quad |\Psi_2\rangle = c |0, 1\rangle + d |1, 0\rangle, \quad (8.4)$$

otherwise the qubit B is in a superposition state. In such a states, $|\Psi_1\rangle$ and $|\Psi_2\rangle$, no prediction is possible for single outcomes since results of a projective measurement are determined with probabilities

$$\begin{aligned} P_{|\Psi_1\rangle}(0) &= \langle \Psi_1 | (|0\rangle \langle 0|_A \otimes \mathbb{I}_B) | \Psi_1 \rangle = |a|^2 \\ P_{|\Psi_1\rangle}(1) &= \langle \Psi_1 | (|1\rangle \langle 1|_A \otimes \mathbb{I}_B) | \Psi_1 \rangle = |b|^2 \\ P_{|\Psi_2\rangle}(0) &= \langle \Psi_2 | (|0\rangle \langle 0|_A \otimes \mathbb{I}_B) | \Psi_2 \rangle = |c|^2 \\ P_{|\Psi_2\rangle}(1) &= \langle \Psi_2 | (|1\rangle \langle 1|_A \otimes \mathbb{I}_B) | \Psi_2 \rangle = |d|^2 \end{aligned} \quad (8.5)$$

However, the *combined* measurement results on the two subsystems are perfectly correlated: once a measurement is obtained on the first subsystem, *e.g.* $|0\rangle_A$, the two-body state, *e.g.* $|\Psi_1\rangle$, is projected onto the state $|0, 0\rangle$; consequently, one can predict the measurement result of the other subsystem, which is 0.

For a system of two qubits a set of maximally entangled states, characterized by maximally mixed subsystems, are given by the so-called Bell states:

$$|\Psi_1^\pm\rangle = \frac{|0, 0\rangle \pm |1, 1\rangle}{\sqrt{2}} \quad ; \quad |\Psi_2^\pm\rangle = \frac{|0, 1\rangle \pm |1, 0\rangle}{\sqrt{2}} \quad (8.6)$$

which forms a orthonormal base in the Hilbert space of two qubits. The states $|\Psi_{1,2}^+\rangle$ describe a correlated pair, whereas $|\Psi_{1,2}^-\rangle$ are anti-correlated.

8.1.2 Mixed states and quantum correlations

A pure quantum state is a state which can be described by a single ket vector $|\Psi\rangle$ and its associated density matrix is fully defined as $\rho = |\Psi\rangle\langle\Psi|$. Contrary, a mixed quantum state is a statistical ensemble of pure states,

$$\rho = \sum_s p_s |\Psi_s\rangle\langle\Psi_s|, \quad (8.7)$$

where p_s is the fraction of the ensemble in each pure state $|\Psi_s\rangle$ fulfilling $\sum_s p_s = 1$ with $p_s \geq 0$, and cannot be described with single ket vector, *i.e.* $\rho \neq |\Psi\rangle\langle\Psi|$.

Many classical stochastic processes are thinkable for which individual outcomes are fully unpredictable, whereas the correlations are definite. Consider, for example, a random mechanism that distributes two particles prepared in the states $|0\rangle$ and $|1\rangle$, respectively, to two observers, or parties. Each observer is given one of the particles, and the parties do not know which particle (the one prepared in $|0\rangle$ or the one prepared in $|1\rangle$) they are given. In each run of the experiment, the choice of which particle is given to which observer is completely random, *i.e.* the probability to find the state $|1, 0\rangle$ or $|0, 1\rangle$ is $1/2$. This mechanism thus creates a mixed state,

$$\rho = \frac{1}{2} (|0, 1\rangle\langle 0, 1| + |1, 0\rangle\langle 1, 0|) \quad (8.8)$$

Following the prescription we have applied on the entangled state $|\Psi_2^+\rangle$ in Eq. (8.6), exactly the same correlations of measurement results emerge. Such correlations do not require quantum mechanics at all to occur. However a mixed state such as Eq. (8.8) can only explain correlations that are observed in one specific single-particle basis, whereas the entangled state $|\Psi_2^+\rangle$ exhibits correlations for all common choices of orthogonal local basis settings. Since the exhibited correlations cannot be explained by a random mechanism, they are attributed “non-classical” character, and named quantum correlations. They are a consequence of the entanglement carried by the system.

8.2 Entangled and separable states

We shall focus on bipartite systems, *i.e.* systems composed by two distinct subsystems. Let us consider a pure bipartite quantum state $|\Psi\rangle \in \mathcal{H}_1 \otimes \mathcal{H}_2$; it is called *separable* if and only if it can be written as a tensor product of pure states of the parts, *i.e.* if one can find the subsystem states $|\Phi\rangle_i \in \mathcal{H}_i$ such that

$$|\Psi\rangle_{sep} = |\Phi\rangle_1 \otimes |\Phi\rangle_2 \quad (8.9)$$

It is completely determined in terms of the single-subsystem states $|\Phi\rangle_1$ and $|\Phi\rangle_2$. The outcomes of measurements on a pure separable state are therefore not correlated at all: They are fully defined by the pure states of the subsystems; measurements or any other operation performed on the other subsystem do not change the probabilities of possible outcomes. Indeed, the reduced density matrices

$$\rho_1 = \text{Tr}_2[\rho] \quad \text{and} \quad \rho_2 = \text{Tr}_1[\rho], \quad (8.10)$$

where $\rho = |\Psi\rangle\langle\Psi|$ is the density matrix of the whole, describe pure states. The above reduced density matrices are given by the partial trace over the first or second subsystem, *i.e.*

$$\text{Tr}_1[\rho] = \sum_j^{n_2} \langle\phi_j|_2 \rho |\phi_j\rangle_2 \quad \text{and} \quad \text{Tr}_2[\rho] = \sum_j^{n_1} \langle\phi_j|_1 \rho |\phi_j\rangle_1 \quad (8.11)$$

where n_i denotes the dimension of the Hilbert space of $|\Phi\rangle_i$. More specifically,

$$\rho_1 = |\Phi\rangle_1 \langle\Phi|_1 \quad \text{and} \quad \rho_2 = |\Phi\rangle_2 \langle\Phi|_2 \quad (8.12)$$

such that the density matrix can be written as a tensor product of the reduced ones, $\rho = \rho_1 \otimes \rho_2$, *i.e.* all information about possible measurement outcomes is contained in the reduced density matrices.

Contrary, entangled states cannot be written as direct products, Eq. (8.9), of two single-particle states. The information carried by an entangled state is not completely specified in terms of the states of the subsystems: For the reduced density matrices, we have that $\text{Tr}[(\rho_i)^2] \neq 1$, *i.e.* the states of the subsystems are mixed. Furthermore, for an entangled state $|\Psi\rangle$, one finds $\rho = |\Psi\rangle\langle\Psi| \neq \rho_1 \otimes \rho_2$, *i.e.* the two-particle state contains more information on measurement outcomes than that contained in the two single-particle states ρ_1 and ρ_2 together, in contrast to the above separable state in Eq. (8.9). Moreover, distinct entangled states can give rise to the same reduced density matrices: The states in Eq. (8.3) and in Eq. (8.4) lead to the same reduced density matrices if $a = d$ and $b = c$, which are maximally mixed for the particular case of Bell states, Eq. (8.6), from which it follows that

$$\rho_1 = \text{Tr}_2 [|\Psi_i^\pm\rangle\langle\Psi_i^\pm|] = \frac{1}{2} (|0\rangle\langle 0| + |1\rangle\langle 1|). \quad (8.13)$$

Formally, the separability (and, correspondingly entanglement) underlies on the question of whether the coefficient matrix $\alpha_{i,j}$ in the state representation

$$|\Psi\rangle = \sum_{i,j} \alpha_{i,j} |i,j\rangle \quad (8.14)$$

admits a product representation, *i.e.* $\alpha_{i,j} = \alpha_i^{(1)} \cdot \alpha_j^{(2)}$, in which case the state $|\Psi\rangle$ would be separable.

Mixed states

For mixed two-body states the notion of separability and entanglement can also be defined but, in this case, the mixedness of the reduced density matrices is not equivalent to entanglement. Separable states can be written as mixtures of product states,

$$\rho_{sep} = \sum_s \rho_1^{(s)} \otimes \rho_2^{(s)} \quad (8.15)$$

being $\rho_1^{(i)}$ and $\rho_2^{(i)}$ the sets of single-particle states of the first and of the second subsystem, respectively, and associated probabilities p_s . Such separable states imply correlations between measurement results on the different subsystems, but these correlations can be explained in terms of the probabilities p_s , and, therefore, do not qualify as quantum correlations, *e.g.* the state (8.8) is separable. Entangled states, in contrast, are those for which there is no representation as in Eq. (8.15). They thus need to be described as in Eq. (8.7) where at least one state $|\Psi_s\rangle$ is entangled.

8.3 Schmidt decomposition

By the application of suitable reversible local transformations, *i.e.* unitary operations, one can prove the Schmidt decomposition theorem [271].

- **Theorem: Schmidt decomposition.** Let \mathcal{H}_1 and \mathcal{H}_2 be n - and m -dimensional Hilbert spaces with $n \geq m$. For any vector $v \in \mathcal{H}_1 \otimes \mathcal{H}_2$, there exist orthonormal sets $\{u_1, \dots, u_n\} \subset \mathcal{H}_1$ and $\{v_1, \dots, v_m\} \subset \mathcal{H}_2$ such that $v = \sum_{j=1}^m \lambda_j u_j \otimes v_j$, with $\lambda_j \geq 0$ for $j = 1, \dots, m$ and $\lambda_j = 0$ for $j = m + 1, \dots, n$.

This algebraic tool allows us to rewrite a general quantum state of the form given by Eq. (8.14) as

$$|\Psi\rangle = \sum_{j=1}^S \sqrt{\lambda_j} |\phi_j\rangle_1 |\phi_j\rangle_2 \quad (8.16)$$

where one summation index suffices, in contrast to the general form of Eq. (8.14). The *Schmidt coefficients* λ_j coincide with the eigenvalues of the reduced density matrices given in Eq. (8.12). Since the states $\{|\phi_i\rangle_1\}$ and $\{|\phi_i\rangle_2\}$ constitute a orthogonal basis, they are indeed the eigenstates of the reduced density matrices

$$\rho_1 = \sum_{j=1}^S \lambda_j |\phi_j\rangle_1 \langle \phi_j|_1 \quad \text{and} \quad \rho_2 = \sum_{j=1}^S \lambda_j |\phi_j\rangle_2 \langle \phi_j|_2, \quad (8.17)$$

with the λ_j the associated eigenvalues.

Equivalent states are motivated by the fact that parties which are in possession of the subsystems can perform local unitary operations without any mutual communication. So, equivalent states can be related one to each other via unitary operations that are applied locally and independent on both subsystems as follows:

$$|\Phi\rangle_1 = \hat{U} |\Phi\rangle_2, \quad |\Phi\rangle_2 = \hat{U}^\dagger |\Phi\rangle_1, \quad (8.18)$$

where $\hat{U} = \hat{U}_1 \otimes \hat{U}_2 = e^{-\frac{i}{\hbar}\tau(H_1 \otimes \mathbb{I} + \mathbb{I} \otimes H_2)}$ and \mathbb{I} is the identity operator. Then, two equivalent quantum states have the same amount of entanglement and possess the same Schmidt decomposition. The distribution of the Schmidt coefficients λ_j therefore fully determines the entanglement of a state.

8.4 Entanglement quantification of pure states

The entanglement of a pure bipartite system is “essentially” given by the mixedness of the marginal density matrices associated with each subsystem. A pure bipartite state is entangled if and only if its subsystems are in a mixed state. This means that the disorder of the reduced density matrix is clear indicator that the state is entangled. This feature allows to introduce quantitative measures for the entanglement exhibited by pure states.

- The von Neumann entropy of a density matrix [272, 273], given by

$$S^{(vN)}[\rho] = -\text{Tr}[\rho \ln \rho], \quad (8.19)$$

can be used for such a quantification. The von Neumann entropy of the reduced density matrix, ρ_i , receives the name of *entanglement entropy* or *entanglement of formation* [274] and is the canonical measure to quantify the entanglement of pure bipartite states, that is

$$\varepsilon^{(vN)}(|\Psi\rangle) = S^{(vN)}[\rho_i] = -\text{Tr}[\rho_i \ln \rho_i], \quad (8.20)$$

which, for bipartite systems, fulfills that $S^{(vN)}[\rho_1] = S^{(vN)}[\rho_2]$. Entanglement of formation boils down to the original Shannon entropy [41] of a probability distribution defined by the Schmidt coefficients λ_j :

$$\varepsilon^{(vN)}(|\Psi\rangle) = S[\{\lambda_1, \dots, \lambda_S\}] = -\sum_{j=1}^S \lambda_j \ln \lambda_j. \quad (8.21)$$

It is maximized by the maximally mixed state, so maximally entangled states are characterized by maximally mixed subsystems. An example of maximally entangled states is given by the Bell states $|\Psi_i^\pm\rangle$, defined in Eq. (8.6), for which the reduced density matrix given by Eq. (8.13), provides the maximum possible value of the von Neumann entropy for two qubit systems:

$$\varepsilon^{(vN)}(|\Psi_i^\pm\rangle) = \ln 2. \quad (8.22)$$

- Another practical quantitative indicator of the amount of entanglement of pure bipartite systems is given by the *linear entropy*,

$$\varepsilon^{(L)}(|\Psi\rangle) = \frac{N_i}{N_i - 1} (1 - \text{Tr}[\rho_i^2]), \quad (8.23)$$

where N_i is the dimension of the reduced density matrix ρ_i so that the linear entropy belongs to the interval $[0, 1]$. The quantity

$$P = \text{Tr}[\rho_i^2] \quad (8.24)$$

is the *purity* of the subsystem ρ_i which, for a probability distribution defined by the weights λ_j (or a Schmidt coefficients distribution) is given by $P = \sum_{j=1}^S \lambda_j^2$.

The purity of the reduced density matrix is known to be a proper measure of the degree of mixedness of ρ_i . That is, we can restate the separability criterion for pure states:

$$\begin{aligned} P = \text{Tr}[\rho_i^2] = 1 &\Rightarrow \rho_i \text{ is pure} \Rightarrow |\Psi\rangle \text{ is separable} \\ P = \text{Tr}[\rho_i^2] < 1 &\Rightarrow \rho_i \text{ is mixed} \Rightarrow |\Psi\rangle \text{ is entangled.} \end{aligned} \quad (8.25)$$

For Bell states, Eq. (8.6), the maximum possible value of the linear entropy, $\varepsilon^{(L)}(|\Psi_i^\pm\rangle) = 1$, is obtained.

Although the linear entropy is not a strictly measure of entanglement –it does not meet all the axioms for the monotonicity under *local operations and classical communication* (LOCC) [275], as the entropy of formation does– it is an useful indicator of the entanglement in the sense that it quantify the degree of mixedness of the reduced density matrix. The linear entropy in Eq. (8.23) coincides, up to multiplicative and additive constants, with the *concurrence* (see [276]).

There are some other measures of entanglement for pure bipartite state in the literature, such as the *Schmidt rank* S [277] or the *concurrence* [276, 278], however the linear entropy has several computational advantages from both analytical and numerical points of view. In particular, and contrary to those measures as well as the entropy of formation in Eq. (8.20), the computation of the linear entropy, does not require the diagonalization of the reduced density matrix ρ_i . In the course of the Part II and Part III of this thesis, we will characterize the entanglement content of a pure bipartite quantum state via linear entropy, which proved to be a powerful tool for elucidating many aspects of the entanglement properties of pure states (see, for instance, [5, 279, 238, 260, 265, 280, 281, 282]).

8.4.1 Entanglement for identical fermions

Correlations between two identical fermions that are only due to the antisymmetric nature of the two-particle state do not contribute to the state's entanglement [233, 283, 284, 285, 286, 287, 288]. The entanglement of the two-fermion state is given by the quantum correlations existing on top of these minimum ones. Quantum correlations in systems of

indistinguishable fermions arise if more than one *Slater determinant* (a fully antisymmetric combination of all orthogonal single-particle states) is involved. Therefore, a pure state of identical fermions is entangled if and only if its Slater rank is above 1 and the definition of a separable system given by Eq. (8.9) is useless because the Hilbert space of the system can not be expressed as the tensor product of the single particle Hilbert spaces.

In a system composed by two identical fermions, for example, a separable state can be defined as

$$|\Psi\rangle_{sep} = \frac{1}{\sqrt{2}} (|\Phi_1\rangle |\Phi_2\rangle - |\Phi_2\rangle |\Phi_1\rangle) \quad (8.26)$$

where $|\Phi\rangle_1$ and $|\Phi\rangle_2$ are two orthogonal and normalized single-particle states.

The Schmidt decomposition admits a natural generalization for a system of two identical fermions. Given a pure state $|\Psi\rangle$, it is possible to find an orthonormal basis $\{|\phi_j\rangle, j = 1, 2, \dots\}$ of the single-particle states, such that the two-fermions pure state $|\Psi\rangle$ can be written as

$$|\Psi\rangle = \sum_{j=1}^S \sqrt{\frac{\lambda_j}{2}} (|\phi_{2j}\rangle_1 |\phi_{2j-1}\rangle_2 - |\phi_{2j-1}\rangle_1 |\phi_{2j}\rangle_2). \quad (8.27)$$

The simplest fermionic system admitting entanglement is composed by two fermions with a single-particle Hilbert space of dimension four.

When the Slater rank of a N -fermions pure state $|\Psi\rangle_N$ is one, *i.e.* the state is separable, the purity of the single-fermion reduced density matrix, ρ_r , is $P = \text{Tr}[\rho_r^2] = 1/N$, which leads to the separability criterion [280]

$$\begin{aligned} P = \text{Tr}[\rho_r^2] = \frac{1}{N} &\Rightarrow |\Psi\rangle_N \text{ has Slater rank} = 1 \Rightarrow |\Psi\rangle_N \text{ is separable} \\ P = \text{Tr}[\rho_r^2] < \frac{1}{N} &\Rightarrow |\Psi\rangle_N \text{ has Slater rank} > 1 \Rightarrow |\Psi\rangle_N \text{ is entangled.} \end{aligned} \quad (8.28)$$

Thereby, practical quantitative measure for the amount of entanglement exhibited by a pure state $|\Psi\rangle_N$ of a system of N identical fermions (see [280] and references therein) is that given by the linear entropy of the single-fermion reduced density matrix ρ_r ,

$$\varepsilon^{(L)}(|\Psi\rangle_N) = 1 - N\text{Tr}[\rho_r^2], \quad (8.29)$$

This measure is normalized to adopt values in the interval $[0, 1]$.

In Chapter 9, we study systems of identical fermions so we will use this measure as given by Eq. (8.29), however in Chapter 10 the system studied consists of many distinguishable particles, so that the appropriate measure to carry out such a study is that given in Eq. (8.23).

The Moshinsky model with three electrons, and with two electrons in an uniform magnetic field

In this chapter we investigate the entanglement-related features of the eigenstates of two exactly soluble atomic models: a one-dimensional three-electron Moshinsky model, and a three-dimensional two-electron Moshinsky system in an external uniform magnetic field. The amount of entanglement exhibited by the wavefunctions corresponding to the ground, first and second excited states of the three-electron model are analytically computed. We found that the amount of entanglement of the system tends to increase with energy and, in the case of excited states, a finite amount of entanglement in the limit of vanishing interaction. We also analyze the entanglement properties of the ground and first few excited states of the two-electron Moshinsky model in the presence of a magnetic field. The dependence of the eigenstates' entanglement on the energy, as well as its behavior in the regime of vanishing interaction, are similar to those observed in the three-electron system. On the other hand, the entanglement exhibits a monotonically decreasing behavior with the strength of the external magnetic field. For strong magnetic fields the entanglement approaches a finite asymptotic value that depends on the interaction strength. For both systems studied here we consider a perturbative approach in order to shed some light on the entanglement's dependence on energy and also to clarify the finite entanglement exhibited by excited states in the limit of weak interactions.

The chapter is organized as follows. In Section 9.1 entanglement in systems of identical fermions in a continuous variable framework is briefly discussed. The measure used in order to quantify the amount of entanglement of pure states is reviewed, focusing on appropriate measure for two- and three-electrons systems. In Section 9.2, the entanglement properties of the eigenstates of the Moshinsky model with three electrons are investigated. The entanglement features of the three-dimensional Moshinsky model with two electrons in the presence of a uniform magnetic field are studied in Section 9.3. Then, in Section 9.4 we consider a perturbative approach to clarify some entanglement features found in the previous models. Finally, some conclusions are drawn.

9.1 Entanglement measure

We shall apply the measure given by Eq. (8.29) to a pure state $|\Psi\rangle$ of a one dimensional system consisting of three spin- $\frac{1}{2}$ fermions (electrons). We deal with infinite-

dimensional Hilbert spaces and, since the maximal value of the entanglement in a d -dimensional space is $1 - 1/d$, the measure in Eq. (8.29) adopts values within the interval $[0, 1)$. This pure state has an associated wave function given, in self-explanatory notation, by $\Psi(x_1\sigma_1, x_2\sigma_2, x_3\sigma_3) = \langle x_1\sigma_1, x_2\sigma_2, x_3\sigma_3 | \Psi \rangle$ with $|x_1\sigma_1, x_2\sigma_2, x_3\sigma_3\rangle = |x_1, x_2, x_3\rangle \otimes |\sigma_1, \sigma_2, \sigma_3\rangle$. Here $x_{1,2,3}$ are the coordinates of the three electrons, and the dichotomic variables $\sigma_{1,2,3}$ (each adopting the possible values \pm and corresponding to the S_z component of spin) describe the spin degrees of freedom of the three electrons. In order to evaluate the amount of entanglement of the system we have to compute the following integrals:

$$\langle x_1\sigma_1 | \rho_r | x'_1\sigma'_1 \rangle = \sum_{\sigma_2, \sigma_3 = \pm} \int_{-\infty}^{\infty} \langle x_1\sigma_1, x_2\sigma_2, x_3\sigma_3 | \rho | x'_1\sigma'_1, x_2\sigma_2, x_3\sigma_3 \rangle dx_2 dx_3 \quad (9.1)$$

where $\langle x_1\sigma_1 | \rho_r | x'_1\sigma'_1 \rangle$ are the elements of the one-particle reduced density matrix $\rho_r(x_1, x'_1)$, $\rho = |\psi\rangle\langle\psi|$ and

$$\langle x_1\sigma_1, x_2\sigma_2, x_3\sigma_3 | \rho | x'_1\sigma'_1, x_2\sigma_2, x_3\sigma_3 \rangle = \Psi(x_1\sigma_1, x_2\sigma_2, x_3\sigma_3) \Psi^*(x'_1\sigma'_1, x_2\sigma_2, x_3\sigma_3).$$

The square reduced spin density matrix is given by

$$\langle x_1\sigma_1 | \rho_r^2 | x'_1\sigma'_1 \rangle = \sum_{\sigma = \pm} \int_{-\infty}^{\infty} \langle x_1\sigma_1 | \rho_r | x\sigma \rangle \langle x\sigma | \rho_r | x'_1\sigma'_1 \rangle dx$$

and finally the expression for the trace is

$$Tr[\rho_r^2] = \sum_{\sigma = \pm} \int_{-\infty}^{\infty} \langle x\sigma | \rho_r^2 | x\sigma \rangle dx.$$

In the three-electron case it is not possible to find totally antisymmetric wave functions factorizable into coordinate and spin parts; however in the two-electron case, following Ref. [238] we focus on states with factorized wave functions. The corresponding density matrix takes the form

$$\rho = \rho^{(c)} \otimes \rho^{(s)} \quad (9.2)$$

and then, the entanglement measure evaluated on these states is given by

$$\varepsilon = 1 - 2Tr[(\rho_r^{(c)})^2]Tr[(\rho_r^{(s)})^2], \quad (9.3)$$

where $\rho_r^{(c)}$ and $\rho_r^{(s)}$ are the single-particle reduced coordinate and spin density matrices. So, in the case of two-electron system studied in section 4, we consider separately the cases of parallel and antiparallel spin wave function. In the case of parallel spins, described by $|++\rangle$ or $|--\rangle$, the coordinate wave function must be antisymmetric and we have $Tr[(\rho_r^{(s)})^2] = 1$. On the other hand, if we have antiparallel spins we can distinguish two cases: symmetric coordinate wave function with spin wave function of the form $\frac{1}{\sqrt{2}}(|+-\rangle - |-+\rangle)$ or antisymmetric coordinate wave function with spin wave function $\frac{1}{\sqrt{2}}(|+-\rangle + |-+\rangle)$,

both of them with $Tr[(\rho_r^{(s)})^2] = \frac{1}{2}$. And finally, to calculate the amount of entanglement we will compute the integrals

$$\langle \mathbf{r}_1 | \rho_r^{(c)} | \mathbf{r}'_1 \rangle = \int_{\mathbb{R}^3} \langle \mathbf{r}_1 \mathbf{r}_2 | \rho^{(c)} | \mathbf{r}'_1 \mathbf{r}_2 \rangle d\mathbf{r}_2 = \int_{\mathbb{R}^3} \Psi(\mathbf{r}_1, \mathbf{r}_2) \Psi^*(\mathbf{r}'_1, \mathbf{r}_2) d\mathbf{r}_2 \quad (9.4)$$

and the trace of the coordinate part is

$$Tr[(\rho_r^{(c)})^2] = \int_{\mathbb{R}^3} |\langle \mathbf{r}_1 | \rho_r^{(c)} | \mathbf{r}'_1 \rangle|^2 d\mathbf{r}_1 d\mathbf{r}'_1 \quad (9.5)$$

9.2 The three-electron Moshinsky atom

The Moshinsky atom [261] is a system formed by harmonically interacting particles confined in a common external isotropic harmonic potential. The total Hamiltonian of the one-dimensional Moshinsky atom with three electrons is

$$H = -\frac{1}{2} \left(\frac{\partial^2}{\partial x_1^2} + \frac{\partial^2}{\partial x_2^2} + \frac{\partial^2}{\partial x_3^2} \right) + \frac{1}{2} \omega^2 (x_1^2 + x_2^2 + x_3^2) \pm \frac{1}{2} \lambda^2 [(x_1 - x_2)^2 + (x_2 - x_3)^2 + (x_3 - x_1)^2] \quad (9.6)$$

where x_1, x_2 and x_3 are the coordinates of the three particles, ω is the natural frequency of the external harmonic field, and λ is the natural frequency of the interaction harmonic field. The positive sign in the last term describes an attractive interaction between the electrons and the negative a repulsive interaction. We use atomic units ($m_e = 1, \hbar = 1$) throughout, unless indicated otherwise.

Introducing the Jacobi coordinates for three particles,

$$R_1 = \frac{1}{\sqrt{3}}(x_1 + x_2 + x_3), R_2 = \frac{1}{\sqrt{6}}(-2x_1 + x_2 + x_3) \quad \text{and} \quad R_3 = \frac{1}{\sqrt{2}}(x_2 - x_3), \quad (9.7)$$

the Hamiltonian separates in the following way:

$$H = \left(-\frac{1}{2} \frac{\partial^2}{\partial R_1^2} + \frac{1}{2} \beta_1 R_1^2 \right) + \left(-\frac{1}{2} \frac{\partial^2}{\partial R_2^2} + \frac{1}{2} \beta_2 R_2^2 \right) + \left(-\frac{1}{2} \frac{\partial^2}{\partial R_3^2} + \frac{1}{2} \beta_3 R_3^2 \right) \quad (9.8)$$

where $\beta_1 = \omega^2, \beta_2 = \beta_3 = \Lambda^2 = \omega^2 \pm 3\lambda^2$ (again, the + sign corresponds to an attractive interaction, while the - sign corresponds to a repulsive one) and Λ is the frequency corresponding to the coordinates R_2 , and R_3 . In the case of a repulsive interaction it is necessary to impose the constraint $\lambda < \frac{\omega}{\sqrt{3}}$ in order to obtain bound eigenstates. The general eigenfunctions of the system are

$$\Psi(x_1, x_2, x_3) = \Psi(R_1, R_2, R_3) = \Psi_{n_{R_1}}(R_1) \Psi_{n_{R_2}}(R_2) \Psi_{n_{R_3}}(R_3) \quad (9.9)$$

with

$$\Psi_{n_{R_i}}(R_i) = \left(\frac{\beta_i^{1/4}}{2^{n_{R_i}} n_{R_i}! \pi^{1/2}} \right)^{\frac{1}{2}} e^{-\frac{1}{2} \sqrt{\beta_i} R_i^2} \mathcal{H}_{n_{R_i}}(\beta_i^{1/4} R_i), \quad (9.10)$$

where $\mathcal{H}_n(x)$ denote the Hermite polynomials. The eigenenergies of these states are

$$E = E_{R_1} + E_{R_2} + E_{R_3} = \omega \left(n_{R_1} + \frac{1}{2} \right) + \Lambda (n_{R_2} + n_{R_3} + 1) \quad (9.11)$$

We will denote by $|n_{R_1} n_{R_2} n_{R_3}\rangle$ the eigenstates of the Hamiltonian in Eq.(9.8), which are characterized by the three quantum numbers n_{R_1} , n_{R_2} and n_{R_3} . To fully define the three-electron system's eigenstates we must take into account combinations of such functions of the coordinates together with the spin ones $|\sigma_1 \sigma_2 \sigma_3\rangle$ to obtain total antisymmetric wave functions. In this case the wave functions corresponding to the energy eigenstates never can be chosen to be separable into coordinates and spin, there are no spin functions totally antisymmetric by themselves. The Hamiltonian commutes with the spin observables, since it does not explicitly involve the spins. In particular, it commutes with the total z -component of spin angular momentum S_z . Consequently, it is possible to choose energy eigenstates that are also eigenstates of S_z . It is plain that the wave functions associated with these eigenstates can always be written (up to a global normalization constant) in one of the forms

$$|\Phi^{(++)}\rangle |+-\rangle + |\Phi^{(+-)}\rangle |-+\rangle + |\Phi^{(---)}\rangle |-++\rangle, \quad (9.12)$$

$$|\Phi^{(+++)}\rangle |+++ \rangle, \quad (9.13)$$

or in the forms obtained substituting $+$ by $-$ (and viceversa) in the above expressions. In Eqs. (9.12)-(9.13) the kets $|\Phi^{(\sigma_1, \sigma_2, \sigma_3)}\rangle$ correspond to the translational degrees of freedom and have associated coordinate wave functions $\Phi^{(\sigma_1, \sigma_2, \sigma_3)}(x_1, x_2, x_3) = \langle x_1, x_2, x_3 | \Phi^{(\sigma_1, \sigma_2, \sigma_3)} \rangle$. For the states given by Eqs. (9.12-9.13) to be fully antisymmetric the coordinate wave functions $\Phi^{(\sigma_1, \sigma_2, \sigma_3)}(x_1, x_2, x_3)$ must satisfy the following set of relations. If $\sigma_1 = \sigma_2$ we must have $\Phi^{(\sigma_1, \sigma_2, \sigma_3)}(x_2, x_1, x_3) = -\Phi^{(\sigma_1, \sigma_2, \sigma_3)}(x_1, x_2, x_3)$, (that is, in this case the coordinate wave function $\Phi^{(\sigma_1, \sigma_2, \sigma_3)}(x_1, x_2, x_3)$ has to be antisymmetric with respect to x_1 and x_2). On the other hand, if $\sigma_1 = -\sigma_2$ we must have $\Phi^{(\sigma_1, \sigma_2, \sigma_3)}(x_2, x_1, x_3) = -\Phi^{(\sigma_2, \sigma_1, \sigma_3)}(x_1, x_2, x_3)$. Similar relations hold in connection with the pairs of labels (σ_2, σ_3) and (σ_3, σ_1) . These relations imply, in particular, that the wave function $\Phi^{(+++)}(x_1, x_2, x_3)$ (and also $\Phi^{(---)}(x_1, x_2, x_3)$) must be fully antisymmetric with respect to the three coordinates x_1, x_2, x_3 . Finally it is clear that, in order to be energy eigenstates, the states (9.12)-(9.13) must involve spatial wave functions $\Phi^{(\sigma_1, \sigma_2, \sigma_3)}(x_1, x_2, x_3)$ that are themselves eigenfunctions of the Hamiltonian given by Eq. (9.6). In particular, the three coordinate eigenfunctions associated with Eq. (9.12) have to be eigenfunctions of Eq. (9.6) corresponding to the same energy eigenvalue. The ground state and few excited eigenstates of the three-electron system that we are going to study in the present work do not correspond to the form (9.13). Thus, we are going to restrict our considerations to eigenstates of the form (9.12). A direct way to construct the ground and first few excited states according to the structure (9.12) is to use combinations of the forms

$$\begin{aligned}
|n_1 n_2 n_3\rangle = \mathcal{N} & \left[\left(|n_{R_1} n_{R_2} n_{R_3}\rangle - |n_{R'_1} n_{R'_2} n_{R'_3}\rangle \right) |+-\rangle + \right. \\
& + \left(|n_{R'_1} n_{R'_2} n_{R'_3}\rangle - |n_{R_1} n_{R_2} n_{R_3}\rangle \right) |+ -\rangle + \\
& \left. + \left(|n_{R_1} n_{R_2} n_{R_3}\rangle - |n_{R''_1} n_{R''_2} n_{R''_3}\rangle \right) |-++\rangle \right] \quad (9.14)
\end{aligned}$$

or

$$\begin{aligned}
|n_1 n_2 n_3\rangle = \mathcal{N}' & \left[|n_{R'_1} n_{R'_2} n_{R'_3}\rangle |+-\rangle + |n_{R'_1} n_{R'_2} n_{R'_3}\rangle |+ -\rangle + \right. \\
& \left. + |n_{R_1} n_{R_2} n_{R_3}\rangle |-++\rangle \right], \quad (9.15)
\end{aligned}$$

where

$$\begin{aligned}
R_1 = R'_1 = R''_1, \quad R'_2 = \frac{1}{\sqrt{6}}(x_1 - 2x_2 + x_3), \quad R''_2 = \frac{1}{\sqrt{6}}(x_1 + x_2 - 2x_3), \\
R'_3 = \frac{1}{\sqrt{2}}(x_3 - x_1), \quad R''_3 = \frac{1}{\sqrt{2}}(x_1 - x_2), \quad (9.16)
\end{aligned}$$

$$n_1 = n_{R_1} = n_{R'_1} = n_{R''_1}, \quad n_2 = n_{R_2} = n_{R'_2} = n_{R''_2}, \quad n_3 = n_{R_3} = n_{R'_3} = n_{R''_3},$$

and \mathcal{N} , \mathcal{N}' are appropriate normalization constants. Note that the three spatial wave functions corresponding respectively to the three kets $|n_{R_1} n_{R_2} n_{R_3}\rangle$, $|n_{R'_1} n_{R'_2} n_{R'_3}\rangle$ and $|n_{R''_1} n_{R''_2} n_{R''_3}\rangle$ (which appear in (9.14) and in (9.15)) are obtained via cyclic permutations of the particles coordinates $\{x_1, x_2, x_3\}$ in the definition of the Jacobi coordinates. Therefore, it is evident that these three spatial wave functions are eigenfunctions of (9.6) sharing the same eigenenergy. We will use combinations of type (9.14) if the quantum number n_3 is even, and of type (9.15) when it is odd, ensuring in this way the antisymmetry of the wave function. As already mentioned, we have chosen these states because they are also special in the sense that they all are eigenstates of S_z . States of the forms (9.14) and (9.15) correspond to a wave function with total spin $S_z = S_z^{(1)} + S_z^{(2)} + S_z^{(3)} = +\frac{1}{2}$ of the three-electron system but one can also construct eigenstates of the same type with total spin $S_z = -\frac{1}{2}$. As the entanglement of the $S_z = -\frac{1}{2}$ states is the same as the entanglement of states with $S_z = +\frac{1}{2}$, in the rest of this chapter we will mainly focus on states with $S_z = +\frac{1}{2}$.

We must remember that these states are written in Jacobi relative coordinates of a three-particle system and the quantum numbers n_1 , n_2 and n_3 refer to these coordinates. However, to determine the amount of entanglement between the particles we have to express the wave functions associated with the eigenstates in terms of the coordinates and spins of the particles,

$$\Psi_{n_1 n_2 n_3}(x_1 \sigma_1, x_2 \sigma_2, x_3 \sigma_3) = \langle x_1 \sigma_1, x_2 \sigma_2, x_3 \sigma_3 | n_1 n_2 n_3 \rangle \quad (9.17)$$

In the case of the eigenfunctions (9.17) of the Moshinsky system the entanglement measure ε can be computed in an exact analytical way. However, for highly excited states the corresponding expressions become very awkward. For the sake of simplicity, we are

going to calculate this quantity only for the ground state and the first and second excited states. In each case we shall provide the final closed expressions for ε (arising from the evaluation of the aforementioned integrals) and discuss the behavior of the eigenstate's entanglement. The value of ε corresponding to the state $|n_1 n_2 n_3\rangle$ (with $S_z = +\frac{1}{2}$) will be denoted by $\varepsilon_{n_1 n_2 n_3}$. As a compact alternative notation for the alluded state we shall also use $|n_1 n_2 n_3\rangle_{R_1 R_2 R_3}$.

We compute the state's entanglement in terms of the dimensionless parameter $\tau = \frac{\lambda}{\omega}$, which constitutes a measure of the relative strength of the interaction between two particles in the Moshinsky system. Remark that the system is decoupled when $\tau = 0$. The larger the value of τ , the larger is the (relative) contribution of the interaction term in the Moshinsky atom.

9.2.1 Ground state

Let $A = \sqrt{1 \pm 3\tau^2}$. Using the right spin combination given by (9.14) we can express the entanglement of the ground state in terms of the parameter τ as

$$\varepsilon_{010} = 1 - \frac{\sqrt{2A + 5A^2 + 2A^3}}{4(2 + 5A + 2A^2)^3} (59 + 232A + 390A^2 + 232A^3 + 59A^4), \quad (9.18)$$

We see from (9.18) that the entanglement of the ground state depends upon the parameters of the Moshinsky atom only through the dimensionless quantity τ . Decoupling the system, that is, making $\tau \rightarrow 0$ (which corresponds, for instance, to $\lambda \rightarrow 0$ or equivalently $\Lambda \rightarrow \omega$) makes $\varepsilon_{010} = 0$ showing that in the decoupled system the ground state is not entangled. On the other hand, with maximum coupling $\tau \rightarrow \infty$ ($\tau \rightarrow \frac{1}{\sqrt{3}}$) for attractive (repulsive) interactions we find that $\varepsilon_{010} = 1$, that is, the entanglement measure adopts its maximum possible value.

9.2.2 First excited states

The first excited state in energy, when the system is coupled ($\tau > 0$) and with attractive interaction, is $|110\rangle_{R_1 R_2 R_3}$ and the next one with higher energy is $|011\rangle_{R_1 R_2 R_3}$, the excitation order being reversed in the case of repulsive interaction. Both states have the same energy when we decouple the system, that is, when $\tau \rightarrow 0$. For these states, using (9.14) and (9.15) respectively, we have

$$\varepsilon_{110} = 1 - \frac{A^{1/2}}{4(2+A)^{9/2}(1+2A)^{9/2}} (177 + 1034A + 6213A^2 + 12582A^3 + 15392A^4 + 12582A^5 + 6213A^6 + 1034A^7 + 177A^8) \quad (9.19)$$

and

$$\varepsilon_{011} = 1 - \frac{A^{1/2}}{640(2+A)^{9/2}(1+2A)^{9/2}} (3057 + 24608A + 93180A^2 + 196704A^3 + 251366A^4 + 196704A^5 + 93180A^6 + 24608A^7 + 3057A^8). \quad (9.20)$$

Decoupling the system makes $\varepsilon_{011} = \varepsilon_{110} = \frac{8}{27}$, so in the limit of a decoupled system the first excited states are entangled. On the other hand, with maximum coupling we find that $\varepsilon_{011} = \varepsilon_{110} = 1$, that is, the entanglement is maximum.

To both states ($|011\rangle_{R_1 R_2 R_3}$ and $|110\rangle_{R_1 R_2 R_3}$) having $S_z = +\frac{1}{2}$, which we will denote by $|011\rangle_+$ and $|110\rangle_+$, one can associate the states $|011\rangle_-$ and $|110\rangle_-$ respectively with the same energy and same entanglement but with $S_z = -\frac{1}{2}$. Then, as these are degenerate states because the energy does not depend on the spin, we compute the amount of entanglement of a combination of them in the following way:

$$\begin{aligned} |\Psi_{011}\rangle &= \cos\theta |011\rangle_+ + \sin\theta |011\rangle_- \\ |\Psi_{110}\rangle &= \cos\theta |110\rangle_+ + \sin\theta |110\rangle_- \end{aligned} \quad (9.21)$$

where $0 \leq \theta < 2\pi$. These states exhibit an amount of entanglement that is independent of the parameter θ . To understand this behavior let us consider the unitary transformation U (acting on the single-particle Hilbert space) defined by

$$\begin{aligned} U|\phi_k\rangle|+\rangle &= |\phi_k\rangle|p\rangle, \quad k = 1, 2, \dots, \\ U|\phi_k\rangle|-\rangle &= |\phi_k\rangle|n\rangle, \quad k = 1, 2, \dots, \end{aligned} \quad (9.22)$$

where ($|\varepsilon_k\rangle = |\phi_k\rangle|\pm\rangle$, $k = 1, 2, \dots$) is a single-particle orthonormal basis (with the kets $|\phi_k\rangle$ corresponding to the spatial degrees of freedom) and

$$\begin{aligned} |p\rangle &= \cos\theta|+\rangle - \sin\theta|-\rangle, \\ |n\rangle &= \sin\theta|+\rangle + \cos\theta|-\rangle. \end{aligned} \quad (9.23)$$

It can be verified after some algebra that

$$\begin{aligned} |\Psi_{011}\rangle &= (U \otimes U \otimes U)|011\rangle_+, \\ |\Psi_{110}\rangle &= (U \otimes U \otimes U)|110\rangle_+. \end{aligned} \quad (9.24)$$

Now, it is clear that the amount of entanglement of a three-fermions state does not change under the effect of unitary transformations of the form $U \otimes U \otimes U$ and, consequently, the entanglement of the states defined in Eq. (9.21) does not depend upon θ .

9.2.3 Second excited states

For these states we have that the lowest-energy second excited state when the system is coupled and with attractive interaction is $|210\rangle_{R_1 R_2 R_3}$, the next one with higher energy is $|111\rangle_{R_1 R_2 R_3}$, and the following three states, all of them with the same energy, are $|012\rangle_{R_1 R_2 R_3}$, $|021\rangle_{R_1 R_2 R_3}$ and $|003\rangle_{R_1 R_2 R_3}$. All these states have the same energy when the system is decoupled.

Defining the parameter $B = \frac{A^{1/2}}{(2+A)^{13/2}(1+2A)^{13/2}}$, using Eq. (9.14) for the states $|210\rangle_{R_1 R_2 R_3}$ and $|012\rangle_{R_1 R_2 R_3}$, and Eq. (9.15) for the states $|111\rangle_{R_1 R_2 R_3}$, $|021\rangle_{R_1 R_2 R_3}$

and $|003\rangle_{R_1 R_2 R_3}$, we found

$$\varepsilon_{210} = 1 - \frac{B}{16} (2419 + 19480A + 218138A^2 + 564200A^3 + 1466241A^4 + 2943840A^5 + 3743124A^6 + 2943840A^7 + 1466241A^8 + 564200A^9 + 218138A^{10} + 19480A^{11} + 2419A^{12}),$$

$$\varepsilon_{111} = 1 - \frac{B}{64} (9171 + 80546A + 700555A^2 + 2659770A^3 + 6668841A^4 + 11416740A^5 + 13615794A^6 + 11416740A^7 + 6668841A^8 + 2659770A^9 + 700555A^{10} + 80546A^{11} + 9171A^{12}),$$

$$\varepsilon_{012} = 1 - \frac{B}{256} (42739 + 506008A + 3123242A^2 + 11179160A^3 + 26922957A^4 + 44982480A^5 + 53234988A^6 + 44982480A^7 + 26922957A^8 + 11179160A^9 + 3123242A^{10} + 506008A^{11} + 42739A^{12}),$$

$$\varepsilon_{021} = 1 - \frac{B}{4096} (727363 + 8982520A + 54219206A^2 + 196856600A^3 + 469858317A^4 + 776694000A^5 + 915625428A^6 + 776694000A^7 + 469858317A^8 + 196856600A^9 + 54219206A^{10} + 8982520A^{11} + 727363A^{12}),$$

and

$$\varepsilon_{003} = 1 - \frac{B}{4096} (762395 + 9419160A + 61156086A^2 + 232139320A^3 + 576896949A^4 + 982782000A^5 + 1171448436A^6 + 982782000A^7 + 576896949A^8 + 232139320A^9 + 61156086A^{10} + 9419160A^{11} + 762395A^{12}),$$

Taking the limit for the decoupling case of the system makes $\varepsilon_{111} = \varepsilon_{210} = \varepsilon_{012} = \frac{4}{9}$, $\varepsilon_{021} = \frac{43}{108}$ and $\varepsilon_{003} = \frac{1}{4}$, showing again that these excited states are entangled in the decoupled system. In the maximum coupling limit we find for all second-excited states that the entanglement reaches again its maximum value.

The behavior of the eigenstates' entanglement as a function of the parameter τ (which corresponds to the relative strength of the interaction between the two particles) is depicted in Figure 9.1 for an attractive interaction and in Figure 9.2 for a repulsive interaction.

Comparing Figures 9.1 and 9.2 one observes that in the repulsive case (Fig. 9.2) maximum entanglement is reached when the parameter τ approaches the finite limit value $\frac{1}{\sqrt{3}} \approx 0.577$. In the attractive case (Fig. 9.1) entanglement behaves in a different way: maximum entanglement corresponds to the limit $\tau \rightarrow \infty$. This difference between the

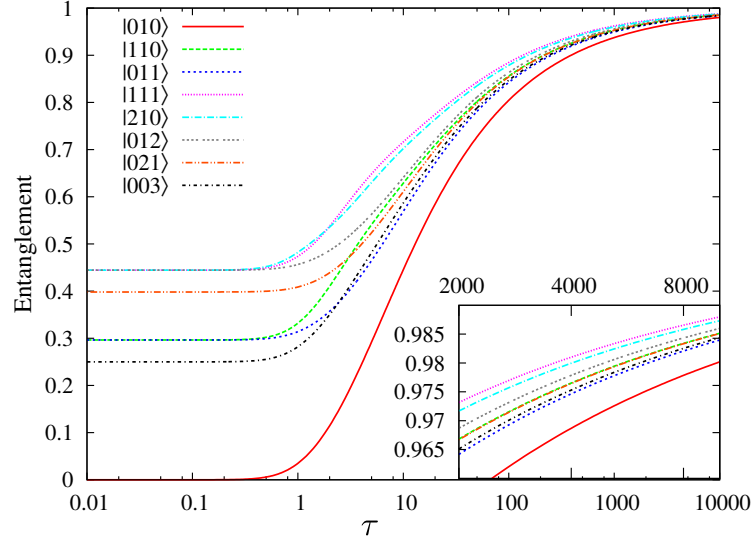


Figure 9.1: Entanglement of the ground, first and second excited states of one-dimensional Moshinsky atom with three electrons attractively interacting. All depicted quantities are dimensionless.

attractive and the repulsive cases is due to the fact that the Moshinsky model with repulsive interaction admits bound states only for τ -values in the finite range $[0, \frac{1}{\sqrt{3}})$. On the other hand, in the attractive case the Moshinsky model admits bound states for all $\tau \geq 0$. In the case of the repulsive interaction the eigenstates of the system are no longer bounded for $\tau \geq \frac{1}{\sqrt{3}}$. Thus, the eigenstates exhibit a qualitative structural change at the “critical” value $\tau_c = \frac{1}{\sqrt{3}}$, resembling a quantum phase transition. A similar situation occurs in the case of the Moshinsky atom with two electrons in a uniform magnetic field studied in the next section (see Figure 9.4). This system, when the interaction is repulsive, admits bound states only for τ -values smaller than the critical value $\tau_c = 1$.

9.3 Two-electron Moshinsky atom in a magnetic field

The Hamiltonian of the two-electron Moshinsky atom in a three dimensional space is

$$H_M = \frac{p_1^2}{2m_e} + \frac{p_2^2}{2m_e} + \frac{1}{2}m_e\omega^2(r_1^2 + r_2^2) \pm \frac{\lambda^2}{2}(\mathbf{r}_1 - \mathbf{r}_2)^2$$

where subscripts 1 and 2 denote each of the electrons. As before, the positive (negative) sign refers to an attractive (repulsive) interaction between the electrons. To study the presence of an uniform magnetic field acting on the system, we perform the following change in the Hamiltonian:

$$\mathbf{p}_1 \rightarrow \mathbf{p}_1 + \frac{e}{c}\mathbf{A} \quad \text{and} \quad \mathbf{p}_2 \rightarrow \mathbf{p}_2 + \frac{e}{c}\mathbf{A} \quad \text{with} \quad \mathbf{A} = \frac{1}{2}(\mathbf{B} \wedge \mathbf{r}),$$

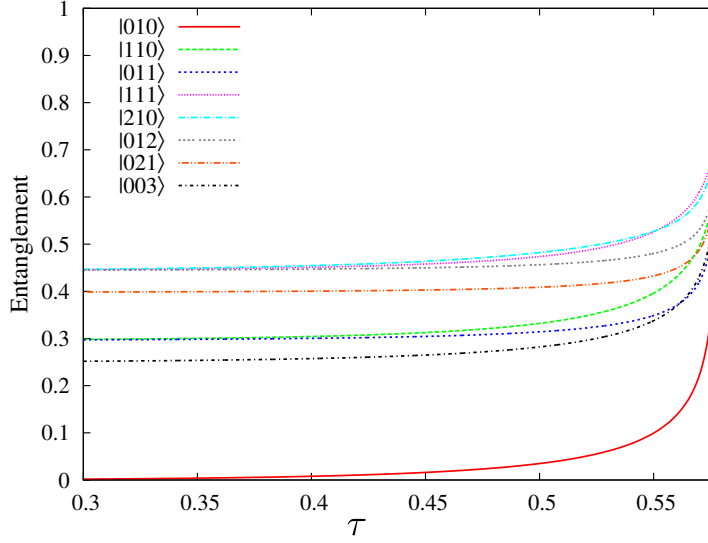


Figure 9.2: Entanglement of the ground, first and second excited states of one-dimensional Moshinsky atom with three interacting electrons for the repulsive case. All depicted quantities are dimensionless.

being \mathbf{B} the magnetic field. Assuming that the magnetic field is homogeneous and have z -axis direction, that is $\mathbf{B} = B\hat{z}$, we can write:

$$p_i^2 \rightarrow p_i^2 + \left(\frac{eB}{2c}\right)^2 (x_i^2 + y_i^2) + \frac{eB}{c}(x_i p_{yi} - y_i p_{xi}) \quad \text{with } i = 1, 2. \quad (9.25)$$

By replacing (9.25) in the Hamiltonian H_M and setting atomic units ($m_e = \hbar = 1$, $c = 1/\alpha$), we obtain

$$H = \frac{1}{2}(p_1^2 + p_2^2) + \frac{\omega^2}{2}(r_1^2 + r_2^2) + \frac{b^2}{2}(x_1^2 + y_1^2 + x_2^2 + y_2^2) + b(L_{1z} + L_{2z}) \pm \frac{\lambda^2}{2}(\mathbf{r}_1 - \mathbf{r}_2)^2 \quad (9.26)$$

where

$$b = \frac{B}{2c} \quad ; \quad L_{iz} = (x_i p_{yi} - y_i p_{xi}) \quad \text{and} \quad \mathbf{r}_i = (x_i, y_i, z_i) \quad \text{with } i = 1, 2. \quad (9.27)$$

We change the variables to the center of mass (CM) and relative coordinates, *i.e.*

$$\mathbf{R} = \frac{1}{\sqrt{2}}(\mathbf{r}_1 + \mathbf{r}_2) \quad \text{and} \quad \mathbf{r} = \frac{1}{\sqrt{2}}(\mathbf{r}_1 - \mathbf{r}_2) \quad (9.28)$$

respectively. This transformation satisfies the relations

$$p_1^2 + p_2^2 = p_R^2 + p_r^2$$

and

$$L_{1z} + L_{2z} = L_{Rz} + L_{rz} = (R_x p_{Ry} - R_y p_{Rx}) + (r_x p_{ry} - r_y p_{rx}), \quad (9.29)$$

and therefore, introducing Eqs. (9.28) and (9.29) in the Hamiltonian (9.26) we obtain

$$H = \frac{1}{2}(p_R^2 + p_r^2) + \frac{\omega^2}{2}(R^2 + r^2) + \frac{b^2}{2}(R_x^2 + R_y^2 + r_x^2 + r_y^2) + b(L_{Rz} + L_{rz}) \pm \frac{\lambda^2}{2}r^2, \quad (9.30)$$

which is separable in the CM and relative coordinates, so that we can express the Hamiltonian H as

$$H = H_R + H_r$$

where

$$H_R = \frac{1}{2}(p_{R_x}^2 + p_{R_y}^2) + \frac{\omega^2 + b^2}{2}(R_x^2 + R_y^2) + \frac{1}{2}(p_{R_z}^2 + \omega^2 R_z^2) + bL_{Rz} \quad (9.31)$$

and

$$H_r = \frac{1}{2}(p_{r_x}^2 + p_{r_y}^2) + \frac{\omega^2 + b^2}{2}(r_x^2 + r_y^2) + \frac{1}{2}(p_{r_z}^2 + \omega^2 r_z^2) + bL_{rz} \pm \frac{\lambda^2}{2}r^2. \quad (9.32)$$

Introducing a dilation canonical transformation for the Hamiltonian H_R , namely

$$\begin{aligned} p'_{Ri} &= (\omega^2 + b^2)^{-\frac{1}{4}} p_{Ri}, \quad R'_i = (\omega^2 + b^2)^{\frac{1}{4}} R_i \quad \text{with } i = x, y \\ p'_{Rz} &= \omega^{-\frac{1}{2}} p_{Rz}, \quad R'_z = \omega^{\frac{1}{2}} R_z, \end{aligned} \quad (9.33)$$

and

$$\begin{aligned} p'_{ri} &= (\omega^2 + b^2 \pm \lambda^2)^{-\frac{1}{4}} p_{ri}, \quad r'_i = (\omega^2 + b^2 \pm \lambda^2)^{\frac{1}{4}} r_i \quad \text{with } i = x, y \\ p'_{rz} &= (\omega^2 \pm \lambda^2)^{-\frac{1}{4}} p_{rz}, \quad r'_z = (\omega^2 \pm \lambda^2)^{\frac{1}{4}} r_z, \end{aligned} \quad (9.34)$$

we obtain

$$H'_R = \frac{H_R}{\omega} = \frac{1}{2} \left(1 + \frac{b^2}{\omega^2} \right)^{\frac{1}{2}} (p'^2_{R_x} + p'^2_{R_y} + R'^2_x + R'^2_y) + \frac{1}{2}(p'^2_{R_z} + R'^2_z) + \frac{b}{\omega} L_{R'z}, \quad (9.35)$$

$$\begin{aligned} H'_r &= \frac{H_r}{(\omega^2 \pm \lambda^2)^{\frac{1}{2}}} = \frac{1}{2} \left(1 + \frac{b^2}{\omega^2 \pm \lambda^2} \right)^{\frac{1}{2}} (p'^2_{r_x} + p'^2_{r_y} + r'^2_x + r'^2_y) + \\ &\quad + \frac{1}{2}(p'^2_{r_z} + r'^2_z) + \frac{b}{(\omega^2 \pm \lambda^2)^{\frac{1}{2}}} L_{r'z}. \end{aligned} \quad (9.36)$$

The Hamiltonian describing the whole system will be therefore

$$H = \omega H'_R + (\omega^2 \pm \lambda^2)^{\frac{1}{2}} H'_r. \quad (9.37)$$

Using cylindrical coordinates, that is

$$\rho_R = (R'^2_x + R'^2_y)^{\frac{1}{2}}, \quad \varphi_R = \arctan \left(\frac{R'_y}{R'_x} \right), \quad z_R = R'_z, \quad (9.38)$$

$$\rho_r = (r'^2_x + r'^2_y)^{\frac{1}{2}}, \quad \varphi_r = \arctan \left(\frac{r'_y}{r'_x} \right), \quad z_r = r'_z, \quad (9.39)$$

we immediately have the eigenfunctions of H'_R y H'_r , given by [262]

$$\Psi_{\nu_R m_R n_R}(\mathbf{R}) = \frac{1}{\sqrt{2\pi}} R_{\nu_R |m_R|}(\rho_R) e^{im_R \varphi_R} \chi_{n_R}(z_R), \quad (9.40)$$

$$\Psi_{\nu_r m_r n_r}(\mathbf{r}) = \frac{1}{\sqrt{2\pi}} R_{\nu_r |m_r|}(\rho_r) e^{im_r \varphi_r} \chi_{n_r}(z_r), \quad (9.41)$$

where $R_{\nu|m|}(\rho)$ are the two-dimensional oscillator radial eigenstates, whose normalized expressions are

$$R_{\nu|m|}(\rho) = \left(\frac{2\nu!}{(\nu + |m|)!} \right)^{\frac{1}{2}} \rho^{|m|} e^{-\frac{\rho}{2}} \mathcal{L}_{\nu}^{|m|}(\rho^2) \quad (9.42)$$

being $\mathcal{L}_{\nu}^{|m|}$ the Laguerre polynomials, with the quantum numbers ν and m taking the values $\nu = 0, 1, 2, \dots$ and $m = 0, \pm 1, \pm 2, \dots$ respectively. The functions $\chi_{\tau}(z)$ are the eigenstates of the unidimensional harmonic oscillator which are given by

$$\chi_n(z) = \left(\frac{1}{2^n n! \pi^{\frac{1}{2}}} \right)^{\frac{1}{2}} e^{-\frac{z^2}{2}} \mathcal{H}_n(z) \quad (9.43)$$

where $\mathcal{H}_n(z)$ are the Hermite polynomials and n takes the values $n = 0, 1, 2, \dots$

The final eigenstates of the Hamiltonian (9.37) will be

$$|\nu_R m_R n_R, \nu_r m_r n_r\rangle = |\nu_R m_R n_R\rangle \otimes |\nu_r m_r n_r\rangle \quad (9.44)$$

and the wave function

$$\begin{aligned} \Psi_{\nu_R m_R n_R, \nu_r m_r n_r}(\mathbf{r}_1, \mathbf{r}_2) &= \Psi_{\nu_R m_R n_R, \nu_r m_r n_r}(\mathbf{R}, \mathbf{r}) |J| = \\ &= \langle \mathbf{r}_1; \mathbf{r}_2 | \nu_R m_R n_R, \nu_r m_r n_r \rangle \end{aligned} \quad (9.45)$$

where J is the Jacobian of the canonical transformation given by Eqs. (9.33) and (9.34).

The eigenvalues of the harmonic oscillators in one and two dimensions are $(n + \frac{1}{2})$ and $(2\nu + |m| + 1)$, respectively. Defining the quantities

$$y_R = \left(1 + \frac{b^2}{\omega^2} \right)^{\frac{1}{2}} + \frac{b}{\omega} \quad \text{and} \quad y_r = \left(1 + \frac{b^2}{\omega^2 \pm \lambda^2} \right)^{\frac{1}{2}} + \frac{b}{(\omega^2 \pm \lambda^2)^{\frac{1}{2}}}, \quad (9.46)$$

we obtain the eigenvalues of the Hamiltonians H'_R and H'_r in the form

$$\begin{aligned} E'_{\nu_R m_R n_R}(y_R) &= \frac{y_R}{2} (2\nu_R + |m_R| + m_R + 1) + \\ &+ \frac{1}{2y_R} (2\nu_R + |m_R| - m_R + 1) + \left(n_R + \frac{1}{2} \right), \end{aligned} \quad (9.47)$$

$$\begin{aligned} E'_{\nu_r m_r n_r}(y_r) &= \frac{y_r}{2} (2\nu_r + |m_r| + m_r + 1) + \\ &+ \frac{1}{2y_r} (2\nu_r + |m_r| - m_r + 1) + \left(n_r + \frac{1}{2} \right). \end{aligned} \quad (9.48)$$

Then, the total energy of the system, which is the eigenvalue of the Hamiltonian H , is given by

$$E_{\nu_R m_R n_R \nu_r m_r n_r}(\omega, b) = \omega E'_{\nu_R m_R n_R}(y_R) + (\omega^2 \pm \lambda^2)^{\frac{1}{2}} E'_{\nu_r m_r n_r}(y_r). \quad (9.49)$$

We calculate the exact form of the trace of the reduced density matrix associated to a general eigenfunction (9.44) of the two-electron Moshinsky system with magnetic field for the ground and the first excited states in n_R, n_r, ν_R and ν_r . Next we are going to provide and discuss the corresponding amounts of entanglement exhibited by each eigenstate (arising from the evaluation of the aforementioned integrals). In what follows, $\varepsilon_{\nu_R m_R n_R, \nu_r m_r n_r}$ denotes value of ε when evaluated on the state $|\nu_R m_R n_R, \nu_r m_r n_r\rangle$ that we also will denote $|\nu_R m_R n_R, \nu_r m_r n_r\rangle_{Rr}$. In order to obtain physically acceptable solutions in the case of a repulsive interaction between the particles we have to take into account the constraint $\lambda < \omega$.

9.3.1 Ground state

The ground state is symmetric in coordinates, so we must combine it with the only antisymmetric spin function to ensure the antisymmetry of the wave function. Let $\sigma = \frac{b}{\omega}$ and $\tau = \frac{\lambda}{\omega}$ as before. In this case we have

$$\begin{aligned} \varepsilon_{000,000} = 1 - \frac{2 + 2\sigma^2 + \tau^2 - 2\sqrt{1 + \sigma^2}\sqrt{1 + \sigma^2 + \tau^2}}{\tau^4 (1 + \sqrt{1 + \tau^2})} &\times \\ &\sqrt{\frac{1}{1 - \frac{4}{\tau^2} + \frac{4+5\tau^2}{\tau^2\sqrt{1+\tau^2}}}} \sqrt{\frac{\tau^2+2(1+3\sqrt{1+\tau^2})}{1+\sqrt{1+\tau^2}}} \\ &\times 8\sqrt{1 + \sigma^2}\sqrt{1 + \tau^2}\sqrt{1 + \sigma^2 + \tau^2}. \quad (9.50) \end{aligned}$$

Decoupling the system makes $\varepsilon_{000,000} = 0$, therefore in the decoupled system the ground state is not entangled. With maximum coupling $\tau \rightarrow \infty$ ($\tau \rightarrow 1$) in the attractive (repulsive) case, we find that $\varepsilon_{000,000} = 1$; that is, the entanglement measure is maximum. The behavior of entanglement as a function of the parameters τ and σ is shown in Figure 9.3. Figures 9.3a and 9.3b correspond, respectively, to the attractive and the repulsive cases. More detailed information concerning the asymptotic behavior of entanglement is provided in Figure 9.4.

From Fig. (9.3) it can be observed that in the limit of large magnetic fields, that is $\sigma \rightarrow \infty$, the entanglement reaches a constant value which depends on the relative strength of interaction given by the parameter τ , i.e.

$$\lim_{\sigma \rightarrow \infty} \varepsilon_{000,000} = 1 - \frac{8(1 + \tau^2) \left(2 + \tau^2 - 2\sqrt{1 + \tau^2}\right)}{\tau^4 (1 + \sqrt{1 + \tau^2})} \sqrt{\frac{2 + \tau^2 + 6\sqrt{1 + \tau^2}}{1 + \sqrt{1 + \tau^2}}} \sqrt{\frac{1}{1 - \frac{4}{\tau^2} + \frac{4+5\tau^2}{\tau^2\sqrt{1+\tau^2}}}} \quad (9.51)$$

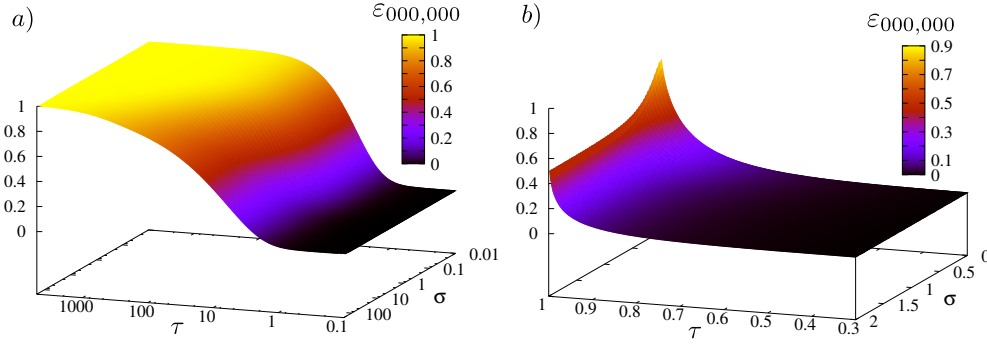


Figure 9.3: Entanglement of the ground state of the three-dimensional Moshinsky atom with two interacting electrons and a magnetic field. a) Attractive interaction, b) Repulsive interaction. All depicted quantities are dimensionless.

9.3.2 First excited states

We study the excited states in ν_R , ν_r and n_R that have symmetric coordinates wave functions and therefore must be combined with the antisymmetric or antiparallel spin function. We also study in this section the excited state in n_r which is antisymmetric in coordinates and therefore, it can be combined with parallel or antiparallel spin functions. Excited eigenstates in ν_R and ν_r and in n_R and n_r have the same energy respectively when the system is decoupled. In this case we obtain

$$\begin{aligned} \varepsilon_{000,100} = \varepsilon_{100,000} &= 1 - \frac{(8 + 8\sigma^4 + 8\tau^2 + \tau^4 + 8\sigma^2(2 + \tau^2))}{\sqrt{\frac{1+\tau^2+\sqrt{1+\tau^2}}{2+\tau^2+6\sqrt{1+\tau^2}}} \sqrt{\frac{2+\tau^2+6\sqrt{1+\tau^2}}{1+\sqrt{1+\tau^2}}}} \times \\ &\times \frac{4\sqrt{1+\sigma^2}\sqrt{1+\tau^2}\sqrt{1+\sigma^2+\tau^2}}{(1+\sqrt{1+\tau^2}) (\sqrt{1+\sigma^2+\sqrt{1+\sigma^2+\tau^2}})^6}, \quad (9.52) \\ \varepsilon_{000,001} = \varepsilon_{001,000} &= 1 - \alpha \frac{2\sqrt{1+\sigma^2}\sqrt{1+\sigma^2+\tau^2} (6 + 3\tau^2 + 2\sqrt{1+\tau^2})}{(1+\sqrt{1+\tau^2})^3 (\sqrt{1+\sigma^2+\sqrt{1+\sigma^2+\tau^2}})^2} \times \\ &\times \sqrt{\frac{1+\tau^2+\sqrt{1+\tau^2}}{2+\tau^2+6\sqrt{1+\tau^2}}} \sqrt{\frac{2+\tau^2+6\sqrt{1+\tau^2}}{1+\sqrt{1+\tau^2}}} \quad (9.53) \end{aligned}$$

where $\alpha = 1(2)$ for antiparallel (parallel) spins.

Taking the decoupled limit system, we obtain the following entanglement values regardless of the magnetic field value: $\varepsilon_{100,000}^a = \varepsilon_{000,100}^a = \frac{3}{4}$ and $\varepsilon_{001,000}^a = \varepsilon_{000,001}^a = \frac{1}{2}$ for the first excited states with antiparallel spin, which are entangled, and $\varepsilon_{000,001}^p = 0$ for the only possible state with parallel spin. We have used ε^a (ε^p) to indicate the entanglement of states with antiparallel (parallel) spin.

On the other hand, with maximum coupling we find that $\varepsilon_{100,000}^a = \varepsilon_{000,100}^a = \varepsilon_{001,000}^a = \varepsilon_{000,001}^a = \varepsilon_{000,001}^p = 1$, so the entanglement is maximum.

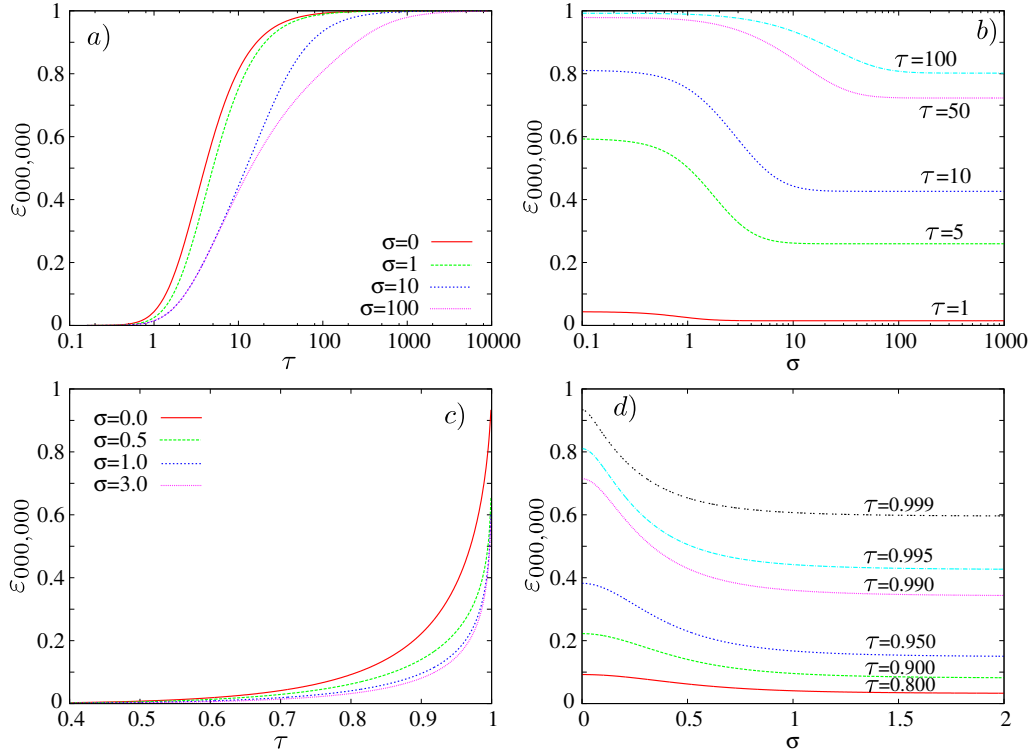


Figure 9.4: Entanglement of the ground state of the three-dimensional Moshinsky atom with two interacting electrons in a uniform magnetic field, a) as a function of τ for different values of σ with attractive interaction, b) as a function of σ for different values of τ with attractive interaction, c) as a function of τ for different values of σ with repulsive interaction and d) as a function of σ for different values of τ with repulsive interaction. All depicted quantities are dimensionless.

In the limit for large magnetic fields, i.e. $\sigma \rightarrow \infty$, we obtain

$$\begin{aligned} \lim_{\sigma \rightarrow \infty} \varepsilon_{100,000} = \lim_{\sigma \rightarrow \infty} \varepsilon_{000,100} &= 1 - \frac{3\sqrt{1+\tau^2}}{2(1+\sqrt{1+\tau^2})} \times \\ &\times \left(\sqrt{\frac{1+\tau^2+\sqrt{1+\tau^2}}{2+\tau^2+6\sqrt{1+\tau^2}}} \sqrt{\frac{2+\tau^2+6\sqrt{1+\tau^2}}{1+\sqrt{1+\tau^2}}} \right)^{-1}, \end{aligned} \quad (9.54)$$

$$\begin{aligned} \lim_{\sigma \rightarrow \infty} \varepsilon_{001,000} = \lim_{\sigma \rightarrow \infty} \varepsilon_{000,001} &= 1 - \alpha \frac{3(6+3\tau^2+2\sqrt{1+\tau^2})}{(1+\sqrt{1+\tau^2})^3} \times \\ &\times \sqrt{\frac{1+\tau^2+\sqrt{1+\tau^2}}{2+\tau^2+6\sqrt{1+\tau^2}}} \sqrt{\frac{2+\tau^2+6\sqrt{1+\tau^2}}{1+\sqrt{1+\tau^2}}} \end{aligned} \quad (9.55)$$

which, as we observe, depends on the value of the interaction.

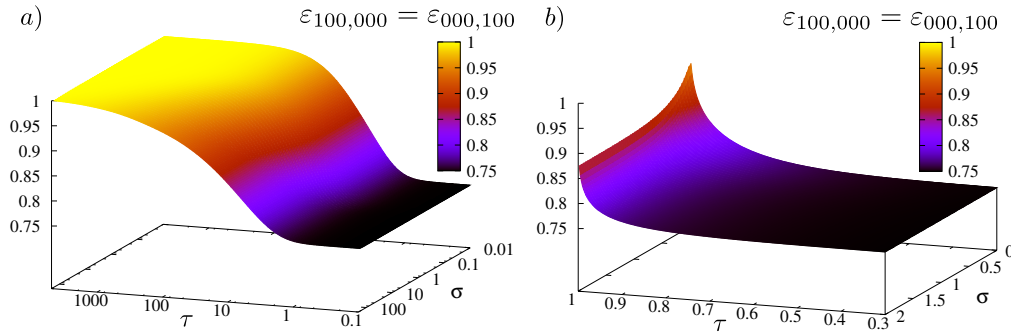


Figure 9.5: Entanglement of the first excited state in ν_R and ν_r of the three dimensional Moshinsky atom with two interacting electrons and magnetic field. a) Attractive interaction, b) Repulsive interaction. All depicted quantities are dimensionless.

The behavior of the entanglement exhibited by these states is shown in Figure 9.5 (for excited states with $\nu_r = 1$ and $\nu_R = 1$) and in Figure 9.6 (for excited states with $n_r = 1$ and $n_R = 1$).

It transpires from the calculations summarized in Figures 9.3-9.6 that the amount of entanglement exhibited by the eigenstates of the Moshinsky atom tends to decrease with the strength of the magnetic field. To understand the physics behind this trend let us first recall the general way in which entanglement depends on the strength of the interaction between the two particles constituting the system. Entanglement tends to increase with the relative strength of the interaction. However, it is important to stress that the determining factor here is not the “absolute” strength of the interaction, but its strength as compared with the strength of the external confining potential. In other words, entanglement increases both if one increases the strength of the interaction keeping constant the external potential or, alternatively, if the strength of the confining potential is weakened while keeping constant the interaction. These general trends have been observed in all the atomic models where entanglement has been studied in detail: the Moshinsky model, the Crandall model, and also in Helium and in Helium-like atomic systems [238, 245]. For instance, when one considers decreasing values of the nuclear charge Z in Helium-like systems (weakening the Coulombic confining potential) the entanglement of the system’s ground state increases [245]. These general patterns admit a clear and intuitive physical interpretation. When the external confining potential becomes physically dominant (as compared with the interaction) the behavior of the system resembles the behavior of a system of independent, non-interacting particles, and entanglement tends to decrease. On the other hand, when the interaction is dominant (as compared with the confining potential) the system’s behavior departs from that of a system of non-interacting particles and entanglement tends to increase.

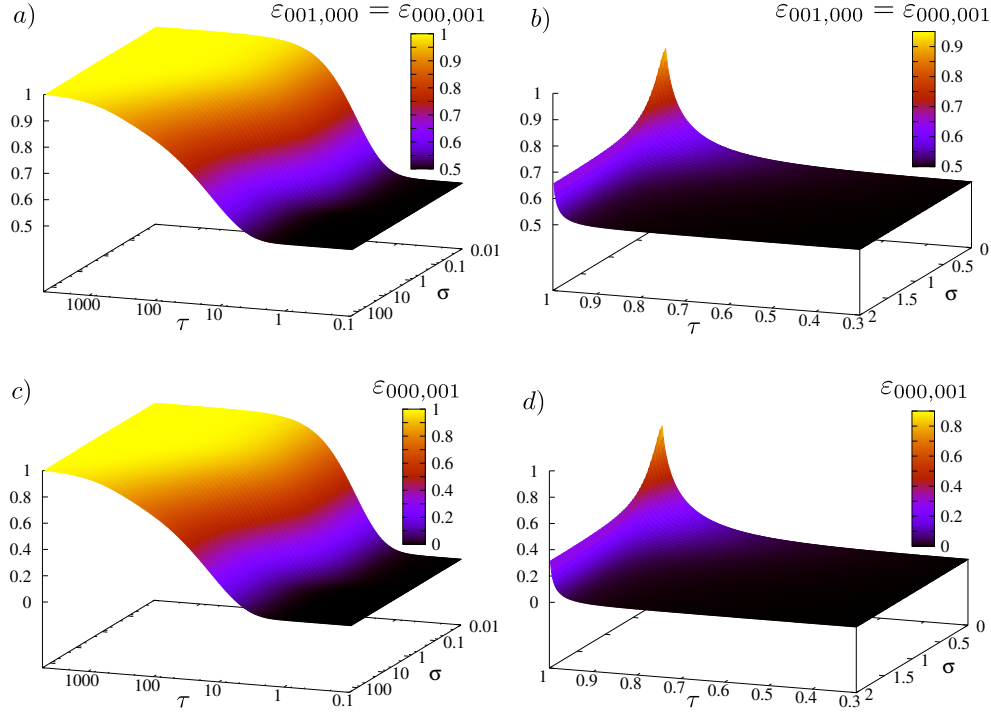


Figure 9.6: Entanglement of the first excited state in n_R and n_r of the three dimensional Moshinsky atom with two interacting electrons and magnetic field. a) Attractive interaction, antiparallel spin, b) Repulsive interaction, antiparallel spin, c) Attractive interaction, parallel spins, d) Repulsive interaction, parallel spins. All depicted quantities are dimensionless.

9.3.3 Confining effect of the magnetic field

The dependence of entanglement with the magnetic field can now be physically understood. This dependence follows the same general patterns explained above. Indeed, the basic fact about the magnetic field in the Moshinsky model (which of course is a common external field acting on both particles) determining its effect upon entanglement is the following: increasing the strength of the magnetic field tends to increase the confining effect of the combined external fields (that is, the harmonic external field and the magnetic field characterized by ω and b respectively). To illustrate this basic property let us briefly consider the behavior of a single particle (in $3D$ -space) under the combined effects of the external fields (harmonic field plus uniform magnetic field) involved in the Moshinsky model that we study here. The probability density, in cylindrical coordinates, corresponding to a pure state $|\nu mn\rangle$ of the one-particle system is given by

$$\rho_{\nu,m,n}(r_c, \theta, z) = \frac{2^{-n} \nu! \sqrt{\omega} \Lambda_b^{(1+|m|)}}{\pi^{3/2} n! (\nu + |m|)!} e^{-z^2 \omega - r_c^2 \Lambda_b} r_c^{2|m|} \left(\mathcal{H}_n(z\sqrt{\omega}) \mathcal{L}_\nu^{|m|}(\Lambda_b r_c^2) \right)^2 \quad (9.56)$$

where $\Lambda_b = \sqrt{b^2 + \omega^2}$, $r_c = \sqrt{x^2 + y^2}$ and $\theta = \arctan\left(\frac{y}{x}\right)$.

A direct way to study the dependence of the confinement of this particle on the strength of the magnetic field is to compute the entropy of the spatial probability density and determine its behavior with the magnetic field (decreasing values of the entropy correspond to increasing confinement). The linear and von Neumann entropy for single-particle density functions correspond to the disequilibrium, Eq. (1.7), and the Shannon entropy, Eq. (1.4), discussed in Part I of the Thesis, as follows:

$$S^{(L)} = 1 - \text{Tr}[\rho^2] \rightarrow 1 - D[\rho] = 1 - \int [\rho(\mathbf{r})]^2 d\mathbf{r} \quad (9.57)$$

$$S^{(vN)} = -\text{Tr}[\rho \ln(\rho)] \rightarrow S[\rho] = - \int \rho(\mathbf{r}) \ln[\rho(\mathbf{r})] d\mathbf{r}. \quad (9.58)$$

For the ground state $|gs\rangle = |000\rangle$ of the probability density (9.56), the above quantities are given, respectively, by

$$S_{|gs\rangle}^{(L)}(\omega, b) = 1 - \frac{\sqrt{\omega} \sqrt{b^2 + \omega^2}}{2\sqrt{2}\pi^{3/2}} \quad (9.59)$$

and

$$S_{|gs\rangle}^{(vN)}(\omega, b) = \frac{1}{2} \left[3(1 + \ln \pi) - \ln \omega - \ln(b^2 + \omega^2) \right]. \quad (9.60)$$

The entropies $S_{|gs\rangle}^{(L)}$ and $S_{|gs\rangle}^{(vN)}$ describing the spatial “spreading” of the probability density associated with ground state wave function are plotted against the magnetic field in Figure 9.7a. We can see from this figure how the entropy is a monotonically decreasing function of the magnetic field. This also occurs for the firsts excited states where we found for the lineal entropies

$$S_{|001\rangle}^L(\omega, b) = 1 - \frac{3\sqrt{\omega} \sqrt{b^2 + \omega^2}}{8\sqrt{2}\pi^{3/2}} \quad (9.61)$$

$$S_{|100\rangle}^L(\omega, b) = S_{|010\rangle}^L(\omega, b) = 1 - \frac{\sqrt{\omega} \sqrt{b^2 + \omega^2}}{4\sqrt{2}\pi^{3/2}}, \quad (9.62)$$

see figure Figure 9.7b. As shown in these expressions, Eqs. (9.59)-(9.62), the entropy is a decreasing function of b as well as of ω , showing that the harmonic potential is also confining. Since they are information measures of a single-particle density functions describing not only correlation properties between two subsystems, as entanglement does, but describing the global spreading of the density within the whole space, it is not surprising that the parameters ω , b and λ (as we shall see in Eq. (9.65) below), can not be rescaled in such entropies as in the entanglement obtained in previous Sections 9.3.1 and 9.3.2. These linear (9.58) and von Neumann (9.57) entropies, in contrast to those computed using single-particle reduced density matrices quantifying the entanglement, can assume values in the range $S^{(L)} \in [1, -\infty]$ and $S^{(vN)} \in \mathbb{R}$ respectively.

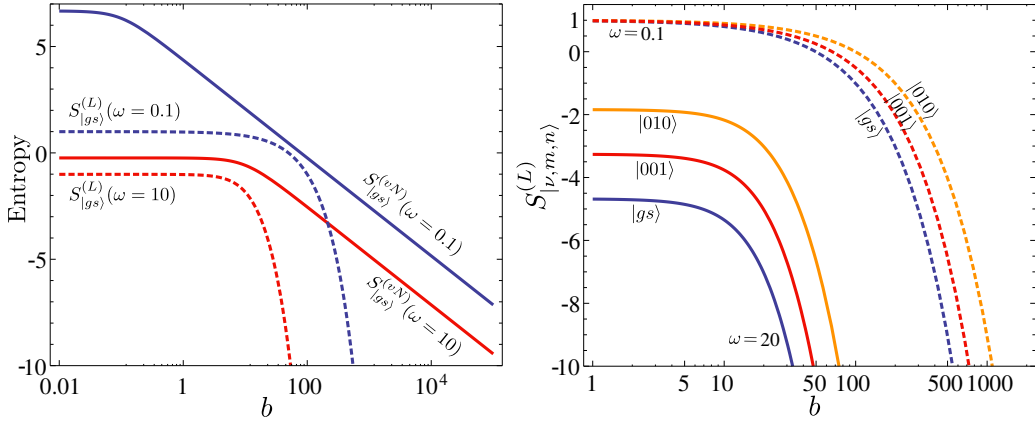


Figure 9.7: a) Linear (dashed lines) and von Neumann (solid lines) entropies of the ground state for $\omega = 0.1$ (blue lines) and $\omega = 10$ (red lines) b) linear entropy of the ground (blue lines) and first excited states $|001\rangle$ (red lines) and $|010\rangle$ (orange lines) as a function of b for $\omega = 0.1$ (dashed lines) and $\omega = 20$ (solid lines)

In what follows, we show how the confinement also occurs in the system given by Eq. (9.26) studied in the previous sections where more than one particle are involved. The ground state, describing this system, is given by the equation (9.44) as $|gs\rangle = |000, 000\rangle$. Computing the single-particle density function as described in Appendix A, given in this case by

$$\rho_{gs}^{(1)}(\mathbf{r}_1) = \int_{\mathbb{R}} |\Psi_{000,000}(\mathbf{r}_1, \mathbf{r}_2)|^2 d\mathbf{r}_2 \quad (9.63)$$

where $\Psi_{000,000}$ is the wavefunction (9.45), we obtain

$$\rho_{gs}^{(1)}(r_{1c}, \theta_1, z_1) = \frac{2\sqrt{2}}{\pi^{3/2}} \frac{\sqrt{\omega\Lambda_\lambda\Lambda_b\Lambda_{b\lambda}}}{\sqrt{\omega + \Lambda_\lambda(\Lambda_b + \Lambda_{b\lambda})}} e^{-\frac{2r_{1c}^2\Lambda_b\Lambda_{b\lambda}}{\Lambda_b + \Lambda_{b\lambda}} - \frac{2z_1^2\omega(\lambda^2 + \omega(\omega - \Lambda_\lambda))}{\lambda^2}}, \quad (9.64)$$

where $\Lambda_\lambda = \sqrt{\lambda^2 + \omega^2}$, $\Lambda_{b\lambda} = \sqrt{b^2 + \lambda^2 + \omega^2}$ and $r_{1c} = \sqrt{x_1^2 + y_1^2}$ and whereby the linear entropy is obtained as follows:

$$S_{|000,000\rangle}^L(\omega, b, \lambda) = 1 - \frac{(\lambda^2\omega\Lambda_b^2\Lambda_\lambda\Lambda_{b\lambda}^2)}{\sqrt{\omega(\lambda^2 + \omega(\omega - \Lambda_\lambda))}} \times \left(\pi^{3/2}(\omega + \Lambda_\lambda)(\Lambda_b + \Lambda_{b\lambda})^2 (\lambda^2\Lambda_b + b^2(\Lambda_b - \Lambda_{b\lambda}) + \omega^2(\Lambda_b - \Lambda_{b\lambda})) \right)^{-1}. \quad (9.65)$$

It can be clearly appreciated that confinement increases with the intensity of the magnetic field b and with the harmonic potential ω as shown in Fig. 9.8a) and b). On the contrary, the interaction between particles λ has a confining ability limited by both the magnetic field and the harmonic potential. As we can see in Fig. 9.8c), the linear entropy

$S_{|000,000\rangle}^L$ decreases with interaction to a finite limit which depends on b . A similar behavior is observed for different values of ω . According to what we saw in the previous sections 9.3.1 and 9.3.2, the confinement effect of the interaction does not jeopardize the correlations between the two particles since for large values of λ the entanglement is large and confinement finite.

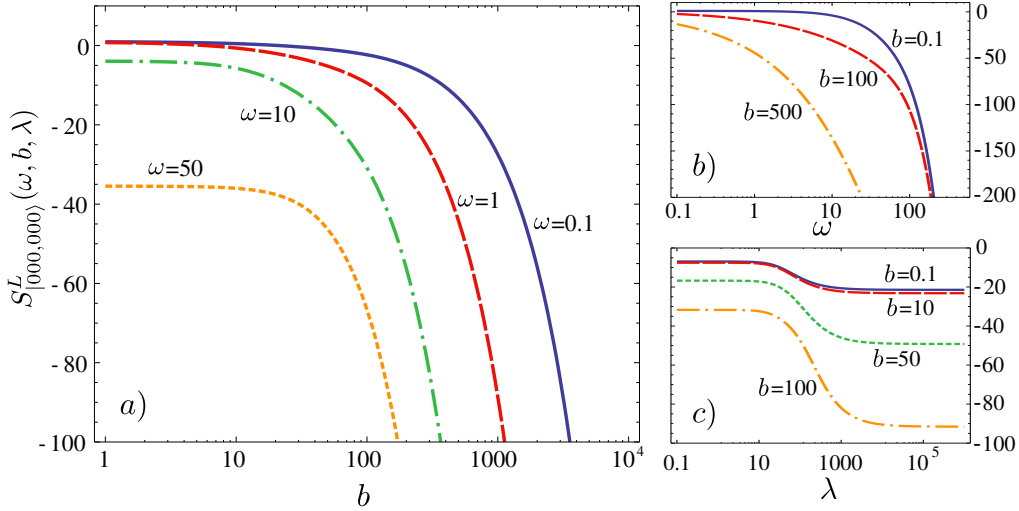


Figure 9.8: Linear entropy of the single-particle ground state density describing the system (9.26) a) as a function of b with $\lambda = 100$ for different values of ω , b) as a function of ω with $\lambda = 100$ for different values of b , and c) as a function of the interaction between particles λ with $\omega = 25$ for different values of b .

The single-particle spatial probability densities of the two-particle system, corresponding to the eigenfunctions of the Moshinsky system (9.26), also become more confined when the magnetic field becomes more intense. As already explained in the previous Section 9.3.2, this behavior is consistent with the decrease of entanglement with an increasing magnetic field.

9.4 Perturbative Approach

In this section we consider a perturbative approach to the two previously studied models, regarding the term that describe the interaction (between the three or two electrons) as a small perturbation ($\lambda^2 \sim 0$). Let us consider both systems governed by a Hamiltonian of the form

$$H = H_0 + \lambda^2 H', \quad (9.66)$$

where the unperturbed Hamiltonian H_0 takes different forms for each case (see Eqs. (9.70) and (9.80)). H_0 corresponds to three independent (non-interacting) particles and two independent particles in a magnetic field, respectively, and $\lambda^2 H'$ describes the interaction between the electrons, being λ a small parameter. A perturbative treatment of this system

involves an expansion of its eigenenergies and eigenstates in terms of powers of λ^2 . If this approach is valid we expect the gross properties of the energy spectrum to be given by the eigenvalues of the unperturbed Hamiltonian. It is clear that within this scenario the leading zeroth-order contribution to the energy spectrum is independent of the detailed structure of the perturbation H' . However, the situation is different when, instead of the energy, we calculate the entanglement of the system's eigenstates. When the unperturbed energy eigenvalues are degenerate the leading (zeroth-order) contribution to the eigenfunction's entanglement does depend, in general, on the details of the perturbation.

Let us consider an m -fold degenerate energy level of H_0 , with an associated set of m orthonormal eigenstates $|\psi_j\rangle$, $j = 1, \dots, m$. Since H_0 describes non-interacting particles, the m eigenstates $|\psi_j\rangle$ can always be chosen to be Slater determinants written in terms of a family of orthonormal single-particle states $|\phi_j^{(1,2,3)}\rangle$ in the case of three particles and in terms of $|\phi_j^{(1,2)}\rangle$ in the case of two particles. So we have for a three-particle system

$$|\psi_j\rangle = \frac{1}{\sqrt{6}} \left(|\phi_j^{(1)}\rangle |\phi_j^{(2)}\rangle |\phi_j^{(3)}\rangle - |\phi_j^{(1)}\rangle |\phi_j^{(3)}\rangle |\phi_j^{(2)}\rangle + |\phi_j^{(2)}\rangle |\phi_j^{(3)}\rangle |\phi_j^{(1)}\rangle - |\phi_j^{(2)}\rangle |\phi_j^{(1)}\rangle |\phi_j^{(3)}\rangle + |\phi_j^{(3)}\rangle |\phi_j^{(1)}\rangle |\phi_j^{(2)}\rangle - |\phi_j^{(3)}\rangle |\phi_j^{(2)}\rangle |\phi_j^{(1)}\rangle \right),$$

and for a two-particle system

$$|\psi_j\rangle = \frac{1}{\sqrt{2}} \left(|\phi_j^{(1)}\rangle |\phi_j^{(2)}\rangle - |\phi_j^{(2)}\rangle |\phi_j^{(1)}\rangle \right).$$

All the members of the subspace \mathcal{H}_s spanned by the states $|\psi_j\rangle$ are eigenstates of H_0 corresponding to the same eigenenergy. The different members of this subspace have, in general, different amounts of entanglement. Typically, the interaction H' will lift the degeneracy, at least partially, of the degenerate energy level. If we solve the eigenvalue problem corresponding to the (perturbed) Hamiltonian H and take the limit $\lambda \rightarrow 0$, the perturbation H' will "choose" one particular basis $\{|\psi'_k\rangle_{\lambda \rightarrow 0}\}$ among the infinite possible basis of \mathcal{H}_s . The states constituting this special basis will be entangled in general. These states are of the form [289]

$$|\psi'_k\rangle_{\lambda \rightarrow 0} = \sum_{j=1}^m c_{kj} |\psi_j\rangle, \quad (9.67)$$

where the m -dimensional vectors $v_k^T = (c_{k1}, \dots, c_{km})$ are the eigenvectors of the $m \times m$ \tilde{H} matrix with elements given by

$$\tilde{H}_{ij} = \langle \psi_i | H' | \psi_j \rangle. \quad (9.68)$$

It is then clear that, in the limit $\lambda \rightarrow 0$, the eigenstates of H will in general be entangled.

Let \tilde{m} be the number of different single-particle states within the family $\{|\phi_j^{(1,2,3)}\rangle, 1, \dots, m\}$ or $\{|\phi_j^{(1,2)}\rangle, 1, \dots, m\}$. \tilde{m} tends to increase with m which, in turn, tends to increase with energy; that is, \tilde{m} tends to increase as one considers higher excited states. This explains (at least in part) why the range of entanglement values available to the

eigenstates $\{|\psi'_k\rangle_{\lambda \rightarrow 0}\}$ tends to increase with energy. Indeed, the amount of entanglement that can be achieved for a given energy of a N -fermion system admits an upper bound given by

$$\varepsilon_{SL} = 1 - \frac{N}{\tilde{m}}, \quad (9.69)$$

9.4.1 Moshinsky model with three electrons

Let the unperturbed Hamiltonian be

$$H_0 = -\frac{1}{2} \frac{\partial^2}{\partial x_1^2} - \frac{1}{2} \frac{\partial^2}{\partial x_2^2} - \frac{1}{2} \frac{\partial^2}{\partial x_3^2} + \frac{1}{2} \omega^2 x_1^2 + \frac{1}{2} \omega^2 x_2^2 + \frac{1}{2} \omega^2 x_3^2 \quad (9.70)$$

and the perturbation

$$\lambda^2 H' = \lambda^2 \frac{1}{2} [(x_1 - x_2)^2 + (x_2 - x_3)^2 + (x_1 - x_3)^2]. \quad (9.71)$$

Then, we have $H = H_0 + \lambda^2 H'$. When $\lambda = 0$ the model consists of three-independent harmonic oscillators with the same natural frequency. Let $|n\pm\rangle$ ($n = 0, 1, 2, \dots$) be the eigenstates of each of these oscillators. For the first excited state which is four-fold degenerate, let $\{|0, \pm\rangle, |1, \pm\rangle, |2, \pm\rangle\}$ be the single-particle orthonormal basis. Then, for $\lambda = 0$, we can choose the four eigenstates with zero entanglement, all of them with the same energy as $|011\rangle_{R_1 R_2 R_3}$ and $|110\rangle_{R_1 R_2 R_3}$:

$$\begin{aligned} |\psi_1\rangle &= |0+, 0-, 2+| \\ |\psi_2\rangle &= |0+, 0-, 2-| \\ |\psi_3\rangle &= |0+, 1+, 1-| \\ |\psi_4\rangle &= |0-, 1+, 1-| \end{aligned} \quad (9.72)$$

where we have introduced the notation

$$|i, j, k\rangle = \frac{1}{\sqrt{6}} (|i, j, k\rangle - |i, k, j\rangle + |j, k, i\rangle - |j, i, k\rangle + |k, i, j\rangle - |k, j, i\rangle)$$

and $i, j, k = 0\pm, 1\pm, 2\pm$.

For the first excited energy level of H_0 ($E = \frac{7}{2}\omega$), we have

$$\tilde{H} \propto \begin{pmatrix} 4 & 0 & \frac{1}{\sqrt{2}} & 0 \\ 0 & 4 & 0 & \frac{1}{\sqrt{2}} \\ \frac{1}{\sqrt{2}} & 0 & \frac{7}{2} & 0 \\ 0 & \frac{1}{\sqrt{2}} & 0 & \frac{7}{2} \end{pmatrix}, \quad (9.73)$$

and the corresponding eigenvectors can be written as

$$\begin{aligned}
|\psi'_1\rangle &= \sqrt{\frac{2}{3}}\left(-\frac{1}{\sqrt{2}}|\psi_2\rangle + |\psi_4\rangle\right) \\
|\psi'_2\rangle &= \sqrt{\frac{2}{3}}\left(-\frac{1}{\sqrt{2}}|\psi_1\rangle + |\psi_3\rangle\right) \\
|\psi'_3\rangle &= \frac{1}{\sqrt{3}}(\sqrt{2}|\psi_2\rangle + |\psi_4\rangle) \\
|\psi'_4\rangle &= \frac{1}{\sqrt{3}}(\sqrt{2}|\psi_1\rangle + |\psi_3\rangle). \tag{9.74}
\end{aligned}$$

In the decoupled limit the eigenstates $|011\rangle_{R_1 R_2 R_3}$ and $|110\rangle_{R_1 R_2 R_3}$ tend to the above states (or any combination of them) which have $\varepsilon = \frac{8}{27}$. This value coincides with the entanglement for the first excited state obtained from the exact calculation in the limit $\tau \rightarrow 0$ (equivalently $\lambda \rightarrow 0$).

The states $|\psi'_1\rangle$ and $|\psi'_2\rangle$ ($|\psi'_3\rangle$ and $|\psi'_4\rangle$) share the same energy eigenvalue. A linear combination of eigenstates sharing the same eigenenergy is also a valid energy eigenstate. Then, let us consider for instance $|\psi'_{34}\rangle = \cos\theta|\psi'_3\rangle + \sin\theta|\psi'_4\rangle$, ($0 \leq \theta < 2\pi$). As already discussed at the end of Subsection III.B, the entanglement of these linear combinations does not depend on θ .

We have seen that in the case of some excited states of the Moshinsky model an arbitrarily weak interaction between the particles leads to a finite amount of entanglement. This naturally suggests the following issues: to what extent is this weak-interaction entanglement robust? What happens with this entanglement if some other small perturbation acts upon the system? The detailed entanglement features of the eigenstates corresponding to this scenario will evidently depend on the precise form of the new perturbation. Therefore, these entanglement properties can only be studied in a case-by-case way. However, it is possible to gain some valuable insights on the robustness of the weak-interaction entanglement by recourse to a statistical approach. We can consider the typical features of the weak-interaction entanglement corresponding to a random perturbation.

Let us consider again the four eigenstates in Eq. (9.72) of the unperturbed (with no interaction) system. Any weak perturbation acting on top of the already considered weak interaction will lead (in the lowest order of perturbation theory for a degenerate eigenenergy) to a new set of four perturbed energy eigenstates that will be linear combinations of the four unperturbed states (9.72). That is, the new perturbed states are orthonormal states belonging to the four-dimensional linear space spanned by the states (9.72). We can consider the statistical distribution of entanglement values corresponding to random states in this subspace uniformly distributed according to the Haar measure (see [290, 291] and references therein). To this end we generate three-electron states randomly distributed according to the Haar measure of the form

$$|\psi'\rangle = \sum_{i=1}^4 c_i |\psi_i\rangle, \tag{9.75}$$

with $|\psi_i\rangle$, $i = 1, \dots, 4$ as given in Eq. (9.72). A state of the form $|\psi'\rangle$ can be thought as

Following a similar procedure and after a laborious algebra we compute the entanglement of the eigenvectors of \tilde{H} :

$$\begin{aligned}\varepsilon(|\psi'_1\rangle) &= \varepsilon(|\psi'_6\rangle) = 0 \\ \varepsilon(|\psi'_7\rangle) &= \varepsilon(|\psi'_8\rangle) = \varepsilon(|\psi'_9\rangle) = \varepsilon(|\psi'_{10}\rangle) = \frac{4}{9} \\ \varepsilon(|\psi'_3\rangle) &= \varepsilon(|\psi'_4\rangle) = \frac{1}{4} \\ \varepsilon(|\psi'_2\rangle) &= \varepsilon(|\psi'_5\rangle) = \frac{20}{49}\end{aligned}\quad (9.78)$$

where $|\psi'_j\rangle$ ($j = 1, \dots, 10$) are the eigenvectors of the \tilde{H} matrix. The states $|\psi'_j\rangle$ with $j = 1, \dots, 6$ share the same eigenvalue. The same occurs for the state pairs $(|\psi'_7\rangle, |\psi'_8\rangle)$ and $(|\psi'_9\rangle, |\psi'_{10}\rangle)$. As we mentioned before, the interaction lift only partially the degeneracy. The degeneracy due to the spin degree of freedom ($S_z = \pm\frac{1}{2}$) is present in all the states. The obtained values agree with some of those calculated in section 3. Different combinations of the states sharing eigenvalues result in the non-coincident entanglement $\varepsilon_{021} = \frac{43}{108}$. For instance, let $|\psi'_{56}\rangle = p\psi'_5 + \sqrt{1-p^2}\psi'_6$, ($0 \leq p \leq 1$); then,

$$\varepsilon(p) = \frac{4}{147}p^2(8p^2 + 7), \quad (9.79)$$

and ε_{021} is re-obtained for $p \sim 0.992$.

9.4.2 Moshinsky model with two electrons in an uniform magnetic field

We consider also a perturbative approach for a three-dimensional Moshinsky atom with two electrons in a magnetic field. Let the unperturbed Hamiltonian be

$$H_0 = \frac{1}{2}(p_1^2 + p_2^2) + \frac{\omega^2}{2}(r_1^2 + r_2^2) + \frac{b^2}{2}(x_1^2 + y_1^2 + x_2^2 + y_2^2) + b(L_{1z} + L_{2z}) \quad (9.80)$$

and the perturbation,

$$\lambda^2 H' = \frac{\lambda^2}{2}(\mathbf{r}_1 - \mathbf{r}_2)^2. \quad (9.81)$$

The eigenenergies of H_0 are given by Eq. (9.49), taking $\nu_R = \nu_1$, $\nu_r = \nu_2$, $m_R = m_1$, $m_r = m_2$, $n_R = n_1$, $n_r = n_2$ and setting $\lambda = 0$. Then, for the excited states of H_0 with energy given by

$$E_{\nu m} = \omega \left(2y + \frac{2}{y} + 1 \right), \quad y = \left(1 + \frac{b^2}{\omega^2} \right)^{\frac{1}{2}} + \frac{b}{\omega},$$

$\tau_{1,2} = 0$ or $\nu_{1,2} = 0$, $m_1 = \{\pm 1, 0\}$, $m_2 = \{0, \pm 1\}$ and $\tau_{1,2} = 0$, we obtain resulting of setting one of the quantum numbers ν_1 , ν_2 , $|m_1|$, $|m_2|$ equal to one and the rest equal to zero. So,

$$\tilde{H} \propto \begin{pmatrix} c_1 & 0 & 0 & 0 & 0 & 0 & 0 & 0 \\ 0 & c_1 & 0 & 0 & 0 & c_2 & -c_2 & 0 \\ 0 & 0 & c_1 & 0 & 0 & -c_2 & c_2 & 0 \\ 0 & 0 & 0 & c_1 & 0 & 0 & 0 & 0 \\ 0 & 0 & 0 & 0 & c_1 & 0 & 0 & 0 \\ 0 & c_2 & -c_2 & 0 & 0 & c_1 & 0 & 0 \\ 0 & -c_2 & c_2 & 0 & 0 & 0 & c_1 & 0 \\ 0 & 0 & 0 & 0 & 0 & 0 & 0 & c_1 \end{pmatrix},$$

where $c_1 = \frac{1}{2\omega} + \frac{2}{\sqrt{b^2 + \omega^2}}$ and c_2 is obtained numerically, its exact numerical value being not relevant for the next calculations.

\tilde{H} has six degenerate eigenvectors and two non-degenerate ones that take the following entanglement values: $\{0, \frac{1}{2}, \frac{3}{4}\}$. The entanglement value obtained from the exact computations in the limit $\lambda \rightarrow 0$ of the states with the same energy, $|100, 000\rangle_{Rr}$ and $|000, 100\rangle_{Rr}$, coincide with one of the above values ($\varepsilon = \frac{3}{4}$).

We consider also states setting $n_1 = 1$ or $n_2 = 1$ and the rest equal to zero, with energy given by

$$E_n = \omega \left(y + \frac{1}{y} + 2 \right)$$

and with y defined as before. For these excited states we obtain

$$\tilde{H} \propto \begin{pmatrix} d_1 + d_2 & 0 & 0 & 0 \\ 0 & d_1 & d_2 & 0 \\ 0 & d_2 & d_1 & 0 \\ 0 & 0 & 0 & d_1 + d_2 \end{pmatrix},$$

where $d_1 = \frac{1}{\omega} + \frac{1}{\sqrt{b^2 + \omega^2}}$ and $d_2 = \frac{1}{2\omega}$. This matrix has three eigenvectors corresponding to the same eigenvalues and with entanglement $\{0, \frac{1}{2}\}$ and one non-degenerate eigenvector with entanglement $\frac{1}{2}$. Again the obtained results are in perfect accordance with the entanglement obtained for states $|001, 000\rangle_{Rr}$ and $|000, 001\rangle_{Rr}$ in the decoupled regime.

Conclusions

We explored the entanglement properties of two versions of the Moshinsky model: one comprising three electrons and another one consisting of two electrons in a uniform external magnetic field. The eigenstates entanglement of the three-electron system considered here depends only on the dimensionless parameter τ describing the relative strength of the interaction between the particles (as compared with the strength of the external confining potential). We obtained closed analytical expressions for the entanglement of the ground, first and second excited states. As a general trend we found that the entanglement exhibited for these states tends to increase both with the state's energy and with the strength of the interaction between the particles (that is, with τ). Non-vanishing entanglement is obtained in the limit of vanishing interaction in the case of excited states. This (apparent) discontinuous behavior of the entanglement is related to the degeneracy of the energy levels of the

“unperturbed” Hamiltonian describing non-interacting particles. The non-vanishing entanglement in the limit of zero interaction is determined by the particular basis of H_0 “chosen” by the interaction. We also found that in the case of an attractive interaction the eigenstates’ entanglement approaches its maximum possible value in the limit of an infinitely large interaction. On the other hand, in the case of a repulsive interaction the maximum possible entanglement is obtained when the interaction strength approaches a finite, critical limit corresponding to $\tau_c = \frac{1}{\sqrt{3}}$. The system does not admit bound eigenstates when the strength of the (repulsive) interaction is equal or larger than the one corresponding to τ_c .

As far as the entanglement’s dependence on the interaction strength and the energy are concerned, the behavior of the Moshinsky model with two electrons in an uniform magnetic field is similar to the one observed in the three-electron model. With regards to the external magnetic field, we found that the eigenstates’ entanglement decreases when considering increasing magnetic fields. In the limit of very strong magnetic fields the entanglement approaches a finite asymptotic value that depends on the interaction strength. The essential aspect of the magnetic field in the Moshinsky model that determines its effect upon the amount of entanglement exhibited by the system’s eigenstates is the following: increasing the intensity of the magnetic field tends to increase the confining effect of the combined external fields (that is, the harmonic external field and the magnetic field). For a given strength of the interaction between the particles, this increasing confinement leads (according to a general pattern that has been observed in all atomic models where entanglement was studied in detail) to a decrease in the eigenstates’ entanglement. As happens in the case of the three-electron model, a perturbative treatment highlights the essential role played by the degeneracy of the energy levels of the interactionless system in determining how the eigenstates’ entanglement depends on the interaction strength and on the energy.

Entanglement and Born-Oppenheimer approximation in an exactly solvable quantum many-body system

The very definition of entanglement relies on the partitioning of a system into subsystems, such that one physical system can exhibit very different entanglement properties, depending on the assumed convention [5]. Efficiently solvable systems permit to find a particular partition for which the wavefunction is separable, even in the presence of otherwise entangling interaction. For example, the hydrogen atom is naturally treated in the center-of-mass and relative coordinates, in which the wavefunction factorizes, instead of the electron and proton coordinates, in which the wavefunction appears to be highly entangled [292]. Such beneficial change of coordinates is, however, impossible for non-integrable systems, and entanglement in quantum many-body systems comes along typically with unconquerable complexity, which represents a serious challenge to any numerical or analytical approach. In a quantum chaotic system, there is no basis in the Hilbert space that permits an efficient description, by definition. Quantities developed in quantum information reflect the failure of any strategy that relies on the truncation of the Hilbert space, *e.g.* by the statistics of Schmidt coefficients of the wavefunction described under any bipartition [293]. Conversely, fundamental restrictions on entanglement, *e.g.* by area laws [294], can render efficient simulations of quantum-many-body systems possible [295]. An understanding of entanglement can, thus, be of great importance for practical numerical solutions.

A system that is particularly prone to complexity is a many-electron atom, in which the long-range Coulomb interaction renders any exact solution impossible, already for helium [296]. For such a system, entanglement is, on the one hand, tantamount to the enormous complexity present in the system. On the other hand, the clear hierarchy between the masses of the atomic constituents (electrons and the nucleus) suggests that most of the entanglement properties can already be understood from purely kinematic considerations, and that they are also featured by simple integrable models.

One well established computational technique in physical chemistry and molecular physics is the Born-Oppenheimer approximation [297, 298, 299], which allows an efficient treatment of many-nuclei many-electron systems by exploiting the intrinsic separation of scales that is rooted in the mass ratio between electrons and nuclei. The range of validity of the Born-Oppenheimer approximation has been studied and tested for different systems,

e.g. in atomic models with respect to the variation of the mass of a negative charged particle [300], in molecules under magnetic fields [301] or as well as in chemical reactions [302].

Here, we study the correlations between different bipartitions of the one-dimensional Moshinsky few-body model, that consists of N_n “nuclei” and N_e “electrons”. The external confinement and all particle-particle interactions are harmonic, which allows an analytical approach. We study the dependence of entanglement in the ground and the first few excited states on the particle-particle interaction strength, on the number of particles, and on the particle masses. Consistent with kinematic intuition, the entanglement between two subsystems vanishes when the subsystems have very different masses, while it attains its maximal value for comparable masses. The validity and the break-down of the Born-Oppenheimer Ansatz can be understood from a quantum information point of view.

The chapter is organized as follows. In Section 10.1 we describe the Moshinsky model we are going to study, and we briefly review the entanglement measures to be used throughout the chapter, as well as the Born-Oppenheimer approximation. In Section 10.2 we present the exact solution of the many-particle Moshinsky model with masses m_n and m_e . Based on this solution, we investigate the entanglement properties of the eigenstates of the three-particle case in Section 10.3 and, in Section 10.4, we extend the study of entanglement to systems with an arbitrary number of particles. In Section 10.5 we deal with the Born-Oppenheimer approximation for this many-particle Moshinsky model. We explore its validity with the parameters of the theory and analyze the entanglement computed with this approximation. Finally, some conclusions are drawn.

10.1 Preliminaries

10.1.1 Moshinsky-like many-particle model

The system here considered consists of $N = N_n + N_e$ distinguishable particles, N_n “nuclei” with mass m_n and N_e “electrons” with mass m_e . All particles interact harmonically with each other and with the external confining potential.

The particle-particle interaction strengths between a nucleus and an electron, between two electrons, and between two nuclei are denoted by τ_{ne} , τ_{ee} and τ_{nn} , respectively; they are measured in units of the confining potential strength k . All masses are measured in units of the electron mass m_e , *i.e.* the nucleus mass is adjusted via the mass ratio $M = m_n/m_e$, and all actions are measured in units of \hbar .

The dimensionless Hamiltonian of the system is

$$\begin{aligned}
 H_x = & \sum_{i=1}^{N_n} \frac{P_{x_i}^2}{2M} + \sum_{j=1}^{N_e} \frac{p_{x_j}^2}{2} + \frac{1}{2} \left(\sum_{i=1}^{N_n} X_i^2 + \sum_{j=1}^{N_e} x_j^2 \right) + \\
 & + \frac{\tau_{nn}}{2} \left(\sum_{i=1}^{N_n} \sum_{k=i+1}^{N_n} (X_i - X_k)^2 \right) + \frac{\tau_{ee}}{2} \left(\sum_{j=1}^{N_e} \sum_{k=j+1}^{N_e} (x_j - x_k)^2 \right) + \\
 & + \frac{\tau_{ne}}{2} \left(\sum_{i=1}^{N_n} \sum_{j=1}^{N_e} (X_i - x_j)^2 \right), \tag{10.1}
 \end{aligned}$$

where (X_j, P_{x_j}) and (x_j, p_{x_j}) denote the positions and momenta of the nuclei (in uppercase letters) and electrons (in lowercase letters), respectively.

10.1.2 Quantum entanglement

In this chapter we focus on the entanglement in eigenstates of the many-particle system described above, for which we consider different bipartitions. The entanglement of a pure bipartite system is essentially given by the mixedness of the marginal density matrices associated with each subsystem. We study the two following partitions: First, we consider the partition of the system into a single-particle subsystem and a $(N - 1)$ -particle subsystem, where the single particle can be a nucleus or an electron. Second, we study the partition of the system into the two groups of all N_n nuclei and all N_e electrons. Comparing the correlations exhibited in the different partitions, we can characterize the degree of entanglement between particles of the same and of different types.

A practical quantitative indicator for the entanglement in a pure bi-partite system of distinguishable particle is the linear entropy given in Eq. (8.23). In the present applications as in the previous chapter, we deal with infinite-dimensional Hilbert spaces, such that the measure in Eq. (8.23) adopts values within the interval $[0, 1)$, since the maximal value of the entanglement in a d -dimensional space is $1 - 1/d$.

Given a bipartition (A, B) of a system of N particles into (N_A, N_B) particles, we compute the trace that appears in Eq. (8.23) as

$$\text{Tr}[\rho_A^2] = \int_{\mathbb{R}} |\langle \mathbf{x}_A | \rho_A | \mathbf{x}'_A \rangle|^2 d\mathbf{x}_A d\mathbf{x}'_A, \quad (10.2)$$

with the ρ_A matrix elements,

$$\langle \mathbf{x}_A | \rho_A | \mathbf{x}'_A \rangle = \int_{\mathbb{R}} \langle \mathbf{x}_A \mathbf{x}_B | \rho | \mathbf{x}'_A \mathbf{x}_B \rangle d\mathbf{x}_B = \int_{\mathbb{R}} \Psi(\mathbf{x}_A, \mathbf{x}_B) \Psi^*(\mathbf{x}'_A, \mathbf{x}_B) d\mathbf{x}_B, \quad (10.3)$$

where \mathbf{x}_A (\mathbf{x}_B) are N_A -dimensional (N_B -dimensional) position coordinates denoting the global set of coordinates $\{x_1 \cdots x_{N_A}\}$ ($\{x_{N_A+1} \cdots x_N\}$) of the particles that belong to the subsystem A (B).

For the many-particle system H_x , we denote hereafter the $(N_n$ -nuclei)- $(N_e$ -electrons) entanglement (or nuclei-electrons entanglement) by $\varepsilon(N_n, N_e)$, the (1-nucleus)- $((N - 1)$ -particles) entanglement (or single-nucleus entanglement) by $\varepsilon_n(N_n, N_e)$ and the (1-electron)- $((N - 1)$ -particles) entanglement (or single-electron entanglement) by $\varepsilon_e(N_n, N_e)$. The single-electron (single-nucleus) entanglement captures the uncertainty that a single electron (nucleus) has due to correlations with other particles. These correlations can be of very distinct qualitative nature, since electrons can be correlated one with each other, or with the nuclei. This is also reflected in the nuclei-electrons entanglement.

10.1.3 Born-Oppenheimer approximation

As already mentioned in the Introduction, the study of the mass effects on the entanglement features of composite systems naturally leads to consider the connection between

entanglement and the celebrated Born-Oppenheimer approximation. Here we provide a brief review of this important approach.

The Born-Oppenheimer (BO) approximation [297] is probably the most fundamental approximation in quantum chemistry [298] and in molecular physics [299]. From a practical point of view, it allows one to determine the electronic structure of a molecule in a given particular configuration of its nuclear part. The physical motivation behind the BO approximation is that the nuclei are much heavier than the electrons. If we denote by \mathbf{x} and \mathbf{X} all of the electron positions $\{x_i\}$ and nuclear positions $\{X_i\}$, respectively, we can consider \mathbf{X} as a “parameter” that define the effective Hamiltonian for the electrons. For any fixed configuration of the molecule one has to solve a Schrödinger equation that involves only the electronic degrees of freedom. The eigenvalues and eigenfunctions depend on the particular nuclear configuration. Once one has solved the electronic Schrödinger equation, the effective Hamiltonian for the nuclei can be obtained by adding the corresponding one-nucleus Hamiltonian terms.

In order to gain a more detailed insight, let us apply the approximation to the here-considered “molecule” composed of N_n nuclei and N_e electrons. The time-independent Schrödinger equation for the system associated to Eq. (10.1) is

$$[T_n + T_e + V]\psi(\mathbf{X}; \mathbf{x}) = E\psi(\mathbf{X}; \mathbf{x}), \quad (10.4)$$

where T_n and T_e denote the kinetic energy operator for the nuclei and electrons, respectively, and V the total potential energy of the system. In the BO approximation [297] one sets the Ansatz wave function

$$\Psi_{\mathbf{s}, \mathbf{q}}^{BO} = F_{\mathbf{s}}(\mathbf{X})\phi_{\mathbf{q}}(\mathbf{X}; \mathbf{x}), \quad (10.5)$$

where \mathbf{s} and \mathbf{q} denote the nuclei and electrons quantum state, respectively.

The time-independent Schrödinger equation for the electrons moving in the field of fixed nuclei at the positions $\{X_i\}$, known as the electronic wave equation, is given by

$$(T_e + V)\phi_{\mathbf{q}}(\mathbf{X}; \mathbf{x}) = E_{\mathbf{q}}^{elec}(\mathbf{X})\phi_{\mathbf{q}}(\mathbf{X}; \mathbf{x}), \quad (10.6)$$

where $E_{\mathbf{q}}^{elec}$ and the wave function $\phi_{\mathbf{q}}$ for each electronic state \mathbf{q} depend parametrically on the nuclear coordinate \mathbf{X} . The nuclear wave function $F_{\mathbf{s}}(\mathbf{X})$ satisfies

$$\left[T_n + E_{\mathbf{q}}^{elec}(\mathbf{X}) - E \right] F_{\mathbf{s}}(\mathbf{X}) = 0. \quad (10.7)$$

10.2 Exact solution of the many particle system

In this section we solve the Schrödinger equation $H_x|\Psi\rangle = E_x|\Psi\rangle$ analytically, being H_x the Hamiltonian in Eq. (10.1) described in the previous section. For this purpose we introduce the dilatation coordinate change

$$X_j \rightarrow \frac{X'_j}{\sqrt{M}} \quad (10.8)$$

for nuclei, which allows us to express the one-dimensional Hamiltonian, $H'_x = H_x$, in terms of the $N \times N$ interaction matrix A as follows:

$$\begin{aligned}
H'_x &= \sum_{j=1}^{N_n} \frac{P_j'^2}{2} + \sum_{i=1}^{N_e} \frac{p_i^2}{2} + \frac{1}{2} \sum_{j=1}^{N_n} A_{i,i} X_j'^2 + \\
&+ \frac{1}{2} \sum_{i=1}^{N_e} A_{N_n+i, N_n+i} x_i^2 - \sum_{j=1}^{N_n} \sum_{i=1}^{N_e} A_{j, N_n+i} X_j' x_i - \\
&- \sum_{i=1}^{N_e} \sum_{j=i+1}^{N_e} A_{N_n+i, N_n+j} x_i x_j - \sum_{i=1}^{N_n} \sum_{j=i+1}^{N_n} A_{i,j} X_i' X_j'.
\end{aligned} \tag{10.9}$$

The elements of A are given by

$$\begin{aligned}
A_{j,j} &= \frac{(1 + N_e \tau_{ne} + (N_n - 1) \tau_{nn})}{M}, \\
A_{i+N_n, i+N_n} &= (1 + N_n \tau_{ne} + (N_e - 1) \tau_{ee}), \\
A_{j, i+N_n} &= -\frac{\tau_{ne}}{\sqrt{M}}, \\
A_{j,l} &= -\frac{\tau_{nn}}{M} \quad \text{for } j \neq l, \\
A_{i+N_n, m+N_n} &= -\tau_{ee} \quad \text{for } i \neq m.
\end{aligned} \tag{10.10}$$

where the indices j and l (i and m) run between 1 and N_n (1 and N_e) and refer to nuclear (electronic) coordinates.

The coordinate changes which makes the Hamiltonian (10.9) separable are given by the eigenvectors of the interaction matrix A . This matrix has $N_e - 1$ and $N_n - 1$ degenerate values in the electron and nuclei cases. Now, for the corresponding eigenvector we choose the Jacobi variables $\{r_1, \dots, r_{N_e-1}\}$ and $\{R_1, \dots, R_{N_n-1}\}$, for electrons and nuclei, respectively, as follows:

$$\begin{aligned}
r_i(x_1, \dots, x_{i+1}) &= \sum_{k=1}^i \frac{x_k - x_{i+1}}{\sqrt{i + k^2}}, \\
R_j(X'_1, \dots, X'_{j+1}) &= \sum_{k=1}^j \frac{X'_k - X'_{j+1}}{\sqrt{j + k^2}},
\end{aligned} \tag{10.11}$$

with $i = 1, \dots, N_e - 1$ and $j = 1, \dots, N_n - 1$. This particular choice of Jacobi coordinates makes the Hamiltonian to be separable as independent harmonic oscillator in those Jacobi coordinates given in Eq. (10.11) without any prefactor. Moreover it makes the single-particle entanglement dependent only on the last quantum number of these coordinates (see Table 10.1). The remaining two eigenvalues of A are not degenerated, so that, their corresponding eigenvectors are predefined, and give the coordinate changes

$$\begin{aligned}
U_1(X'_1, \dots, X'_{N_n}, x_1, \dots, x_{N_e}) &= \frac{N_n(a+b)}{\sqrt{N_e + N_n(a+b)^2}} R_{N_n} + \\
&+ \frac{N_e}{\sqrt{N_e + N_n(a+b)^2}} r_{N_e},
\end{aligned} \tag{10.12}$$

$$\begin{aligned}
U_2(X'_1, \dots, X'_{N_n}, x_1, \dots, x_{N_e}) &= \frac{N_n(a-b)}{\sqrt{N_e + N_n(a-b)^2}} R_{N_n} + \\
&+ \frac{N_e}{\sqrt{N_e + N_n(a-b)^2}} r_{N_e}, \quad (10.13)
\end{aligned}$$

where

$$\begin{aligned}
r_{N_e}(x_1, \dots, x_{N_e}) &= \frac{1}{N_e} \sum_{i=1}^{N_e} x_i, \\
R_{N_n}(X'_1, \dots, X'_{N_n}) &= \frac{1}{N_n} \sum_{j=1}^{N_n} X'_j \quad (10.14)
\end{aligned}$$

are the centers of mass of electrons and nuclei, respectively, and

$$\begin{aligned}
a &= \frac{M-1-2\tau_{ne}+M\tau_{ne}}{2\sqrt{M}\tau_{ne}}, \\
b &= \frac{\sqrt{-4M(1+3\tau_{ne})+(1+M+2\tau_{ne}+M\tau_{ne})^2}}{2\sqrt{M}\tau_{ne}}. \quad (10.15)
\end{aligned}$$

The coordinates U_1 and U_2 are linear combinations of the center-of-mass of the nuclei, R_{N_n} , and the center-of-mass of the electrons, r_{N_e} , with pre-factors that depend on the electron-nucleus interaction strength τ_{ne} , the mass ratio M , and the number of electrons and nuclei, N_e and N_n . In the limit of large electron-nucleus interaction, $\tau_{ne} \rightarrow \infty$, the coordinates become the center-of-mass and the relative coordinates of the set of nuclei and electrons:

$$\begin{aligned}
\lim_{\tau_{ne} \rightarrow \infty} U_1 &= \sqrt{N_e + MN_n} \frac{N_e r_{N_e} + MN_n R_{N_n}}{N_e + MN_n}, \\
\lim_{\tau_{ne} \rightarrow \infty} U_2 &= \sqrt{\frac{MN_e N_n}{N_e + MN_n}} (r_{N_e} - R_{N_n}). \quad (10.16)
\end{aligned}$$

When electrons and nuclei have the same mass, *i.e.* $M \rightarrow 1$, the coordinates allow again the above natural interpretation:

$$\begin{aligned}
U_1^{M \rightarrow 1} &= \sqrt{N_e + N_n} \frac{N_e r_{N_e} + N_n R_{N_n}}{N_e + N_n}, \\
U_2^{M \rightarrow 1} &= \sqrt{\frac{N_e N_n}{N_e + N_n}} (r_{N_e} - R_{N_n}), \quad (10.17)
\end{aligned}$$

for any value of the interaction τ_{ne} .

In the transformed coordinates $\{r_1, \dots, r_{N_e-1}\}$, $\{R_1, \dots, R_{N_n-1}\}$ and $\{U_1, U_2\}$, the Hamiltonian (10.9) separates as

$$\begin{aligned}
H'_x &= \sum_{l=1,2} \left(-\frac{1}{2} \frac{\partial^2}{\partial U_l^2} + \frac{1}{2} \beta_l U_l^2 \right) + \\
&+ \sum_{j=1}^{N_n-1} \left(-\frac{1}{2} \frac{\partial^2}{\partial R_j^2} + \frac{1}{2} \beta^{(n)} R_j^2 \right) + \sum_{i=1}^{N_e-1} \left(-\frac{1}{2} \frac{\partial^2}{\partial r_i^2} + \frac{1}{2} \beta^{(e)} r_i^2 \right), \quad (10.18)
\end{aligned}$$

where

$$\beta_{1/2} = \frac{1 + M + N_e \tau_{ne} + N_n M \tau_{ne}}{2M} \mp \frac{N_n b \tau_{ne}}{\sqrt{M}}, \quad (10.19)$$

$$\beta^{(n)} = \frac{1 + N_e \tau_{ne} + N_n \tau_{nn}}{M}, \quad (10.20)$$

$$\beta^{(e)} = 1 + N_n \tau_{ne} + N_e \tau_{ee}. \quad (10.21)$$

In other words, the system has been decomposed into a set of independent harmonic oscillators in the variables U_1, U_2, R_j and r_i , with frequencies $\sqrt{\beta_1}, \sqrt{\beta_2}, \sqrt{\beta^{(n)}}, \sqrt{\beta^{(e)}}$, respectively. The eigenfunctions of the Hamiltonian

$$\begin{aligned} \Psi'_{u_1, u_2, \mathbf{n}, \mathbf{e}}(X'_1, \dots, X'_{N_n}, x_1, \dots, x_{N_e}) &= \prod_{l=1}^2 \Phi_{u_l}^{\beta_l}(U_l(X'_1, \dots, X'_{N_n}, x_1, \dots, x_{N_e})) \times \\ &\times \prod_{j=1}^{N_n-1} \Phi_{n_j}^{\beta^{(n)}}(R_j(X'_1, \dots, X'_{j+1})) \times \\ &\times \prod_{i=1}^{N_e-1} \Phi_{e_i}^{\beta^{(e)}}(r_i(x_1, \dots, x_{i+1})), \end{aligned} \quad (10.22)$$

are expressed in terms of the one-dimensional harmonic oscillator solution

$$\Phi_\nu^\beta(y) = \left(\frac{\beta^{1/4}}{2^n n! \pi^{1/2}} \right)^{\frac{1}{2}} e^{-\frac{1}{2} \sqrt{\beta} y^2} \mathcal{H}_n(\beta^{1/4} y), \quad (10.23)$$

where $\mathcal{H}_\nu(y)$ denote the Hermite polynomials.

The quantum numbers $u_1, u_2, \mathbf{n}, \mathbf{e}$ correspond to the excitation of each collective coordinate (10.11)-(10.13) described above; that is, the quantum numbers u_i are associated to the excitation of coordinates U_i , and \mathbf{n} (\mathbf{e}) denotes the set of quantum numbers $\{n_1, \dots, n_{N_n-1}\}$ ($\{e_1, \dots, e_{N_e-1}\}$) associated to the excitation of the nuclei (electrons) relative coordinates $\{R_1, \dots, R_{N_n-1}\}$ ($\{r_1, \dots, r_{N_e-1}\}$). All correlations between nuclei and electrons are defined via the correlations between their respective centers of mass R_{N_n} and r_{N_e} , which are coupled only through the coordinates U_1 and U_2 , as shown in Eqs. (10.12) and (10.13).

The eigenfunctions of the initial Hamiltonian H_x are obtained by undoing the dilatation coordinates change (10.8) in the eigenfunction given in Eq. (10.22), *i.e.*

$$\Psi_{u_1, u_2, \mathbf{n}, \mathbf{e}}(\mathbf{X}, \mathbf{x}) = M^{-\frac{N_n}{4}} \Psi'_{u_1, u_2, \mathbf{n}, \mathbf{e}}(\sqrt{M} X_1, \dots, \sqrt{M} X_{N_n}, x_1, \dots, x_{N_e}). \quad (10.24)$$

While the above eigenfunctions depend on the rescaled interactions between particles with the strength of the confining potential k , as well as the mass ratio, the eigenenergies are explicitly dependent on all parameters governing the physical scale of the system, that is,

the energy of the system, $E_x = \sqrt{\frac{k}{m_e}} E'_x$, is given by

$$E_x = \sqrt{\frac{k}{m_e}} \left(\sum_{l=1}^2 \sqrt{\beta_l} \left(u_l + \frac{1}{2} \right) + \sum_{j=1}^{N_n-1} \sqrt{\beta^{(n)}} \left(n_j + \frac{1}{2} \right) + \sum_{i=1}^{N_e-1} \sqrt{\beta^{(e)}} \left(e_i + \frac{1}{2} \right) \right). \quad (10.25)$$

Hereafter, we denote the pure states of the system (10.1) by $|u_1, u_2, \mathbf{n}, \mathbf{e}\rangle$, resulting the wavefunction in Eq. (10.24) corresponding to this state, that is

$$\Psi_{u_1, u_2, \mathbf{n}, \mathbf{e}}(\mathbf{X}, \mathbf{x}) = \langle \mathbf{X}, \mathbf{x} | u_1, u_2, \mathbf{n}, \mathbf{e} \rangle. \quad (10.26)$$

Then, the density matrix of an arbitrary state of the many-particle system is given by

$$\rho_{u_1, u_2, \mathbf{n}, \mathbf{e}} = |u_1, u_2, \mathbf{n}, \mathbf{e}\rangle \langle u_1, u_2, \mathbf{n}, \mathbf{e}|. \quad (10.27)$$

Besides the mass and number of particles, the values of the entanglement of the three different types discussed (nuclei-electrons, single-nucleus and single-electron entanglement) additionally depend on the parameters and quantum numbers shown in Table 10.1.

Parameters	ε	ε_n	ε_e
Interactions	τ_{ne}	τ_{ne}, τ_{nn}	τ_{ne}, τ_{ee}
Quantum numbers	u_1, u_2	u_1, u_2, n_{N_n-1}	u_1, u_2, e_{N_e-1}
Mass and # particles	M, N_n, N_e	M, N_n, N_e	M, N_n, N_e

Table 10.1: Parameters which the different types of entanglement depend on.

As shown in this table the single-particle entanglements ε_n and ε_e depend on the quantum number u_1, u_2, n_{N_n-1} for any nucleus, and on u_1, u_2, e_{N_e-1} for any electron. So, single-particle entanglement is unaffected by the excitation of any of the remaining quantum numbers.

Intuitively, one would read off from table 10.1 that we can really treat the system of nuclei and the system of electrons as two entities that interacts one with the other, since the interactions between the electrons or between the nuclei do not matter, and similarly for each kind of entanglement here. But surprisingly, this does not happen. One can see from the change of variables U_1 and U_2 that only in the limiting cases of $\tau_{ne} \rightarrow \infty$ and $M \rightarrow 1$ (see Eqs. (10.16) and (10.17)), the correlations between nuclei and electrons are induced by coordinates which are precisely the center of mass and the relative coordinate of the corresponding center of mass R_{N_n} and r_{N_e} (the center of mass of the nuclei and electrons, respectively). Otherwise, the coordinates U_1 and U_2 depends on R_{N_n} and r_{N_e} in a flamboyant way, and this intuitive reading is wrong.

10.3 Entanglement of the three-particle model

We turn here to the particular case of a three-particle system with one nucleus ($N_n = 1$) and two electrons ($N_e = 2$). The possibility of choosing different particle mass ratio M

allows us to qualitatively model two different physical systems: A helium-like atom for $M \gg 1$ and a diatomic molecule (H_2^+ type) with one “electron” for $M \ll 1$ as shown in Figs. 10.1a) and b), respectively. We keep the notation for the nuclei m_n and electrons m_e even though $m_e \gg m_n$ ($M \ll 1$).

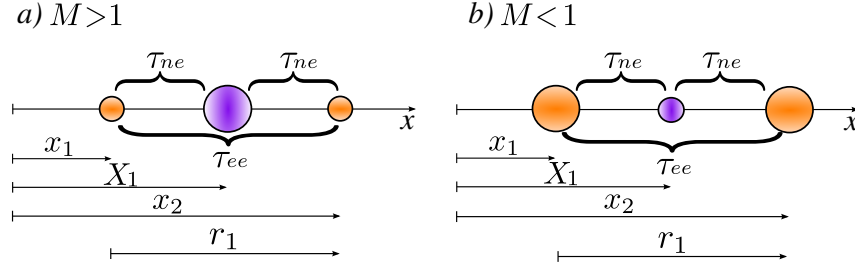


Figure 10.1: Three harmonically interacting particles in a confining external harmonic potential, namely $N_n = 1$ and $N_e = 2$, which roughly describes a) *He*-like system for $M \gg 1$ and b) H_2^+ -like system for $M \ll 1$. The sizes of the circles symbolize the masses of the particles.

The eigenstates of this three-particle system depend on the quantum numbers $|u_1, u_2, e_1\rangle$. In this case, the coordinates U_1 and U_2 , Eqs. (10.12) and (10.13), are a specific linear combination of the nuclear coordinate X_1 and the center of mass of the electrons, and r_1 is the relative coordinate of the two electrons.

In the limit of vanishing interactions ($\tau_{ne} \rightarrow 0$, $\tau_{ee} \rightarrow 0$) the energy of the state $|u_1, u_2, e_1\rangle$, Eq. (10.25), simplifies to

$$E_0 = \sqrt{\frac{k}{m_e}} \times \begin{cases} 1 + \frac{1}{\sqrt{M}} \left(\frac{1}{2} + u_1\right) + u_2 + e_1 & \text{for } M \geq 1, \\ 1 + u_1 + \frac{1}{\sqrt{M}} \left(\frac{1}{2} + u_2\right) + e_1 & \text{for } 0 < M < 1. \end{cases} \quad (10.28)$$

The energy in Eq. (10.28) will be necessary to understand the physics of the states entanglement in this limit of vanishing interactions. In the following subsection we determine analytically the entanglement amount given by Eq. (8.23), for various low-lying states of these three systems; namely, the ground state $|000\rangle$ and the first excited states $|100\rangle$, $|010\rangle$ and $|001\rangle$.

10.3.1 Nucleus-electrons entanglement

The nucleus-electrons entanglement ε shows the correlations between the nucleus and the two electron subsystem. It depends on the quantum numbers u_1 and u_2 and the interaction strength τ_{ne} , but it does not depend neither on the excitation of the electron relative coordinate e_1 nor the interaction between them τ_{ee} , as shown in Table 10.1, *i.e.* the nucleus does not care about the inter-electronic structure. Therefore, the nucleus entanglement of the states $|000\rangle$ and $|00e_1\rangle$, for any excitation e_1 , are precisely the same and, which in turn, are less entangled than any excited state in u_1 or u_2 (see Fig. 10.2).

As the general trend shown in Refs. [238, 245, 265], here the entanglement increases with the interaction, τ_{ne} , for all states. Decoupling the nucleus of the rest of the system

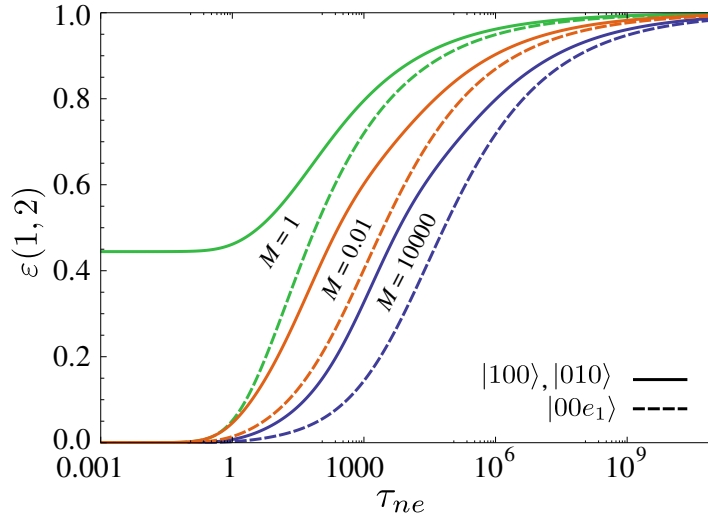


Figure 10.2: Nuclei-electrons entanglement of the three-particle case as a function of the nuclei-electrons interaction strength τ_{ne} of the ground state and first few excited states, for different mass ratio M . Mass ratios $M > 1$ describe a He -like system, $M < 1$ a H_2^+ -like system and $M = 1$ a systems with three particles with the same mass.

(i.e., taking the limit $\tau_{ne} \rightarrow 0$) makes entanglement to vanish except for $M = 1$ in the case of states $|010\rangle$ and $|100\rangle$, which exhibit a finite amount of entanglement. Due to the degeneracy of the energy in this limit given by Eq. (10.28) (energy is degenerate in u_1 and u_2 when $M = 1$), a very tiny interaction is enough to provoke high entangled states. This finite amount of entanglement can be related via perturbation theory to the alluded degeneracy of the energy levels of the Hamiltonian describing non-interacting particles (see Ref. [260]). The finite entanglement in the vanishing interaction limit is determined by a particular basis of the degenerated sates of the non interacting particles Hamiltonian.

So, while in the limit of vanishing interaction one can only understand the physics of this system within a quantum framework, in the case of strongly interacting particles one can appeal to the classical kinematic intuition. In Fig. 10.3 we plot ε as a function of the mass ratio M for different values of the interaction τ_{ne} . For $\tau_{ne} \rightarrow \infty$ the maximum entanglement occurs when $M = 2$, which corresponds to subsystems with the same mass and, as masses become more different the entanglement between those particles gradually fades. A kinematic interpretation is in order: The more equal masses two coupled systems have, the more they will influence each other reciprocally. So, in terms of the physical limits: For a weak interaction, particles are independent, even if they have the same mass (if there is no degeneracy in this limit, see in Fig 10.3 the jump in entanglement for $\tau_{ne} = 0.01$). For very large or very small masses, the heavy particles are not influenced much by the light ones and, additionally, the light particles still are in a rather pure state.

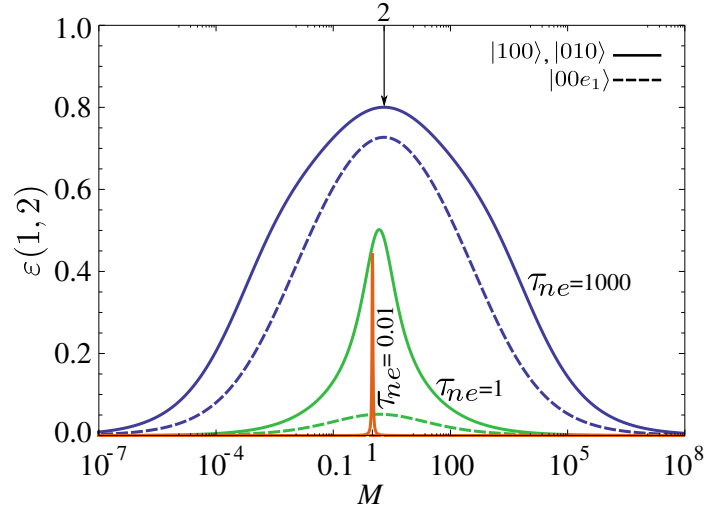


Figure 10.3: Nucleus-electrons entanglement of the three-particle case as a function of the ratio mass M for the ground state and first few excited states and for different values of the interaction τ_{ne} .

10.3.2 Electron entanglement

The electron entanglement ε_e shows the correlations between one electron and the remaining particles of the system, namely the other electron and the nucleus. It depends on both relative interaction strengths τ_{ne} and τ_{ee} , and on all quantum numbers, u_1 , u_2 and e_1 .

In the limit of vanishing interactions, $\tau_{ne} \rightarrow 0$ and $\tau_{ee} \rightarrow 0$, a finite amount of entanglement is observed for the states $|100\rangle$ ($|010\rangle$) and $|001\rangle$ if $M \leq 1$ ($M \geq 1$). From Eq. (10.28) we note that the energy level of the state $|100\rangle$ ($|010\rangle$) is degenerate with $M \leq 1$ ($M \geq 1$) but not with $M > 1$ ($M < 1$). The energy level of the state $|001\rangle$ is degenerate for all M and a finite amount of entanglement is always obtained in the vanishing interactions limit (see Fig. 10.4).

We plot in Figs. 10.5a) and b) the electron entanglement ε_e as a function of τ_{ne} . As a general trend, the entanglement again increases with the strength of the interaction. However, two well-defined behaviors can be observed depending on the strength of the interaction τ_{ee} : For vanishing values of τ_{ee} (see Fig. 10.5b) the entanglement monotonically increases as a function of τ_{ne} . A finite amount of entanglement is obtained in the limit $\tau_{ne} \rightarrow 0$ for both excited states $|001\rangle$ and $|010\rangle$, which can be explained with alluded degeneracy in u_2 and e_1 of the energy in Eq. (10.28).

In Fig. 10.5a) we plot the single-electron entanglement with finite value of $\tau_{ne} = 50$. In the limit $\tau_{ne} \rightarrow 0$ the entanglement remains finite for all states; this finite amount of entanglement is due to the interelectron interaction, the electron being solely entangled with the other electron via τ_{ee} . As τ_{ne} increases, there is a kind of competition between the interactions τ_{ne} and τ_{ee} followed by a decrease of the entanglement amount. This occurs because, with the increasing interaction τ_{ne} , the nucleus becomes relevant in the system, as well as the mass difference between the two subsystems. Note that the minimum entanglement is obtained in the region $\tau_{ne} \sim \tau_{ee}$.

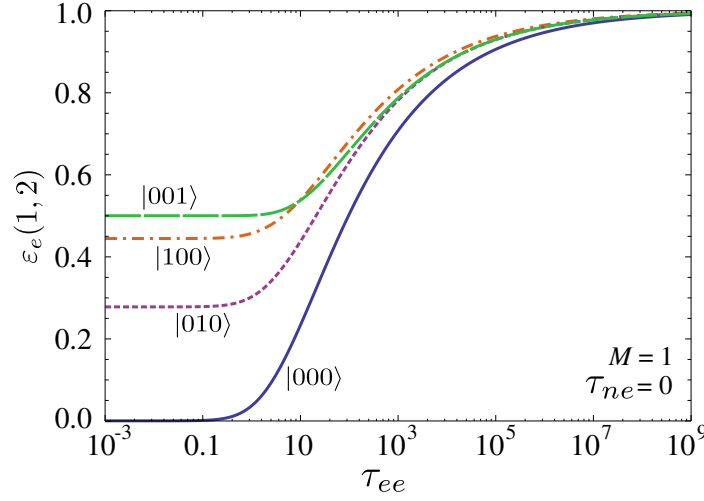


Figure 10.4: One-particle entanglement of the systems of three identical particles ($M = 1$) as a function of τ_{ee} with $\tau_{ne} \rightarrow 0$ for the ground state and first few excited states.

The entanglement $\varepsilon_e(1, 2)$ of the state $|010\rangle$ tends to the entanglement of the ground state in the limit $M \rightarrow 0$ and to the entanglement of the excited state $|001\rangle$ for $M \rightarrow \infty$ as shown in Figs. 10.5 c) and d). The entanglement of the state $|100\rangle$ behaves in the opposite way, approaching the entanglement value of the state $|001\rangle$ when $M \rightarrow 0$ and to the ground-state entanglement value in the limit $M \rightarrow \infty$. In addition, when the interactions are strong and comparable (see Fig. 10.5c where $\tau_{ne} = \tau_{ee} = 1000$) a kinematic interpretation is in order: In the limiting case $M \rightarrow 0$, *i.e.* the mass of the two subsystems (electron vs. nucleus-electron) becomes comparable, all states exhibit a finite and large amount of entanglement; the entanglement is that given by the electron-electron correlation and the effect of the nucleus (very light particle) on the electrons is negligible which just follow the kinematics of electrons. On the other hand, in the limit of $M \rightarrow \infty$ the nucleus acts on electrons as a confining external potential which tends to reduce the entanglement amount between electrons, see Section 9.3.3.

10.4 Entanglement of the many-particle model

A great advantage of the model at issue here is that one can determine analytically the entanglement. By using the Hamiltonian (10.1) of the system and its exact eigenstates given in Section 10.2, we can evaluate analytically the entanglement by means of the linear entropy defined by Eq. (8.23). In this section we determine the ground-state entanglement values for various bi-partitions of the many-particle Moshinsky model described in Section 10.1.1. As already pointed out, we are going to consider the following three types of entanglement: the nuclei-electron entanglement $\varepsilon(N_n, N_e)$, which corresponds to the entanglement between all the nuclei and all the electrons, the nucleus entanglement $\varepsilon_n(N_n, N_e)$, which gives the entanglement between a single nucleus and the rest of the system, and the electron entanglement $\varepsilon_e(N_n, N_e)$, which quantifies the entanglement be-

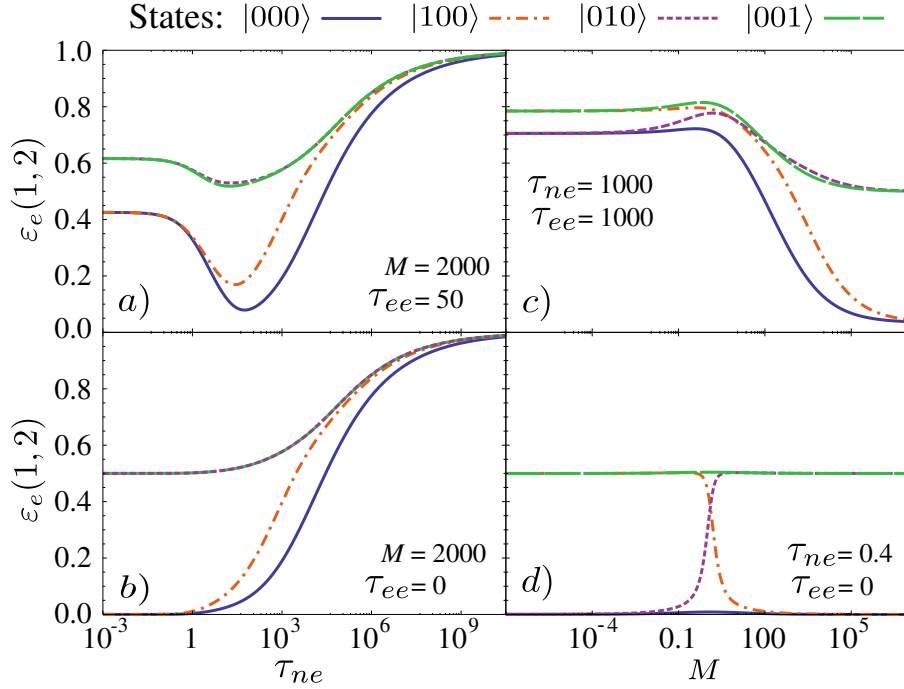


Figure 10.5: Electron entanglement of the three-particle ground state and first few excited states. On the left side as a function of the nucleus-electron interaction τ_{ne} with finite interaction $\tau_{ee} = 50$ (a), with vanishing interaction $\tau_{ee} = 0$ (b). On the right side, as a function of the mass ratio M for different values of the interaction strengths $\tau_{ne} = \tau_{ee} = 1000$ (c), and $\tau_{ne} = 0.4$, $\tau_{ee} = 0$ (d).

tween a single electron and the rest of the system.

10.4.1 Nuclei-electrons entanglement

Let us here study the ground-state entanglement $\varepsilon(N_n, N_e)$ between nuclei and electrons. For non negligible interaction τ_{ne} we have found that this entanglement displays a remarkable general trend: it is maximum when the mass ratio M almost fulfill $M \simeq N_e/N_n$. This is illustrated in Figure 10.6, where we plot $\varepsilon(N_n, N_e)$ for different pairs (N_n, N_e) . This behavior can be understood from the coordinate change U_1 and U_2 in the limit of large interaction in Eq. (10.16). The coordinates U_1 and U_2 present all possible correlations between nuclei and electrons, and the coefficients of the linear combination in R_{N_n} and r_{N_e} take the same value when $M = N_e/N_n$ is fulfilled.

For any interaction τ_{ne} , the maximum of entanglement lies down exactly at $M = N_e/N_n$ only when $N_n = N_e$ ($M = 1$), that is for systems with equal numbers of nuclei and electrons. When the number of nuclei and electrons are the same the nuclei-electrons entanglement behaves as the entanglement of a two-particle system with unequal masses $m_1 = m_n N_n$ and $m_2 = m_e N_e$ and with some interaction strength τ . However, this does not happen if the considered subsystems have a different number of particles even when the entanglement does not depend on the inter-electron interaction, nor on the inter-nuclei in-

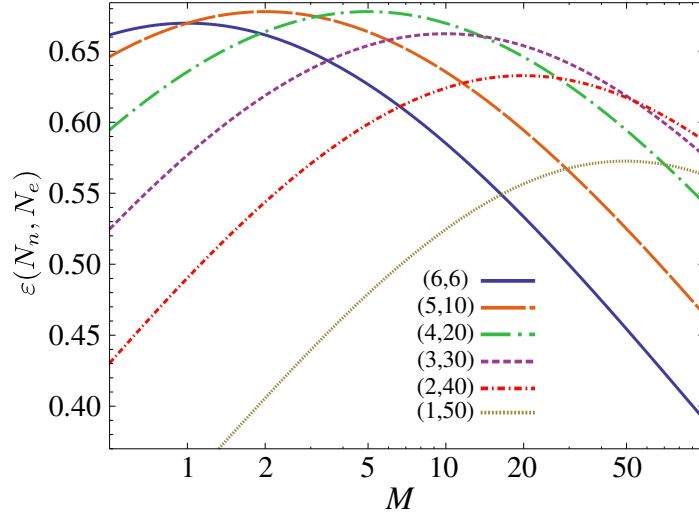


Figure 10.6: Nuclei-electrons entanglement $\varepsilon(N_n, N_e)$ for different number of nuclei and electrons (N_n, N_e) as a function of M with the interaction value $\tau_{ne} = 100$. Maximum of $\varepsilon(N_n, N_e)$ is obtained when $M \simeq N_e/N_n$.

teraction. The parameters M , N_e and N_n can not be rescale and one cannot consider each subsystem as a single entity. In systems with $N_n \neq N_e$ the maximum of entanglement depends on the relative nucleus-electron interaction strength τ_{ne} . In Figure 10.7 we show the mass ratio M vs. nucleus-electron interaction τ_{ne} which makes maximum the entanglement $\varepsilon(N_n, N_e)$. For small values of τ_{ne} the maximum entanglement is always located when $M < N_e/N_n$. On the other hand, when τ_{ne} increases, the maximum of entanglement moves up to the extreme value $M = N_e/N_n$ (*i.e.* the two subsystems have equal masses) which occurs when at the limit $\tau_{ne} \rightarrow \infty$.

The potential function appearing in the Hamiltonian (10.1) is a quadratic function of the complete set of vector positions $X_1, \dots, X_{N_n}, x_1, \dots, x_{N_e}$. Notice that the coefficients corresponding to X_i^2 and x_j^2 , which are respectively $\Lambda_n/2 = (1/2) + (\tau_{ne}/2)N_e + (\tau_{nn}/2)(N_n - 1)$ and $\Lambda_e/2 = (1/2) + (\tau_{ne}/2)N_n + (\tau_{ee}/2)(N_e - 1)$, grow linearly with N_n and N_e , while the coefficients corresponding to cross terms like $X_i \cdot X_j$, $X_i \cdot x_j$, and $x_i \cdot x_j$, do not (indeed, these coefficients are independent of N_n and N_e). In the case of the nuclei-electron entanglement, $\varepsilon(N_n, N_e)$, the number of correlations cross terms which contribute effectively to the reduced density matrix, $X_i \cdot x_j$, increases as $N_n \cdot N_e$. Therefore, the reduced density matrix can not be approximated by the ground state associated with the independent many-particle potential. That is why entangled states are obtained increasing both N_n and N_e in the case of nuclei-electrons entanglement shown in Fig 10.8.

Regarding the size of the system in terms of the number of particles, N_n and N_e , the region of higher-entanglement states is always located at the neighbourhood of the points where $N_n M = N_e$ is fulfilled, see Fig. 10.8. As we gradually increase the number of particles of one of the two species, electrons or nuclei, the entanglement fades away. However for larger number of nuclei N_n (electrons N_e) a wider number of electrons (nuclei) range gives highly entangled states, which is consistent with the above explanation. If we

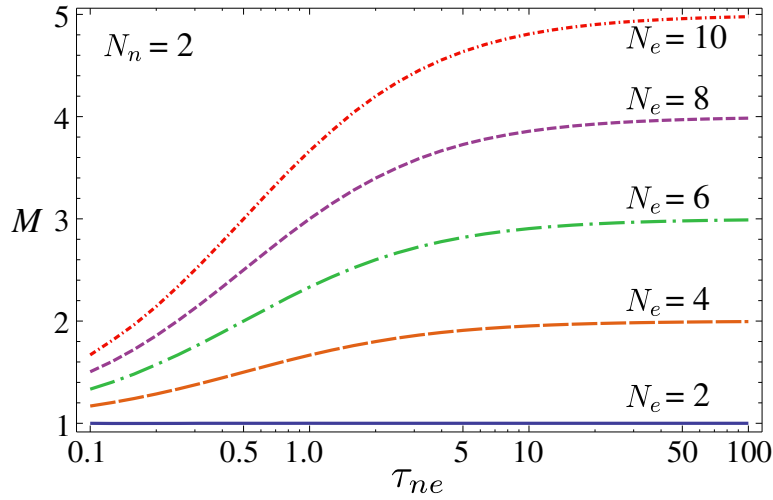


Figure 10.7: Maximum nuclei-electrons entanglement for two nuclei, $N_n = 2$, and different number of electrons $N_e = 2, 4, 6, 8, 10$ as a function of the mass ratio M and the interaction τ_{ne}

increase both the number of nuclei and the number of electrons to infinity, the entanglement reaches its maximum possible value. For very large number of nuclei (electrons), *i.e.* $N_n \gg N_e/M$ ($N_e \gg MN_n$) and the masses of the subsystems become very different if M is not very large, the entanglement tends to zero because the contribution of the correlation cross terms, $X_i \cdot x_j$, to the reduced density matrix become negligible as compared to the independent particles terms $(\Lambda_n/2) \sum_{i=1}^{N_n} X_i^2 + (\Lambda_e/2) \sum_{j=1}^{N_e} x_j^2$.

As shown Figs. 10.8 a), b) and c), the entanglement is enhanced with τ_{ne} for all systems following $N_n = MN_e$; moreover, the higher the mass, the greater is the number of electrons than nuclei needed to obtain high entangled states, as it is illustrated in Figs. 10.8 b) and d).

10.4.2 Single-particle entanglement: Nucleus and electron entanglement

We study here the nucleus entanglement $\varepsilon_n(N_n, N_e)$ and the electron entanglement $\varepsilon_e(N_n, N_e)$, which give the entanglement between a single particle and the rest of the many-particle system, in terms of the numbers of nuclei and electrons. In Figure 10.9 we show the dependence of these two types of entanglement on the number of nuclei and electrons for a fixed set of values of the parameters M , τ_{ne} , τ_{ee} and τ_{nn} (in particular, $M = 1000$) to highlight the entanglement behavior. The left (right) graphs give the values of the nucleus (electron) entanglement. Let us also point out that the solid red line in the left graphs of the figure corresponds to the entanglement values of the systems where the two subsystems have equal masses, what implies that $N_n = 2 - N_e/M$, so that $1 < N_n < 2$. In this case of equal subsystem masses one always deal with highly entangled states. Notice that in the electron case, such a red line does not trivially appears because we are implicitly assuming that $M > 1$.

For large values of either N_n or N_e (or both) the leading part of the potential function,

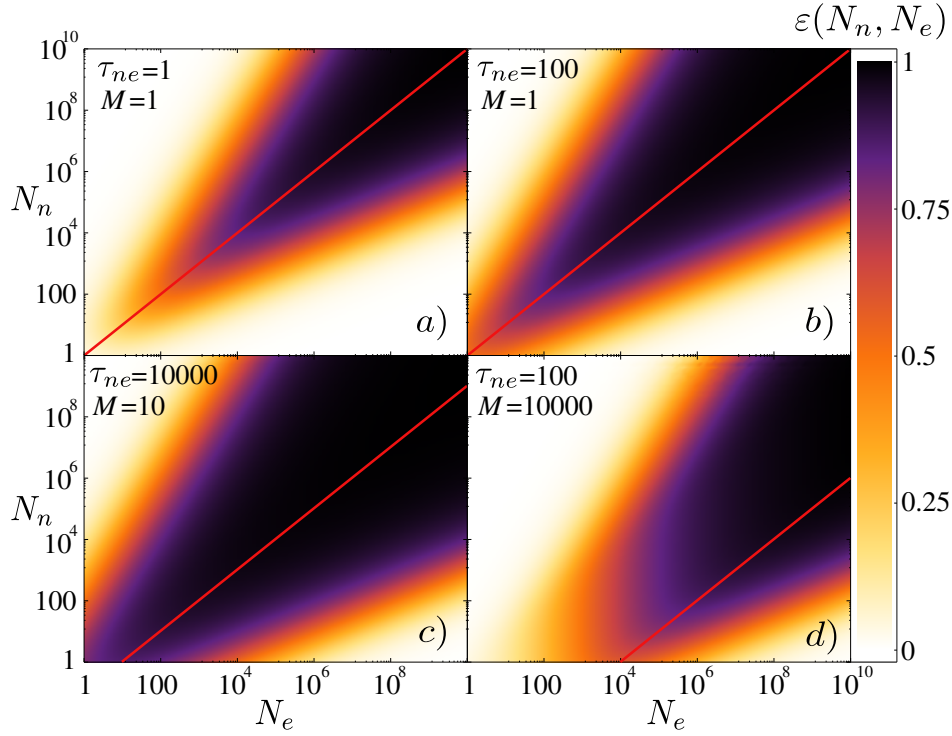


Figure 10.8: Nuclei-electrons entanglement as a function of the number of particles, N_n nuclei and N_e electrons, of the system for various relative nucleus-electron interaction strengths and mass ratios. In panel a) $\tau_{ne} = 1$, $M = 1$, b) $\tau_{ne} = 100$, $M = 1$, c) $\tau_{ne} = 10000$, $M = 10$, and d) $\tau_{ne} = 100$, $M = 10000$. Solid red lines correspond to systems where $M \equiv \frac{m_n}{m_e} = \frac{N_e}{N_n}$, so that the two subsystems (nuclei and electrons) have equal masses.

which effectively contributes to the single-particle reduced density matrix (obtained by integrating in the positions of the remaining $N_n - 1$ or $N_e - 1$ particles), is of the form $(\Lambda_n/2) \sum_{i=1}^{N_n} X_i^2 + (\Lambda_e/2) \sum_{j=1}^{N_e} x_j^2$. This form of the potential function describes a set of $N_n + N_e$ independent harmonic oscillators. Due to this, as N_n or N_e increases, the single particle reduced density matrix corresponding to a nucleus (electron) approaches the density matrix describing the ground state associated with the single particle potential $(\Lambda_n/2)X^2$ ($(\Lambda_e/2)x^2$). This means that for large values of N_n or N_e the reduced single particle density matrices of nuclei and electrons approach pure states disentangled from the rest of the system.

We observe in Fig. 10.9 that both nucleus and electron entanglements decrease (the color is getting less dark) when the number of nuclei and/or electrons are increasing. This decreasing rate is much larger for the electron entanglement than for the nucleus entanglement. This behavior is due to the difference between the masses of the subsystems which is much larger when we consider a single-electron as one of the subsystems. So, in Figs. 10.9a and 10.9b, we note that the nucleus entanglement is larger than the electron entanglement for the same set of relative parameters ($M = 1000$, $\tau_{ne} = 100$ and $\tau_{ee} = \tau_{nn}0100$). In

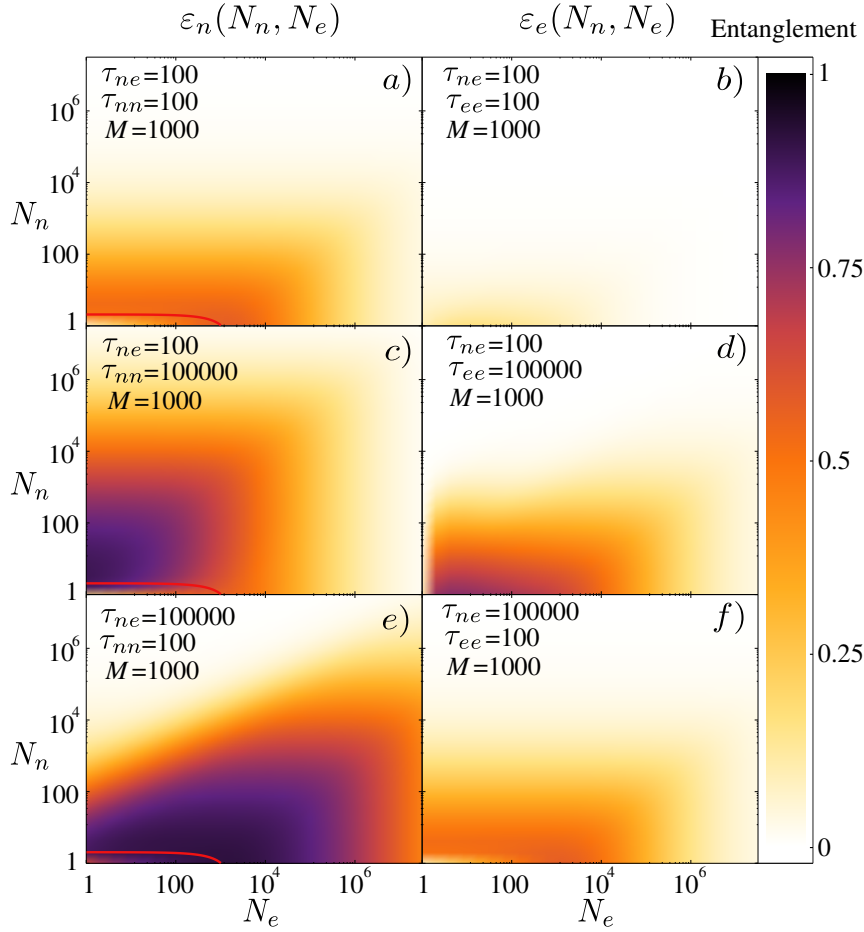


Figure 10.9: Nucleus entanglement (left panels) and electron entanglement (right panels) as a function of the number nuclei N_n and electrons N_e of the system for some relative interaction τ_{ne} , τ_{ee} , τ_{nn} and for the mass ratio $M = 1000$. Solid red lines contain the entanglement values of the subsystems with the number of nuclei and electrons fulfilling the equal subsystem masses relationship $M = (N_n - 1)M + N_e$.

both cases the entanglement decreases larger when the number of nuclei is increasing than when the number of electron does.

In Figs. 10.9c and 10.9d we shows both single-article entanglement when the particle-particle interaction strength is a thousand times stronger (namely, $\tau_{nn} = 100000$ and $\tau_{ee} = 100000$ in the former and latter cases, respectively), keeping fixed the other two parameters ($M = 1000$, $\tau_{ne} = 100$). In both cases we found higher entangled states than the exhibited in Figs. 10.9a) and b) respectively, indicating that the entanglement becomes much more robust when the interparticle interaction strength is increasing.

Finally, in Figs. 10.9e and 10.9f, the relative nucleus-electron interaction strength τ_{ne} is enhanced by a thousand factor (namely, $\tau_{ne} = 100000$) with respect to the cases a) and b). We find that the increasing τ_{ne} provokes a more robust entanglement in the two cases, although the enhancement rate is much larger for the nucleus entanglement than for the

electron entanglement when either the number of nuclei and/or the number of electrons is increasing. This effect is especially pronounced in the nucleus entanglement when N_e is increasing.

In order to clarify the entanglement behaviour for increasing size of the system we introduce the following dimensionless parameters describing the total mass ratios of the three different bipartitions of the system:

$$\gamma = \frac{N_n M}{N_e}, \quad (10.29)$$

$$\gamma_n = \frac{(N_n - 1)M + N_e}{M}, \quad (10.30)$$

$$\gamma_e = N_n M + N_e - 1. \quad (10.31)$$

As we have seen in this section the entanglement strongly depends on the relation between the masses of the consider subsystems. For very large or vanishing values of the total mass ratios γ , γ_n and γ_e entanglement tends to zero, and for finite values of these parameters the entanglement exhibits a finite value. Therefore, we can conclude that these total mass ratios are the decisive parameters that tell us how the entanglement behaves in the limit of very large system size. In table 10.2 we summarize the relation between the entanglement and the total mass ratio in those limits.

Parameters	γ	γ_n	γ_e	ε	ε_n	ε_e
$M \rightarrow \infty$	∞	$N_n - 1$	∞	0	finite	0
$N_n \rightarrow \infty$	∞	∞	∞	0	0	0
$N_e \rightarrow \infty$	0	∞	∞	0	0	0
$N_n \rightarrow \infty$ $N_e \rightarrow \infty$	M	∞	∞	maximum	0	0

Table 10.2: Asymptotic behavior of the entanglement with the size of the system.

10.5 Born-Oppenheimer approximation in the many-particle Moshinsky model

To find the approximate eigensolutions of the Hamiltonian H_x given by Eq. (10.1) we also use the Born-Oppenheimer approximation described in Section 10.1.3. In order to solve the differential equations for nuclei and electrons under the BO approximation we use again the dilatation coordinate change given in Eq. (10.8). The eigenfunctions $\Psi_{s,q}^{BO}(\mathbf{X}; \mathbf{x})$ and eigenenergies $E_q^{Elec}(\mathbf{X})$ are obtained introducing in Eqs. (10.6) and (10.7) the Jacobi coordinates change given by Eqs. (10.11) and (10.14). The nuclear and electronic quantum numbers sets $\{s_1, \dots, s_{N_n}\}$ and $\{q_1, \dots, q_{N_e}\}$ have been denoted for convenience by \mathbf{s} and \mathbf{q} , respectively. This treatment of the problem allows us to find a simple expression for the many-particle eigenfunctions of the Hamiltonian (10.1) in terms of Jacobi coordinates, as

$$\Psi_{s,q}^{BO}(\mathbf{X}; \mathbf{x}) = F_s(\mathbf{X}) \phi_q(\mathbf{X}; \mathbf{x}), \quad (10.32)$$

10.5. Born-Oppenheimer approximation in the many-particle Moshinsky model 167

being the nuclear eigenfunctions

$$F_{\mathbf{s}}(\mathbf{X}) = \prod_{i=1}^{N_n-1} \Phi_{s_i}^{\beta^{(n)}} \left(\sqrt{M} R_i(X_1, \dots, X_{i+1}) \right) \times \\ \times \Phi_{s_{N_n}}^{\beta_{N_n}^R} \left(\sqrt{M} R_{N_n}(X_1, \dots, X_{N_n}) \right) \quad (10.33)$$

and the electronic eigenfunctions

$$\phi_{\mathbf{q}}(\mathbf{X}; \mathbf{x}) = \prod_{j=1}^{N_e-1} \Phi_{q_j}^{\beta^{(e)}} (r_j(x_1, \dots, x_{j+1})) \times \\ \times \Phi_{q_{N_e}}^{\beta_{N_e}^e} (r_{N_e}(x_1, \dots, x_{N_e}) - \delta R_{N_n}(X_1, \dots, X_{N_n})) \quad (10.34)$$

with $\delta = \frac{\tau_{ne} \sqrt{N_n N_e}}{1 + N_n \tau_{ne}}$ and $\{r_j, R_i\}$ being the Jacobi variables defined in Eqs. (10.11) and (10.14). The one-dimensional harmonic eigenfunctions Φ_n^β are given by Eq. (10.23), likewise, the frequencies $\beta^{(n)}$ and $\beta^{(e)}$ are the same as obtained in the previous exact solution, as given by Eqs. (10.20) and (10.21), and the frequencies corresponding to the center of mass coordinates are given by

$$\beta_{N_n}^{(n)} = \frac{1 + (N_n + N_e) \tau_{ne}}{M(1 + N_n \tau_{ne})}, \quad \beta_{N_e}^{(e)} = 1 + N_n \tau_{ne}, \quad (10.35)$$

The energy of the hamiltonian system (10.1) under the Born-Oppenheimer approximation is

$$E_{\mathbf{s}, \mathbf{q}}^{BO} = \frac{k}{\sqrt{m_e}} \left(\sum_{j=1}^{N_n} \sqrt{\beta_j^{(n)}} \left(\frac{1}{2} + s_j \right) + \sum_{i=1}^{N_e} \sqrt{\beta_i^{(e)}} \left(\frac{1}{2} + q_i \right) \right). \quad (10.36)$$

We denote from now on the state associated to the wavefunction in Eq. (10.32) by $|\mathbf{s}; \mathbf{q}\rangle = |s_1, \dots, s_{N_n}; q_1, \dots, q_{N_e}\rangle$, i.e.

$$\Psi_{\mathbf{s}, \mathbf{q}}^{BO}(\mathbf{X}; \mathbf{x}) = \langle \mathbf{X}; \mathbf{x} | \mathbf{s}; \mathbf{q} \rangle, \quad (10.37)$$

so, the density matrix associated to the system H_x is given by

$$\rho_{\mathbf{s}, \mathbf{q}} = |\mathbf{s}; \mathbf{q}\rangle \langle \mathbf{s}; \mathbf{q}|, \quad (10.38)$$

As in the exact solution case all correlations between nuclei and electrons are induced by their respective centers of mass but in a different way.

The validity of the Born-Oppenheimer approach is closely related to the mass of the particles. It assumed that the motion of heavy particles (nuclei) is much slower than light ones (electrons). In this model it is straightforward to interpret that the independent harmonic frequencies of nuclei, $\sqrt{\beta^{(n)}}$, decreases with M , which fits the contribution of the counterpart (nuclei and electron) to the wavefunction, but not the electron ones, $\sqrt{\beta^{(e)}}$. When the particles are affected by an external potential with the same strength, the approximation becomes increasingly accurate as the mass difference of the particles (between nuclei and electrons) is increases.

As we have seen in previous Sections 10.3.1 and 10.4.1 the entanglement between nuclei and electrons vanishes for large M (also for small M). In the exact solution of the many-particle system, this is not evident given the complex dependence of the wave function on the mass M , but using the Born-Oppenheimer approximation one clearly realizes that this dependence is embedded in the nuclear frequencies of the independent harmonic oscillators, $\sqrt{\beta^{(n)}}$ and $\sqrt{\beta_{N_n}^r}$, of the wave function. Thus, when M increases (with $M > 1$), the contribution of nuclei to the total wavefunction becomes more relevant than the electronic one. For very large mass ratio ($M \rightarrow \infty$), the nuclear density $|F_s(\mathbf{X})|^2$ is getting closer to a delta-like function at the nuclear positions. Therefore, the electrons “feel” the nuclei as an external confining potential, and nuclei are virtually unaffected by electrons, thus losing any possibility of generating entangled states between nuclei and electrons.

The overlap is actually the toughest test that we can do, because it is not only related to observables, but to the wave function. The overlap between the exact and approximate one-dimensional wavefunctions in Eqs. (10.26) and (10.37) is given by the integral

$$\Theta_{u_1, u_2, \mathbf{n}, \mathbf{e} | \mathbf{s}; \mathbf{q}} = \langle u_1, u_2, \mathbf{n}, \mathbf{e} | \mathbf{s}; \mathbf{q} \rangle = \int_{-\infty}^{\infty} d\mathbf{X} d\mathbf{x} \Psi_{u_1, u_2, \mathbf{n}, \mathbf{e}}(\mathbf{X}, \mathbf{x}) \Psi_{\mathbf{s}; \mathbf{q}}^{BO}(\mathbf{X}; \mathbf{x}). \quad (10.39)$$

Here, we merely study the ground state, $\Theta_{gs} = \Theta_{0,0,0,0|0;0}$. All the wave function components Φ_V^β of the exact and approximate wave functions are the same, except those corresponding to the quantum numbers u_1 and u_2 of the exact wave function as well as s_{N_n} and q_{N_e} of the approximate one. So the overlap is independent of all quantum numbers except $u_1 = s_{N_n}$ and $u_2 = q_{N_e}$, as well as independent of the electron-electron τ_{ee} and nucleus-nucleus τ_{nn} interaction strengths.

In this section we compare the many-particle nuclei-electrons entanglement of the ground state computed with both methods, exact and approximate, as well as the overlap between the exact and approximate wavefunctions.

10.5.1 Helium-like atoms

We compare here the exact solution of the Helium-like atom ($N_n = 1$ and $N_e = 2$) obtained in Section 10.3 with the the Born-Oppenheimer ones. In Figure 10.10 we show the ground-state case of the overlap measure Θ_{gs} in Eq. (10.39) and compare the values of the entanglement ε exactly computed with the Born-Oppenheimer approximation.

From Figure 10.10 one can infer that: For large value of the interaction τ_{ne} the approximation is able to describe high entanglement states over a wide range of masses $M \gg 1$, being more accurate for increasing values of M until entanglement disappears. The atom size is of the order of the Bohr radius a_0 and the smaller atomic trap size of $b \sim 10^6 a_0$, so, the relative interaction strength is of the order of $\tau_{ne} = \lambda_{ne}/k \sim 10^{12}$. Taking into account this and that the proton-electron mass ratio is of the order $M_{HA} \approx 1836.15$, one finds that a Helium atom in a commonly harmonic trap has a highly (nucleus-electron) entangled state. The trace of the square marginal density matrix is of the order of $\text{Tr}[\rho_n^2] = 6.09507 \cdot 10^{-6}$, and the result provided by the BO approach has a relative error of 0.054%.

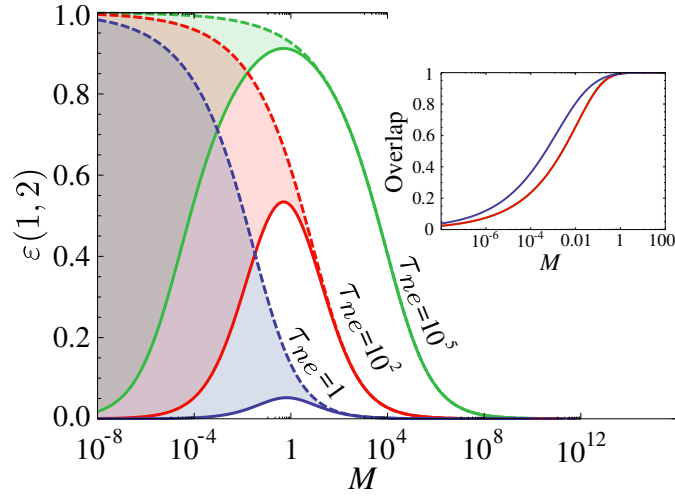


Figure 10.10: Nucleus-electrons entanglement $\varepsilon(1, 2)$ exactly computed (solid lines) and with the Born-Oppenheimer approximation (dashed lines) as well as the overlap $\Theta_{0,0}$ (inset figure) of the ground state as a function of the mass ratio M for different values of the relative nuclei-electrons interaction strengths $\tau_{ne} = 1, 10, 1000$. Shaded areas symbolize the deviation from the exact computed entanglement.

In addition to the BO approximation, when M is not very large, one may employ another commonly used approach to compute the linear entropy, as shown in Ref. [303]. Considering the integrals in Eq. (10.2) and using Eq. (10.5) one can assume that the nuclear wave function $F(\mathbf{X}')$ can be approximated by $F(\mathbf{X})$ when $|\mathbf{X} - \mathbf{X}'|$ is of the order of the atom size, whenever the relative nuclei-electrons interaction strength τ_{ne} is large enough. Moreover, we do not lose sight of the short mass range which is valid for both approximations; For very large M this last approximation gets worse and for M closer to 1 BO Approximation fails (see Fig. 10.11). This approach could simplify the computations of the entanglement in more complex and realistic systems. For the Helium atom, using both approaches, we found that the accuracy is mainly that given by the BO approximation, the relative error is almost the same that the relative error obtained using only the BO approximation, being able to describe high entangled states as shown in Fig. 10.11.

10.5.2 N-particles system

As noted in previous sections (see Figure 10.10) the accuracy of the Born-Oppenheimer approach is closely related to the mass ratio of the particles; we found as well a strong dependence on the number of particles composing the system. Besides the mass ratio M , in the system H_x studied here the accuracy of the Born-Oppenheimer approximation is strongly dependent on the numbers of nuclei N_n and electrons N_e ; more specifically, the accuracy of the approximation is better when the mass ratio between nuclei and electrons is large (*i.e.*, when $\gamma_{BO} = \frac{MN_n}{N_e} \gg 1$). This parameter can be increased in three different ways: Increasing M and N_n , in which case γ_{BO} can reach the maximum value $\gamma_{BO} \rightarrow \infty$, or decreasing N_e in which case the maximum value is given by $\gamma_{BO} = MN_n$. Fixing

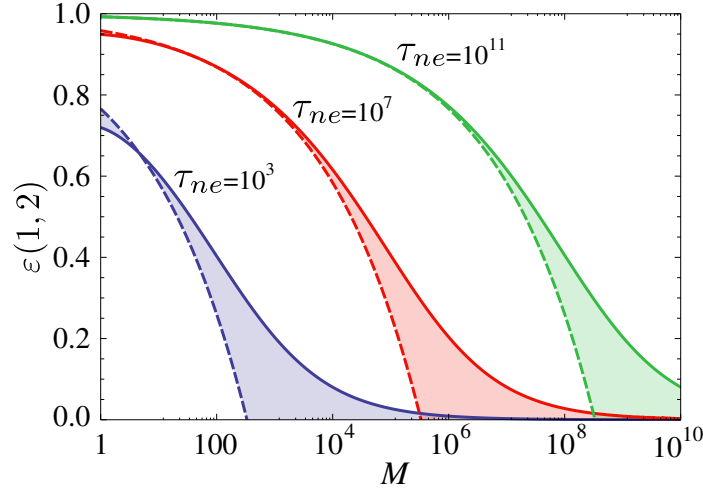


Figure 10.11: Dependence of the nuclei-electrons entanglement on the mass ratio M , computed exactly (solid lines) and with the Born-Oppenheimer approximation together with the further assumption that $|\mathbf{R} - \mathbf{R}'|$ is of the order of the atom size (dashed lines) for different values of the relative nucleus-electron interaction strength $\tau_{ne} = 10^3, 10^6, 10^9$.

any two parameters out of $(N_n, N_e$ and $M)$, the ground state overlap Θ_{gs} tends to 1 when $\gamma_{BO} \rightarrow \infty$ and all curves collapse (see Fig. 10.12 a)). Then, the three types of entanglement analyzed here, $\varepsilon(N_n, N_e)$, $\varepsilon_n(N_n, N_e)$ and $\varepsilon_e(N_n, N_e)$, are well described by the Born-Oppenheimer approximation whenever the parameter γ_{BO} is large enough.

The decisive parameter for the accuracy of the BO approximation in Eq. (10.37) is the total mass ratio γ_{BO} which coincides with the parameter $\gamma = \gamma_{BO}$ defined in Eq. (10.29). Therefore, in the limit of $\gamma_{BO} \rightarrow \infty$ one can assume that the approximation is correct, the nuclear component of the density is given by delta functions of the nuclei positions and there are no correlations between electrons and nuclei; entanglement $\varepsilon(N_n, N_e)$ must be null. On the other hand, this does not happen in the cases of $\varepsilon_n(N_n, N_e)$ and $\varepsilon_e(N_n, N_e)$ whose subsystems mass relation fulfills $\gamma_n \neq \gamma_{BO} \neq \gamma_e$. Finite or vanishing amount of $\varepsilon_n(N_n, N_e)$ and $\varepsilon_e(N_n, N_e)$ (see Figs. 10.12c) and d)) are according to the criteria of vanishing entanglement for $\gamma_{n,e} \rightarrow \infty$ and finite amount of entanglement for finite $\gamma_{n,e}$.

Conclusions

In this chapter we have investigated the entanglement properties of an one-dimensional N -particle system consisting of N_n nuclei and N_e electrons that interact harmonically with each other and, moreover, they are confined by an harmonic external potential. We have obtained closed analytical expressions for the amount of entanglement of (i) the ground and a few low lying excited states when $N = 3$, and (ii) the ground-state of the N -particle system. We focus on the entanglement associated with three different ways of partitioning the system. On the one hand, we consider the entanglement between all the electrons (regarded as one subsystem) and all the nuclei. On the other hand, we study the

10.5. Born-Oppenheimer approximation in the many-particle Moshinsky model 171

entanglement between one electron (nucleus) and the rest of the system.

While the nuclei-electrons entanglement depends upon the relative strength of the nucleus-electron interaction τ_{ne} , the nucleus (electron) entanglement depends on both τ_{ne} and τ_{nn} (τ_{ee}) that measures the relative nucleus-nucleus (electron-electron) interaction strength. As a general trend in all three cases, we found that entanglement increases as a function of the (corresponding) interaction parameter, approaching its maximum possible value in the limit of an infinitely large interaction. When the mass ratio is $M = 1$, excited states exhibit a finite amount of entanglement even in the case of arbitrarily weak interaction. The latter is related to the degeneracy of the energy levels of the Hamiltonian describing non-interacting particles.

For the N -particle system we computed the entanglement exhibited by the three different bipartitions of the ground state as a function of the system size and the mass ratio. For the three bipartitions we studied the adequate relationship between the number of particles and the mass ratio in order to obtain highly entangled states. We found that for large enough values of τ_{ne} , the nuclei-electrons entanglement is maximum when the mass of the two considered subsystems is (almost) the same. However, when the interaction strength tends to zero $\tau_{ne} \rightarrow 0$, the maximum entanglement is obtained when $M = 1$. All the three studied entanglements vanish when the corresponding subsystems have very different masses. We explored the connection of this fact, when $M \gg 1$, and the validity of the BO approximation. To estimate the quality of this approximation we studied the overlap between the exact wave functions and the BO ones. We have also compared the entanglement of the exact wave functions of the system and the entanglement provided by the BO approximation. We found that the overlap increases for increasing values of M . The decay of the entanglement due to the increasing difference of the masses of the subsystems is well described by the entanglement of the wavefunctions corresponding to the BO approximation, which gives rise to a nuclear density approaching a Dirac delta function located at the nuclei positions.

The main mass effects on the entanglement properties of the system investigated here comprise two regimes: On the one hand we have subsystems of widely different masses, and on the other hand we have subsystems having comparable masses. In the first case we found that the entanglement between the two parts tends to vanish when the mass ratio goes to infinity (or to zero). This result is fully consistent with what happens in quantum chemistry and molecular physics, where the mass of nuclei is indeed much larger than the electron mass. In this regime the Born-Oppenheimer approximation applies. It is worth stressing, however, that the Born-Oppenheimer Ansatz does not constitute a zero-entanglement approximation. In fact, we have shown in the present work that the Born-Oppenheimer approximation provides a good description of the system even in cases where it exhibits an appreciable amount of entanglement. The second of the aforementioned regimes, where the masses of the subsystems are approximately equal, is the one where entanglement takes its maximum value. In summary, when it comes to mass end entanglement, interacting parts of the model studied here exhibit a "like-to-like" behavior: when the system is partitioned in two interacting subsystems, these parts tend to be highly entangled with each other when they have similar masses. It would be interesting to investigate to what extent this is a universal trend verified by composite quantum systems with continuous degrees of freedom.

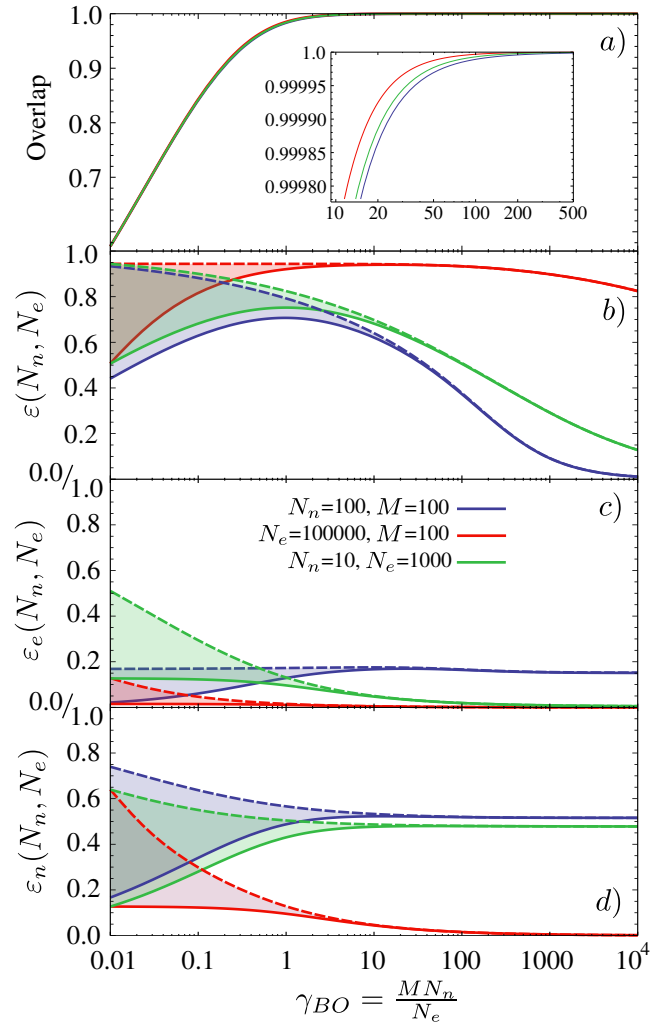


Figure 10.12: Comparison of the exact and BO approximation of the many-particle system increasing γ_{BO} in three different ways: increasing M , increasing N_n or decreasing N_e . *a)* Overlap between the exact and approximated wavefunctions. *b)* Nuclei-electrons, *c)* single-electron and *d)* single-nucleus entanglement computed with both exact and BO wavefunctions.

Part III

Entanglement and interference of composite bosons

Table of Contents

Introduction	177
11 Composite bosons: Foundations	179
11.1 Second quantization	179
11.2 Many-coboson states	180
11.2.1 Composite boson operator	180
11.2.2 Non-ideal behavior of many-coboson states	181
11.2.3 Normalization factor: Fermions and bosons	182
12 Bosonic behavior of entangled Fermions	185
12.1 Normalization factor of two-fermion composite bosons	185
12.1.1 Normalization and entanglement	185
12.1.2 Normalization ratio as a measure of bosonic behavior	187
12.2 Tight bounds on the normalization ratio	187
12.2.1 Extremal entangled states	188
12.2.2 Normalization ratio for extremal states	189
12.3 Illustration and interpretation of bounds	190
12.3.1 Upper and lower bounds	190
12.3.2 Limit of many particles	191
Conclusions	193
13 Collective interference of composite two-fermion bosons	195
13.1 Beam splitter dynamics: Hong-Ou-Mandel (HOM) effect	196
13.1.1 Two particles interference	196
13.1.2 Many bosons interference	201
13.1.3 Bosons macroscopic approach	202

13.2 Physical model	203
13.3 Coboson state, preparation	204
13.4 Behavior of cobosons under beam-splitter dynamics	206
13.5 Evaluation of counting statistics	210
13.6 Many cobosons interference in the macroscopic approach	213
Conclusions	214
Appendix A Single-particle densities	217
Appendix B Proof of bounds on the cobosons normalization ratio	219
B.1 Uniforming and peaking operations	219
B.2 Normalization ratio under operations	220
Concluding remarks	225
Conclusiones	229
Bibliography	235

Introduction

The composition principle, based on the treatment of composite particles as elementary objects despite their underlying structure, is a fundamental pillar of natural science [304]. In the microscopic world governed by quantum mechanics, from hadrons at the highest achievable energies [305] to ultracold molecules [306], the composition principle allows us to treat particles with integer spin as elementary bosons. This treatment can greatly simplify the understanding of the many-body behavior and the statistical physics of composite bosons; but when can we confidently apply it and reliably treat two bound fermions as a boson?

The hierarchy of energy scales in nature would appear to provide an answer, and one intuitively expects that the bosonic behavior of bound fermions relies on their strong binding. For example, weakening the bound between fermions indeed leads to the Bose-Einstein-Condensates Bose-Superconductivity (BEC-BCS) crossover [307]. However, even when the constituents of *cobosons* [308], *i.e.* of compounds constituted of two fermions, are perfectly bounded, it is not granted that the creation and annihilation operators of cobosons obey the bosonic commutation relations and exhibit perfect bosonic behavior: The Pauli principle for the underlying constituents may become relevant and thus jeopardize bosonic dynamics [309, 303, 310, 311, 308, 312, 313, 314]. For good bosonic behavior, the occupation probability of any single-fermion state must be low enough, such that the constituent fermions of the cobosons do not compete for available single-fermion states.

A satisfactory answer to the above question was given by C.K. Law [309] using the tools of quantum information: Independently of the actual physical system and of the binding strength between the constituents, the bosonic behavior of cobosons is intimately related to the *entanglement* between the constituting fermions, and the impact of the Pauli principle fades away with increasing entanglement. This result was substantially improved by C. Chudzicki, O. Oke and W.K. Wootters, who obtained rigorous upper and lower bounds on the “non-ideal” bosonic behavior in terms of the entanglement in Ref. [303]. Recently, several works have been done in this direction, *e.g.* the validity of Pauli principle in composite systems of two identical fermions, one of them entangled with a distinguishable particle, where the exclusion principle cannot be applied have been studied in [315]. The necessary conditions for systems composed by two distinguishable fermions to exhibit bosonic behavior based on the entanglement, local operations, classical communication and the majorization criterion for probability distributions have been studied in Ref. [316] or regarding composite bosons as deformed oscillators enabling to study non-ideal boson states and their inter-component entanglement in [317].

Then, two bound and entangled fermions form a composite boson, which can be treated as an elementary boson as long as the Pauli principle does not affect the behavior of many of such composite bosons. The departure of ideal bosonic behavior is quantified by the normalization ratio of multi-composite-boson states. In Chapter 12, we derive the two-fermion-states that extremize the normalization ratio for a fixed single-fermion purity P , and establish general tight bounds for this indicator. For very small purities, $P < 1/N^2$

with N being the number of such composite bosons, the upper and lower bounds converge, which allows to quantify accurately the departure from perfectly bosonic behavior, for any state of many composite bosons.

The concept of matter waves represents a cornerstone of quantum physics. It was proposed by de Broglie in 1923 [318] and, since then, many experiments have demonstrated diffraction of electrons [319], atoms [320] and molecules [321]. These early achievements led to the field of atom optics and interferometry [320, 322].

Sources of macroscopically coherent matter waves became available with the realization of Bose-Einstein condensates (BECs) [323]. The interference between two BECs was first observed by Andrews et al [324]. This landmark experiment evidenced interference between two independent sources and revealed the relative phase between them as described theoretically in Ref. [325]. Trapped ultracold atoms typically feature very large electron-state entanglement [303, 311] and interferometers with large entangled atomic ensembles are also achievable using Bose-Einstein condensates [326]. However, the impact of imperfect bosonic behavior is greater the lower the entanglement is between fermions. Macroscopically coherent molecular matter waves was found in molecular Bose-Einstein condensates (mBECs) of two bound fermionic atoms [327, 306], whose interaction is tunable by Feshbach resonance [328]. The interference of two such mBECs have been conducted to demonstrate interference as a tool for investigating condensates of atom pairs [329]. Feshbach molecules are constituted by artificially bound atoms in a lower interaction regime and, therefore, constituting one of the composite two-fermion systems in which the non-ideal bosonic character will be necessarily patent.

In Chapter 13 we demonstrated that the composite character of two-fermion bosons manifests itself in the interference of many composites as a deviation from the ideal bosonic behavior. We represent a state of many composite as a superposition of different numbers of perfect bosons and fermions, which allows us to provide the full Hong-Ou-Mandel-like counting statistics of interfering composites. Our theory quantitatively relates the deviation from the ideal bosonic interference pattern to the entanglement of the fermions within a single composite boson.

First of all, in Chapter 11, we review the concepts and methods that are necessary for an accurate treatment of composite particles and for the understanding of its quantum statistics.

Composite bosons: Foundations

In this chapter we review some fundamental concept related to composite bosons which consist of two elementary particles, fermions or bosons. Their commutation relations, states of many of these composite particles and the framework in which they endorse, *i.e.* second quantization are drawn.

11.1 Second quantization

In this part of the thesis we use the second quantization framework which by construction admits only states that possess the required symmetry property and, consequently, all information about the state is already contained in the mere indication of the occupation number of each single particle state. Fermionic and bosonic states can thus be represented in the occupation representation of the state $|\Psi\rangle$ of the system, corresponding to Fock states, as follows:

$$|r_1, r_2, \dots, r_N\rangle_{F/B} \equiv |\Psi\rangle_{F/B} = |\underbrace{\phi_1, \dots, \phi_1}_{r_1}; \underbrace{\phi_2, \dots, \phi_2}_{r_2}; \dots; \underbrace{\phi_N, \dots, \phi_N}_{r_N}\rangle_{F/B} \quad (11.1)$$

where r_i is the the number of particles which are in a state labeled by i . We use the bosonic particle creation operator, \hat{g}_k^\dagger , for the construction of Fock states of bosons, which increases by one the number of particles in a specific single-particle quantum state,

$$\hat{g}_k^\dagger |r_1, \dots, r_k, \dots, r_N\rangle_B = \sqrt{r_k + 1} |r_1, \dots, r_k + 1, \dots, r_N\rangle_B. \quad (11.2)$$

These properties lead to the bosonic commutation relations,

$$[\hat{g}_i, \hat{g}_j^\dagger] = \delta_{i,j}, \quad \text{and} \quad [\hat{g}_i, \hat{g}_j] = [\hat{g}_i^\dagger, \hat{g}_j^\dagger] = 0. \quad (11.3)$$

For fermions, the Pauli principle prohibits the multiple occupation of any single-particle state such that the fermionic creation operator must fulfil

$$\hat{f}_k^\dagger |r_1, \dots, r_k, \dots, r_N\rangle_F = \delta_{r_k,0} (-1)^{r_1 + \dots + r_{k-1}} |r_1, \dots, r_k + 1, \dots, r_N\rangle_F \quad (11.4)$$

where we use the fermionic creation operator \hat{f}_k^\dagger and which leads to the anti-commutation relations for fermions,

$$\{\hat{f}_i, \hat{f}_j^\dagger\} = \delta_{i,j}, \quad \text{and} \quad \{\hat{f}_i, \hat{f}_j\} = \{\hat{f}_i^\dagger, \hat{f}_j^\dagger\} = 0. \quad (11.5)$$

Particularly, adding one and two fermions to the vacuum state $|0\rangle$ provides

$$\hat{f}_i^\dagger |0\rangle_F = |1\rangle_F, \quad \text{and} \quad \hat{f}_i^\dagger |1\rangle_F = -|1, 1\rangle_F \quad (11.6)$$

respectively.

11.2 Many-coboson states

To describe states of many-composite bosons, we follow the formalism of [309, 303]. We examine the composite representation of two-particle systems in a pure state in terms of the creation \hat{c}^\dagger and annihilation \hat{c} operators. The state of many-cobosons is defined and its non-ideal bosonic character is pointed out and related to the normalization factor χ_N , which we analyze for maximally entangled states.

11.2.1 Composite boson operator

Consider a composite boson formed from two distinguishable particles A and B described by wavefunction $\Psi(x_a, x_b)$, where $x_{a/b}$ are vectors in any dimensions. As seen in previous section, we can always write this wave function in its Schmidt decomposition, Eq. (8.16), yields

$$\Psi(x_a, x_b) = \sum_{j=0}^S \sqrt{\lambda_j} \phi_j^{(a)}(x_a) \phi_j^{(b)}(x_b) \quad (11.7)$$

i.e. a sum over only one index j , being $\phi_j^{(a)}(x_a)$ and $\phi_j^{(b)}(x_b)$ the Schmidt modes, which constitute orthonormal bases for the states of particles A and B . Schmidt coefficients λ_i are the non-negative eigenvalues of each of the single-particle reduced density matrices satisfying $\sum_j \lambda_j = 1$, and the number of Schmidt coefficients is denoted by S .

In the second quantized representation, the state generated by the coboson creation operator

$$\hat{c}^\dagger = \sum_{j=0}^S \sqrt{\lambda_j} \hat{a}_j^\dagger \hat{b}_j^\dagger \quad (11.8)$$

acting on the vacuum, $|1\rangle = \hat{c}^\dagger |0\rangle$, corresponds to the wavefunction in Eq. (11.7). The operator \hat{a}^\dagger creates a particle A in the state (or Schmidt mode) $\phi_j^{(a)}(x_a)$ and \hat{b}^\dagger creates a particle B in the state $\phi_j^{(b)}(x_b)$. Thereby, the bound particles, \hat{a}_j^\dagger and \hat{b}_j^\dagger , compose the coboson \hat{c}^\dagger as a arbitrary superposition of all single-particle state j weighted by λ_j . The creation and annihilation cobosons operators, \hat{c}^\dagger and \hat{c} , obey the commutation relations

$$[\hat{c}, \hat{c}] = [\hat{c}^\dagger, \hat{c}^\dagger] = 0 \quad (11.9)$$

always, for both bound fermions and bound bosons. On the other hand, we find that

$$[\hat{c}, \hat{c}^\dagger] = (1 + s\Delta), \quad (11.10)$$

where $s = -1$ if A and B are fermions and $s = +1$ if they are bosons. The operator Δ is defined by

$$\Delta = \sum_{j=1}^S \lambda_j \left(\hat{a}_j^\dagger \hat{a}_j + \hat{b}_j^\dagger \hat{b}_j \right), \quad (11.11)$$

which has nonzero matrix elements, depending on the states involved. Therefore, \hat{c} and \hat{c}^\dagger are not strictly bosonic operators (Δ , in Eq. (11.10), does not necessarily adopt the value $\Delta = 1$).

11.2.2 Non-ideal behavior of many-coboson states

To examine the properties of \hat{c} and \hat{c}^\dagger , we consider a system containing two or more composite bosons which state is obtained by (anti)symmetrizing the product state of single-composite bosons, $\Psi(x_{1,a}, x_{2,b}) \cdots \Psi(x_{N,a}, x_{N,b})$, if the constituent particles are (fermion) boson. In terms of the creation operator \hat{c}^\dagger , we can write the properly (anti)symmetrized state of N composite bosons as

$$|N\rangle = (\chi_N)^{-1/2} \frac{(\hat{c}^\dagger)^N}{\sqrt{N!}} |0\rangle. \quad (11.12)$$

where χ_N is a normalization constant such that $\langle N|N\rangle = 1$, necessary because \hat{c}^\dagger is not a perfect bosonic creation operator. For N composite bosons, $(\hat{c}^\dagger)^N = \hat{c}_1^\dagger \cdots \hat{c}_N^\dagger$, and the commutation relations are given by

$$[\hat{c}_m, \hat{c}_k] = [\hat{c}_m^\dagger, \hat{c}_k^\dagger] = 0, \quad \text{and} \quad [\hat{c}_m, \hat{c}_k^\dagger] = \delta_{m,k}(1 + s\Delta), \quad (11.13)$$

so, in this case

$$\Delta = \sum_{j=1}^S \lambda_j \left(\hat{a}_{k,j}^\dagger \hat{a}_{k,j} + \hat{b}_{k,j}^\dagger \hat{b}_{k,j} \right), \quad (11.14)$$

being $\hat{a}_{k,j}^\dagger$ and $\hat{b}_{k,j}^\dagger$ the operators of the bound particles which compose the coboson \hat{c}_k^\dagger as an arbitrary superposition of the $\hat{c}_k^\dagger = \sum_{j=1}^S \sqrt{\lambda_j} \hat{a}_{k,j}^\dagger \hat{b}_{k,j}^\dagger$.

The state that results from adding a coboson to the state $|N\rangle$ does not necessarily behave as a boson operator fulfilling $\hat{c}^\dagger |N\rangle \rightarrow \sqrt{N+1} |N+1\rangle$. Rather, in Ref. [309], it follows from the definition in Eq. (11.12) that

$$\hat{c}^\dagger |N\rangle = \alpha_N \sqrt{N+1} |N+1\rangle, \quad (11.15)$$

where

$$\alpha_N = \sqrt{\frac{\chi_N}{\chi_{N-1}}} \quad (11.16)$$

is a constant. Similarly, instead of $\hat{c} |N\rangle \rightarrow \sqrt{N} |N-1\rangle$, for the annihilation operator one has

$$\hat{c} |N\rangle = \alpha_N \sqrt{N} |N-1\rangle + |\varepsilon_N\rangle, \quad (11.17)$$

where the correction term $|\varepsilon_N\rangle$ is orthogonal to $|N\rangle$. Such a correction term is necessary because the set of states $\{|1\rangle, \dots, |N\rangle\}$ is a subset of the entire Hilbert space associated

with the constituent particles. A nonideal bosonic operator would inevitably cause transitions into the states not described by Eq. (11.12).

From Eq. (11.17), one can assume that the annihilation operator \hat{c} is bosonic if the following two conditions are satisfied:

$$\alpha_N = 1, \quad (11.18)$$

$$\langle \varepsilon_N | \varepsilon_N \rangle = 0. \quad (11.19)$$

The actual value $\langle \varepsilon_N | \varepsilon_N \rangle$ is given by [309, 330, 331]

$$\langle \varepsilon_N | \varepsilon_N \rangle = 1 - \frac{\chi_N}{\chi_{N-1}} + (N-1) \frac{\chi_{N+1}}{\chi_N}. \quad (11.20)$$

Therefore, the conditions (11.18) and (11.19) are controlled by the ratio of normalization constants. An ideal composite boson emerges in the limit $\frac{\chi_{N+1}}{\chi_N} \rightarrow 1$. We will explain in detail the relation of this normalization ratio with the entanglement in Chapter 12.

11.2.3 Normalization factor: Fermions and bosons

The quantity χ_N is given by [331, 309]

$$\chi_N = \frac{1}{N!} \langle 0 | \hat{c}^N (\hat{c}^\dagger)^N | 0 \rangle = \sum_{p_1, \dots, p_N} \lambda_{p_1} \lambda_{p_2} \cdots \lambda_{p_N} \quad (11.21)$$

The sum runs over all the indices appearing in the summand, with the different restriction if the constituent are fermions or bosons. By counting the states allowed for fermions and bosons, it can be shown that χ_N^F and χ_N^B are given by [309]

$$\chi_N^F = N! \sum_{0 \leq p_1 < \dots < p_N \leq S} \lambda_{p_1} \lambda_{p_2} \cdots \lambda_{p_N}, \quad \text{if } A, B \text{ are fermions,} \quad (11.22)$$

$$\chi_N^B = N! \sum_{0 \leq p_1 \leq \dots \leq p_N \leq S} \lambda_{p_1} \lambda_{p_2} \cdots \lambda_{p_N}, \quad \text{if } A, B \text{ are bosons.} \quad (11.23)$$

The computation of these summations can be rather complicated for an arbitrary distribution of Schmidt coefficients in general and exact analytical expressions in closed forms, for both fermions and bosons, are rare. Nevertheless, in the case of fermions, χ_N^F , useful methods have been discussed in Refs. [332, 333]. These expressions give $\chi_N^F = 0$ if the number N of two-fermion composite bosons exceeds the number of Schmidt modes with nonzero Schmidt coefficients. In that case $(\hat{c}^\dagger)^N | 0 \rangle = 0$ and we cannot define the state $|N\rangle$.

For a given number S of Schmidt coefficients, the maximally entangled state is known to be the uniform state, *i.e.* all the Schmidt modes are occupied with the same probability ($\lambda_i = \frac{1}{S}$ for $i = 1, \dots, S$). In such state the normalization constants are easily analytically determined as follows:

$$\chi_N^F = \frac{S!}{S^N (S-N)!}, \quad \text{and} \quad \chi_N^B = \frac{(N+S-1)!}{S^N (S-1)!} \quad (11.24)$$

The uniform state of a composite boson is above-normalized when the compounds are fermions, that is, the normalization factor is above unity $\chi_N^F \geq 1$, which increases with N and decreases with S . On the other hand, for bosons, it is below-normalized, $0 < \chi_N^B \leq 1$, and is increasing (decreasing) with S (N). In the limit of a very large number of Schmidt coefficients, the normalization of the state is well preserved, that is $\lim_{S \rightarrow \infty} \chi_N^F = \lim_{S \rightarrow \infty} \chi_N^B = 1$. This means that by adding a coboson to the state $|N\rangle$, normalization is not preserved unless the number of accessible single-particle states S is large enough.

Bosonic behavior of entangled Fermions

As an indicator for the entanglement between the fermions, one may use the purity P of the reduced states of each fermion [5]: $1/P$ is the effective number of Schmidt modes, *i.e.* of populated single-fermion states. To treat cobosons as ideal bosons, evading the Pauli principle, there need to be many more single-particle states ($1/P$) than composites (N), *i.e.* $N \cdot P \ll 1$ [309]. The original argument in Ref. [309] was based on specific wavefunctions, and generalized to arbitrary states in Ref. [303], where general upper and lower bounds to the indicator of bosonic behavior (the ratio of normalization constants of many-coboson states that will be introduced in previous chapter) were found.

Here, we strength further the relationship between entanglement, as characterized by the purity of the single-fermion states, and the compositeness character of cobosons: We improve existing bounds and derive the explicit form of those quantum states that maximize and minimize the normalization ratio for a given purity P . Our bounds are optimal, since they are saturated by the extremal states found. The tight upper bound comes close to the lower bound when $N^2 \cdot P \ll 1$, *i.e.* in this regime, not only the deviation from perfectly bosonic behavior is small, but it can also be bounded very tightly via the purity.

In Section 12.1, we first present the formalism for the treatment of N -coboson states and review previous results on the normalization ratio related to the entanglement. Our main result, tight bounds for the normalization ratio, are derived in Section 12.2. Examples and a discussion of limiting extremal cases are then given in Section 12.3. We conclude with a combinatorial interpretation of the findings and an outlook on possible extensions and applications.

12.1 Normalization factor of two-fermion composite bosons

In what follows we consider that cobosons are constituted by two fermions. In this section we show the relationship between the power sum of the Schmidt coefficients distribution, which contains the particular case of the purity, and the normalization factor χ_N . We also present the normalization ratio, χ_{N+1}/χ_N , as a power series of the purity and review the original bound on this normalization ratio found in Ref. [303].

12.1.1 Normalization and entanglement

The creation operator given in Eq. (11.8), for a coboson constituted of distinguishable fermions can always be written in the Schmidt decomposition [309, 303], as described in

Section 11.2. Moreover, it is useful to write it in a Slater form [334] as

$$\hat{c}^\dagger = \sum_{j=1}^S \sqrt{\lambda_j} \hat{f}_{2j}^\dagger \hat{f}_{2j-1}^\dagger, \quad (12.1)$$

i.e. as a sum over only one index, where the λ_j are the Schmidt coefficients, and \hat{f}_j^\dagger creates a fermion in the Schmidt mode j . When we set $\hat{a}_j = \hat{f}_{2j}^\dagger$ and $\hat{b}_j = \hat{f}_{2j-1}^\dagger$ the form (11.8) is recovered.

The coboson normalization factor χ_N (χ_N^F in Eq. (11.22)), of a state of N composite bosons, Eq. (11.12), witnesses the possible departure from the familiar bosonic behavior [332, 309, 303, 313, 335]. The factor χ_N , leading to the normalization of the many-coboson state, $1 = \langle N|N \rangle$, is a completely symmetric polynomial in the Schmidt coefficients λ_j [336],

$$\chi_N = N! \sum_{1 \leq j_1 < \dots < j_N \leq S} \prod_{m=1}^N \lambda_{j_m}. \quad (12.2)$$

For ideal bosons, $\chi_N = 1$ for all N , while $\chi_N = 0$ when the number of cobosons N is larger than the number of available fermionic single-particle states, S .

The probability distribution $\vec{\lambda}$ is characterized by its power-sums [336, 316, 332]

$$M(m) = \sum_{j=1}^S \lambda_j^m, \quad (12.3)$$

where $M(1) = 1$ due to normalization, and $0 < M(2) = P \leq 1$ is the purity of the distribution $\vec{\lambda}$. Power-sums are also called frequency moments, which are directly related to the Rényi entropy of the distribution $\vec{\lambda}$, $H_{\text{Rényi}}^m(\vec{\lambda}) = \ln(M(m)) / (1 - m)$, which is the discrete version of the Rényi entropy $R_q[\rho]$ given in Eq. (1.5). The $M(m)$ are independent among themselves, but Jensen's and Hölder's inequalities [337] apply:

$$M(k-1)^{\frac{k-1}{k-2}} \leq M(k) \leq M(k-1)^{\frac{k}{k-1}}. \quad (12.4)$$

Using power-sums, the normalization constant can be expressed recursively [316],

$$\chi_N = (N-1)! \sum_{m=1}^N \frac{(-1)^{1+m}}{(N-m)!} M(m) \cdot \chi_{N-m}, \quad (12.5)$$

where we set $\chi_0 = 1$ for convenience.

Combinatorially speaking, the quantity χ_N is the probability that, given a set of N objects which are each randomly assigned a property j (with $1 \leq j \leq S$) with probability λ_j , all objects carry different properties. For example, for $S = 365$ and $\lambda_j = 1/365$, we obtain the solution to the “birthday problem”, *i.e.* the likelihood that all members of a group of N people have a different birthday. The power-sum $M(m)$ is the probability that, selecting m objects that each carry a property distributed according to λ_j , all m objects have the same property. Therefore, we have the simple relationship $\chi_2 = 1 - M(2)$, while the χ_N with $N \geq 3$ are functions of all $M(m)$ with $m \leq N$, as given by Eq. (12.5).

12.1.2 Normalization ratio as a measure of bosonic behavior

The normalization factor χ_N of a N -coboson state reflects the probability to create a state of N cobosons by the N -fold application of the coboson creation operator on the vacuum as pointed out in Section 11.2.2. The resulting state reads

$$\frac{(\hat{c}^\dagger)^N}{\sqrt{N!}} |0\rangle = \sum_{j_1 \neq j_2 \cdots \neq j_N}^{1 \leq j_m \leq S} \left(\prod_{k=1}^N \sqrt{\lambda_{j_k}} \hat{f}_{2j_k}^\dagger \hat{f}_{2j_{k-1}}^\dagger \right) |0\rangle, \quad (12.6)$$

i.e. it is a weighted superposition of *all* possibilities to distribute the pairs of fermions among the pairs of Schmidt modes (for fermion species a and b). Every pair of Schmidt modes $\hat{f}_{2j}^\dagger \hat{f}_{2j-1}^\dagger |0\rangle$ is – at most – occupied by one fermion pair, in close analogy to the birthday problem.

The normalization *ratio*, χ_{N+1}/χ_N , has emerged as a decisive indicator for the bosonic behavior of a state of N cobosons. For example, adding an additional coboson to a N -coboson state, *i.e.* applying the coboson creation operator, leads to the state (11.15)

$$\hat{c}^\dagger |N\rangle = \sqrt{\frac{\chi_{N+1}}{\chi_N}} \sqrt{N+1} |N+1\rangle, \quad (12.7)$$

i.e. the state is below-normalized: It is possible that the addition of the $(N+1)$ st coboson be inhibited by the Pauli principle, which occurs with probability $1 - \chi_{N+1}/\chi_N$. Similarly, the departure of the expectation value of the commutator $[\hat{c}, \hat{c}^\dagger]$, which is unity in the ideal case, reads [309]

$$\langle N | [\hat{c}, \hat{c}^\dagger] |N\rangle = 2 \frac{\chi_{N+1}}{\chi_N} - 1. \quad (12.8)$$

The evaluation of χ_N scales prohibitively as the number of particles N increases, even when using the recursive formula (12.5) [338]. Approximations to the normalization factor in terms of easily accessible quantities, such as the purity $P \equiv M(2)$, are thus desirable. From Eq. (12.5) and for small $N \cdot P$, a series expansion can be derived [316, 314],

$$\begin{aligned} \frac{\chi_{N+1}}{\chi_N} &\approx 1 - N \cdot P + N^2(M(3) - P^2) + \\ &+ \mathcal{O}(N^3(M(4) + 2P^3 - 2P M(3))). \end{aligned} \quad (12.9)$$

On the other hand, an upper and a lower bound to the normalization ratio were found [303],

$$1 - P \cdot N \leq \frac{\chi_{N+1}}{\chi_N} \leq 1 - P. \quad (12.10)$$

However, the upper bound $1 - P$ is independent of N and cannot be saturated, and the form of typical states that maximize the ratio is not known.

12.2 Tight bounds on the normalization ratio

Here, we derive tighter bounds, find the quantum states that saturate these bounds, and give a physical interpretation for their optimality.

12.2.1 Extremal entangled states

We are interested in the possible values of the normalization ratio χ_{N+1}/χ_N for a given P . In order to find the extremal values of χ_{N+1}/χ_N , we maximize and minimize this quantity under the constraints $M(1) = 1, M(2) = P$.

Given a finite P , the number S of non-vanishing λ_j is bound from below by L , the smallest integer that is equal to or larger than $1/P$:

$$S \geq L = \left\lceil \frac{1}{P} \right\rceil. \quad (12.11)$$

Distributions $\vec{\lambda}$ with $S - 1$ equal coefficients [339] constitute extremal states, and will turn out to minimize or maximize χ_{N+1}/χ_N . We thus define

$$\begin{aligned} \lambda_1^{(\pm)} &= \frac{1 \pm \sqrt{(S-1)(SP-1)}}{S}, \\ \lambda_{j \in \{2 \dots S\}}^{(\pm)} &= \frac{1 - \lambda_1^{(\pm)}}{S-1}. \end{aligned} \quad (12.12)$$

When we choose $S = L$, we obtain the *uniform distribution* $\vec{\lambda}^{(u)} = \vec{\lambda}_{(S=L)}^{(-)}$ with $\lambda_1^{(u)} \leq \lambda_{j \in \{2, \dots, L\}}^{(u)}$. This distribution minimizes the number of non-vanishing Schmidt coefficients.

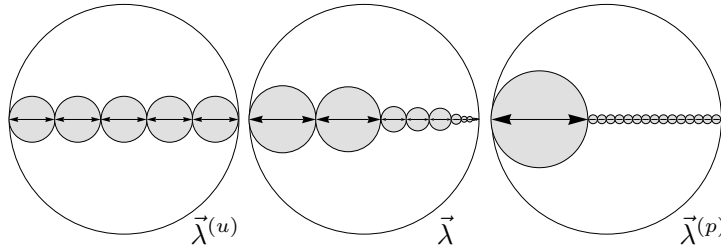


Figure 12.1: Visualization of probability distributions $\vec{\lambda}$ with a maximal number of Schmidt coefficients $S \leq 16$ and purity $P = 1/5$. The diameter of each filled circle represents the probability λ_j , its area is proportional to λ_j^2 . The diameters sum to unity, while the total area adds up to P . Distributions with the same occupied gray area thus have the same purity P , the three distributions shown cannot be distinguished via their purity P , but only through higher-order power-sums. Given $P = 1/5$, different distributions $\vec{\lambda}$ can lead to different normalization factors χ_N . The uniform distribution $\vec{\lambda}^{(u)}$ minimizes the normalization ratio, while the peaked distribution $\vec{\lambda}^{(p)}$ maximizes it under the chosen constraint $S \leq 16$.

For $S \geq L$, we find a *peaked distribution* $\vec{\lambda}^{(p)} = \vec{\lambda}_{(S \geq L)}^{(+)}$ that satisfies $\lambda_1^{(p)} \geq \lambda_{j \in \{2, \dots, S\}}^{(p)}$. In the limit $S \rightarrow \infty$, the peaked coefficient $\lambda_1^{(p)}$ converges to \sqrt{P} , while all other coefficients become vanishingly small, while the distribution always remains normalized and possesses the purity P . Choosing $P = 1/S$ implies $L = S$ and $\vec{\lambda}^{(p)} = \vec{\lambda}^{(u)}$, all coefficients are then identical and a maximally entangled state is obtained. In Fig. 12.1, we illustrate the uniform distribution $\vec{\lambda}^{(u)}$, a randomly chosen distribution $\vec{\lambda}$, and the peaked distribution $\vec{\lambda}^{(p)}$ with the same purity $P = 1/5$ and $S \leq 16$.

The peaked and the uniform distributions have extremal properties: For example, they saturate the bounds on the higher-order power-sums $M(k \geq 3)$, given by Eq. (12.4). In the limit $S \rightarrow \infty$, we have

$$M^{(p)}(k) = \sqrt{P} \cdot M^{(p)}(k-1), \quad (12.13)$$

and, for fractional values $P = 1/L$, we find for the uniform distribution:

$$M^{(u)}(k) = P \cdot M^{(u)}(k-1). \quad (12.14)$$

Combinatorially speaking, given the probability to find a pair of objects with the same property (*i.e.* given the value $P = M(2)$), the probability $M(3)$ to find three objects with the same property for three randomly chosen objects is maximized by the $\vec{\lambda}^{(p)}$ and minimized by the $\vec{\lambda}^{(u)}$ distributions.

12.2.2 Normalization ratio for extremal states

Since only two different non-vanishing values of λ_j appear for the uniform and the peaked distributions, the normalization ratio can be computed explicitly for these extremal distributions:

$$\frac{\chi_{N+1}^{(p)}}{\chi_N^{(p)}} = \frac{(S-N)(1-P) \left(S-1 + N\sqrt{(S-1)(SP-1)} \right)}{(S-1) \left(S + S(N-1)P - N \left[1 - \sqrt{(S-1)(SP-1)} \right] \right)}, \quad (12.15)$$

$$\frac{\chi_{N+1}^{(u)}}{\chi_N^{(u)}} = \frac{(L-N)(1-P) \left(L-1 - N\sqrt{(L-1)(LP-1)} \right)}{(L-1) \left(L + L(N-1)P - N \left[1 + \sqrt{(L-1)(LP-1)} \right] \right)}, \quad (12.16)$$

where $\chi_N^{(u/p)}$ is the normalization factor for the uniform/peaked distribution. We can now formulate our tight bounds on χ_{N+1}/χ_N , given an arbitrary distribution $\vec{\lambda}$ of S Schmidt coefficients:

$$1 - P \cdot N \stackrel{(i)}{\leq} \frac{\chi_{N+1}^{(u)}}{\chi_N^{(u)}} \stackrel{(ii)}{\leq} \frac{\chi_{N+1}}{\chi_N} \stackrel{(iii)}{\leq} \frac{\chi_{N+1}^{(p)}}{\chi_N^{(p)}} \leq \lim_{S \rightarrow \infty} \frac{\chi_{N+1}^{(p)}}{\chi_N^{(p)}} \stackrel{(iv)}{=} \mathcal{U}_N(P) \stackrel{(v)}{\leq} 1 - P, \quad (12.17)$$

where $\chi_{N+1}^{(p)}/\chi_N^{(p)}$ is computed for the finite S defined by $\vec{\lambda}$, and we define the upper bound

$$\mathcal{U}_N(P) = 1 - \frac{P \cdot N}{1 + (N-1)\sqrt{P}}. \quad (12.18)$$

The inequalities in Eq. (12.10) are represented here by the extremal lower and upper bounds (i) and (v), which were first shown in Ref. [303], for an alternative proof see Ref. [335]. We prove the new bounds (ii) to (iv) in Appendix B, and discuss their physical implications in the following Section 12.3.

12.3 Illustration and interpretation of bounds

All bounds for $N = 2$ are illustrated in Fig. 12.2.

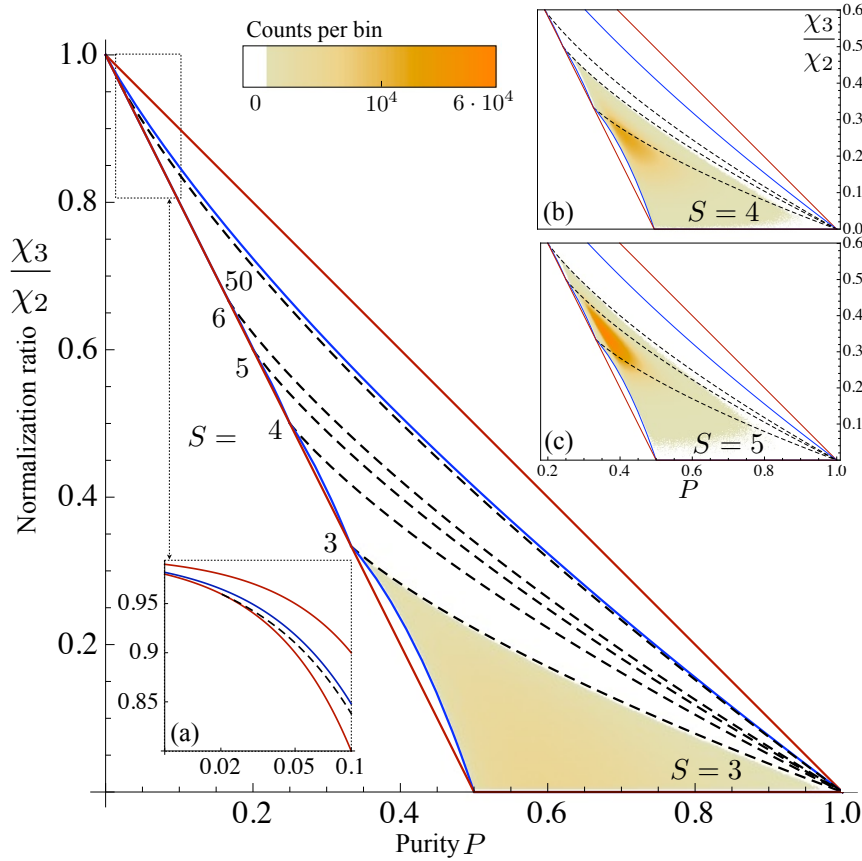


Figure 12.2: Bounds for the normalization ratio χ_3/χ_2 as a function of the purity P . The red solid lines indicate the extremal bounds in Eq. (12.17) found in Ref. [303]. The solid blue lines denote the tight bounds in Eq. (12.17) that can be achieved for any value of P . For a given maximal number of Schmidt-coefficients S , the black dashed lines are the corresponding upper bounds (for peaked states $\lambda^{(p)}$), which merge with the lower bound at $P = 1/S$. Inset (a): The scale in P is logarithmic, the (black dashed) upper bound for $S = 50$ is close to the total upper bound at $P = 1/10$, but it merges with the lower bound at $P = 1/50$. The distributions show the values numerically obtained for the normalization factor and the purity, for different fixed Schmidt numbers, $S = 3$ (main figure) and $S = 4, 5$ (insets (b), (c)).

12.3.1 Upper and lower bounds

The authors of Ref. [303] showed that the lower bound $1 - N \cdot P$ in Eq. (12.10) is attained for fractional values of P , *i.e.* for $P = 1/L = 1/S$. Setting $L = 1/P$ in Eq. (12.16) reproduces the bound, and $\chi_{N+1}^{(u)}/\chi_N^{(u)} = 1 - N \cdot P$. The saturation can also be observed

in Fig. 12.2: The tight lower bound (blue line) coincides with $1 - N \cdot P$ (red line) for fractional values of the purity $P = 1/S$. When $P \ll 1$, and thus $P \approx 1/L$, the tight bound (12.16) differs only marginally, while for large purities $P \lesssim 1/N$ the tight bound can differ significantly from $1 - N \cdot P$. In the limit $P \rightarrow 1/N$, the tight bound (12.16) and the previous bound $1 - N \cdot P$ differ by a factor $(1 + N)/2$.

In contrast to the previously established upper bound $1 - P$, our tight upper bound (12.17), *iv* depends on the number of particles N . When the number of non-vanishing Schmidt coefficients S is finite, the bound (12.15) is more efficient than the limiting case $S \rightarrow \infty$: In Fig. 12.2, the dashed black lines show the upper bound for finite S , while the blue line indicates the absolute upper bound. When the purity is decreased for a constant S , the upper and lower bounds eventually merge when $P = 1/S$ is attained (see also inset (a)).

The upper bound can be expanded in powers of \sqrt{P} :

$$\begin{aligned} \mathcal{U}_N(P) &= 1 - \sum_{k=2}^{\infty} P^{k/2} \frac{(1-N)^k N}{(N-1)^2} \\ &= 1 - \lim_{n \rightarrow \infty} \frac{N [(N-1)P + (1-N)^n P^{(n+1)/2}]}{(N-1)(1 + (N-1)\sqrt{P})}, \end{aligned} \quad (12.19)$$

with convergence radius $P < 1/(N-1)^2$. To second order, we then find

$$\mathcal{U}_N(P) \approx 1 - P \cdot N + P^{3/2}(N^2 - N) + \mathcal{O}(P^2), \quad (12.20)$$

i.e. the upper and lower bounds coincide in the limit $P \rightarrow 0$. Indeed, for $P \ll 1/(N-1)^2 \approx 1/N^2$, the denominator in Eq. (12.18), $1 + (N-1)\sqrt{P}$, is of the order of unity. This behavior is illustrated in Fig. 12.3, where we plot the deviation from perfect bosonic behavior, $1 - \chi_{N+1}/\chi_N$. The N -dependence of the new upper bound is apparent, as well as the convergence of the upper bound to the lower bound. In particular, the purity essentially defines the normalization ratio in the range $P \cdot N^2 \ll 1$.

In order to illustrate the typical behavior of random cobosons, we generated $3 \cdot 10^8$ random distributions $\vec{\lambda}$ [340], sampled according to the Haar measure [341, 340, 342]. Pairs $(P, \chi_3/\chi_2)$ are counted in a grid with 1000×1000 bins, which is translated to a color-code in Fig. 12.2. We generated states with $S = 3$ (main figure), $S = 4$ (inset (b)) and $S = 5$ (inset (c)) non-vanishing Schmidt coefficients. The bounds for finite S are indeed reached by randomly generated states. We also observe a concentration of states around the peak value of $(P, \chi_3/\chi_2)$ when the number of Schmidt modes S is increased: The vast majority of randomly generated states in high dimensions share very similar entanglement properties [343].

12.3.2 Limit of many particles

Surprisingly, increasing the number of particles at constant purity P does not always fully destroy bosonic behavior: The lower bound $1 - N \cdot P$ admittedly decreases with N when $P > 0$ and vanishes for $P = 1/N$ – the corresponding uniform state $\lambda^{(u)}$ consists of

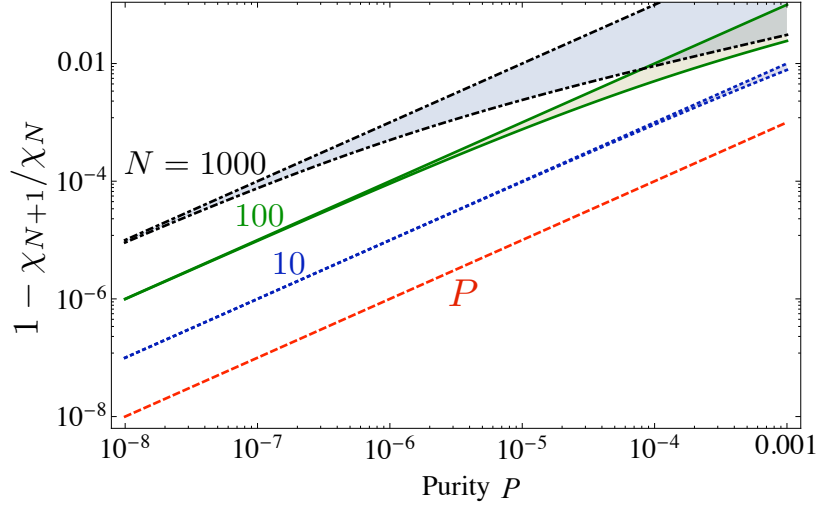


Figure 12.3: Deviation of the normalization ratio from unity, $1 - \chi_{N+1}/\chi_N$, as a function of the purity P , in log-log-representation. The red dashed line is the N -independent upper bound to χ_{N+1}/χ_N , *i.e.* here it represents the lower bound P to the deviation. The black dot-dashed, green solid and blue dotted lines indicate the tight bounds for $N = 1000$, $N = 100$, and $N = 10$, respectively. The previously found bound $1 - N \cdot P$ [303] and the tight bound (12.16) do not differ significantly in the present regime $P \ll 1$, they thus cannot be distinguished in the plot. The normalization ratio can take any value in the respective shaded areas. The deviation from ideal behavior as well as the gap between the upper and lower bound decrease with decreasing P .

a finite number $L = \lceil 1/P \rceil$ of Schmidt modes, such that at most L particles can be accommodated and $\chi_{L+1} = 0$. The peaked state, however, leads to non-vanishing χ_{N+1}/χ_N for arbitrarily large particle numbers: In the limit $N \rightarrow \infty$, we have

$$\mathcal{U}_N(P) \xrightarrow{N \rightarrow \infty} 1 - \sqrt{P}. \quad (12.21)$$

That is to say, for the peaked state the departure from bosonic behavior, as quantified by the ratio χ_{N+1}/χ_N , amounts to at most \sqrt{P} , for *any* number of particles N . This counter-intuitive result can be understood by the extremal form of the distribution $\vec{\lambda}^{(p)}$: When a fermion pair populates a Schmidt mode other than the first one (which is populated with probability \sqrt{P}), it can essentially be neglected for the impact of the Pauli principle on the next fermion pair, since there are arbitrarily many such modes that are occupied with vanishing probability (in the limit $S \rightarrow \infty$). Assuming that $N \gg 1$ particles were successfully prepared, the probability that the first pair of Schmidt modes is populated by some fermion pair is $1 - \sqrt{P}^N$, *i.e.* very close to unity. Adding an $(N + 1)$ st particle is thus successful when this last particle does not end in the first Schmidt mode, *i.e.* the success probability is $1 - \sqrt{P}$, just as given in (12.21). Colloquially speaking, there are always enough Schmidt modes to accommodate another particle. The last added particle must not, however, end in the first Schmidt mode, since the latter is occupied with nearly unit probability.

Although an N -coboson state still behaves bosonic to a certain degree, the normalization factor for such a state, given the peaked distribution $\vec{\lambda}^{(p)}$, is

$$\chi_N^{(p)} = \left(1 - \sqrt{P}\right)^{N-1} \left(1 + (N-1)\sqrt{P}\right), \quad (12.22)$$

which converges to zero for any $0 < P \leq 1$ in the limit $N \rightarrow \infty$. The analogous normalization factor for a uniform distribution (assuming $P = 1/L$) reads

$$\chi_N^{(u)} = \frac{1}{L^N} \frac{L!}{(L-N)!}, \quad (12.23)$$

which decays faster in N than $\chi_N^{(p)}$ and vanishes identically for $N > L$.

Conclusions and outlook

The N -coboson normalization ratio χ_{N+1}/χ_N was established as an important indicator for the composite behavior of non-elementary bosons [309]. Our main result is a new, N -dependent upper bound for χ_{N+1}/χ_N , and the explicit representation of the states that saturate this bound.

In the limit of small purities $P < 1/N^2$, the bosonic behavior of an N -coboson state is very tightly defined by P , since the lower and upper bounds merge. In practice, the purity of a bound pair of particles often satisfies $P \ll 1/N^2$, e.g. for atoms in a trapped BEC [311, 303]. Our bounds thus provide a simple and reliable way to quickly check the departure of bosonic behavior of any type of cobosons. With a combinatorial argument, we can understand this clear determination of bosonic behavior: For small purities $PN^2 < 1$, the probability to not finding N objects with different properties is essentially determined by the probability to find exactly one pair of objects with the same property, which is defined by $M(2)$. Triplets and larger combinations that depend on higher-order $M(k)$ are then essentially negligible.

When the purity is not very small, $P \approx 1/N$, however, the form of the wavefunction does play a role for bosonic behavior, which is then not entirely defined by P . It might be possible to access entanglement properties of bound fermions via the higher power-sums $M(m)$, which can be obtained by measuring χ_N [344].

Formally speaking, we found bounds to the completely symmetric polynomial (12.2) in terms of the first and second power-sums (12.3), $M(1) = 1$ and $M(2) \equiv P$. For tighter bounds, one could specify also the third power-sum, $M(3)$, and repeat the maximizing- and minimizing procedure of Appendix B to find those states that minimize/maximize χ_{N+1}/χ_N for given $M(1)$, $M(2)$, $M(3)$; this procedure could be extended to even higher orders. It is, however, not immediate how operations that are analogous to (B.3) and (B.4) but which leave $M(3)$ invariant can be constructed. In the typically encountered domain of small purities, $P \ll 1/N^2$, this endeavor is not an urgent desideratum, since the encountered bounds as a function of P are already tight. On the other hand, using relations between Rényi entropies of different orders [345, 346], our bounds can be re-formulated in terms of other indicators for entanglement, such as the Shannon entropy of $\vec{\lambda}$.

Given a fixed purity P , the uniform distribution $\vec{\lambda}^{(u)}$ minimizes the probability that the Pauli principle is irrelevant, while the peaked distribution maximizes it. In other words, the N^2 -coefficient $(M(3) - P^2)$ in the expansion (12.9) is maximized. Although a peaked or canyon distribution leads, in general, to a normalization ratio that is smaller than for the uniform distribution [335], this is mainly due to the consequent change of purity. For fixed purity P , the bosonic behavior of the uniform distribution is actually inferior with respect to the peaked one.

Combinatorially speaking, we have considered a variant of the birthday problem with non-uniform probabilities [338]. Here, Schmidt modes or single-particle quantum states take the role of birthdays [338, 347] or surnames [348]. Rather counter-intuitively, the optimal bosonic behavior for a fixed purity $P \equiv M(2)$ is found by *maximizing* the probability to find three objects with the same properties, *i.e.* $M(3)$. This result can be understood as follows: Any pair of objects that have the same property is as deleterious as any triplet (or any other m -tuple). The probability to find a pair, however, *decreases* with increasing $M(3)$. This decrease has a larger impact on the overall probability to find all objects with different properties than the consequent increase of the probability to find triplets with $M(3)$. For example, for $N = 3$, the probability to find a pair amounts to $3(P - M(3))$, the probability to find a triplet is $M(3)$. The overall probability to find all objects with different properties amounts to $1 - 3P + 2M(3)$.

To complement the analytical bounds, we have numerically generated random states, which do not only show a concentration around the most probable value of the purity P [343], but they also cluster around a certain value of the normalization ratio, consistent with the concentration-of-measure phenomenon. It remains to be studied how random states in higher dimensions behave in general, *i.e.* what is the *typical* normalization ratio and the distribution of states with a given purity.

Collective interference of composite two-fermion bosons

The quantum statistics of bosons is most apparent in correlation functions and counting statistics. Characteristic bosonic signatures are encountered for thermal states, which feature the Hanbury Brown and Twiss effect [349, 350, 351, 352], as well as in meticulously prepared Fock-states [353, 354, 355, 356], which exhibit Hong-Ou-Mandel-like (HOM) interference. Deviations from the ideal bosonic pattern in HOM setups are often caused by inaccuracies in the preparation of Fock-states and in the alignment of the setup, which induce partial distinguishability between the particles [353, 357, 358, 359]. Another source for deviations from perfect bosonic behavior has received only little attention, limited to mixed states [360, 344]: Since most bosons are composites (“cobosons”) made of an even number of fermions, reminiscences of underlying fermionic behavior are expected in many-coboson interference. In analogy to partially distinguishable particles [358, 359], one can intuitively anticipate that the many-coboson wave-function partially behaves in a fermionic way, with impact on the resulting counting statistics.

Here, we investigate such compositeness effects in HOM interferometry of cobosons. The ideal bosonic interference pattern is jeopardized by the Pauli principle that acts on the underlying fermions, an effect that becomes relevant when the constituents populate only a small set of single-fermion states. The effective number of single-fermion states can be related to the entanglement between the fermions, via the Schmidt decomposition. Not only does entanglement thus guarantee the irrelevance of the Pauli-principle for coboson states, but it also constitutes the very many-body coherence property that ensures that many-coboson interference matches the ideal bosonic pattern [355, 356]. The many-coboson wavefunction can be described as a superposition of different numbers of perfect bosons and fermions, with weights that are determined by the Schmidt coefficients. Using that intuitive representation, we compute the exact counting statistics in many-coboson interference and thus provide direct experimental observables for compositeness. Properties of the collective wave-function of the fermionic constituents can thus be extracted from coboson interference signals, while in the limit of truly many particles, particularly simple forms for the interference pattern emerge.

The bottomline of our discussion, the observable competition of fermions for single-particle states, is a rather general phenomenon that is not restricted to any particular physical system. To render our analysis of many-coboson interference tangible, however, we focus on an interferometric setup that can be realized with trapped ultracold atoms.

The agenda of this chapter is the following. In Section 13.1 we present the original Hong-Ou-Mandel effect on a beam splitter dynamics and the tangible two particle (of dif-

ferent nature) interference as well as the many-bosons interference and its macroscopic approach. We characterize the physical interference model of cobosons by a Fermi-Hubbard lattice model in Section 13.2 and in Section 13.3 argue the cobosons ground state preparation of this system. In Section 13.4 we show how the cobosons state describing the behavior of cobosons under beam-splitter dynamics is imitated exactly by a superposition of states with a different number of perfect bosons and fermions, and in Section 13.5 we carry out its corresponding valuation of counting statistics on the beam splitter dynamics as well as its macroscopic approach in Section 13.6. Finally the most important conclusions are given.

13.1 Beam splitter dynamics: Hong-Ou-Mandel (HOM) effect

The nature of bosons and fermions manifests itself impressively in the interference processes. Beam splitters are the simplest scattering setup, an essential component of many experiments designed to observe quantum effects [355]. When two identical particles are brought into a beam splitter and impinge on two opposite output ports simultaneously, one intuitively expects to find coincident events, *i.e.* events with one particle at each output port.

From the standpoint of classical probability theory, in a many particles interference one should expect that the counting statistic is governed by a binomial distribution in each of the output, occurring coincident events. Since fermions obey the Pauli principle, two fermions will never exit at the same mode of the beam splitter, and coincident events always occur. However, bosons always leave the setup together leading to an opposite effect. The original theoretical prediction and experimental realization were performed by C.K. Hong, Z.Y. Ou and L. Mandel in 1987 (Ref. [353]) where they predicted that coincidence rate of the output events will drop to zero when the input photons are perfectly identical regarding all properties and overlap perfectly in time, see Fig. 13.1. When the two photons are perfectly distinguishable, the “dip” completely disappears.

This correlated behavior, for both fermions and bosons, stems from the indistinguishability of the particles alone; no interaction between them takes place, which underlines the intriguing and intrinsically quantum character of the effect.

13.1.1 Two particles interference

Here we show the simplest cases of two particles that are scattered on a perfect beam splitter. The physical behavior can be understood in terms of an interplay of static two-path interference and the state space structure of bosons and fermions. We present four different scenarios which depend on the nature of the particles, distinguishable or indistinguishable (for identical particles we presents the cases where \hat{a}_q^\dagger corresponds to elementary bosons and fermions) as well as composites of two perfectly bound distinguishable fermions.

- **Distinguishable particles**

We can apply classical probability theory since no many-particle quantum effects take place. For a balanced beam splitter setup the probability for a single particle that is prepared in one input mode to fall into one of the output modes is $p = 1/2$

13.1. Beam splitter dynamics:

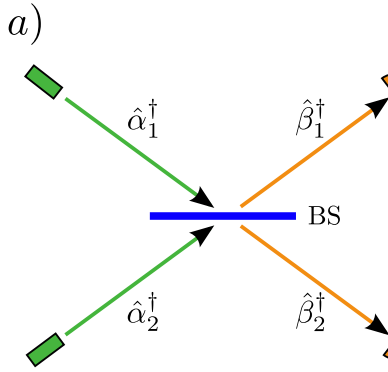


Figure 13.1: *a)* Beam splitter (BS) setup. *b)* Original prediction shown in [353] where variation of the position of the beam splitter gives rise to a vanishing coincidence events. The solid line denotes the ideal theoretical prediction, the dotted line takes into account experimental imperfections which reduce the visibility.

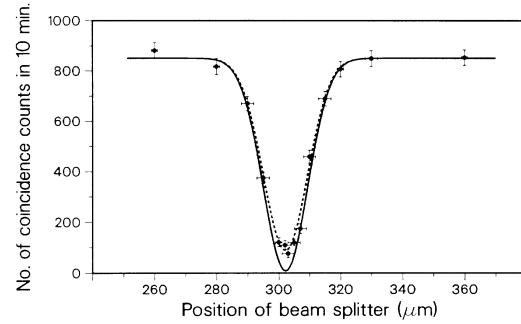


FIG. 2. The measured number of coincidences as a function of beam-splitter displacement $c \delta \tau$, superimposed on the solid theoretical prediction shown in [353] where $\Delta\omega = 3 \times 10^{13} \text{ rad s}^{-1}$. For the dashed curve the factor $2RT/(R^2 + T^2)$ in Eq. (11) was multiplied by 0.9. The vertical error bars are based on estimates of the measurement spread of the photoelectric pulses and the slewing of the discriminator pulses, a range of time intervals centered around the expected time of coincidence spread of several nanoseconds. For the purpose of the measurement, pulse pairs received within a 7.5-ns interval were treated as coincidences. Pulse pairs received within an interval of 35 to 80 ns were regarded as accidentals, and when scaled by the factor 7.5/45 provided a measure of the number of accidental coincidences that occur within any 7.5-ns interval.

and hence the probability $P_D(s_1, s_2)$ to find s_1 and s_2 particles in the first and in the second output mode, respectively, is given by a binomial distribution

$$P_D(s_1, s_2) = \binom{s_1 + s_2}{s_1} p^{s_1} (1-p)^{s_2} \quad (13.1)$$

For two particles one obtains the following possible probabilities

$$P_D(2, 0) = P_D(0, 2) = \frac{1}{4} \quad \text{and} \quad P_D(1, 1) = \frac{1}{2} \quad (13.2)$$

Since this situation can be fully understood in terms of classical probabilities, we will refer to it as the classical or distinguishable-particle situation.

• Identical particles

Let us consider $\hat{\alpha}_q^\dagger$ the creation operator of a distinguishable particle in mode q . Then, the initial state of two particles in the two input ports as depicted in Figure 13.1, can be written as

$$|\Psi_{in}\rangle = \hat{\alpha}_1^\dagger \hat{\alpha}_2^\dagger |0\rangle. \quad (13.3)$$

The action of the perfect beam splitter amounts to redirecting the incoming particles into a coherent superposition of the output modes [356, 358, 355]. The creation operators for particles in the input modes consequently evolve as follows:

$$\hat{\alpha}_1^\dagger \rightarrow \frac{1}{2} (\hat{\beta}_1^\dagger + \hat{\beta}_2^\dagger), \quad \text{and} \quad \hat{\alpha}_2^\dagger \rightarrow \frac{1}{2} (\hat{\beta}_1^\dagger - \hat{\beta}_2^\dagger). \quad (13.4)$$

Implementing this single-particle dynamics to the initial state in Eq. (13.3), we find the final state

$$|\Psi_{fin}\rangle = \frac{1}{2} \left((\hat{\beta}_1^\dagger)^2 - (\hat{\beta}_2^\dagger)^2 + \hat{\beta}_1^\dagger \hat{\beta}_2^\dagger - \hat{\beta}_2^\dagger \hat{\beta}_1^\dagger \right) |0\rangle, \quad (13.5)$$

and transmissivity show the combination $2RT/(R^2 + T^2)$ that N_c should fall close does not fall quite that lack of overlap of the side lobes, causing interference. The solid curve with $R/T=0.95$ and $\Delta\omega = 3 \times 10^{13} \text{ rad s}^{-1}$ if we identify $c \delta \tau$ with $(x - 302.5)$ in micrometers factor $2RT/(R^2 + T^2)$ less than perfect overlap. It will be seen that, exceeded quite well, corroborated about 100 fs.

We have therefore picosecond time interval implication the length of a fourth-order interference order interference, this path differences be kept wavelength. The method in which pairs of single comes less efficient for cause the ‘‘visibility’’ of and cannot exceed 50% the resolution could be in time.

This work was supported by the National Science Foundation and by the

¹See, for example, E. T. Whittaker, *Short Light Pulses*, Cambridge University Press, Cambridge, 1984, 2nd ed.
²I. Abram, R. K. Raj, *Phys. Rev. Lett.* **57**, 2516 (1986).
³D. C. Burnham and D. J. Kleppner, *Phys. Rev. Lett.* **36**, 84 (1970).
⁴C. K. Hong and L. Mandel, *Phys. Rev. Lett.* **54**, 2011 (1985).
⁵S. Friberg, C. K. Hong, and L. Mandel, *Phys. Rev. Lett.* **57**, 2516 (1986).
⁶R. Ghosh and L. Mandel, *Phys. Rev. Lett.* **57**, 2516 (1986).
⁷Z. Y. Ou, C. K. Hong, and L. Mandel, *Phys. Rev. Lett.* **57**, 2516 (1986).
⁸R. Ghosh, C. K. Hong, and L. Mandel, *Phys. Rev. Lett.* **57**, 2516 (1986).
⁹R. J. Glauber, *Phys. Rev.* **141**, 261 (1963).

where we did not yet make any assumption on the species of the particles (bosons or fermions). While first two terms of this equation describes the situation in which one particle is reflected and the other is transmitted, the third and fourth terms describe two distinct processes: Both particles are either reflected or both particles are transmitted by the beam splitter.

– Fermions

For fermions, $\hat{\beta}_q^\dagger = \hat{f}_q^\dagger$, the anti-commutation relation given in Eq. (11.5), leading to $\hat{f}_1^\dagger \hat{f}_2^\dagger = -\hat{f}_2^\dagger \hat{f}_1^\dagger$ which is compatible with Pauli principle, inducing constructive interference between the terms describing coincident events. The first two terms cancel each other, in such a way that always one particle is located in each output in the final state

$$|\Psi_{fin}^F\rangle = \frac{1}{2} \left(\hat{f}_1^\dagger \hat{f}_2^\dagger - \hat{f}_2^\dagger \hat{f}_1^\dagger \right) |0\rangle = \hat{f}_1^\dagger \hat{f}_2^\dagger |0\rangle = |1, 1\rangle \quad (13.6)$$

and $P_F(1, 1) = |\langle \Psi_{fin}^F | 1, 1 \rangle_F|^2 = 1$.

– Bosons

From the commutation relation given in Eq. (11.3), for bosons $\hat{\beta}_q^\dagger = \hat{g}_q^\dagger$, one has that $\hat{g}_1^\dagger \hat{g}_2^\dagger = \hat{g}_2^\dagger \hat{g}_1^\dagger$. Consequently, the third and fourth terms in Eq. (13.5) interfere destructively. For two bosons interference we obtain the final state

$$|\Psi_{fin}^B\rangle = \frac{1}{2} \left((\hat{g}_1^\dagger)^2 - (\hat{g}_2^\dagger)^2 \right) |0\rangle = \frac{1}{\sqrt{2}} (|2, 0\rangle - |0, 2\rangle) \quad (13.7)$$

which describes a coherent superposition of both particles in port 1, and in port 2, so that $P_B(2, 0) = P_B(0, 2) = |\langle \Psi_{fin}^B | 2, 0 \rangle_B|^2 = \frac{1}{2}$. As we have already pointed out, there are no coincident events.

• Composite Two-Fermion Bosons

As motivation, and in order to get a deeper understanding of the interference processes with many-coboson, we present here the simplest case, *i.e.* two interfering composite bosons which consist of two distinguishable bound fermions. The creation operator given in Eq. (11.8), for a coboson constituted of two distinguishable fermions, can always be written in a Slater form [334], just as given in Eq. (12.1),

$$\hat{c}_q^\dagger = \sum_{j=1}^S \sqrt{\lambda_j} \hat{f}_{q,2j-1}^\dagger \hat{f}_{q,2j}^\dagger := \sum_{j=1}^S \sqrt{\lambda_j} \hat{d}_{q,j}^\dagger, \quad (13.8)$$

where q is the number of external modes and j runs over all (S) internal degrees of freedom of the elementary fermions $\hat{f}_{q,2j}^\dagger$ and $\hat{f}_{q,2j-1}^\dagger$. This last subscript includes spin-like degree of freedom used to distinguish the two particles, even subscript, $2j$, could be understood as up spin and odd subscript, $2j-1$, as spin down or vice versa. Two fermions of different species that are always bound to a bi-fermionic particle can be described by

$$\hat{d}_{q,j}^\dagger = \hat{f}_{q,2j}^\dagger \hat{f}_{q,2j-1}^\dagger, \quad (13.9)$$

which fulfils the algebraic properties of a hardcore-boson operator [361] given by

$$\text{for } p \neq q \text{ or } j \neq k : [\hat{d}_{p,j}^\dagger, \hat{d}_{q,k}^\dagger] = 0, \quad (13.10)$$

$$\forall q, j : \left(\hat{d}_{q,j}^\dagger\right)^2 = \left(\hat{d}_{q,j}\right)^2 = 0, \quad \{\hat{d}_{q,j}^\dagger, \hat{d}_{q,j}\} = 1, \quad (13.11)$$

and

$$[\hat{d}_{p,j}, \hat{d}_{q,k}^\dagger] = \delta_{p,q} \delta_{j,k} \left(1 - \hat{f}_{k,2q}^\dagger \hat{f}_{k,2q} - \hat{f}_{k,2q-1}^\dagger \hat{f}_{k,2q-1}\right), \quad (13.12)$$

which is fully consistent with Eq. (11.13), under the assumption that the numbers of fermions of each species coincide. In other words, $\hat{d}_{q,j}^\dagger$ creates a pair of bound bosons or fermions in the external mode q and in the internal state j . For bound fermions, the (typically repulsive) interaction between pairs in the same state is irrelevant, since the Pauli principle inhibits such population.

The state prepared in the two input modes of a beam splitter reads

$$|\Psi_{in}^C\rangle = c_1^\dagger c_2^\dagger |0\rangle = \sum_{j,k=1}^S \sqrt{\lambda_j \lambda_k} \hat{d}_{1,j}^\dagger \hat{d}_{2,k}^\dagger |0\rangle, \quad (13.13)$$

which is already normalized, since $\sum_{j=1}^S \lambda_j = 1$. The dynamics of bound particles through the beam-splitter is described by

$$\hat{d}_{1,j}^\dagger \rightarrow \frac{1}{\sqrt{2}} \left(\hat{d}_{1,j}^\dagger + \hat{d}_{2,j}^\dagger\right) \quad \text{and} \quad \hat{d}_{2,j}^\dagger \rightarrow \frac{1}{\sqrt{2}} \left(\hat{d}_{1,j}^\dagger - \hat{d}_{2,j}^\dagger\right), \quad (13.14)$$

i.e., we indentify $\hat{\alpha}_q^\dagger$ and $\hat{\beta}_q^\dagger$ with the two bound fermion operators $\hat{d}_{q,j}^\dagger$ in which there are also S internal degrees of freedom.

It will turn out useful to decompose the initial state in two orthogonal components,

$$|\Psi_{in}^C\rangle = |\Psi_{in}^\perp\rangle + |\Psi_{in}^\parallel\rangle, \quad (13.15)$$

where

$$|\Psi_{in}^\parallel\rangle = \sum_{j=1}^S \lambda_j \hat{d}_{1,j}^\dagger \hat{d}_{2,j}^\dagger, \quad (13.16)$$

describes the part of the wave-function where bound pairs in the two different modes are in the same internal state, and

$$|\Psi_{in}^\perp\rangle = \sum_{k \neq j=1}^S \sqrt{\lambda_j \lambda_k} \hat{d}_{1,j}^\dagger \hat{d}_{2,k}^\dagger, \quad (13.17)$$

describes the part of the wave-function where two bound pairs in different external modes are also in different internal states always. This component of the wave-functions depends on the purity P of the single-particle-states since

$$\langle \Psi_{in}^\parallel | \Psi_{in}^\parallel \rangle = \sum_{j=1}^S \lambda_j^2 = P. \quad (13.18)$$

During time-evolution, $|\Psi^\parallel\rangle$ does not change, since the Pauli principle inhibits the multiple occupation of any spatial mode, *i.e.*

$$|\Psi_{in}^\parallel\rangle \rightarrow |\Psi_{fin}^\parallel\rangle = |\Psi_{in}^\parallel\rangle, \quad (13.19)$$

is the component which exhibits perfect fermionic behavior. Much in contrast, the other component can be re-written as

$$|\Psi_{in}^\perp\rangle = \sum_{k>j=1}^S \sqrt{\lambda_j \lambda_k} \left(\hat{d}_{1,k}^\dagger \hat{d}_{2,j}^\dagger + \hat{d}_{2,k}^\dagger \hat{d}_{1,j}^\dagger \right), \quad (13.20)$$

displaying a perfect bosonic behavior: Every single summand is manifestly fully symmetric under the exchange of the “labels” j and k , so that

$$\begin{aligned} |\Psi_{in}^\perp\rangle \rightarrow |\Psi_{fin}^\perp\rangle &= \sum_{k>j=1}^S 2\sqrt{\lambda_j \lambda_k} \left(\hat{d}_{1,k}^\dagger \hat{d}_{1,j}^\dagger - \hat{d}_{2,k}^\dagger \hat{d}_{2,j}^\dagger \right) |0\rangle \\ &= \left(\frac{\hat{c}_1^\dagger \hat{c}_1^\dagger}{2} - \frac{\hat{c}_2^\dagger \hat{c}_2^\dagger}{2} \right) |0\rangle. \end{aligned} \quad (13.21)$$

Finally we obtain

$$\begin{aligned} |\Psi_{in}^C\rangle \rightarrow |\Psi_{fin}^C\rangle &= |\Psi_{fin}^\perp\rangle + |\Psi_{fin}^\parallel\rangle = \\ &= \left(\frac{\hat{c}_1^\dagger \hat{c}_1^\dagger}{2} - \frac{\hat{c}_2^\dagger \hat{c}_2^\dagger}{2} \right) |0\rangle + |\Psi_{in}^\parallel\rangle, \end{aligned} \quad (13.22)$$

from which we can infer the probability $P_C(s_1, s_2)$ to find s_1 and s_2 composite bosons in the first and in the second output mode, respectively. Taking into account that

$$P_C(1, 1) = |\langle 1, 1 | \Psi_{in}^C \rangle|^2 = |\langle \Psi_{in}^\parallel | \Psi_{fin}^\parallel \rangle|^2 = P \quad (13.23)$$

one follows that

$$P_C(2, 0) = P_C(0, 2) = \frac{1 - P}{2}. \quad (13.24)$$

The perfect bosonic behavior is almost attained, just the correction $|\Psi^\parallel\rangle$ remains, which can also be understood as kind of partial distinguishability [362]. Since the counting statistics of $|\Psi^\parallel\rangle$ gives always one composite particle in each mode, it immediately jeopardizes the Hong-Ou-Mandel dip that would be expected for perfect bosons. From the population imbalance after beam splitter dynamics, Eqs. (13.23) and (13.24), one can immediately read off the purity of the fundamental fermions in the HOM-dip. In other words, the full composite-particle wavefunction behaves as a superposition of a bosonic part and a fermionic one, and the perfect bosons HOM-dip is obtained for maximally entangled states.

13.1.2 Many bosons interference

Our purpose is to provide a general formalism of the interference process for many composite bosons. In general, as we have seen in previous section, the many-particle state space structure prohibits multiple populations of fermions whereas it privileges that for bosons. The description of the interference process for many-bosons is, therefore, much more complicated. Here, we generalize the discussion above, and consider the case where a beam splitter receives groups of particles described by Fock states of elementary bosons. In such case, the dynamics of the unbalanced beam splitter is governed by the evolution of the creation operator $\hat{\alpha}_q^\dagger$ as follows:

$$\hat{\alpha}_1^\dagger \rightarrow \frac{1}{\sqrt{2}} \left(\sqrt{R} \hat{g}_1^\dagger - i\sqrt{T} \hat{g}_2^\dagger \right), \quad \text{and} \quad \hat{\alpha}_2^\dagger \rightarrow \frac{1}{\sqrt{2}} \left(\sqrt{R} \hat{g}_1^\dagger + i\sqrt{T} \hat{g}_2^\dagger \right) \quad (13.25)$$

where R and T are the reflection and transmission coefficients of the beam splitter. When it receives two beams of bosons described by the quantum state

$$|\Psi_{in}^B(N_1, N_2)\rangle = \frac{1}{\sqrt{N_1!N_2!}} \left(\hat{g}_1^\dagger \right)^{N_1} \left(\hat{g}_2^\dagger \right)^{N_2} |0\rangle \quad (13.26)$$

(Fock states in Bose-Einstein condensates at very low temperatures), the amplitude for finding m_1 and m_2 particles in the output mode, given the sources with N_1 and N_2 particles, respectively, is given by the overlap of the state in Eq. (13.26) with the final state

$$|\Psi_{fin}^B(m_1, m_2)\rangle = \frac{1}{\sqrt{m_1!m_2!}} \left(\hat{\alpha}_1^\dagger \right)^{m_1} \left(\hat{\alpha}_2^\dagger \right)^{m_2} |0\rangle, \quad (13.27)$$

to which we apply the operator evolution described by Eq. (13.25), that is

$$A(m_1, m_2; N_1, N_2) = \frac{1}{\sqrt{m_1!m_2!N_1!N_2!}} \langle 0 | \left(\hat{\alpha}_1 \right)^{m_1} \left(\hat{\alpha}_2 \right)^{m_2} \left(\hat{g}_1^\dagger \right)^{N_1} \left(\hat{g}_2^\dagger \right)^{N_2} |0\rangle \quad (13.28)$$

The general expression of this amplitude after time evolution is found in the work of Laloë and Mullin [363], which is given by

$$A(m_1, m_2; N_1, N_2) = \frac{\sqrt{N_1!N_2!}}{\sqrt{m_1!m_2!}} \sum_{p,q} \frac{m_1!m_2!(\sqrt{T})^{p+m_2-q}(i\sqrt{R})^{q+m_1-p}}{p!(m_1-p)!q!(m_2-q)!} \times \\ \times \delta_{p+q, N_1} \delta_{m_1+m_2-p-q, N_2}. \quad (13.29)$$

This is a somewhat complicated expression that can be solved by several methods as described in Ref. [355]; here we compute the δ -functions to eliminate the summation variable p as follows:

$$A(m_1, m_2; N_1, N_2) = \\ = \sqrt{m_1!m_2!N_1!N_2!} \sum_{q=\max\{0, n_1-m_1\}}^{\min\{n_1, m_2\}} \frac{(\sqrt{T})^{n_1+m_2-2q}(i\sqrt{R})^{m_1-n_1+2q}}{(n_1-q)!(m_1-n_1+q)!q!(m_2-q)!} \quad (13.30)$$

Therefore, the probability of finding m_1 and m_2 bosons in the first and second output modes, respectively, reads

$$P_B(m_1, m_2; N_1, N_2) = |A(m_1, m_2; N_1, N_2)|^2. \quad (13.31)$$

A single beam splitter is sufficient to obtain interesting quantum effects, provided it receives Fock states at its two inputs. The “population oscillations” related to the Hong-Ou-Mandel effect in Eq. (13.31) take place, but they cannot be understood as a simple superposition of many separate two-photon-experiments. Actually, many-boson effects take place as a consequence of quantum statistics, what can be understood as a consequence of the tendency of two Fock states to acquire a relative phase under the effect of quantum measurement. Since this phase is completely unknown, quantum oscillations are superimposed. Experimentally, the major difficulty for observing these effects is the production of Fock states with well-defined populations. However, the experimental techniques that have been developed for BECs seem well suited for experiments on such input states. This expression will be use in Section 13.5 for probability distributions of many-cobosons corresponding to the purely bosonic behavior terms.

13.1.3 Bosons macroscopic approach

To obtain efficient approximation of the many-bosons ($N \gg 1000$) counting statistics, and taking also into account dynamical interference effects up to a certain extent, we use the *macroscopic wavefunction* (MWF) Ansatz [355, 362]. It is a suitable tool motivated physically by the experimentally confirmed interference fringes in the scattering of independent BECs and, as recently proven, even in molecular systems [329].

For two modes, and in order to model the relative phase of two BECs as a random variable, we use the interference of two Fock states at a two-mode beam splitter, as was described in Refs. [362, 355, 364, 365, 366, 367, 368]. A first Ansatz for the description of a initial product state of two Fock states is given by

$$|\psi_{in}^{MWF}\rangle = \sqrt{I_1} |\phi_1^g\rangle + \sqrt{I_2} |\phi_2^g\rangle, \quad (13.32)$$

where the $|\phi_j^g\rangle$ are the two single-particle input states. This MWF is a superposition of the two different input mode wavefunctions, weighted with the fraction of particles $I_j = N_j/N$ in the respective input mode j , where $N = N_1 + N_2$. This representation of the state in Eq. (13.32), however, contains a fixed relative phase between the components in the different modes. In order to describe a situation which corresponds to scenario in which exactly N_j particles are prepared in modes j and a random phase emerges at every run of the experiment, we introduce explicitly this random phase between the components of the wavefunction, and consider the state given in Ref. [355]

$$|\psi_{in}^{MWF}(\vec{\gamma})\rangle = e^{i\gamma_1} \sqrt{I_1} |\phi_1^g\rangle + e^{i\gamma_2} \sqrt{I_2} |\phi_2^g\rangle, \quad (13.33)$$

where the γ_j are random phases. After the scattering on the unbalanced beam splitter, with the time-evolution of the single-particle states similarly governed by Eq. (13.25), the MWF reads

$$\begin{aligned} |\psi_{fin}^{MWF}(\vec{\gamma})\rangle &= \left(e^{i\gamma_1} \sqrt{R} \sqrt{I_1} - i\sqrt{T} e^{i\gamma_2} \sqrt{I_2} \right) |\phi_1^g\rangle + \\ &+ \left(e^{i\gamma_1} \sqrt{R} \sqrt{I_1} - i\sqrt{T} e^{i\gamma_2} \sqrt{I_2} \right) |\phi_2^g\rangle. \end{aligned} \quad (13.34)$$

Since the global phase of the state is not relevant, we can set $\gamma_1 = 0$, so that the probability of finding the amplitude I of the wavefunction in the first output mode is given by

$$\mathcal{P}(I) = \frac{1}{2\pi} \int_0^{2\pi} \delta \left(I - \left| \sqrt{RI_1} - ie^{i\gamma_2} \sqrt{TI_2} \right|^2 \right) d\gamma_2. \quad (13.35)$$

This expression corresponds to a random walk in the complex plane with two steps [362], and in that case one can solve the integral analytically, resulting

$$\mathcal{P}_{\text{MWF}}(I; I_1, I_2) = \begin{cases} 0 & 1 < \frac{(I - RI_1 - TI_2)^2}{4RTI_1I_2} \\ \left(\pi \sqrt{4RTI_1I_2 - (I - RI_1 - TI_2)^2} \right)^{-1} & 1 \geq \frac{(I - RI_1 - TI_2)^2}{4RTI_1I_2} \end{cases} \quad (13.36)$$

The probability distribution $\mathcal{P}_{\text{MWF}}(I; I_1, I_2)$ is called ‘‘classical calculation’’ in Ref. [355], since it can be interpreted as a result of the interference of classical electromagnetic fields with amplitudes $\sqrt{I_j}$. The MWF approach is later generalized to many-cobosons scenarios in Section 13.6.

13.2 Physical model

For a tangible model of composite bosons, we consider fermions of two distinguishable species, a and b , which interact attractively via a contact interaction U , and which are prepared in two weakly coupled one-dimensional lattices, as depicted in Fig. 13.2.

The single-particle tunnelling rates between the wells in horizontal (vertical) direction are denoted by $J_{0,h}$ ($J_{0,v}$), such that the Hamiltonian on the level of the individual fermions is given by

$$\begin{aligned} \hat{H} = & -U \sum_{q=1}^2 \sum_{j=1}^S \hat{a}_{q,j}^\dagger \hat{b}_{q,j}^\dagger \hat{b}_{q,j} \hat{a}_{q,j} + \frac{1}{2} \sum_{q=1}^2 \sum_{j=1}^S \varepsilon_j \left(\hat{a}_{q,j}^\dagger \hat{a}_{q,j} + \hat{b}_{q,j}^\dagger \hat{b}_{q,j} \right) - \\ & - \frac{J_{0,h}}{2} \sum_{q=1}^2 \sum_{j=1}^{S-1} \left(\hat{a}_{q,j}^\dagger \hat{a}_{q,j+1} + \hat{b}_{q,j}^\dagger \hat{b}_{q,j+1} + \text{H.c.} \right) - \\ & - \frac{J_{0,v}}{2} \sum_{j=1}^S \left(\hat{a}_{1,j}^\dagger \hat{a}_{2,j} + \hat{b}_{1,j}^\dagger \hat{b}_{2,j} + \text{H.c.} \right), \quad (13.37) \end{aligned}$$

where $q = 1, 2$ denotes the two one-dimensional sublattices, and $j = 1, \dots, S$ the potential wells along each lattice. The attractive interaction U is always strong, $U \gg J_{0,v}, J_{0,h}$. Therefore, two fermions of the two different species are always bounded to a bi-fermionic particle described by

$$\hat{d}_{q,j}^\dagger = \hat{a}_{q,j}^\dagger \hat{b}_{q,j}^\dagger = \hat{f}_{q,2j}^\dagger \hat{f}_{q,2j-1}^\dagger, \quad (13.38)$$

as provided before in Eq. (13.9), which fulfils the algebraic commutation properties given in Eqs. (13.10) and (13.11).

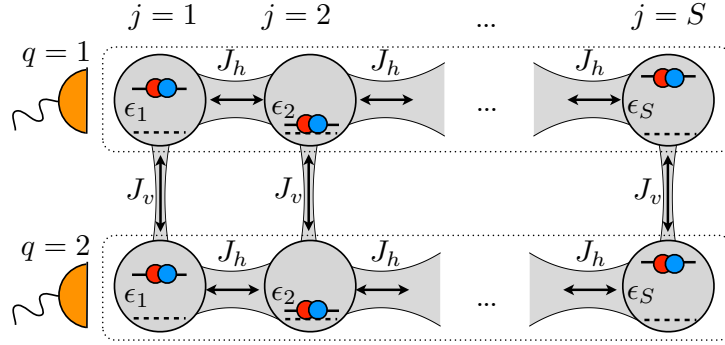


Figure 13.2: Setup for the interference of engineered cobosons. N_1 (N_2) strongly bound bi-fermions are prepared in the upper (lower) lattice at $J_v \ll J_h$, such that each bi-fermion is governed by the local energies ϵ_j and the tunneling rate J_h . The barrier between the lattices is then ramped down, such that $J_v \gg J_h$ and vertical tunnelling takes place. The total number of bi-fermions in the upper and lower lattice is then counted.

Due to the strong attractive interaction between the fermions, they can only tunnel as a pair through off-resonant processes, with rates

$$J_h = \frac{J_{0,h}^2}{U}, \quad J_v = \frac{J_{0,v}^2}{U}, \quad (13.39)$$

for the interlattice and intralattice directions, respectively. We thus obtain the effective Hamiltonian of strongly bound bi-fermion pairs that are trapped in a two-dimensional potential landscape with different horizontal and vertical coupling rates [369], as depicted in Fig. 13.2, which is described by the Hamiltonian

$$\begin{aligned} \hat{H} = & -\frac{J_h}{2} \sum_{q=1}^2 \sum_{j=1}^{S-1} \hat{d}_{q,j}^\dagger \hat{d}_{q,j+1} - \frac{J_v}{2} \sum_{j=1}^S \hat{d}_{1,j}^\dagger \hat{d}_{2,j} + h.c. \\ & + \sum_{q=1}^2 \sum_{j=1}^S \epsilon_j \left(\hat{d}_{q,j}^\dagger \hat{d}_{q,j} \right), \end{aligned} \quad (13.40)$$

where $\hat{d}_{q,j}^\dagger = \hat{f}_{q,2j}^\dagger \hat{f}_{q,2j-1}^\dagger$ creates a bi-fermion consisting of an a - and a b -type (or even- and odd-type) fermions in the j th site of the upper or lower lattice ($q = 1, 2$); J_h (J_v) is the effective tunneling strength along (between) the lattices, and ϵ_j defines a local energy landscape.

13.3 Coboson state, preparation

We assume that, initially, $J_h \gg J_v$, and multi-coboson states are prepared in the horizontally extended lattice q by Eq. (13.8), that is

$$\hat{c}_q^\dagger = \sum_{j=1}^S \sqrt{\lambda_j} \hat{d}_{q,j}^\dagger = \sum_{j=1}^S \sqrt{\lambda_j} \hat{f}_{q,2j}^\dagger \hat{f}_{q,2j-1}^\dagger. \quad (13.41)$$

A coboson is thus a horizontally delocalized bi-fermion, and the S coefficients λ_j are then the *Schmidt coefficients* of the two-fermion state. As already highlighted, the distribution $\vec{\lambda}$ is conveniently characterized by its moments

$$M(m) = \sum_{j=1}^S \lambda_j^m, \quad (13.42)$$

where normalization implies $M(1) = 1$ and $M(2) = P$ is the purity of either reduced single-fermion state. We consider an initial state of N_1 cobosons in the upper and N_2 cobosons in the lower one,

$$|\Psi\rangle = \frac{(\hat{c}_1^\dagger)^{N_1}}{\sqrt{\chi_{N_1} \cdot N_1!}} \frac{(\hat{c}_2^\dagger)^{N_2}}{\sqrt{\chi_{N_2} \cdot N_2!}} |0\rangle, \quad (13.43)$$

where we assume $N_1 \geq N_2$, and χ_N is the coboson normalization factor [332, 309, 303, 312, 282], a symmetric polynomial [336] given by $\chi_N = \Omega(\underbrace{\{1, \dots, 1\}}_N)$, with

$$\Omega(\{x_1, \dots, x_N\}) = \sum_{\substack{i \neq j \Rightarrow p_i \neq p_j \\ p_1, \dots, p_N \\ 1 \leq p_j \leq S}} \prod_{q=1}^N \lambda_{p_q}^{x_q}. \quad (13.44)$$

While the main purpose of our analysis is the investigation of compositeness for the collective interference exhibited by the state in Eq. (13.43), it is worthwhile to indicate a procedure by which such a state with many cobosons in the same state may be produced as the result of an experimental protocol.

We may start with an extended lattice with a total of SN_1 sites (remember $N_1 \geq N_2$ by assumption), such that site kS (with $k = 1, \dots, N_1 - 1$) is coupled to site $kS + 1$ with a strength $J_s \ll J_h$, and $\varepsilon_{kS+j} = \varepsilon_j$ for $k = 1, \dots, N_1$. We exploit the exact mapping of hardcore-bosons to fermions in one dimension to obtain the ground-state of N_1 and N_2 bi-fermions in the first and second extended lattices as a direct product of the lowest N_1 and N_2 single-particle states, respectively,

$$|\text{GS}(N_1, N_2)\rangle = \left[\prod_{j=1}^{N_1} \left(\sum_{l=1}^{SN_1} \omega_{j,l} \hat{d}_{1,l}^\dagger \right) \right] \left[\prod_{j=1}^{N_2} \left(\sum_{l=1}^{SN_1} \omega_{j,l} \hat{d}_{2,l}^\dagger \right) \right] |0\rangle, \quad (13.45)$$

where the matrix $\omega_{j,l}$ contains the coefficients $l = 1 \dots SN_1$ of the j th single-particle eigenfunction in one sublattice. After preparing the ground state with N_1 and N_2 particles in each sublattice, we project away the component of the many-body wavefunction in which particles are present in the sites $S + 1, \dots, SN_1$ of either lattice. Consequently, a particle initially prepared in the j th eigenstate in lattice q is projected (with finite probability) onto the state created by

$$\sum_{l=1}^S \omega_{j,l} \hat{d}_{q,l}^\dagger. \quad (13.46)$$

Our choice above of the potential landscape with $J_s \ll J_h$ ensures that the N_1 energetically lowest single-particle wave-functions have a node around $l = S$ and that the coefficients $\omega_{j,l}$ with $1 \leq l \leq S$ are very similar for the first N_1 eigenfunctions,

$$\omega_{j,l} \approx \omega_{1,l} \quad \forall j, l / 2 \leq j \leq N_1, 1 \leq l \leq S. \quad (13.47)$$

After projecting out components that populate the auxiliary sites $j = S + 1, \dots, SN_1$, the many-particle-state is consequently very close to a state of N_q -fold population of the co-boson state

$$\hat{c}_q^\dagger = \alpha \sum_{l=1}^S \omega_{1,l} \hat{d}_{q,l}^\dagger = \sum_{l=1}^S \sqrt{\lambda_l} \hat{d}_{q,l}^\dagger, \quad (13.48)$$

where α ensures normalization and we thus set $\lambda_l = |\alpha \omega_{1,l}|^2$. Note that the Pauli principle ensures that, unlike for hardcore bosons, the preparation of fermions into this state is impossible: One then always finds at least one particle in the sites $S + 1, \dots, SN_1$, and the projection always fails.

We take the initial state as given in Eq. (13.43), and thus consider coboson operators for the two lattices $q = 1, 2$ as given by Eq. (13.48). By appropriately modelling the local energies ε_j , the resulting distribution of Schmidt coefficients λ_l can be controlled to a wide extent.

13.4 Behavior of cobosons under beam-splitter dynamics

To assess the behavior of the cobosons, we let the bi-fermions tunnel vertically between the two lattices by setting $J_v \gg J_h$ and letting the system evolve for a time of the order $1/J_v$. Thus, beam-splitter-like dynamics couples the two lattices, while tunneling processes within the lattices, induced by J_h , can be neglected on this time-scale. The Schmidt modes j are therefore left unchanged. Time-evolution until t implements a beam-splitter with reflectivity $R = \cos^2(tJ_v/2)$. In principle, the counting statistics of bi-fermions in the two lattices can be obtained by integrating the dynamics induced by Eq. (13.40) for the initial state $|\Psi\rangle$ given in Eq. (13.43) and taking the expectation values of the counting operators

$$\hat{A}_{n_1, n_2} = \sum_{\substack{1 \leq j_k, l_m \leq S \\ j_1 \neq j_2 \neq \dots \neq j_{n_1}, k=1 \\ l_1 \neq l_2 \neq \dots \neq l_{n_2}}} \prod_{k=1}^{n_1} \hat{d}_{1, j_k}^\dagger \hat{d}_{1, j_k} \prod_{m=1}^{n_2} \hat{d}_{2, l_m}^\dagger \hat{d}_{2, l_m}, \quad (13.49)$$

which witness the probability to find exactly n_1 (n_2) bi-fermions in the first (second) lattice. This procedure, however, is computationally expensive and does not offer an intuitive physical picture. By exploiting the symmetry properties of the state in Eq. (13.43), one can show that the behavior of cobosons is imitated exactly by a superposition of states with a different number of perfect bosons and fermions, in analogy to partially distinguishable particles [358, 359].

We would like to describe the counting statistics of the state $|\Psi\rangle$ of Eq. (13.43) in an efficient manner. For that purpose, we insert the definition of the coboson creation operator, Eq. (13.48), into the initial state, Eq. (13.43):

$$\frac{[\hat{c}_1^\dagger]^{N_1} [\hat{c}_2^\dagger]^{N_2}}{\sqrt{\chi_{N_1} N_1! \chi_{N_2} N_2!}} |0\rangle = \frac{1}{\sqrt{\chi_{N_1} N_1! \chi_{N_2} N_2!}} \times \sum_{\substack{1 \leq k_j, l_j \leq S \\ k_1 \neq \dots \neq k_{N_1} \\ l_1 \neq \dots \neq l_{N_2}}} \left[\prod_{m=1}^{N_1} \sqrt{\lambda_{k_m}} \hat{d}_{1, k_m}^\dagger \right] \left[\prod_{n=1}^{N_2} \sqrt{\lambda_{l_n}} \hat{d}_{2, l_n}^\dagger \right] |0\rangle. \quad (13.50)$$

All indices k_m (l_n) appertain to the upper (lower) lattice. It may occur that $k_m = l_n$ for some m, n , *i.e.* two bi-fermions can occupy the same well j in the two different lattices. The sum in Eq. (13.50) can be written in terms of a given number of pairs p that fulfil $k_m = l_n$. There can be between none and N_2 of such pairs (remember $N_1 \geq N_2$): In the former case, $k_m \neq l_n$ for all m, n ; in the latter, $k_m = l_n$ for all $m \leq N_2$ (disregarding permutation of indices). The state initial state $|\Psi\rangle$ thus becomes

$$|\Psi\rangle = \sum_{p=0}^{N_2} |\Phi(p)\rangle, \quad (13.51)$$

where

$$|\Phi(p)\rangle = \sqrt{\binom{N_2}{p} \binom{N_1}{p} \frac{p!}{\chi_{N_1} N_1! \chi_{N_2} N_2!}} \times \sum^{(N_2, p)} \left[\prod_{m=1}^{N_1} \sqrt{\lambda_{k_m}} \hat{d}_{1, k_m}^\dagger \right] \left[\prod_{n=1}^{N_2} \sqrt{\lambda_{l_n}} \hat{d}_{2, l_n}^\dagger \right] |0\rangle, \quad (13.52)$$

and the sum $\sum^{(N_2, p)}$ runs over all indices k_m, l_n ($1 \leq m \leq N_1, 1 \leq n \leq N_2$) that fulfil

$$i \neq j : k_i \neq k_j, l_i \neq l_j, \quad (13.53)$$

$$1 \leq m \leq p : k_m = l_m, \quad (13.54)$$

$$p < m \leq N_1, p < n \leq N_2 : k_m \neq l_n. \quad (13.55)$$

Reordering indices and setting $\tilde{N} = N_1 + N_2 - 2p$, we can rewrite the sum in Eq. (13.52) as

$$|\Phi(p)\rangle = \sqrt{\binom{N_2}{p} \binom{N_1}{p} \frac{p!}{\chi_{N_1} N_1! \chi_{N_2} N_2!}} \sum_{\substack{1 \leq s_j \leq S \\ s_1 \neq s_2 \neq \dots \neq s_p}} \sum_{\substack{\forall l, m: r_l \neq s_m \\ 1 \leq r_1 < \dots < r_{\tilde{N}} \leq S}} \sum_{\sigma \in S_{\{r_1, \dots, r_{\tilde{N}}\}}} \underbrace{\left[\prod_{j=1}^p \lambda_{s_j} \hat{d}_{1, s_j}^\dagger \hat{d}_{2, s_j}^\dagger \right]}_{\text{fermionic}} \left[\prod_{j=1}^{\tilde{N}} \sqrt{\lambda_{\sigma(j)}} \right] \underbrace{\left[\prod_{m=1}^{N_1-p} \hat{d}_{1, \sigma(m)}^\dagger \right] \left[\prod_{n=1}^{N_2-p} \hat{d}_{2, \sigma(N_1-p+n)}^\dagger \right]}_{\text{bosonic}}, \quad (13.56)$$

where the indices $r_1 \dots r_{\tilde{N}}$ replace the $k_{m>p}$ and $l_{m>p}$, the indices l_1, \dots, l_p replace the $k_{m\leq p}$, and $S_{\{r_1, \dots, r_{\tilde{N}}\}}$ denotes the permutations of the r_j .

By inspecting Eq. (13.56), we can infer the time-evolution of each $|\Phi(p)\rangle$ -component of the many-coboson state (13.51), as it is induced by the Hamiltonian (13.40) in the here-considered limit $J_h \ll J_v$: Each summand in (13.56) contains p pairs of bi-fermions that occupy the same well in the two lattices – they take into account the summands with $k_m = l_m$ ($1 \leq m \leq p$) of Eq. (13.52). Due to the Pauli principle, these bi-fermions cannot tunnel and thus behave in a fermionic way. The other bi-fermions, described by the indices $r_1, \dots, r_{\tilde{N}}$ (which correspond to the indices $n, m > p$ in Eq. (13.52)), always occupy different wells, such that the Pauli principle does not apply and tunneling is possible. One such summands of Eq. (13.56) is depicted in Fig. 13.3. Since the state of the bi-fermions that can tunnel is fully symmetric under the exchange of any two bi-fermions between the lattices (note the sum over all permutations of the lattice indices in Eq. (13.56)), such state is manifestly bosonic, as also illustrated in Fig. 13.4.

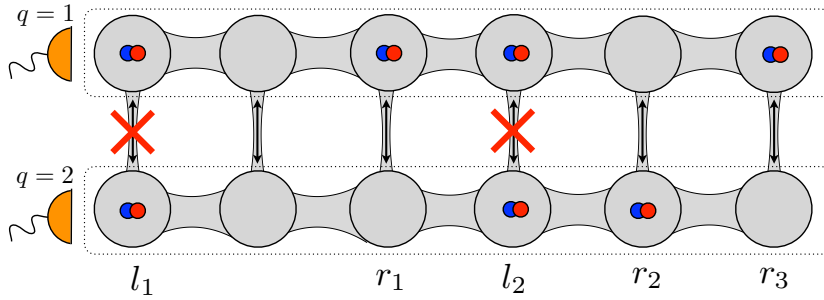


Figure 13.3: One summand of Eq. (13.56), with $N_1 = 4, N_2 = 3$: Two pairs of bi-fermions ($p = 2$) are located in the same wells l_1 and l_2 , and cannot tunnel. All other bi-fermions can tunnel, and interfere with other terms in the sum (see Fig. 13.4).

The total state $|\Phi(p)\rangle$ thus exhibits the same counting statistics as a state $|\phi(p)\rangle$ of p pairs of distinct fermions and $N_1 + N_2 - 2p$ perfect bosons:

$$|\phi(p)\rangle = \left[\prod_{q=1}^2 \frac{(\hat{g}_q^\dagger)^{N_q-p}}{\sqrt{(N_q-p)!}} \right] \left[\prod_{j=1}^p \hat{f}_{1,j}^\dagger \hat{f}_{2,j}^\dagger \right] |0\rangle, \quad (13.57)$$

where \hat{g}_q^\dagger ($\hat{f}_{q,j}^\dagger$) creates a boson (j -type fermion) in the sublattice q while the actual location along the lattice is omitted (remember that the number of bi-fermions in each lattice is counted, independently of the location of the bi-fermions along the lattice). Since no interference between different p occurs, the initial state $|\Psi\rangle$ (Eq. (13.43)) behaves like a superposition of states $|\phi(p)\rangle$ with different numbers of ideal fermions, in analogy to partially distinguishable particles [358]:

$$|\psi\rangle = \sum_{p=0}^{N_2} \sqrt{w_p} |\phi(p)\rangle, \quad (13.58)$$

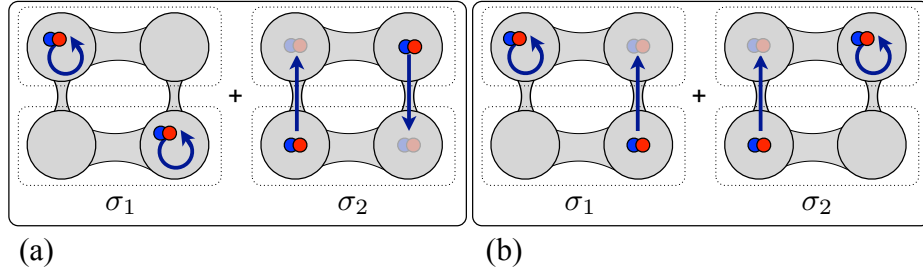


Figure 13.4: Emergence of Hong-Ou-Mandel-like bunching for bi-fermions. Each component of the wave-function in (13.56), corresponding to a permutation σ_1 , interferes with another component σ_2 in which the bi-fermions swap the wells they occupy. (a) Destructive interference: The two processes (both bi-fermions remain in the same lattice, or both bi-fermions tunnel) lead to the same final state with one particle in each lattice. The right-hand-side process, however, acquires a phase of $i^2 = -1$ due to tunneling, such that the two processes interfere destructively. (b) Constructive interference: The final state with both bi-fermions in the same lattice is fed by two processes with one tunnelling event, i.e. both paths acquire the same phase and constructive interference takes place.

where

$$w_p = \langle \Phi(p) | \Phi(p) \rangle = \binom{N_1}{p} \binom{N_2}{p} \frac{p!}{\chi_{N_1} \chi_{N_2}} \Omega(\underbrace{\{2, \dots, 2\}}_p, \underbrace{\{1, \dots, 1\}}_{N_1+N_2-2p}), \quad (13.59)$$

is the weight of the component with p pairs of fermionically behaving bi-fermions, and $\Omega(\{x_1, \dots, x_N\})$ is given by Eq. (13.44). The quantity $\Omega(\{x_1, \dots, x_N\})$ can be evaluated using the power-sums (13.42) of the distribution $\vec{\lambda}$,

$$\begin{aligned} \Omega(\{x_1, \dots, x_N\}) &= M(x_1) \Omega(\underbrace{\{x_2, \dots, x_N\}}_{N-1}) - \\ &- \sum_{m=2}^N \Omega(\underbrace{\{x_1 + x_m, x_2, \dots, x_{m-1}, x_{m+1}, \dots, x_N\}}_{N-1}), \end{aligned} \quad (13.60)$$

i.e. $\Omega(\{x_1, \dots, x_N\})$ depends on power-sums $M(m)$ up to order $m = N$.

Combinatorially speaking, w_p is the probability that, given two groups of N_1 and N_2 objects with properties distributed according to $\vec{\lambda}$, and assuming that all objects in either group carry different properties, one finds p pairs of objects with the same property when the two groups are merged. In the present context, w_p denotes the population of the state components in which the Pauli principle affects p pairs of bi-fermions. The term $|\phi(0)\rangle$ thus describes perfect bosonic behavior, its weight $w_0 = \chi_{N_1+N_2}/(\chi_{N_1} \chi_{N_2})$ can be bounded via the purity P and the particle numbers N_1, N_2 [303, 282]:

$$\frac{(L - N_1)!(L - N_2)!}{(L - N_1 - N_2)!L!} \leq w_0 \leq \frac{(1 - \sqrt{P})(1 + \sqrt{P}(N_1 + N_2 - 1))}{(1 + \sqrt{P}(N_2 - 1))(1 + \sqrt{P}(N_1 - 1))}, \quad (13.61)$$

where $L = \lceil \frac{1}{P} \rceil$.

13.5 Evaluation of counting statistics

The counting statistics that is exhibited by the substitute state $|\psi\rangle$, Eq. (13.58), can be inferred by inserting the single-particle time-evolution for the creation operators, Eq. (13.25) for bosons and similarly for fermions, into each state $|\phi(p)\rangle$,

$$\hat{g}_q^\dagger \rightarrow \sqrt{R}\hat{g}_q^\dagger - i\sqrt{T}\hat{g}_{3-q}^\dagger \quad (13.62)$$

$$\hat{f}_{q,j}^\dagger \rightarrow \sqrt{R}\hat{f}_{q,j}^\dagger - i\sqrt{T}\hat{f}_{3-q,j}^\dagger, \quad (13.63)$$

where $q = 1, 2$, and $R = \cos^2(J_v t/2)$ and $T = \sin^2(J_v t/2)$ are the reflection and transmission coefficients of the beam-splitter dynamics.

The evaluation of the overlap can be done following the methods presented in Refs. [355, 356, 358]. We can now derive the counting statistics of cobosons after time-evolution until $t = \pi/2/J_v$, which corresponds to a balanced beam-splitter with $R = T = 1/2$. The probability $P_{\text{tot}}(m)$ to find m cobosons in the upper lattice is the sum of the resulting probabilities from the different contributions in Eq. (13.58),

$$P_{\text{tot}}(m) = \sum_{p=0}^{N_2} w_p \cdot P(m, p), \quad (13.64)$$

where $P(m, p)$ is the probability to find m particles of any species in the upper lattice, given the state $|\phi(p)\rangle$ defined in Eq. (13.57) and the beam-splitter reflectivity $R = 1/2$.

The probability $P(m, p)$ to find m particles in the upper lattice can then be inferred by taking the overlap of the state in Eq. (13.57) with

$$|\phi_{\text{fin}}(p)\rangle = \frac{(\hat{g}_1^\dagger)^{m-p} (\hat{g}_2^\dagger)^{N-m-p}}{\sqrt{(m-p)!(N-m-p)!}} \prod_{j=1}^p f_{1,j}^\dagger f_{2,j}^\dagger |0\rangle, \quad (13.65)$$

i.e. with the Fock-state of $m-p$ bosons and p fermions in the first mode and $N-m-p$ bosons and p fermions in the second mode, after time-evolution as described by Eq. (13.62). Since fermions obey the Pauli principle and coincident events always occur leading to p fermions in each output mode, the probability is given by Eq. (13.31) as follows:

$$P(m, p) = |\langle \phi(p) | \phi_{\text{fin}}(p) \rangle|^2 = P_B(m-p, N-m-p; N_1-p, N_2-p). \quad (13.66)$$

The simplest case is given by two interfering cobosons ($N_1 = N_2 = 1$), recovering the expressions in Eqs. (13.23) and (13.24), for which we find $w_0 = P$ and $w_1 = 1 - P$:

$$P_{\text{tot}}(1) = P, \quad P_{\text{tot}}(0) = P_{\text{tot}}(2) = \frac{1-P}{2}. \quad (13.67)$$

For $P \rightarrow 1$, the Pauli principle dominates and one always finds one particle in each lattice. In contrast to the interference of unbound boson pairs that can break up dynamically [370], a perfect bosonic dip emerges here in the limit of vanishing purity, $P \rightarrow 0$.

Higher-order power sums $M(m)$ with $m \geq 3$ become relevant when more than two cobosons interfere. For example, the interference of $N_2 = 1$ with N_1 cobosons reflects the normalization ratio χ_{N+1}/χ_N [335, 332, 309, 303, 316]:

$$P_{\text{tot}}(m) = \frac{\chi_{N_1+1}}{\chi_{N_1}} P(m, 0) + \left(1 - \frac{\chi_{N_1+1}}{\chi_{N_1}}\right) P(m, 1). \quad (13.68)$$

In general, the balance among all the weights w_0, \dots, w_{N_2} governs the counting statistics. Since the weights w_p depend on power-sums $M(m)$ up to order $N_1 + N_2$, the characteristics of the distribution $\vec{\lambda}$ can be established through interference signals. For $N_1 = N_2 = 2$, we illustrate the decomposition given by Eq. (13.58) in Fig. 13.5. The ideal boson interference pattern $P(m, 0)$ is jeopardized by the finite purity $P = 1/4$, and the contributions of the single fermion-pair and double fermion-pair part in the wave-function lead to the altered signal $P_{\text{tot}}(m)$.

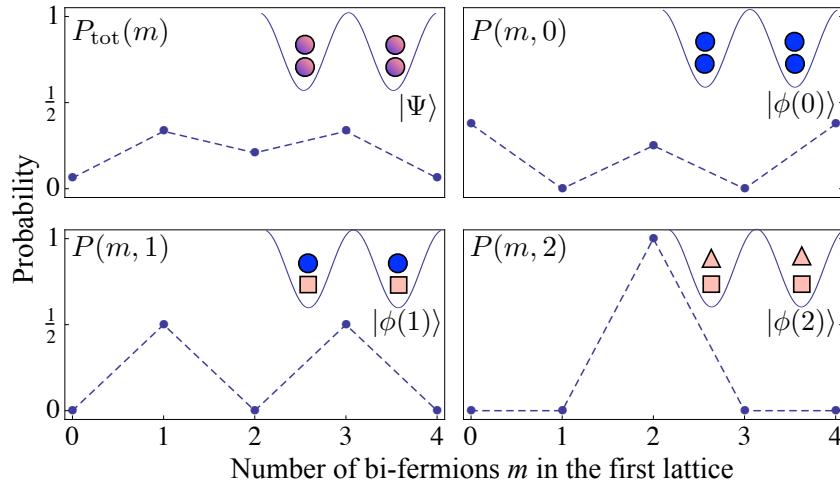


Figure 13.5: Counting statistics for the coboson-state $|\Psi\rangle$ with $N_1 = N_2 = 2$, and of its components with different numbers of bosons and fermions $|\phi(p)\rangle$, $p = 0, 1, 2$. Dark blue circles represent bosonically behaving bi-fermions, light orange symbols stand for fermionically behaving bi-fermions. The total counting statistics $P_{\text{tot}}(m)$ is the weighted sum in Eq. (13.64) over the different components of the wave-function. While $|\phi(0)\rangle$ exhibits perfect bosonic behavior, $|\phi(p \geq 1)\rangle$ are partially fermionic, which leaves a signature in the counting statistics. Here, $R = 1/2$ and $\lambda_1 = \dots = \lambda_4 = 1/4$, such that $w_0 = w_2 = 1/6$, $w_1 = 2/3$.

Distributions with the same purity P may have different higher-order power sums $M(m)$, with consequently distinct counting statistics. Keeping P constant, the counting statistics is extremized by two particular distributions: the upper bound in Eq. (13.61) is saturated by peaked distribution $\vec{\lambda}^{(p)}$ with $\lambda_1^{(p)} > \lambda_2^{(p)} = \dots = \lambda_S^{(p)}$, in the limit $S \rightarrow \infty$; the lower bound is saturated by the uniform distribution $\vec{\lambda}^{(u)}$ with $\lambda_1^{(u)} \leq \lambda_2^{(u)} = \dots = \lambda_{L \equiv \lceil 1/P \rceil}^{(u)}$, for fractional purities $P = 1/L$ [282]. The counting statistics for $N_1 = N_2 = 6$ is shown in Fig. 13.6. The weights $w_j^{(u/p)}$ of the uniform (peaked) distributions differ

considerably (see lower panel), which is reflected by the counting statistics (upper panel; note that $P(m) = P(12 - m)$ due to symmetry). Only one Schmidt coefficient in the peaked distribution is finite in the limit $S \rightarrow \infty$, thus only the weights $w_0^{(p)}$ and $w_1^{(p)}$ are non-vanishing: the interference patterns of 12 and of 10 bosons take turns. Instead, all weights $w_{0 \leq j \leq 6}^{(u)}$ alternate for the uniform distribution. Kinks emerge at fractional values of P , when a new non-vanishing Schmidt coefficient emerges. For $P \rightarrow 1/6$, fully fermionic behavior is attained, and one always finds six cobosons in each lattice.

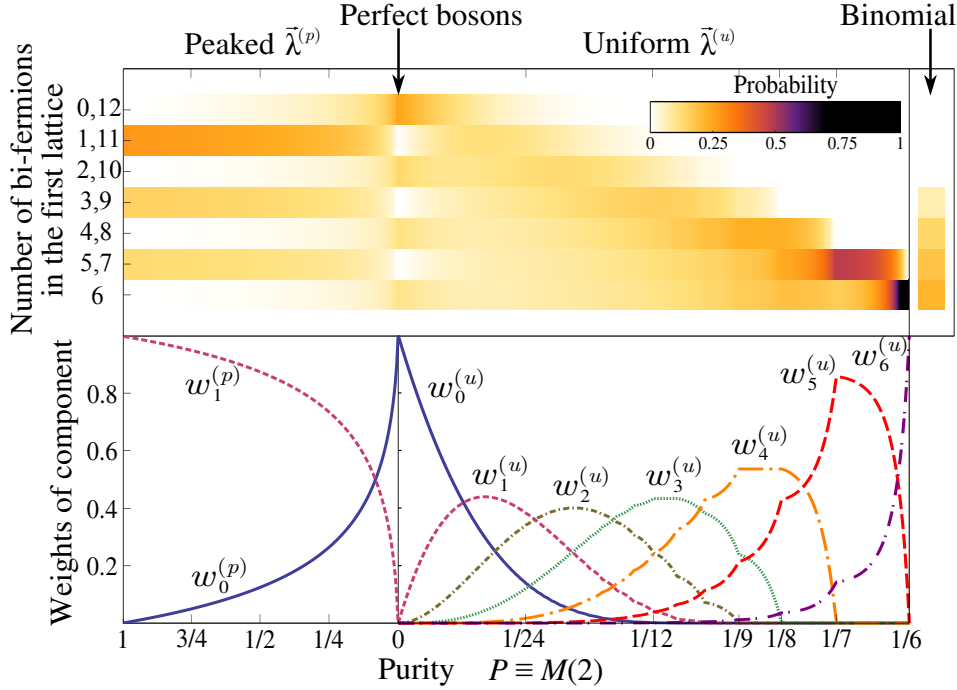


Figure 13.6: Upper panel: Counting statistics $P_{\text{tot}}(m)$ as a function of the purity, for the uniform (u) (right-hand part) and peaked (p) (left-hand part) distributions $\bar{\lambda}^{(u/p)}$. Lower panel: Corresponding weights $w_j^{(p/u)}$ of the coboson wavefunction in Eq. (13.58). We set $N_1 = N_2 = 6$, $R = 1/2$. The counting statistics is perfectly bosonic for vanishing purity, $P \rightarrow 0$, while cobosons behave as fermions for the uniform distribution and $P = 1/6$. The number of non-vanishing Schmidt-coefficients in the uniform distribution is $L = \lceil 1/P \rceil$, hence the weights $w_l^{(u)}$ with $l > N - L - 1$ vanish: There are at least $N_1 - L - 1$ pairs of fermions, which results in the kinks in the weights. The binomial distribution corresponds to the statistics of distinguishable particles.

The dependence of $P_{\text{tot}}(k)$ on the power-sums $M(m)$ can be used to infer the latter from measured counting statistics for different N_1, N_2 . The purity P follows immediately for $N_1 = N_2 = 1$ via Eq. (13.67); in general $M(m)$ is inferred by the counting statistics of a total of $N_1 + N_2 = m$ cobosons. Since higher-order power-sums are constrained by Jensen's and Hölder inequalities [337],

$$M(m-1)^{\frac{m-1}{m-2}} \leq M(m) \leq M(m-1)^{\frac{m}{m-1}}, \quad (13.69)$$

bounds for higher-order $M(m)$ become tighter with increasing knowledge of $M(m)$, as depicted in Fig. 13.7.

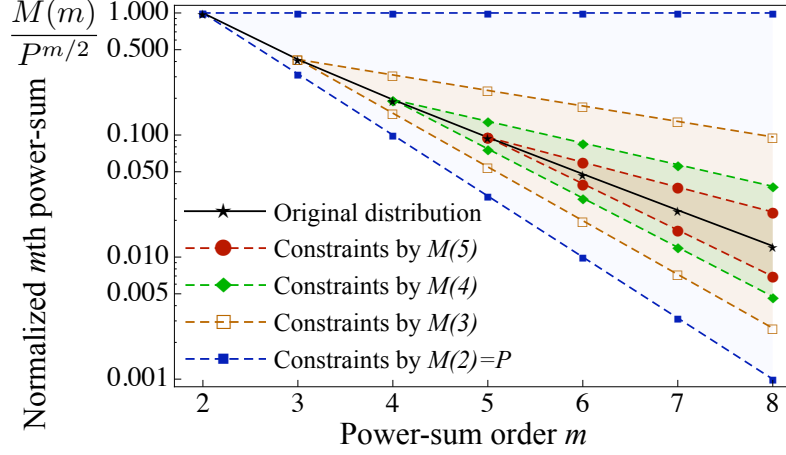


Figure 13.7: Normalized power-sums and constraints. The normalization to $P^{m/2}$ is chosen such that the upper bound is constant. A randomly chosen distribution $\vec{\lambda}$ leads to a certain hierarchy of power-sums (black stars). The measurement of interference signals with N_1 and N_2 cobosons reveals the power-sums up to order $N_1 + N_2$, which leads to the indicated constraints on higher-order $M(m)$ with $m \geq N_1 + N_2 + 1$ (blue, orange, green and red symbols), according to Eq. (13.69).

13.6 Many cobosons interference in the macroscopic approach

When the exact counting statistics cannot be retrieved and many ($N \gtrsim 1000$) cobosons are brought to interference, such as in the interference of BECs [326], the granular structure of the interference pattern becomes secondary. The impact of imperfect bosonic behavior can then be incorporated into a macroscopic wavefunction approach [355], *i.e.* the number of particles is treated as the amplitude of a single-particle wavefunction. Fock-states are modeled by a random phase between the different components of the wavefunction as described in Section 13.1.3. When the fractions $I_j = N_j/(N_1 + N_2)$ of ideal bosons are prepared in the two lattices, the particle fraction I in the upper lattice after beam-splitter dynamics obeys the probability distribution given in Ref. [355], as in Eq. (13.36),

$$\mathcal{P}_{\text{MWF}}(I; I_1, I_2) = \frac{1}{\pi \sqrt{4RTI_1I_2 - (I - RI_1 - TI_2)^2}},$$

for $4RTI_1I_2 > (I - RI_1 - TI_2)^2$, while it vanishes otherwise. For cobosons, a finite fraction of fermions needs to be accounted for in each lattice. The probability distribution for the particle fraction I then becomes

$$\mathcal{P}(I) = \int_0^{I_2} dI_f \mathcal{W}(I_f) \mathcal{P}_{\text{MWF}}(I - I_f; I_1 - I_f, I_2 - I_f),$$

where $\mathcal{W}(I_f)$ is the probability distribution of the fraction of fermions I_f in each lattice. For the uniform state $\vec{\lambda}^{(u)}$ with S Schmidt coefficients ($P = 1/S$),

$$w_p^{(u)} = \frac{N_1!N_2!(S - N_1)!(S - N_2)!}{S!(S + p - N_1 - N_2)!(N_1 - p)!(N_2 - p)!p!}. \quad (13.70)$$

The continuous limit $\mathcal{W}^{(u)}(I_f)$ is obtained for $N_1 + N_2 = N \rightarrow \infty$, when N_1, N_2, p and S are scaled linearly with N :

$$\mathcal{W}^{(u)}(I_f) = \lim_{N \rightarrow \infty} \left(N \cdot w_{(p=I_f \cdot N)}^{(u)} \right) = \delta(I_f - \rho I_1 I_2), \quad (13.71)$$

and the total number of bi-fermions per Schmidt mode is constant, $\rho = N/S$. Since the number of bi-fermions in either lattice is limited by S , it holds $0 < \rho \leq 1/I_1 \leq 2$. The fraction of perfect fermions is thus exactly the fraction of expected pairs of bi-fermions in the same Schmidt-mode, $\rho I_1 I_2$, which gives

$$\mathcal{P}^{(u)}(I) = \mathcal{P}_{\text{MWF}}(I - \rho I_1 I_2; I_1(1 - \rho I_2), I_2(1 - \rho I_1)).$$

The width W of this distribution is closely related to the fraction of fermions,

$$W = 4\sqrt{RTI_1 I_2(1 - \rho I_1)(1 - \rho I_2)}, \quad (13.72)$$

and becomes narrower with increasing number of bi-fermions per Schmidt mode, ρ . In principle, this may jeopardize Fock-state-interferometry with non-elementary particles such as neutral atoms or molecules, since the width of the intensity distribution is used to infer a small phase (which translates here into a reflectivity R).

Conclusions

Trapped ultracold atoms typically feature very small electron-state purities of the order of 10^{-13} [311, 303], such that atom interferometers are not sensitive to the compositeness of the atoms. With attractively interacting fermionic atoms in tunable external potentials [328, 371], the transition between fully bosonic ($P \rightarrow 0$) and fully fermionic ($P \rightarrow 1$) behaviors may be implemented experimentally by varying the size of the available single-fermion space and observing the resulting interference pattern when bi-fermions are brought to interference.

In conclusion, even though two fermions may be arbitrarily strongly bound to a coboson with no apparent substructure, deviations from ideal bosonic behavior can be observable in many-coboson interference. Not the binding energy, but the entanglement between the fermions is observable on the level of the cobosons. The superposition in Eq. (13.58) allows to understand the partially fermionic behavior of cobosons, and ultimately leads to simple expressions for the interference of BEC and mBEC given by Eq. (13.72). The methods that we have exposed can be extended immediately to larger numbers of sublattices and to more complex interference scenarios [356].

Cobosons always constitute *indistinguishable* particles; two cobosons in the two lattices share the same distribution of Schmidt coefficients $\vec{\lambda}$. The impact of partial distinguishability and the effects of compositeness can actually be discriminated in the experiment: While partially distinguishable particles can be described as a superposition of perfect bosons and distinguishable particles [358, 359], cobosons exhibit the behavior of a superposition of bosons and fermions, which naturally leads to differing interference patterns in the two cases (see also the binomial distribution in Fig. 13.6, which is attained for distinguishable particles).

The role of entanglement for bosonic behavior is twofold: It circumvents the Pauli principle for composite bosons [309, 303, 332, 316, 282], and it maintains many-particle coherence. Quantum correlations between the fermions are necessary for the bosonic exchange symmetry in the relevant parts of the wave-function that allows the representation in Eq. (13.58). If mixed states of bi-fermions are prepared instead of entangled states, the exchange symmetry and the encountered bosonic behavior break down – even though the combinatorial argument that relates to the number of accessible states remains valid. The visibility of correlation signals of, *e.g.* large molecules, is thus not only affected by the mixedness of the molecules at finite temperatures, but also by the consequent loss of many-particle coherence.

Single-particle densities

Here, let us define the two notions of single-particle probability densities used in this Thesis, particularly in Part I and Part II. We refer to the single-particle (or one-particle) density function and single-particle density matrix. The entropy associated to these density functionals gives rise to two very different interpretations of the entropic concepts that allow us to quantify different properties of the particles imbedded in the system.

We consider a system of N indistinguishable fermions (with spin $S = \frac{1}{2}$) described by the wavefunction

$$\Psi(\sigma_1 \vec{r}_1, \dots, \sigma_N \vec{r}_N) = \langle \sigma_1 \vec{r}_1, \dots, \sigma_N \vec{r}_N | \Psi \rangle, \quad (\text{A.1})$$

associated with a pure state $|\Psi\rangle$, within a d -dimensional domain $\Delta \subset \mathbb{R}^d$, being σ_i dichotomic variables adopting the possible values $\sigma_i = \pm$, corresponding to the S_z component, which describes the fermions spin degrees of freedom. The density matrix $\rho = |\Psi\rangle \langle \Psi|$ is given by

$$\begin{aligned} \rho(\sigma_1 \vec{r}_1, \dots, \sigma_N \vec{r}_N, \sigma'_1 \vec{r}'_1, \dots, \sigma'_N \vec{r}'_N) &= \\ &= \langle \sigma_1 \vec{r}_1, \dots, \sigma_N \vec{r}_N | \rho | \sigma'_1 \vec{r}'_1, \dots, \sigma'_N \vec{r}'_N \rangle = \\ &= \Psi(\sigma_1 \vec{r}_1, \dots, \sigma_N \vec{r}_N) \cdot \Psi^*(\sigma'_1 \vec{r}'_1, \dots, \sigma'_N \vec{r}'_N). \end{aligned} \quad (\text{A.2})$$

Performing the partial trace of ρ over $N - 1$ particles of the system, we obtain the *single-particle reduced density matrix* (of one arbitrary particle, e.g. \vec{r}_1)

$$\begin{aligned} \rho_r(\sigma_1 \vec{r}_1, \sigma'_1 \vec{r}'_1) &= \langle \sigma_1 \vec{r}_1 | \rho_r | \sigma'_1 \vec{r}'_1 \rangle = \text{Tr}_{N-1}[\rho] = \\ &= \sum_{\substack{\sigma_i = \pm \\ i=2, \dots, N}} \int_{\Delta} \Psi(\sigma_1 \vec{r}_1, \sigma_2 \vec{r}_2, \dots, \sigma_N \vec{r}_N) \Psi^*(\sigma'_1 \vec{r}'_1, \sigma_2 \vec{r}_2, \dots, \sigma_N \vec{r}_N) d\vec{r}_2 \dots d\vec{r}_N \end{aligned} \quad (\text{A.3})$$

which is a two point density containing all correlations of the particle \vec{r}_1 with the rest of the system. We use in Part II this density to compute the amount of entanglement. The qualitative difference between classically and quantum-mechanically correlated states can be appreciated upon these densities with two spatially well-separated constituents.

On the other hand, diagonal elements of $\rho_r(\sigma_1 \vec{r}_1, \sigma'_1 \vec{r}'_1)$ represent the *single-particle density function* of the particle \vec{r}_1 ,

$$\begin{aligned} \rho^{(1)}(\sigma_1 \vec{r}_1) &= \langle \sigma_1 \vec{r}_1 | \rho_r | \sigma_1 \vec{r}_1 \rangle = \\ &= \sum_{\substack{\sigma_i = \pm \\ i=2, \dots, N}} \int_{\Delta} |\Psi(\sigma_1 \vec{r}_1, \sigma_2 \vec{r}_2, \dots, \sigma_N \vec{r}_N)|^2 d\vec{r}_2 \dots d\vec{r}_N, \end{aligned} \quad (\text{A.4})$$

and whose meaning differs markedly. This density is interpreted classically as the probability distribution of finding a fermion in the position \vec{r}_1 , within its domain Δ , and with spin σ_1 for a given state $|\Psi\rangle$ of the system. Since the probabilities to obtain the fermion spin states $+$ and $-$ are the same, the single-particle density function is given just in terms of the fermion position $\rho(\vec{r}_1) = 2\rho^{(1)}(\sigma_1\vec{r}_1)$, as densities used in Part I. In the information-theoretic study carried out on the first part of the Thesis, we also use the single-particle density function in momentum space $\gamma(\vec{p})$; this basic function is given in terms of the d -dimensional Fourier transform of the position wavefunction

$$\begin{aligned} \tilde{\Psi}(\sigma_1\vec{p}_1, \dots; \sigma_N\vec{p}_N) = \\ \frac{1}{(2\pi\hbar)^{3N/2}} \int_{\Delta} \Psi(\sigma_1\vec{r}_1, \dots; \sigma_N\vec{r}_N) e^{-\frac{i}{\hbar} \sum_{i=1}^N \vec{p}_i \cdot \vec{r}_i} d\vec{r}_1 d\vec{r}_2 \dots d\vec{r}_N. \end{aligned} \quad (\text{A.5})$$

It is understood that for all atomic systems and models considered in this Thesis, all integrals are performed over the whole three-dimensional space $\Delta = \mathbb{R}^3$. Normalization to unity is also considered, so that $\int \rho(\vec{r}) d\vec{r} = \int \gamma(\vec{p}) d\vec{p} = 1$. Computations of $\rho(\vec{r})$ and $\gamma(\vec{p})$ for neutral and ionized atomic systems are done, throughout Part I, by means of accurate near-Hartree-Fock wavefunctions given in Refs. [219, 220].

Proof of bounds on the cobosons normalization ratio

In order to show Eq. (12.17) (ii) and (iii), we construct operations on the distribution $\vec{\lambda}$, in Section B.1. These leave the sum of the λ_j and the purity P invariant, while they increase or decrease the normalization ratio, as shown in Section B.2. Since only the extremal distributions $\vec{\lambda}^{(p)}$ and $\vec{\lambda}^{(u)}$ remain invariant under the application of the operations, these distributions maximize and minimize, respectively, the normalization ratio.

B.1 Uniforming and peaking operations

We construct *uniforming* and *peaking* operations on the distributions $\vec{\lambda}$ that act only on three selected λ_j , with the indices $1 \leq j_1 < j_2 < j_3 \leq S$. The operations will leave

$$K_1 = \lambda_{j_1} + \lambda_{j_2} + \lambda_{j_3}, \quad (\text{B.1})$$

$$K_2 = \lambda_{j_1}^2 + \lambda_{j_2}^2 + \lambda_{j_3}^2, \quad (\text{B.2})$$

invariant, and, consequently, also the total sum of the λ_j and of the λ_j^2 . The third power-sum, $M(3)$, however, will be changed by the operations.

In analogy to an analysis of the birthday-problem with non-uniform birthday probabilities [347], we define the two operations, Γ^u and Γ^p , on the probability distribution $\vec{\lambda}$:

$$\begin{aligned} \Gamma^{p/u}(\lambda_{j_1}) &= \frac{1}{3} \left(K_1 \pm \sqrt{6K_2 - 2K_1^2} \right), \\ \Gamma^{p/u}(\lambda_{j_2}) = \Gamma^{p/u}(\lambda_{j_3}) &= \frac{1}{6} \left(2K_1 \mp \sqrt{6K_2 - 2K_1^2} \right), \\ \Gamma^{p/u}(\lambda_{k \neq j_1, j_2, j_3}) &= \lambda_k, \end{aligned} \quad (\text{B.3})$$

where the upper (lower) sign in \pm and \mp refers to the peaking (uniforming) operation Γ^p (Γ^u). For $K_1^2 < 2K_2$, we formally have $\Gamma^u(\lambda_{j_1}) < 0$, and we alternatively set

$$\begin{aligned} \Gamma^u(\lambda_{j_1}) &= 0, \\ \Gamma^u(\lambda_{j_2/j_3}) &= \frac{1}{2} \left(K_1 \pm \sqrt{2K_2 - K_1^2} \right). \end{aligned} \quad (\text{B.4})$$

For convenience of notation, we set

$$\tilde{\lambda}_j^u = \Gamma^u(\lambda_j), \quad \tilde{\lambda}_j^p = \Gamma^p(\lambda_j). \quad (\text{B.5})$$

Colloquially speaking, Γ^u *levels out* the three coefficients $\lambda_{j_1}, \lambda_{j_2}, \lambda_{j_3}$ and thus makes the distribution more uniform, whereas Γ^p makes the distribution more peaked. In both cases, the purity P is kept constant. The operations push a distribution $\vec{\lambda}$ towards the uniform and peaked distribution, respectively, as illustrated in Fig. B.1.

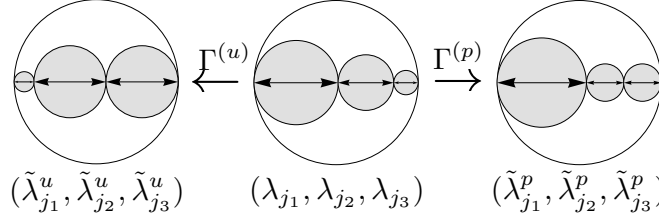


Figure B.1: Action of uniforming and peaking operations Γ^u and Γ^p . The tuple $(\lambda_{j_1}, \lambda_{j_2}, \lambda_{j_3})$ is leveled out by Γ^u , and made more peaked by Γ^p . We show only the coefficients λ_j with indices j_1, j_2, j_3 , all other coefficients λ_k remain constant under the application of the operations, for the choice of indices j_1, j_2, j_3 . The gray area represents the sum of the squared coefficients, being the same for all three distributions.

The uniform (peaked) distribution $\vec{\lambda}^{(u)}$ ($\vec{\lambda}^{(p)}$) is the only one that remains invariant under the application of Γ^p (Γ^u), for all choices of j_1, j_2, j_3 (disregarding permutations of the indices), which can be seen by applying the operations on the distributions.

B.2 Normalization ratio under operations

We now show that the uniforming (peaking) operation $\Gamma^{u(p)}$ reduces (increases) the normalization ratio, *i.e.* we conjecture

$$\frac{\chi_{N+1}(\Gamma^u(\vec{\lambda}))}{\chi_N(\Gamma^u(\vec{\lambda}))} \leq \frac{\chi_{N+1}(\vec{\lambda})}{\chi_N(\vec{\lambda})} \leq \frac{\chi_{N+1}(\Gamma^p(\vec{\lambda}))}{\chi_N(\Gamma^p(\vec{\lambda}))}, \quad (\text{B.6})$$

where we made the dependence of χ_N on the distributions explicit.

Without restrictions of generality and for convenience of notation, we set $j_1 = 1, j_2 = 2, j_3 = 3$, *i.e.* we let the operations act on the first three Schmidt coefficients.

We define

$$\tilde{\chi}_N = \chi_N(\lambda_4, \dots, \lambda_S), \quad (\text{B.7})$$

$$\Lambda = \lambda_1 \lambda_2 \lambda_3 \quad (\text{B.8})$$

i.e. formally $\tilde{\chi}_N$ is a normalization factor, but for an unnormalized distribution $\{\lambda_4, \dots, \lambda_S\}$. With these definitions, we rewrite χ_N as

$$\begin{aligned} \chi_N &= \Lambda \cdot \tilde{\chi}_{N-3} + (\lambda_1 \lambda_2 + \lambda_3 \lambda_2 + \lambda_1 \lambda_3) \tilde{\chi}_{N-2} + \\ &+ (\lambda_1 + \lambda_2 + \lambda_3) \tilde{\chi}_{N-1} + \tilde{\chi}_N. \end{aligned} \quad (\text{B.9})$$

The terms

$$\lambda_1 \lambda_2 + \lambda_3 \lambda_2 + \lambda_1 \lambda_3 = \frac{1}{2} (K_1^2 - K_2), \quad (\text{B.10})$$

$$\lambda_1 + \lambda_2 + \lambda_3 = K_1, \quad (\text{B.11})$$

and $\tilde{\chi}_k$ with $k \in \{N - 3, \dots, N\}$ do not change upon application of $\Gamma^{u/p}$, i.e. only the product Λ is affected by the operations.

Conjecture: It holds

$$\tilde{\lambda}_1^u \tilde{\lambda}_2^u \tilde{\lambda}_3^u \leq \Lambda \leq \tilde{\lambda}_1^p \tilde{\lambda}_2^p \tilde{\lambda}_3^p, \quad (\text{B.12})$$

where $\tilde{\lambda}_j^{u/p}$ is the result of the operation $\Gamma^{u/p}$ on λ_j .

Proof: We re-write the products in terms of K_1, K_2 and λ_1

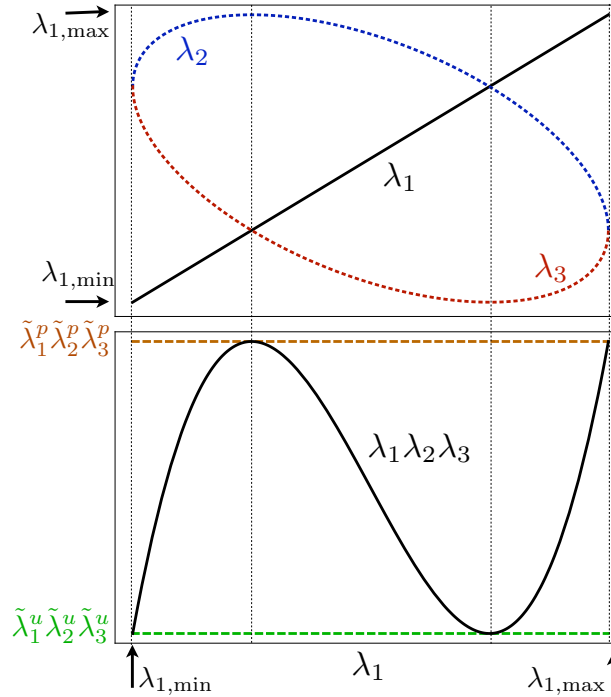


Figure B.2: Upper panel: Possible values of λ_1, λ_2 and λ_3 , given K_1 and K_2 , as a function of λ_1 , in arbitrary units. Lower panel: Behavior of $\lambda_1 \lambda_2 \lambda_3$ as a function of λ_1 , and lower and upper bounds. The lower (upper) bounds are attained if and only if the configuration fulfills $\lambda_{j_1} > \lambda_{j_2} = \lambda_{j_3}$ ($\lambda_{j_1} < \lambda_{j_2} = \lambda_{j_3}$), where $\{j_1, j_2, j_3\}$ is a permutation of $\{1, 2, 3\}$. These points are marked by thin dotted vertical lines.

$$\begin{aligned}
\tilde{\lambda}_1^u \tilde{\lambda}_2^u \tilde{\lambda}_3^u &= \begin{cases} \frac{1}{108} \left(K_1 - \sqrt{6K_2 - 2K_1^2} \right) & \text{for } K_1^2 > 2K_2 \\ \times \left(2K_1 + \sqrt{6K_2 - 2K_1^2} \right)^2 & \\ 0 & \text{for } K_1^2 \leq 2K_2 \end{cases} \\
\Lambda &= \frac{1}{2} \lambda_1 (2\lambda_1^2 - 2\lambda_1 K_1 + K_1^2 - K_2) \\
\tilde{\lambda}_1^p \tilde{\lambda}_2^p \tilde{\lambda}_3^p &= \frac{1}{108} \left(K_1 + \sqrt{6K_2 - 2K_1^2} \right) \\
&\quad \times \left(2K_1 - \sqrt{6K_2 - 2K_1^2} \right)^2
\end{aligned} \tag{B.13}$$

For given K_1 and K_2 , we can find the possible $\lambda_{2/3}$, leaving λ_1 as a free parameter,

$$\lambda_{2/3} = \frac{1}{2} \left(K_1 - \lambda_1 \pm \sqrt{2\lambda_1 K_1 - K_1^2 - 3\lambda_1^2 + 2K_2} \right)$$

The requirement $\lambda_{2/3} \geq 0$ gives

$$\lambda_{1,\max/\min} = \frac{1}{3} \left(K_1 \pm \sqrt{2} \sqrt{3K_2 - K_1^2} \right), \tag{B.14}$$

$$\lambda_{1,\min} \leq \lambda_1 \leq \lambda_{1,\max} \tag{B.15}$$

Given K_1, K_2 , all possible values of λ_1 then fulfill Eq. (B.12). \square

The inequalities in Eq. (B.12) are saturated for $\tilde{\lambda}_j^{u/p} = \lambda_j$ (modulo permutation of the indices). Possible values of λ_j and the behavior of the product $\lambda_1 \lambda_2 \lambda_3 = \Lambda$ are shown in Fig. B.2. With Eq. (B.9), it immediately follows that

$$\chi_N^{(u)} \leq \chi_N \leq \chi_N^{(p)}. \tag{B.16}$$

Using Eq. (B.12), we can set

$$\lambda_1^p \lambda_2^p \lambda_3^p =: \Lambda(1 + \varepsilon),$$

$$\lambda_1^u \lambda_2^u \lambda_3^u =: \Lambda(1 - \delta),$$

with $\varepsilon, \delta \geq 0$, and

$$\begin{aligned}
B_N &= (\lambda_1 \lambda_2 + \lambda_3 \lambda_2 + \lambda_1 \lambda_3) \tilde{\chi}_{N-2} \\
&\quad + (\lambda_1 + \lambda_2 + \lambda_3) \tilde{\chi}_{N-1} + \tilde{\chi}_N.
\end{aligned}$$

For any distribution $\vec{\lambda}$ (which does not need to fulfill $\sum_j \lambda_j = 1$), the Newton-Maclaurin inequality holds [336, 303], which reads

$$\frac{\tilde{\chi}_{N+1}}{\tilde{\chi}_N} \leq \frac{\tilde{\chi}_N}{\tilde{\chi}_{N-1}}. \tag{B.17}$$

We thus have

$$\tilde{\chi}_{N-3} \geq \tilde{\chi}_{N-2}, B_N \geq B_{N+1}. \quad (\text{B.18})$$

Our original conjecture as given by Eq. (B.6) is equivalent to

$$\begin{aligned} \frac{\Lambda(1-\delta)\tilde{\chi}_{N-2} + B_{N+1}}{\Lambda(1-\delta)\tilde{\chi}_{N-3} + B_N} &\leq \frac{\Lambda\tilde{\chi}_{N-2} + B_{N+1}}{\Lambda\tilde{\chi}_{N-3} + B_N} \\ &\leq \frac{\Lambda(1+\varepsilon)\tilde{\chi}_{N-2} + B_{N+1}}{\Lambda(1+\varepsilon)\tilde{\chi}_{N-3} + B_N}, \end{aligned} \quad (\text{B.19})$$

and follows from Eq. (B.18).

Consequently, $\vec{\lambda}^{(p)}$ ($\vec{\lambda}^{(u)}$) maximizes (minimizes) the normalization ratio χ_{N+1}/χ_N for given P and S , which proves (ii) and (iii). The inequality (iv) then follows by taking the indicated limit, $S \rightarrow \infty$.

Concluding remarks

The aim of the work presented in this Thesis was to gain insight into the quantification of the informational content of the quantum many-body systems by means of information-theoretic measures of entropic and complexity types, as well as via entanglement measures.

A.- In Part I we have first used some known one- and two-component information-theoretic measures to quantify various facets of the internal disorder of some non-relativistic and relativistic systems, such as uncertainty, randomness, correlation, organization, complexity, information and delocalization. Beyond the introductory Chapter 1, we began in **Chapter 2** with two elementary quantum systems (the Dirac-delta-like models), analytically solvable, to gain insight into the meaning of the previous information-theoretic quantities. These Dirac models have been used as prototypes to describe and interpret numerous phenomena and processes in many scientific fields, including atomic and molecular physics, condensed matter and quantum computation. Then, in **Chapter 3**, we have analysed the three main relativistic effects of the hydrogenic atom (electronic charge contraction towards the nucleus, nodal disappearance and charge gradient reduction) by means of the entropic and complexity measures as well as via some information planes. Here the main role is played by the Fisher information and the Fisher-Shannon and LMC complexity measures. This is basically because the Fisher information measures the gradient content of the density and the (dimensionless) composite information-theoretic quantities grasp two-fold facets of the electronic distribution: The Fisher-Shannon complexity quantifies the combined balance of the gradient content and the total extent of the electronic charge, and the LMC complexity quantifies the disequilibrium jointly with the spreading of the density in the configuration space. The behavior of these three quantities with respect to the energy and the quantum numbers characterizing the Dirac states have been determined and discussed in detail. Later in **Chapter 4**, some general upper bounds to the entropic moments of the position and momentum single-particle densities of an arbitrary quantum many-body system are derived in terms of the radial expectation values in the conjugate space. They are also applied to some macroscopic energy functionals, such as *e.g.* of Thomas-Fermi and Dirac exchange types, and their validity and accuracy is further examined throughout the periodic table for all neutral atoms.

Secondly, we have introduced in **Chapters 5, 6 and 7** three new tools to study how diverse are two or more quantum many-body systems among each other from an information-theoretical point of view; namely, the one-parameter generalised quantum similarity index, the one-parameter generalised divergence measure or geometric Rényi divergence, and the two-parameter generalised relative complexity. They generalised and improve all the previous corresponding ones published in the literature, including them as particular instances. We have applied these new tools to all neutral atoms as well as cations and anions from hydrogen to lawrencium, what allow to cluster them in an information-theoretical way, allowing their discussion in terms of the corresponding shell-filling patterns.

B.- Quantum entanglement renders efficient simulations of many-particle systems impossible and entails the breakdown of efficient numerical treatments. With the help of analytically solvable models, one can use entanglement to assess the validity and scope of approximation techniques. In **Part II** we investigated the quantum entanglement in ground and excited states of various Moshinsky-like models formed by two, three and many harmonically interacting particles confined in a harmonic potential. The models are solvable which allows an exact determination of entanglement for different bi-partitions of the system. Beyond the opening **Chapter 8**, we studied in **Chapter 9** the 3D two-particle Moshinsky system in presence of a uniform magnetic field and the isolated 1D three-particle cases. Therein, we found and discussed the dependence of the entanglement on the energy of the system and the field strength. The entanglement of the three-particle system considered here depends only on the dimensionless parameter τ describing the relative strength of the interaction between the particles (as compared with the strength of the external confining potential). As a general trend, we found that the entanglement exhibited for these states tends to increase both with the state's energy and with the relative strength τ . Non-vanishing entanglement is obtained in the limit of vanishing interaction in the case of excited states. Moreover, this (apparent) discontinuous behavior of the entanglement is related to the degeneracy of the energy levels of the unperturbed Hamiltonian describing non-interacting particles. As far as the entanglement's dependence on the interaction strength and the energy are concerned, the behavior of the Moshinsky model with two particles in a uniform magnetic field is similar to the one observed in the three-particle model. With regards to the external magnetic field, we found that the entanglement of the eigenstates decreases when considering increasing magnetic fields. In the limit of very strong magnetic fields the entanglement approaches a finite asymptotic value that depends on the interaction strength.

In **Chapter 10**, we analysed the entanglement features of the many-particle Moshinsky model which is formed by N_n heavy particles (nuclei) and N_e light particles (electrons). We focussed on the entanglement associated with three different ways of partitioning the system: the entanglement between all the electrons (regarded as one subsystem) and all the nuclei, the entanglement between one electron and the rest of the system, and the entanglement between one nucleus and the rest of the system. We studied the dependence of entanglement in the ground and the first few excited states on the relative particle-particle interaction strength, on the number of particles, and on the particle masses. While the nuclei-electrons entanglement depends upon the relative strength of the nucleus-electron interaction τ_{ne} , the nucleus (electron) entanglement depends on both τ_{ne} and τ_{nn} (τ_{ee}) that measures the relative nucleus-nucleus (electron-electron) interaction strength. As a general trend in all three cases, we found that entanglement increases as a function of the (corresponding) interaction parameter, approaching its maximum possible value in the limit of an infinitely large interaction. When the mass ratio is $M = 1$, excited states exhibit a finite amount of entanglement even in the case of arbitrarily weak interaction. The latter is related to the degeneracy of the energy levels of the Hamiltonian describing non-interacting particles. Finally, our work realized that, consistent with kinematic intuition, the entanglement between two subsystems vanishes when the subsystems have

very different masses, while it attains its maximal value for comparable masses. Moreover, the validity and the breakdown of the Born-Oppenheimer Ansatz can be understood from a quantum information point of view.

B.- In Part III we have examined in detail the deviations from the ideal bosonic behavior of the cobosons (*i.e.*, bosons formed by two bound and entangled fermions), which are shown to be observable in many coboson interferences. These cobosons can be treated as elementary bosons as long as the Pauli principle does not affect the behavior of many of such composite bosons. The departure of ideal bosonic behavior is quantified by the normalization ratio of multi-composite-boson states. Beyond the opening and introductory **Chapter 11**, we have investigated in **Chapter 12** the relationship between the compositeness character of cobosons and the entanglement, as characterized by the purity of the single-fermion states. More precisely, we have derived the two-fermion states that extremize the normalization ratio for a fixed single-fermion purity P , and establish general tight bounds for this indicator. For very small purities, $P < 1/N^2$ with N being the number of such composite bosons, the upper and lower bounds converge, which allows to quantify accurately the departure from perfectly bosonic behavior, for any state of many composite bosons.

In **Chapter 13** we have shown that the composite character of two-fermion bosons manifests itself in the interference of many composites as a deviation from the ideal bosonic behavior. We have described a state of many composites as a superposition of different numbers of perfect bosons and fermions, which allows us to provide the full Hong-Ou-Mandel-like counting statistics of interfering composites. Our theory has quantitatively related the deviation from the ideal bosonic interference pattern to the entanglement of the fermions within a single composite boson. Even though two fermions may be arbitrarily strongly bound to a coboson with no apparent substructure, deviations from ideal bosonic behavior can be observable in many-coboson interference. Not the binding energy, but the entanglement between the fermions is observable on the level of the cobosons. This theory can be achieved experimentally with attractively interacting fermionic atoms in tunable external potentials, the transition between fully bosonic ($P \rightarrow 0$) and fully fermionic ($P \rightarrow 1$) behaviors may be implemented experimentally by varying the size of the available single-fermion space and observing the resulting interference pattern when bi-fermions are brought to interference. Cobosons always constitute indistinguishable particles; two cobosons in the two lattices share the same distribution of Schmidt coefficients $\vec{\lambda}$. The impact of partial distinguishability and the effects of compositeness can actually be discriminated in the experiment: While partially distinguishable particles can be described as a superposition of perfect bosons and distinguishable particles, cobosons exhibit the behavior of a superposition of bosons and fermions, which naturally leads to differing interference patterns in the two cases.

This thesis as a whole provides a step forward in setting a number of classical and quantum information-theoretic tools to describe and quantify the internal disorder of fermionic and bosonic systems as characterized by means of the single-fermion density and the matrix density.

Conclusiones

En líneas generales esta Tesis trata de contribuir a la cuantificación del contenido informacional de los sistemas cuánticos de muchos cuerpos por medio de varias medidas entrópicas, de complejidad, similitud y divergencia, así como por medio de medidas de entrelazamiento.

A.- En la **Parte I** de la Tesis se ha realizado un estudio teórico-informacional de los sistemas cuánticos desde un punto de vista estadístico clásico, mediante el cual se cuantifican varias facetas de las densidades de probabilidad en los espacios de posiciones y momentos. Para ello se han usado algunas medidas entrópicas (Shannon, Rényi, Fisher y momentos de frecuencia) y de complejidad (Fisher-Shannon, LMC y Cramér-Rao). Además, se han introducido tres nuevas medidas relativas que permiten comparar entre sí dos o más densidades de probabilidad, que extienden y generalizan las medidas de este tipo existentes en la literatura.

Tras el Capítulo 1 de carácter introductorio, en el **Capítulo 2** hemos llevado a cabo un estudio de las medidas teórico-informacionales antes mencionadas en dos modelos físicos que involucran potenciales de tipo delta de Dirac, que son analíticamente resolubles. Estos modelos suelen usarse como prototipos para la descripción de numerosos fenómenos de distintos sistemas cuánticos. Este estudio nos ha permitido una mayor introspección en el significado y utilidad de las medidas entrópicas y de complejidad.

En el **Capítulo 3** hemos analizado los tres efectos relativistas principales del átomo hidrogenoide (la contracción de la carga electrónica hacia el núcleo, la desaparición de los nodos y la reducción del gradiente de la carga) por medio de las medidas entrópicas y de complejidad, así como de algunos planos de información. Hemos encontrado que la información de Fisher y las medidas de complejidad de Fisher-Shannon y LMC juegan un papel muy relevante. Básicamente, esto se debe a que la información de Fisher mide el contenido de gradiente de la densidad y que las medidas de complejidad cuantifican cada una de ellas una doble faceta de la distribución electrónica: la medida de Fisher-Shannon cuantifica el balance combinado del contenido de gradiente y la dispersión de la carga electrónica, y la medida LMC cuantifica el desequilibrio junto con la dispersión de la densidad en el espacio de configuración. Además, hemos determinado y discutido en detalle el comportamiento de estas tres magnitudes con respecto a la energía y a los números cuánticos que caracterizan los estados de Dirac del sistema.

En el **Capítulo 4** hemos obtenido cotas superiores de validez general a los momentos entrópicos de las densidades de probabilidad monoparticulares en los espacios de posiciones y de momentos para un sistema cuántico arbitrario, en términos de los valores esperados radiales en el espacio conjugado. Estas cotas son aplicadas más tarde a algunos funcionales macroscópicos de carácter energético, tales como las energías de Tomas-Fermi y de intercambio de Dirac, y su validez y precisión es analizada a lo largo de la tabla periódica para todos los átomos neutros.

A continuación, en los tres capítulos siguientes hemos introducido tres nuevas her-

ramientas para estudiar cuán diferentes son dos o más sistemas cuánticos de muchos cuerpos entre sí en un marco teórico-informacional; a saber, el índice de similitud cuántico generalizado monoparamétrico, la medida de divergencia geométrica de Rényi, y la complejidad relativa generalizada biparamétrica. Estas nuevas medidas generalizan y mejoran las que existían previamente en la literatura. Además hemos aplicado estas medidas a todos los átomos neutros y cationes, desde el hidrógeno al lawrencio, lo que permite agruparles teórico-informacionalmente, permitiendo así una discusión entrópica común en relación a los patrones de llenado de capas correspondientes y los potenciales de ionización.

En el **Capítulo 5** hemos generalizado el concepto de similitud cuántica existente para densidades de probabilidad monoparticulares en varios sentidos. El índice de similitud cuántico generalizado nos ha permitido (i) enfatizar diferentes regiones de las densidades de probabilidad a comparar mediante un parámetro de orden, (ii) comparar un número arbitrario de densidades monoparticulares y (iii) asignar pesos específicos a cada una de las densidades involucradas. Estas tres extensiones hacen de esta medida un instrumento mucho más útil que su predecesora a la hora de cuantificar similitudes entre diferentes densidades de probabilidad. Por ejemplo, hemos mostrado que esta generalización permite detectar la estructura de capas atómica mediante la comparación de densidades atómicas en espacio de posiciones escogiendo valores apropiados del parámetro de orden, mientras que el índice de similitud cuántico primitivo no era capaz. Es más, nos ha permitido incluso detectar aquellos átomos con un llenado anómalo de capas en el estudio general llevado a cabo, relacionando las subcapas de valencia de los diferentes átomos con la similitud entre ellos.

Las medidas de divergencia de tipo Jensen definidas hasta el momento están basadas en la media aritmética de las densidades para su simetrización. En el **Capítulo 6** se propone una medida alternativa de divergencia de Rényi entre densidades de probabilidad basada en la media geométrica de las mismas (*GRD* de ahora en adelante) y que incluye un parámetro de orden q positivo, al igual que la divergencia de Jensen-Rényi usual (*JRD*). La interpretación de *JRD* como medida de divergencia acota los posibles valores del parámetro de orden a valores comprendidos entre 0 y 1, mientras que para *GRD* no existe dicha restricción. En este capítulo hemos usado la medida *GRD* para comparar densidades monoparticulares atómicas. A partir de un análisis numérico detallado, se establece claramente la relación entre las propiedades de la capa de valencia de los sistemas objeto de comparación y los valores de *GRD*, así como la detección de la presencia de los sistemas que sufren un llenado anómalo de capas. Hemos mostrado la relación existente entre los valores extremos de divergencia y los del potencial de ionización atómica en la comparación de sistemas neutros y catiónicos. Otras aplicaciones también se han llevado a cabo satisfactoriamente, incluyendo los estudios de la capacidad para comparar diferentes modelos cuánticos, y la detección de sistemas atómicos que comparten la misma carga nuclear dentro de un conjunto de tres átomos distintos.

Para definir una medida adecuada de la complejidad relativa entre dos o más distribuciones, es esencial tener en cuenta las propiedades deseables que ha de verificar. Este no es el caso de la definición primitiva, ya que conduce a una interpretación contradictoria desde un punto de vista conceptual. Esta contradicción radica principalmente en el hecho de que puede tomar valores menores que la unidad; es decir, al valor de la complejidad

de un sistema respecto de sí mismo. Estas dificultades pueden evitarse mediante una generalización de la complejidad relativa tal como hemos hecho en el **Capítulo 7**, la cual posee dos parámetros de orden que pueden ser fijados de manera que sea siempre mayor que la unidad. Por otra parte, esta generalización permite introducir el concepto de complejidad relativa entre un número arbitrario de funciones, con la opción de considerar diferentes pesos para cada una de ellas. En este capítulo vemos que la interpretación de la estructura de capas es aún más eficiente cuando se expresa en términos de los diferentes grupos que pertenecen a los sistemas.

B.- El entrelazamiento cuántico hace muy difícil, cuando no imposible, la tarea de simular de forma eficiente los sistemas cuánticos de muchos cuerpos, y constituye la razón principal de que no existan tratamientos numéricos suficientemente precisos. Con la ayuda de modelos analíticamente resolubles, el entrelazamiento puede usarse para estimar la validez y el alcance de las técnicas de aproximación. En la **Parte II** de esta Tesis, hemos investigado el entrelazamiento cuántico tanto en el estado fundamental como en los estados excitados de varios modelos de tipo Moshinsky constituidos por dos, tres y muchas partículas armónicamente interaccionantes que se hallan confinadas en un potencial armónico. Estos modelos resultan ser matemáticamente resolubles, lo que permite una determinación exacta del entrelazamiento para diferentes biparticiones del sistema.

Tras el capítulo introductorio 8, hemos estudiado en el **Capítulo 9** los dos casos siguientes: el sistema $3D$ de dos partículas bajo la acción de un campo magnético uniforme, y el sistema $1D$ de tres partículas aislado.

Brevemente, hemos encontrado y discutido la dependencia del entrelazamiento con la energía y con la intensidad del campo externo aplicado. Además, resulta que el entrelazamiento del sistema de tres partículas solamente depende del parámetro adimensional τ que describe la intensidad relativa de la interacción partícula-partícula con respecto a la intensidad del potencial confinante externo. Es más, como tendencia general hemos encontrado que el entrelazamiento que presentan estos estados aumenta tanto con la energía del estado como con la intensidad relativa τ . El entrelazamiento de los estados excitados se anula en el límite de interacción nula, lo cual está estrechamente relacionado con la degeneración de los niveles de energía del hamiltoniano no-perturbado correspondiente a las partículas no-interaccionantes.

En cuanto al comportamiento del entrelazamiento con respecto a la energía y a la intensidad de la interacción, hemos observado que el sistema de dos partículas en un campo magnético uniforme es similar al caso de las tres partículas. Con respecto al campo magnético externo, hemos encontrado que el entrelazamiento de los autoestados disminuye cuando crece el campo. En el límite de campos muy fuertes, el entrelazamiento tiende a un valor finito que depende de la intensidad de la interacción.

En el **Capítulo 10**, hemos analizado las características del entrelazamiento del modelo de Moshinsky de muchas partículas que está formado por N_n partículas de gran masa (núcleos) y N_e partículas de masa pequeña (electrones). Nos hemos centrado en el entrelazamiento asociado con las tres siguientes particiones del sistema: el entrelazamiento entre todos los electrones (considerados como un subsistema) y todos los núcleos, el entrelazamiento entre un electrón y el resto del sistema, y el entrelazamiento entre un nú-

cleo y el resto del sistema. Hemos estudiado la dependencia del entrelazamiento tanto en el estado fundamental como en varios estados excitados con respecto a la intensidad partícula-partícula relativa, al número de partículas y a sus masas.

Hemos encontrado que mientras el entrelazamiento núcleos-electrones depende de la intensidad relativa de la interacción núcleo-electrón τ_{ne} , el entrelazamiento del núcleo (electrón) con el resto del sistema depende tanto de τ_{ne} como de τ_{nn} (τ_{ee}) que mide la intensidad relativa de la interacción núcleo-núcleo (electrón-electrón). En los tres casos hemos encontrado una tendencia general, el entrelazamiento crece en función de los correspondientes parámetros de interacción, alcanzando el máximo valor posible en el límite de interacción infinitamente grande. Cuando el cociente de masa (núcleo-electrón) es $M = 1$, los estados excitados exhiben una cantidad de entrelazamiento finito incluso en el límite de interacción nula. Este hecho está relacionado con la degeneración de los niveles de energía del Hamiltoniano que describe un sistema de partículas sin interacción.

Por último, en esta parte de la Tesis se mostró que, consistentemente con una intuición cinemática, el entrelazamiento entre los dos subsistemas desaparece cuando dichos subsistemas tienen una masa total muy diferente, mientras que alcanza su valor máximo cuando las masas son comparables. Además, la validez de la aproximación de Born-Oppenheimer se puede entender desde un punto de vista de la información cuántica. Se ha mostrado que esta aproximación es capaz de describir correctamente estados altamente entrelazados y que la validez de este Ansatz está caracterizada por el parámetro de masas $\gamma = MN_n/N_e$ y no únicamente por el cociente de las masas de las partículas (M).

C.- El principio de composición, basado en el tratamiento de las partículas compuestas como objetos elementales a pesar de su estructura subyacente, es un pilar fundamental de la ciencia. Los sistemas compuestos por un número par de fermiones son tratados en física cuántica como bosones perfectos, pero ¿hasta que punto podemos hacer esta suposición sin tener en cuenta la estructura fermiónica de las partículas constituyentes?. Dar una respuesta más precisa a esta cuestión mejorando las cotas ya existentes al comportamiento ideal bosónico, así como buscar el marco experimental donde pueda observarse la no-idealidad de bosones compuestos (o cobosones) ha sido el objetivo de la **Parte III** de esta Tesis.

El cociente de los factores de normalización, χ_{N+1}/χ_N , de un estado de N cobosones resulta ser un importante indicador para el comportamiento de bosones no elementales. En el **Capítulo 12** mostramos las cotas superior e inferior óptimas al cociente χ_{N+1}/χ_N , que dependen de N , y la representación explícita de los estados que saturan estas cotas.

En el límite de purezas muy pequeñas (alto entrelazamiento), $P < 1/N^2$, el comportamiento bosónico de un estado de N cobosones está prácticamente definido por P , puesto que las cotas superior e inferior coinciden. En la práctica las partículas ligadas suelen satisfacer que $P \ll 1/N^2$, por ejemplo, los átomos en condensados de Bose-Einstein. Las cotas descritas en este capítulo proporcionan por lo tanto una forma simple y fiable para comprobar la desviación del comportamiento bosónico de cualquier tipo de cobosones. Sin embargo, cuando la pureza no es muy pequeña, $P \simeq 1/N$, la forma de la función de onda desempeña un papel esencial en el comportamiento bosónico, y no puede describirse exclusivamente por P . En ese caso, para describir el estado y su com-

portamiento bosónico, es necesario recurrir a sumas de potencias de los coeficientes de Schmidt ($M(m)$, siendo $P = M(2)$) con orden mayor que 2.

Para una pureza dada P , la distribución uniforme de coeficientes de Schmidt minimiza la probabilidad de que el principio de Pauli sea irrelevante, o sea, del comportamiento bosónico, mientras que una distribución picuda (todos los coeficientes de Schmidt iguales excepto uno que es mayor) lo maximiza. A pesar de que la distribución picuda da como resultado, en general, un cociente de normalización menor que para la distribución uniforme, esto es debido principalmente al cambio consecuente de la pureza. En realidad, si se fija un valor de la pureza P , el comportamiento bosónico de la distribución uniforme es inferior con respecto a la picuda.

En el **Capítulo 13** investigamos un formalismo general para el estudio del proceso de interferencia tipo Hong-Ou-Mandel de muchos bosones compuestos por dos fermiones. En él mostramos que el estado de N cobosones, en la dinámica de un beam-splitter, puede ser descrito por una superposición de estados con un número determinado de bosones y fermiones perfectos. Esta superposición permite entender el comportamiento parcialmente fermiónico de los cobosones obteniendo, a su vez, expresiones sencillas para el proceso de interferencia.

Los átomos atrapados ultrafríos, en general, poseen purezas de su estado electrónico muy pequeñas, del orden de 10^{-13} , de manera que los interferómetros de átomos no son sensibles al carácter compuesto de los átomos. Sin embargo, con átomos fermiónicos que interactúan atractivamente en potenciales externos manipulables, la transición entre el comportamiento bosónico perfecto ($P \rightarrow 0$) y totalmente fermiónico ($P \rightarrow 1$) puede implementarse experimentalmente variando el número de estados accesibles por un único fermión, y observarse en el patrón de interferencia resultante cuando los bifermiones son detectados después del proceso de interferencia.

En este capítulo demostramos que, a pesar de que dos fermiones pueden estar fuertemente ligados en un cobosón sin subestructura aparente, las desviaciones del comportamiento ideal bosónico pueden ser observadas en la interferencia de muchos cobosones. Por tanto no es la energía de enlace lo que determina la escala observable en la composición de las partículas sino el entrelazamiento entre los fermiones que constituyen el cobosón. La superposición antes mencionada permite entender el comportamiento parcialmente fermiónico de los cobosones, y en última instancia conduce a expresiones simples para la interferencia de un número muy grande ($N \gtrsim 1000$) de cobosones en BEC y en BEC moleculares. Los métodos que hemos expuesto se pueden extender de inmediato a un mayor número de sublatices y para casos de interferencia más complejos.

Los cobosones constituyen siempre partículas indistinguibles; dos cobosones en dos lattices comparten la misma distribución de coeficientes de Schmidt. El impacto de la distinguibilidad parcial y los efectos de composición en realidad pueden ser discernidos en el experimento: mientras que las partículas parcialmente distinguibles pueden ser descritas como una superposición de bosones perfectos y partículas distinguibles, los cobosones exhiben el comportamiento de una superposición de bosones y fermiones, lo que conduce naturalmente a diferentes patrones de interferencia en los dos casos.

El papel del entrelazamiento en el comportamiento bosónico es doble: se evita el principio de Pauli para bosones compuestos, y mantiene la coherencia de muchas partículas.

Las correlaciones cuánticas entre los fermiones son necesarias para que la simetría de intercambio bosónico en las partes pertinentes de la función de onda permita escribir el estado como una superposición. Si se preparan estados mixtos de bifermiones en lugar de estados entrelazados, la simetría de intercambio y el comportamiento bosónico se pierden; a pesar de que el argumento combinatorio, que se relaciona con el número de estados accesibles, sigue siendo válido. La visibilidad en las señales debidas a las correlaciones de, por ejemplo, las moléculas grandes, se ve afectada por lo tanto no sólo por la mezcla de las moléculas a temperaturas finitas, sino también por la consiguiente pérdida de coherencia de muchas partículas.

Bibliography

- [1] A. Peres and W. H. Zurek, *Am. J. Phys.* **50**, 807 (1982). (Cited on pages 1 and 5.)
- [2] R. F. Nalewajski, *Perspectives in Electronic Structures Theory* (Springer, Berlin, 2012). (Cited on pages 1 and 5.)
- [3] R. F. Nalewajski, *Information Theory of Molecular Systems* (Elsevier, Amsterdam, 2006). (Cited on pages 1 and 5.)
- [4] K. Sen, editor, *Statistical Complexity: Applications in Electronic Estructure* (Springer Verlag, Berlin, 2011). (Cited on pages 1, 5, 19, 25, 47 and 97.)
- [5] M. C. Tichy, F. Mintert, and A. Buchleitner, *J. Phys. B: At. Mol. Opt. Phys.* **44**, 192001 (2011). (Cited on pages 1, 5, 15, 111, 119, 149 and 185.)
- [6] D. Bouwmeester, A. Ekert, and A. Zeilinger, *The Physics of Quantum Information: Quantum Cryptography, Quantum Teleportation, Quantum Computation* (Springer, Berlin, 2000). (Cited on pages 1 and 5.)
- [7] G. Gilbert, Y. Weinstein, and M. Hamrick, *Quantum Criptography* (World Scientific, London, 2013). (Cited on pages 1 and 5.)
- [8] N. Nielsen and I. L. Chuang, *Quantum Computation and Quantum Information* (Cambridge University Press, Cambridge, 2000). (Cited on pages 1, 5, 15, 21, 61, 111 and 113.)
- [9] M. M. Wilde, editor, *Quantum Information Theory* (Cambridge U.P., Cambridge, 2013). (Cited on pages 1 and 5.)
- [10] J. Jones and D. Jaksch, *Quantum Information, Computation and Communication* (Cambridge Univ. Press, Cambridge, 2012). (Cited on pages 1, 5 and 113.)
- [11] L. Davidovich, *Introduction to Quantum Optics and Laser Theory* (PUC, Rio de Janeiro, 1984), Mono-graph. (Cited on pages 1 and 5.)
- [12] M. Haroche, S. Brune, J. Raimond, and L. Davidovich, *Mesoscopic quantum coherences in cavity QED in Fundamentals of Quantum Optics III* (Springer Verlag, New York, 1994). (Cited on pages 1 and 5.)
- [13] L. Davidovich, *Measuring the Quantum State of the Electromagnetic Field, in Collective Excitations in Fermi and Bose Systems* (World Scientific, Singapour, 1999). (Cited on pages 1 and 5.)
- [14] L. Davidovich, *Decoherence, quantum information, and quantum-state reconstruction in quantum optics, in Handbook of Theoretical and Computational Nanotechnology* (American Scientific Publishers, 2006). (Cited on pages 1 and 5.)

- [15] G. Auletta, *Cognitive Biology. Dealing with Information from Bacetria to Minds* (Oxford U.P., Oxford, 2011). (Cited on page 1.)
- [16] J. Avery, *Information Theory and Evolution* (World Scientific, London, 2004). (Cited on pages 1 and 5.)
- [17] D. Abbott, P. Davies, and A. Pati, *Quantum Aspects of Life* (Imperial College Press, London, 2009). (Cited on pages 1 and 5.)
- [18] E. Haven and A. Khrennikov, *Quantum Social Science* (Cambridge U.P., Cambridge, 2013). (Cited on pages 1 and 5.)
- [19] R. O. Esquivel *et al.*, *Decoding the Building Blocks of Life from the Perspective of Quantum Information -Book "Advances in Quantum Mechanics", Chapter 27-*. (InTech, 2013). (Cited on pages 1, 5 and 15.)
- [20] E. Schrödinger, *Math. Proc. Cambridge Phil. Soc.* **31**, 555 (1935). (Cited on pages 15 and 113.)
- [21] A. Einstein, B. Podolsky, and N. Rosen, *Phys. Rev.* **47**, 777 (1935). (Cited on pages 15, 111 and 113.)
- [22] C. Macchiavello, G. M. Palma, and A. Zeilinger, *Quantum Computation And Quantum Information Theory* (World Scientific, Singapore, 1999). (Cited on page 15.)
- [23] A. P. Majtey, A. Borrás, M. Casas, P. W. Lamberti, and A. Plastino, *Int. J. Quantum Inf.* **06**, 715 (2008). (Cited on pages 15 and 27.)
- [24] A. P. Majtey, P. W. Lamberti, and D. P. Prato, *Phys. Rev. A* **72**, 052310 (2005). (Cited on pages 15, 28 and 73.)
- [25] P. W. Lamberti, A. P. Majtey, A. Borrás, M. Casas, and A. Plastino, *Phys. Rev. A* **77**, 052311 (2008). (Cited on pages 15, 27, 28 and 73.)
- [26] R. O. Esquivel *et al.*, *J. Phys. B: At. Mol. Opt. Phys.* **44**, 175101 (2011). (Cited on page 15.)
- [27] J. S. Dehesa, A. Martínez-Finkelshtein, and V. N. Sorokin, *Mol. Phys.* **104**, 613 (2006). (Cited on pages 15, 25, 31 and 35.)
- [28] S. R. Gadre, R. D. Bendale, and S. P. Gejji, *Chem. Phys. Lett.* **117**, 138 (1985). (Cited on page 15.)
- [29] M. Ho *et al.*, *J. Chem. Phys.* **108**, 5469 (1998). (Cited on pages 15, 27 and 73.)
- [30] S. Janssens, A. Borgoo, C. V. Alsenoy, and P. Geerlings, *J. Phys. Chem. A* **112**, 10560 (2008), PMID: 18823104. (Cited on pages 15, 27, 64 and 73.)
- [31] S. López-Rosa, J. Antolín, J. C. Angulo, and R. O. Esquivel, *Phys. Rev. A* **80**, 012505 (2009). (Cited on pages 15, 27, 73 and 111.)

- [32] S. López-Rosa *et al.*, *J. Chem. Theor. Comp.* **6**, 145 (2010). (Cited on page 15.)
- [33] P. Hohenberg and W. Kohn, *Phys. Rev.* **136**, B864 (1964). (Cited on page 15.)
- [34] R. K. Pathak and S. R. Gadre, *J. Chem. Phys.* **74**, 5925 (1981). (Cited on pages 15 and 61.)
- [35] R. K. Pathak and L. J. Bartolotti, *Phys. Rev. A* **31**, 3557 (1985). (Cited on pages 15 and 61.)
- [36] R. G. Parr and W. Yang, *Density Functional Theory of Atoms and Molecules* (Oxford University Press, New York, 1989). (Cited on pages 15, 62, 65 and 83.)
- [37] R. O. Esquivel *et al.*, *Some Applications of Quantum Mechanics* (InTech, Rijeka, 2012), . (Cited on pages 19 and 47.)
- [38] R. O. Esquivel *et al.*, *Information-Theoretical Analyses of Systems and Processes of Chemical and Nanotechnological Interest* (Nova Science Publishers, New York, 2011), . (Cited on pages 19 and 47.)
- [39] T. M. Cover and J. A. Thomas, *Elements of Information Theory* (Wiley Interscience, New York, 1991). (Cited on pages 20, 21, 26, 27, 29 and 48.)
- [40] J. Uffink, *Measures of uncertainty and the uncertainty principle*, PhD thesis, University of Utrecht, 1990. (Cited on pages 20, 21 and 22.)
- [41] C. Shannon and W. Weaver, *The Mathematical Theory of Communication* (University of Illinois Press, Urbana, Illinois, 1949). (Cited on pages 20, 27, 62 and 118.)
- [42] L. Rudnicki, *J. Russ. Laser Res.* **32**, 393 (2011). (Cited on page 20.)
- [43] A. Rényi, *Proceedings 4th Berkeley Symposium on Mathematics, Statistics and Probability* **1**, 547 (1961), University of California Press, Berkeley. (Cited on pages 20 and 62.)
- [44] M. Kendall and A. Stuart, *The advances Theory of Statistics* (Charles Griffin and Co. Ltd., London, 1969). (Cited on pages 21 and 62.)
- [45] H. Maassen and J. B. M. Uffink, *Phys. Rev. Lett.* **60**, 1103 (1988). (Cited on pages 21 and 24.)
- [46] M. J. W. Hall, *Phys. Rev. A* **59**, 2602 (1999). (Cited on pages 21 and 22.)
- [47] J. Pipek and I. Varga, *Phys. Rev. A* **46**, 3148 (1992). (Cited on page 21.)
- [48] R. Carbó, L. Leyda, and M. Arnau, *Int. J. Quantum Chem.* **17**, 1185 (1980). (Cited on pages 21, 27, 29, 63 and 77.)
- [49] O. Onicescu, *C. R. Acad. Sci. Paris, Ser. A* **25**, 263 (1966). (Cited on pages 21, 38, 62 and 65.)

- [50] R. López-Ruiz, H. Mancini, and X. Calbet, *Phys. Lett. A* **209**, 321 (1995). (Cited on pages 21, 25, 63 and 98.)
- [51] R. G. Catalán, J. Garay, and R. López-Ruiz, *Phys. Rev. E* **66**, 011102 (2002). (Cited on page 21.)
- [52] R. López-Ruiz, *Biophys. Chem.* **115**, 215 (2005), BIFI 2004 International Conference Biology after the Genoma: A Physical View. (Cited on page 21.)
- [53] J. C. Angulo and J. Antolín, *J. Chem. Phys.* **128**, 164109 (2008). (Cited on pages 21, 25, 26, 73, 97 and 100.)
- [54] R. O. Esquivel *et al.*, *Phys. Chem. Chem. Phys.* **12**, 7108 (2010). (Cited on pages 21, 25 and 97.)
- [55] R. A. Fisher, *Math. Proc. Cambridge Phil. Soc.* **22**, 700 (1925). (Cited on page 21.)
- [56] B. Frieden, *Science from Fisher Information* (Cambridge University Press, Cambridge, England, 2004). (Cited on page 21.)
- [57] M. J. W. Hall, *Phys. Rev. A* **62**, 012107 (2000). (Cited on page 22.)
- [58] M. J. W. Hall, *Phys. Rev. A* **64**, 052103 (2001). (Cited on page 22.)
- [59] J. C. Angulo, *Phys. Rev. A* **50**, 311 (1994). (Cited on pages 23 and 61.)
- [60] J. C. Angulo, *J. Phys. A: Math. Gen.* **26**, 6493 (1993). (Cited on pages 23 and 61.)
- [61] W. Heisenberg, *Z. Phys.* **43**, 172 (1927). (Cited on pages 23 and 61.)
- [62] W. Yue and L. Janmin, *Phys. Scr.* **30**, 414 (1984). (Cited on pages 23 and 61.)
- [63] S. R. Gadre and S. J. Chakravorty, *J. Chem. Phys.* **84**, 7051 (1986). (Cited on pages 23, 61 and 66.)
- [64] P. Sánchez-Moreno, R. González-Férez, and J. Dehesa, *New J. Phys.* **8**, 330 (2006). (Cited on page 23.)
- [65] L. Rudnicki, *Phys. Rev. A* **85**, 022012 (2012). (Cited on page 23.)
- [66] I. Białyński-Birula and J. Mycielski, *Commun. Math. Phys.* **44**, 129 (1975). (Cited on pages 24, 35 and 61.)
- [67] L. Rudnicki, P. Sánchez-Moreno, and J. S. Dehesa, *J. Phys. A: Math. Theor.* **45**, 225303 (2012). (Cited on page 24.)
- [68] J. I. de Vicente and J. Sánchez-Ruiz, *Phys. Rev. A* **77**, 042110 (2008). (Cited on pages 24 and 61.)
- [69] O. Gühne and M. Lewenstein, *Phys. Rev. A* **70**, 022316 (2004). (Cited on pages 24 and 61.)

- [70] A. K. Rajagopal, Phys. Lett. A **205**, 32 (1995). (Cited on page 24.)
- [71] S. Zozor, M. Portesi, P. Sanchez-Moreno, and J. S. Dehesa, Phys. Rev. A **83**, 052107 (2011). (Cited on pages 24 and 64.)
- [72] I. Białyński-Birula-Birula, Phys. Rev. A **74**, 052101 (2006). (Cited on pages 24 and 61.)
- [73] A. Stam, Inf. Cont. **2**, 101 (1959). (Cited on pages 24, 26 and 59.)
- [74] E. Romera, Mol. Phys. **100**, 3325 (2002). (Cited on page 24.)
- [75] P. Sánchez-Moreno, A. R. Plastino, and J. S. Dehesa, J. Phys. A: Math. Theor. **44**, 065301 (2011). (Cited on pages 24 and 35.)
- [76] J. S. Dehesa, R. González-Férez, and P. Sánchez-Moreno, J. Phys. A: Math. Theor. **40**, 1845 (2007). (Cited on pages 25 and 111.)
- [77] I. Białynicki-Birula and L. Rudnicki, *Entropic uncertainty relations in quantum physics, in Statistical Complexity: Applications in Electronic Structure* (Springer, 2011). (Cited on page 25.)
- [78] I. Białynicki-Birula and L. Rudnicki, Phys. Rev. A **81**, 026101 (2010). (Cited on page 25.)
- [79] J. Dehesa, S. López-Rosa, and D. Manzano, *Entropy and complexity analysis of D-dimensional quantum systems, in Statistical Complexity: Applications in Electronic Structure* (Springer, 2011). (Cited on page 25.)
- [80] C. R. Shalizi, K. L. Shalizi, and R. Haslinger, Phys. Rev. Lett. **93**, 118701 (2004). (Cited on page 25.)
- [81] O. Rosso, M. Martin, and A. Plastino, Physica A **320**, 497 (2003). (Cited on page 25.)
- [82] K. C. Chatzisavvas, C. C. Moustakidis, and C. P. Panos, J. Chem. Phys. **123**, 174111 (2005). (Cited on pages 25 and 100.)
- [83] D. Manzano, S. López-Rosa, and J. S. Dehesa, Europhys. Lett. **90**, 48001 (2010). (Cited on pages 25, 47 and 51.)
- [84] J. S. Dehesa, S. López-Rosa, and D. Manzano, Eur. Phys. J. D **55**, 539 (2009). (Cited on pages 25, 47 and 51.)
- [85] T. Yamano, J. Math. Phys. **45**, 1974 (2004). (Cited on pages 25 and 100.)
- [86] J. Antolín, S. López-Rosa, and J. Angulo, Chem. Phys. Lett. **474**, 233 (2009). (Cited on pages 25, 64, 97 and 100.)
- [87] J. Angulo, J. Antolín, and K. Sen, Phys. Lett. A **372**, 670 (2008). (Cited on pages 25 and 26.)

- [88] J. S. Shiner, M. Davison, and P. T. Landsberg, *Phys. Rev. E* **59**, 1459 (1999). (Cited on page 25.)
- [89] D. P. Feldman and J. P. Crutchfield, *Phys. Lett. A* **238**, 244 (1998). (Cited on page 25.)
- [90] X. Calbet and R. López-Ruiz, *Phys. Rev. E* **63**, 066116 (2001). (Cited on pages 25, 26 and 100.)
- [91] M. Martin, A. Plastino, and O. Rosso, *Physica A* **369**, 439 (2006). (Cited on pages 25 and 100.)
- [92] C. Anteneodo and A. Plastino, *Phys. Lett. A* **223**, 348 (1996). (Cited on page 25.)
- [93] E. Romera and J. S. Dehesa, *J. Chem. Phys.* **120**, 8906 (2004). (Cited on page 26.)
- [94] A. Dembo, T. Cover, and J. Thomas, *IEEE Trans. Inf. Theor.* **37**, 1501 (1991). (Cited on pages 26 and 33.)
- [95] S. López-Rosa, J. Angulo, and J. Antolín, *Physica A* **388**, 2081 (2009). (Cited on pages 26, 33, 51 and 59.)
- [96] A. Guerrero, P. Sánchez-Moreno, and J. S. Dehesa, *Phys. Rev. A* **84**, 042105 (2011). (Cited on pages 26 and 59.)
- [97] A. N. Kolmogorov, *Probl. Inf. Transm.* **1**, 3 (1965). (Cited on page 26.)
- [98] G. J. Chaitin, *J. ACM* **13**, 547 (1966). (Cited on page 26.)
- [99] R. J. Solomonoff, *Information Theory and Statistical Learning* (Springer, New York, 2009), chap. Algorithmic Probability: Theory and Applications. (Cited on page 26.)
- [100] S. Arora and B. Barak, *Computational Complexity: A Modern Approach* (Cambridge University Press, Cambridge, 2009). (Cited on page 26.)
- [101] J. Aczel and Z. Daroczy, *On Measures of Information and Their Characterizations* (Academic, New York, 1975). (Cited on page 27.)
- [102] J. Lin, *Inf. Theor. IEEE Trans. Inf.Theor.* **37**, 145 (1991). (Cited on pages 27 and 73.)
- [103] I. Taneja and P. Kumar, *Inf. Sci. (N.Y.)* **166**, 105 (2004). (Cited on page 27.)
- [104] J. Briët and P. Harremoës, *Phys. Rev. A* **79**, 052311 (2009). (Cited on page 27.)
- [105] D. V. Gokhale and S. Kullback, *Information in Contingency Tables* (Marcel Dekker, New York, 1978). (Cited on page 27.)
- [106] C. Chow and C. Liu, *Inf. Theor. IEEE Trans. Inf. Theor.* **14**, 462 (1968). (Cited on page 27.)

- [107] Y. He, A. Hamza, and H. Krim, *Sig. Process., IEEE Trans. on Sig. Process* **51**, 1211 (2003). (Cited on page 27.)
- [108] L. Pardo, *Statistical Inference Based on Divergence Measures* (Taylor and Francis, New York, 2005). (Cited on page 27.)
- [109] X. Huang, S. Li, and Y. Wang, Jensen-shannon boosting learning for object recognition, in *Com. Vision Patt. Recog. IEEE Computer Society Conference Vol. 2*, pp. 144–149 vol. 2, 2005. (Cited on page 27.)
- [110] S. Pavoine, S. Ollier, and D. Pontier, *Theor. Popu. Bio.* **67**, 231 (2005). (Cited on page 27.)
- [111] R. O. Duda, P. E. Hart, and D. G. Stork, *Pattern Classification* (Wiley, New York, 2001). (Cited on page 27.)
- [112] S. Y. Chung and S. Subbiah, *Structure* **4**, 1123 (1996). (Cited on page 27.)
- [113] K. Suzuki, H. Yamada, and S. Hashimoto, *Patt. Recog. Lett.* **28**, 1104 (2007). (Cited on page 27.)
- [114] P. Resnik, *J. Artif. Intell. Res.* **11**, 95 (1999). (Cited on page 27.)
- [115] J. C. Angulo and J. Antolín, *J. Chem. Phys.* **126**, 044106 (2007). (Cited on pages 27, 30, 73, 76, 77 and 83.)
- [116] R. P. Sagar and N. L. Guevara, *J. Mol. Struc.:THEOCHEM* **857**, 72 (2008). (Cited on pages 27, 28 and 73.)
- [117] J. Cioslowski and A. Nanayakkara, *J. Am. Chem. Soc.* **115**, 11213 (1993). (Cited on pages 27 and 30.)
- [118] R. Carbó-Dorca, X. Gironés, and P. Mezey, *Fundamentals of Molecular Similarity* (Kluwer Academic/Plenum Press, New York, 2001). (Cited on pages 27, 29, 30, 64 and 73.)
- [119] J. Mathiassen, A. Skavhaug, and K. Bø, Texture similarity measure using kullback-leibler divergence between gamma distributions, in *Computer Vision - ECCV 2002*, edited by A. Heyden, G. Sparr, M. Nielsen, and P. Johansen, , Lecture Notes in Computer Science Vol. 2352, pp. 133–147, Springer Berlin Heidelberg, 2002. (Cited on page 27.)
- [120] D. B. Russakoff, C. Tomasi, T. Rohlfing, and C. R. Maurer Jr., Image similarity using mutual information of regions, in *Computer Vision - ECCV 2004. Proceedings, Part III*, , Lecture Notes in Computer Science Vol. 3023, pp. 596–607, Berlin/Heidelberg, 2004, Springer-Verlag. (Cited on page 27.)
- [121] B. Balas, *Patt. Recog.* **41**, 972 (2008), Part Special issue: Feature Generation and Machine Learning for Robust Multimodal Biometrics. (Cited on page 27.)

- [122] P. Bernaola-Galván *et al.*, Phys. Rev. Lett. **85**, 1342 (2000). (Cited on page 27.)
- [123] G. Chechik, U. Sharma, V. anfang Shalit, and S. Bengio, J. Mach. Learn. Res. **11**, 1109 (2010). (Cited on page 27.)
- [124] P. Faratin, C. Sierra, and N. Jennings, Artif. Intell. **142**, 205 (2002), International Conference on MultiAgent Systems 2000. (Cited on page 27.)
- [125] C. Zhang and H. Fu, Patt. Recog. Lett. **27**, 1307 (2006). (Cited on page 27.)
- [126] R. Carbó-Dorca, L. Amat, E. Besalú, X. Gironés, and D. Robert, J. Mol. Struct.: THEOCHEM **504**, 181 (2000). (Cited on page 27.)
- [127] R. Carbó-Dorca and S. Damme, Theor. Chem. Acc. **118**, 673 (2007). (Cited on page 27.)
- [128] S. Kullback and R. Leibler, Ann. Math. Stat. **22**, 79 (1951). (Cited on page 27.)
- [129] E. Jaynes, Phys. Rev. **106**, 620 (1957). (Cited on page 27.)
- [130] M. Ho, R. P. Sagar, H. Schmider, D. F. Weaver, and V. H. Smith, Int. J. Quantum Chem. **53**, 627 (1995). (Cited on page 28.)
- [131] A. Borgoo, P. Jaque, A. Toro-Labbe, C. Van Alsenoy, and P. Geerlings, Phys. Chem. Chem. Phys. **11**, 476 (2009). (Cited on page 28.)
- [132] P. Sánchez-Moreno, A. Zarzo, and J. S. Dehesa, J. Phys. A: Math. Theor. **45**, 125305 (2012). (Cited on page 28.)
- [133] C. Rao and T. Nayak, IEEE Trans. Inf. Theor. **31**, 589 (1985). (Cited on pages 28 and 84.)
- [134] A. K. C. Wong and M. You, IEEE Trans. Patt. Anal. Mach. Intell. **PAMI-7**, 599 (1985). (Cited on pages 28 and 84.)
- [135] C. Tsallis, J. Stat. Phys. **52**, 479 (1988). (Cited on pages 28 and 62.)
- [136] J. Antolín, J. C. Angulo, and S. López-Rosa, J. Chem. Phys. **130**, 074110 (2009). (Cited on pages 28 and 83.)
- [137] J. C. Angulo, S. López-Rosa, J. Antolín, and R. O. Esquivel, Int. J. Quant. Chem. **111**, 297 (2011). (Cited on pages 28, 29, 63, 64, 73 and 76.)
- [138] J. Burbea and C. Rao, IEEE Trans. Inf. Theor. **28**, 489 (1982). (Cited on page 28.)
- [139] A. Borgoo, M. Torrent-Sucarrat, F. D. Proft, and P. Geerlings, J. Chem. Phys. **126**, 234104 (2007). (Cited on pages 29, 30 and 73.)
- [140] R. Carbó-Dorca and E. Besalú, J. Mol. Struct.: THEOCHEM **451**, 11 (1998). (Cited on page 29.)

- [141] A. Marshall and I. Olkin, *Theory of Majorization and its Applications* (Academic Press, New York, 1979). (Cited on pages 30, 74 and 84.)
- [142] N. Allan and D. L. Cooper, *J. Math. Chem.* **23**, 51 (1998). (Cited on page 30.)
- [143] A. Borgoo, M. Godefroid, P. Indelicato, F. D. Proft, and P. Geerlings, *J. Chem. Phys.* **126**, 044102 (2007). (Cited on pages 30 and 64.)
- [144] A. Borgoo, M. Godefroid, K. Sen, F. D. Proft, and P. Geerlings, *Chem. Phys. Lett.* **399**, 363 (2004). (Cited on pages 30, 73 and 77.)
- [145] J. Antolín and J. C. Angulo, *Eur. Phys. J. D* **46**, 21 (2008). (Cited on pages 30, 73, 76 and 80.)
- [146] D. Robert and R. Carbó-Dorca, *Int. J. Quantum Chem.* **77**, 685 (2000). (Cited on page 30.)
- [147] A. Nikiforov and V. Uvarov, *Special Functions in Mathematical Physics* (Birkhäuser Verlag, Basel, 1988). (Cited on page 31.)
- [148] N. Temme, *Special Functions: An Introduction to the Classical Functions of Mathematical Physics* (Wiley-Interscience, New York, 1996). (Cited on page 31.)
- [149] V. Majerník and L. Richterek, *J. Phys. A: Math. Gen.* **30**, L49 (1997). (Cited on page 31.)
- [150] V. Majerník, R. Charvot, and E. Majerníková, *J. Phys. A: Math. Gen.* **32**, 2207 (1999). (Cited on page 31.)
- [151] S. López-Rosa, J. Montero, P. Sánchez-Moreno, J. Venegas, and J. Dehesa, *J. Math. Chem.* **49**, 971 (2011). (Cited on page 31.)
- [152] V. Majerník and E. Majerníková, *J. Phys. A: Math. Gen.* **35**, 5751 (2002). (Cited on page 31.)
- [153] R. J. Yáñez, W. Van Assche, and J. S. Dehesa, *Phys. Rev. A* **50**, 3065 (1994). (Cited on page 31.)
- [154] J. S. Dehesa, R. J. Yáñez, A. I. Aptekarev, and V. Buyarov, *J. Math. Phys.* **39**, 3050 (1998). (Cited on page 31.)
- [155] S. Patil and K. Sen, *Phys. Lett. A* **370**, 354 (2007). (Cited on page 31.)
- [156] K. D. Sen and J. Katriel, *J. Chem. Phys.* **125**, 074117 (2006). (Cited on pages 31 and 33.)
- [157] H. Herschbach, J. Avery, and O. Goscinski, editors, *Dimensional Scaling in Chemical Physics* (Kluwer, Dordrecht, 1993). (Cited on pages 31, 32 and 36.)

- [158] R. Robinett, *Quantum Mechanics: Classical Results, Modern Systems, and Visualized Examples* (Oxford University Press, Oxford, 2006). (Cited on pages 31, 32 and 36.)
- [159] I. R. Lapidus, *Am. J. Phys.* **50**, 453 (1982). (Cited on pages 31, 32, 36 and 37.)
- [160] S. Dutta, S. Ganguly, and B. Dutta-Roy, *Eur. J. Phys.* **29**, 235 (2008). (Cited on pages 31, 32 and 36.)
- [161] D. R. Herrick and F. H. Stillinger, *Phys. Rev. A* **11**, 42 (1975). (Cited on page 31.)
- [162] M. Batchelor, X. Guan, and A. Kundu, *J. Phys. A: Math. Theor.* **41**, 352002 (2008). (Cited on pages 31 and 32.)
- [163] A. A. Frost, *J. Chem- Phys.* **25**, 1150 (1956). (Cited on pages 31 and 32.)
- [164] C. M. Rosenthal, *J. Chem. Phys.* **55**, 2474 (1971). (Cited on pages 31, 32 and 36.)
- [165] C. Kittel, *Introduction to Solid State Physics*, 8th ed. (Wiley-Interscience, New York, 2004). (Cited on page 31.)
- [166] Y. G. Peisakhovich and A. A. Shtygashev, *Phys. Rev. B* **77**, 075327 (2008). (Cited on page 31.)
- [167] I. Yanetka, *Phys. Stat. Sol. (b)* **232**, 196 (2002), See also references therein. (Cited on pages 31, 32 and 36.)
- [168] F. Ciccarello, M. Paternostro, M. S. Kim, and G. M. Palma, *Phys. Rev. Lett.* **100**, 150501 (2008). (Cited on pages 31 and 32.)
- [169] P. Harrison, *Quantum Wells, Wires and Dots: Theoretical and Computational Physics of Semiconductor Nanostructures* (Wiley-Interscience, Chichester, 2010). (Cited on page 31.)
- [170] G. Cordourier-Maruri, R. de Coss, and V. Gupta, *Mod. Phys. Lett. B* **25**, 1349 (2011). (Cited on page 31.)
- [171] E. H. Lieb and W. Liniger, *Phys. Rev.* **130**, 1605 (1963). (Cited on page 32.)
- [172] J. B. McGuire, *J. Math. Phys.* **5**, 622 (1964). (Cited on page 32.)
- [173] J. M. Guilarte and J. M. Muñoz Castañeda, *Int. J. Theor. Phys.* **50**, 2227 (2011). (Cited on pages 32 and 36.)
- [174] G. Salis *et al.*, *Phys. Rev. Lett.* **79**, 5106 (1997). (Cited on page 32.)
- [175] E. Kennard, *Z. Phys.* **44**, 326 (1927). (Cited on page 35.)
- [176] S. Zozor and C. Vignat, *Physica A* **375**, 499 (2007). (Cited on pages 35 and 61.)
- [177] S. Zozor, M. Portesi, and C. Vignat, *Physica A* **387**, 4800 (2008). (Cited on page 35.)

- [178] I. R. Lapidus, *Am. J. Phys.* **55**, 172 (1987). (Cited on page 46.)
- [179] M. Belloni, M. A. Doncheski, and R. W. Robinett, *Phys. Scr.* **72**, 122 (2005), See also references therein. (Cited on page 46.)
- [180] H. Müller-Kirsten, *Introduction to quantum mechanics. Schrödinger Equation and Path Integrals* (World Sci, New Jersey, 2006). (Cited on page 46.)
- [181] C. Tsallis, *J. Comp. App. Math.* **227**, 51 (2009), Special Issue of Proceedings of NUMAN 2007 Conference: Recent Approaches to Numerical Analysis: Theory, Methods and Applications. (Cited on page 46.)
- [182] J. Katriel and K. Sen, *J. Comp. App. Math.* **233**, 1399 (2010), Special Functions, Information Theory, and Mathematical Physics. Special issue dedicated to Professor Jesus Sanchez Dehesa on the occasion of his 60th birthday. (Cited on pages 47 and 53.)
- [183] *Proceedings of the RQI-2011 (International Workshop on Relativistic Quantum Theory North)*, (unpublished), Madrid, 2011. (Cited on page 47.)
- [184] A. Peres and D. R. Terno, *Rev. Mod. Phys.* **76**, 93 (2004). (Cited on page 47.)
- [185] D. Manzano, R. J. Yáñez, and J. S. Dehesa, *New J. Phys.* **12**, 023014 (2010). (Cited on pages 47 and 51.)
- [186] A. Borgoo, F. D. Proft, P. Geerlings, and K. Sen, *Chem. Phys. Lett.* **444**, 186 (2007). (Cited on pages 47, 48 and 100.)
- [187] J. Sañudo and R. López-Ruiz, *Phys. Lett. A* **373**, 2549 (2009). (Cited on page 47.)
- [188] P. Maldonado, A. Sarsa, E. Buendía, and F. Gálvez, *Phys. Lett. A* **374**, 3847 (2010). (Cited on page 47.)
- [189] J. Sañudo and R. López-Ruiz, *Int. Rev. Phys. (IREPHY)* **3**, 207 (2009). (Cited on page 47.)
- [190] I. P. Grant, *Relativistic Quantum Theory of Atoms and Molecules. Theory and Computation* (Springer, Berlin, 2007). (Cited on pages 47, 49 and 53.)
- [191] V. M. Burke and I. P. Grant, *Proc. Phys. Soc.* **90**, 297 (1967). (Cited on pages 47 and 53.)
- [192] J. S. Dehesa, S. López-Rosa, A. Martínez-Finkelshtein, and R. J. Yáñez, *Int. J. Quantum Chem.* **110**, 1529 (2010). (Cited on page 47.)
- [193] I. Hamilton and R. A. Mosna, *J. Comp. App. Math.* **233**, 1542 (2010), Special Functions, Information Theory, and Mathematical Physics. Special issue dedicated to Professor Jesus Sanchez Dehesa on the occasion of his 60th birthday. (Cited on page 48.)

- [194] W. Greiner, *Relativistic Quantum Mechanics: Wave Equations*, 3rd ed. (Springer, Berlin, 2000). (Cited on page 49.)
- [195] G. W. F. Drake, *Handbook of Atomic, Molecular and Optical Physics* (AIP Press, New York, 1996). (Cited on page 49.)
- [196] R. A. Swainson and G. W. F. Drake, *J. Phys. A: Math. Gen.* **24**, 79 (1991). (Cited on page 49.)
- [197] O. Klein, *Z. Phys.* **37**, 895 (1926). (Cited on page 49.)
- [198] A. Calogeracos and N. Dombey, *Contemp. Phys.* **40**, 313 (1999). (Cited on page 49.)
- [199] M. Levy, *Proc. Nat. Acad. Sci.* **76**, 6062 (1979). (Cited on page 61.)
- [200] G. A. Henderson, *Phys. Rev. A* **23**, 19 (1981). (Cited on page 61.)
- [201] R. K. Pathak, P. V. Panat, and S. R. Gadre, *Phys. Rev. A* **26**, 3073 (1982). (Cited on page 61.)
- [202] G. Das, S. Ghosh, and V. Sahni, *Solid State Communications* **65**, 719 (1988). (Cited on page 61.)
- [203] S. R. Gadre and S. J. Chakravorty, *Chem. Phys. Lett.* **132**, 535 (1986). (Cited on pages 61 and 65.)
- [204] W. C. Price, *The Uncertainty Principle and Foundations of Quantum Mechanics* (Wiley, New York, 1977). (Cited on page 61.)
- [205] G. Folland and A. Sitaram, *J. Four. Anal. App.* **3**, 207 (1997). (Cited on page 61.)
- [206] P. Busch, T. Heinonen, and P. Lahti, *Phys. Rep.* **452**, 155 (2007). (Cited on page 61.)
- [207] V. Vedral, *Introduction to Quantum Information Science* (Oxford University Press, Oxford, 2006). (Cited on page 61.)
- [208] H. S. Sichel, *J. Roy. Stat. Soc.* **110**, pp. 337 (1947). (Cited on page 61.)
- [209] H. S. Sichel, *Biometrika* **36**, pp. 404 (1949). (Cited on page 61.)
- [210] E. Romera, J. C. Angulo, and J. S. Dehesa, *J. Math. Phys.* **42**, 2309 (2001). (Cited on page 62.)
- [211] I. R. Epstein, *Phys. Rev. A* **8**, 160 (1973). (Cited on pages 62 and 64.)
- [212] J. Antolín, S. López-Rosa, J. C. Angulo, and R. O. Esquivel, *J. Chem. Phys.* **132**, 044105 (2010). (Cited on pages 63, 64, 73 and 76.)
- [213] J. Antolín, P. A. Bouvrie, and J. C. Angulo, *Phys. Rev. A* **84**, 032504 (2011). (Cited on page 63.)

- [214] J. S. Dehesa, F. J. Galvez, and I. Porras, *Phys. Rev. A* **40**, 35 (1989). (Cited on pages 63 and 64.)
- [215] J. C. Angulo and J. S. Dehesa, *J. Chem. Phys.* **97**, 6485 (1992). (Cited on page 64.)
- [216] J. Antolín, A. Zarzo, and J. C. Angulo, *Phys. Rev. A* **48**, 4149 (1993). (Cited on page 64.)
- [217] J. C. Angulo, *Phys. Rev. A* **83**, 062102 (2011). (Cited on page 64.)
- [218] P. Bouvrie, J. Antolín, and J. Angulo, *Chem. Phys. Lett.* **506**, 326 (2011). (Cited on pages 64 and 99.)
- [219] T. Koga, K. Kanayama, S. Watanabe, and A. J. Thakkar, *Int. J. Quant. Chem.* **71**, 491 (1999). (Cited on pages 65, 76, 100 and 218.)
- [220] T. Koga, K. Kanayama, T. Watanabe, T. Imai, and A. J. Thakkar, *Theor. Chem. Acc.* **104**, 411 (2000). (Cited on pages 65, 76, 100 and 218.)
- [221] L. H. Thomas, *Math. Proc. Cambridge Phil. Soc.* **23**, 542 (1927). (Cited on page 68.)
- [222] E. Fermi, *Z. Phys* **48**, 73 (1928). (Cited on page 68.)
- [223] P. A. M. Dirac, *Math. Proc. Cambridge Phil. Soc.* **26**, 376 (1930). (Cited on page 70.)
- [224] C. Tsallis and J. Statis, *Physica* **52**, 479 (1988). (Cited on page 73.)
- [225] J. Angulo, J. Antolín, S. López-Rosa, and R. Esquivel, *Physica A* **390**, 769 (2011). (Cited on page 76.)
- [226] N. H. March, *Phys. Rev. A* **33**, 88 (1986). (Cited on page 92.)
- [227] T. Koga, M. Omura, H. Teruya, and A. J. Thakkar, *J. Phys. B: At. Mol. Opt. Phys.* **28**, 3113 (1995). (Cited on page 94.)
- [228] K. D. Sen, J. Antolín, and J. C. Angulo, *Phys. Rev. A* **76**, 032502 (2007). (Cited on pages 97, 100 and 111.)
- [229] A. Borgoo, P. Geerlings, and K. Sen, *Phys. Lett. A* **375**, 3829 (2011). (Cited on pages 97, 98, 100, 101, 102 and 105.)
- [230] E. Romera, K. D. Sen, and A. Nagy, *J. Stat. Mech.: Theor. Exp.* **2011**, P09016 (2011). (Cited on page 97.)
- [231] A. Nagy and E. Romera, *Int. J. Quantum Chem.* **109**, 2490 (2009). (Cited on page 99.)
- [232] C. Panos, K. Chatzisavvas, C. Moustakidis, and E. Kyrkou, *Phys. Lett. A* **363**, 78 (2007). (Cited on page 100.)

- [233] L. Amico, R. Fazio, A. Osterloh, and V. Vedral, *Rev. Mod. Phys.* **80**, 517 (2008). (Cited on pages 111 and 119.)
- [234] I. Bengtsson and K. Życzkowski, *Geometry of Quantum States: An Introduction to Quantum Entanglement* (Cambridge University Press, Cambridge, 2006). (Cited on page 111.)
- [235] M. Schlosshauer, *Decoherence and the Quantum-to-Classical Transition* (Springer-Verlag, Berlin, 2007). (Cited on page 111.)
- [236] J. Gemmer, M. Michel, and M. G., *Quantum Thermodynamics* (Springer-Verlag, Berlin, 2004). (Cited on page 111.)
- [237] V. Aquilanti, A. C. P. Bitencourt, C. da S Ferreira, A. Marzuoli, and M. Ragni, *Phys. Scrip.* **78**, 058103 (2008). (Cited on page 111.)
- [238] R. J. Yáñez, A. R. Plastino, and J. S. Dehesa, *Eur. Phys. J. D* **56**, 141 (2010). (Cited on pages 111, 112, 119, 122, 136 and 157.)
- [239] O. Osenda and P. Serra, *Phys. Rev. A* **75**, 042331 (2007). (Cited on page 111.)
- [240] O. Osenda and P. Serra, *J. Phys. B: At. Mol. Opt. Phys.* **41**, 065502 (2008). (Cited on page 111.)
- [241] C. Amovilli and N. H. March, *Phys. Rev. A* **69**, 054302 (2004). (Cited on pages 111 and 112.)
- [242] F. Carlier, A. Mandilara, and A. Sarfati, *J. Phys. B: At. Mol. Opt. Phys.* **40**, S199 (2007). (Cited on page 111.)
- [243] J. P. Coe, A. Sudbery, and I. D'Amico, *Phys. Rev. B* **77**, 205122 (2008). (Cited on page 111.)
- [244] J. Pipek and I. Nagy, *Phys. Rev. A* **79**, 052501 (2009). (Cited on pages 111 and 112.)
- [245] D. Manzano, A. R. Plastino, J. S. Dehesa, and T. Koga, *J. Phys. A: Math. Theor.* **43**, 275301 (2010). (Cited on pages 111, 136 and 157.)
- [246] N. Harshman and W. Flynn, *Quantum Inf. Comp.* **11**, 278 (2011). (Cited on page 111.)
- [247] P. Kościk, *Phys. Lett. A* **375**, 458 (2011). (Cited on page 111.)
- [248] J. S. Dehesa, T. Koga, R. J. Yáñez, A. R. Plastino, and R. O. Esquivel, *J. Phys. B: At. Mol. Opt. Phys.* **45**, 015504 (2012), Corrigendum, *J. Phys. B: At. Mol. Opt. Phys.* **45**, 239501 (2012). (Cited on page 111.)
- [249] G. Benenti, S. Siccardi, and G. Strini, *Eur. Phys. J. D* **67**, 83 (2013). (Cited on page 111.)

- [250] C. Das and K. Bhattacharyya, *Phys. Rev. A* **79**, 012107 (2009). (Cited on page 111.)
- [251] R. González-Férez and J. S. Dehesa, *Phys. Rev. Lett.* **91**, 113001 (2003). (Cited on page 111.)
- [252] A. Nagy, *Chem. Phys. Lett.* **449**, 212 (2007). (Cited on page 111.)
- [253] A. Nagy, *Chem. Phys. Lett.* **425**, 154 (2006). (Cited on page 111.)
- [254] A. Plastino and A. Plastino, *Phys. Lett. A* **181**, 446 (1993). (Cited on page 111.)
- [255] A. Nagy and K. Sen, *Phys. Lett. A* **360**, 291 (2006). (Cited on page 111.)
- [256] S. Liu, *J. Chem. Phys.* **126**, 191107 (2007). (Cited on page 111.)
- [257] N. L. Guevara, R. P. Sagar, and R. O. Esquivel, *J. Chem. Phys.* **119**, 7030 (2003). (Cited on page 111.)
- [258] M. L. Glasser and L. M. Nieto, *J. Phys. A: Math. Gen.* **38**, L455 (2005). (Cited on page 111.)
- [259] H. G. Laguna and R. P. Sagar, *Phys. Rev. A* **84**, 012502 (2011). (Cited on pages 111 and 112.)
- [260] A. P. Majtey, A. R. Plastino, and J. S. Dehesa, *J. Phys. A: Math. Theor.* **45**, 115309 (2012). (Cited on pages 111, 119 and 158.)
- [261] M. Moshinsky, *Am. J. Phys.* **36**, 52 (1968), Erratum: *Am. J. Phys.* **36**, 763 (1968). (Cited on pages 111, 112 and 123.)
- [262] M. Moshinsky, N. Méndez, and E. Murow, *Ann. Phys.* **163**, 1 (1985). (Cited on pages 111 and 132.)
- [263] C. L. Benavides-Riveros, J. M. Gracia-Bondía, and J. C. Várilly, *Phys. Rev. A* **86**, 022525 (2012). (Cited on pages 111 and 112.)
- [264] C. Amovilli and N. H. March, *Phys. Rev. A* **67**, 022509 (2003). (Cited on page 112.)
- [265] P. A. Bouvrie, A. P. Majtey, A. R. Plastino, P. Sánchez-Moreno, and J. S. Dehesa, *Eur. Phys. J. D* **66**, 1 (2012). (Cited on pages 112, 119 and 157.)
- [266] W. Heisenberg, *Z. Phys.* **38**, 411 (1926). (Cited on page 112.)
- [267] M. Srednicki, *Phys. Rev. Lett.* **71**, 666 (1993). (Cited on page 112.)
- [268] E. Schrödinger, *Math. Proc. Camb. Phil. Soc.* **32**, 446 (1936). (Cited on page 113.)
- [269] J. Bell, *Physics* **1**, 195 (1964). (Cited on page 113.)
- [270] A. Aspect, P. Grangier, and G. Roger, *Phys. Rev. Lett.* **47**, 460 (1981). (Cited on page 113.)

- [271] D. S. Bernstein, *Matrix Mathematics* (Princeton University Press, Princeton, 2009). (Cited on page 117.)
- [272] J. von Neumann, *Mathematische Grundlagen der Quantenmechanik* (Springer, Berlin, 1955). (Cited on page 118.)
- [273] J. von Neumann, *Mathematical Foundations of Quantum Mechanics* (Princeton University Press, Princeton, 1996). (Cited on page 118.)
- [274] C. H. Bennett, H. J. Bernstein, S. Popescu, and B. Schumacher, *Phys. Rev. A* **53**, 2046 (1996). (Cited on page 118.)
- [275] R. Horodecki, P. Horodecki, M. Horodecki, and K. Horodecki, *Rev. Mod. Phys.* **81**, 865 (2009). (Cited on page 119.)
- [276] W. K. Wootters, *Phys. Rev. Lett.* **80**, 2245 (1998). (Cited on page 119.)
- [277] B. M. Terhal and P. Horodecki, *Phys. Rev. A* **61**, 040301 (2000). (Cited on page 119.)
- [278] P. Rungta, V. Bužek, C. M. Caves, M. Hillery, and G. J. Milburn, *Phys. Rev. A* **64**, 042315 (2001). (Cited on page 119.)
- [279] F. Buscemi, P. Bordone, and A. Bertoni, *Phys. Rev. A* **75**, 032301 (2007). (Cited on page 119.)
- [280] A. R. Plastino, D. Manzano, and J. S. Dehesa, *Europhys. Lett.* **86**, 20005 (2009). (Cited on pages 119 and 120.)
- [281] M. C. Tichy, P. A. Bouvrie, and K. Mølmer, *Phys. Rev. A* **86**, 042317 (2012). (Cited on page 119.)
- [282] M. C. Tichy, P. A. Bouvrie, and K. Mølmer, *Phys. Rev. Lett.* **109**, 260403 (2012). (Cited on pages 119, 205, 209, 211 and 215.)
- [283] K. Eckert, J. Schliemann, D. Bruß, and M. Lewenstein, *Ann. Phys.* **299**, 88 (2002). (Cited on page 119.)
- [284] G. Ghirardi and L. Marinatto, *Phys. Rev. A* **70**, 012109 (2004). (Cited on page 119.)
- [285] G. Ghirardi, L. Marinatto, and T. Weber, *J. Stat. Phys.* **108**, 49 (2002). (Cited on page 119.)
- [286] J. Naudts and T. Verhulst, *Phys. Rev. A* **75**, 062104 (2007). (Cited on page 119.)
- [287] A. Borrás, A. R. Plastino, M. Casas, and A. Plastino, *Phys. Rev. A* **78**, 052104 (2008). (Cited on page 119.)
- [288] V. C. G. Oliveira, H. A. B. Santos, L. A. M. Torres, and A. M. C. Souza, *Int. J. Quantum Inf.* **06**, 379 (2008). (Cited on page 119.)

- [289] B. R. Desai, *Quantum Mechanics with Basic Field Theory* (Cambridge University Press, Cambridge, 2010). (Cited on page 141.)
- [290] J. Batle, M. Casas, A. Plastino, and A. Plastino, *Phys. Lett. A* **296**, 251 (2002). (Cited on page 143.)
- [291] A. Hamadou-Ibrahim, A. R. Plastino, and C. Zander, *J. Phys. A: Math. Theor.* **43**, 055305 (2010). (Cited on page 143.)
- [292] P. Tommasini, E. Timmermans, and A. F. R. de Toledo Piza, *Am. J. Phys.* **66**, 881 (1998). (Cited on page 149.)
- [293] H. Venzl, A. J. Daley, F. Mintert, and A. Buchleitner, *Phys. Rev. E* **79**, 056223 (2009). (Cited on page 149.)
- [294] J. Eisert, M. Cramer, and M. B. Plenio, *Rev. Mod. Phys.* **82**, 277 (2010). (Cited on page 149.)
- [295] D. Perez-Garcia, F. Verstraete, M. Wolf, and J. I. Cirac, *Quantum Inf. Comput.* **7**, 401 (2007). (Cited on page 149.)
- [296] G. Tanner, K. Richter, and J.-M. Rost, *Rev. Mod. Phys.* **72**, 497 (2000). (Cited on page 149.)
- [297] M. Born and J. R. Oppenheimer, *Ann. Phys. (Leipzig)* **84**, 457 (1927). (Cited on pages 149 and 152.)
- [298] D. A. McQuarrie, *Quantum Chemistry*, 2nd ed. (University Science Books, 2007). (Cited on pages 149 and 152.)
- [299] W. Demtröder, *Molecular Physics: Theoretical Principles and Experimental Methods* (Wiley-VCH, Weinheim, 2007). (Cited on pages 149 and 152.)
- [300] S. Takahashi and K. Takatsuka, *J. Chem. Phys.* **124**, 144101 (2006). (Cited on page 150.)
- [301] P. Schmelcher, L. S. Cederbaum, and H. D. Meyer, *J. Phys. B: At. Mol. Opt. Phys.* **21**, L445 (1988). (Cited on page 150.)
- [302] M. H. Alexander, G. Capecchi, and H.-J. Werner, *Science* **296**, 715 (2002). (Cited on page 150.)
- [303] C. Chudzicki, O. Oke, and W. K. Wootters, *Phys. Rev. Lett.* **104**, 070402 (2010). (Cited on pages 169, 177, 178, 180, 185, 186, 187, 189, 190, 192, 193, 205, 209, 211, 214, 215 and 222.)
- [304] R. Healey, *Studies In History and Philosophy of Science Part B: Studies In History and Philosophy of Modern Physics* (2012). (Cited on page 177.)

- [305] CMS Collaboration, V. Khachatryan *et al.*, Phys. Rev. Lett. **105**, 032001 (2010). (Cited on page 177.)
- [306] M. W. Zwierlein *et al.*, Phys. Rev. Lett. **91**, 250401 (2003). (Cited on pages 177 and 178.)
- [307] T. Bourdel *et al.*, Phys. Rev. Lett. **93**, 050401 (2004). (Cited on page 177.)
- [308] M. Combescot, O. Betbeder-Matibet, and F. Dubin, Phys. Rev. A **76**, 033601 (2007). (Cited on page 177.)
- [309] C. K. Law, Phys. Rev. A **71**, 034306 (2005). (Cited on pages 177, 180, 181, 182, 185, 186, 187, 193, 205, 211 and 215.)
- [310] S. S. Avancini, J. R. Marinelli, and G. Krein, J. Phys. A: Math. Gen. **36**, 9045 (2003). (Cited on page 177.)
- [311] S. Rombuts, D. Van Neck, K. Peirs, and L. Pollet, Mod. Phys. Lett. A **17**, 1899 (2002). (Cited on pages 177, 178, 193 and 214.)
- [312] M. Combescot, O. Betbeder-Matibet, and F. Dubin, Phys. Rep. **463**, 215 (2008). (Cited on pages 177 and 205.)
- [313] M. Combescot and O. Betbeder-Matibet, Phys. Rev. Lett. **104**, 206404 (2010). (Cited on pages 177 and 186.)
- [314] M. Combescot, S.-Y. Shiau, and Y.-C. Chang, Phys. Rev. Lett. **106**, 206403 (2011). (Cited on pages 177 and 187.)
- [315] P. Sancho, J. Phys. A: Math. Gen. **39**, 12525 (2006). (Cited on page 177.)
- [316] R. Ramanathan, P. Kurzyński, T. K. Chuan, M. F. Santos, and D. Kaszlikowski, Phys. Rev. A **84**, 034304 (2011). (Cited on pages 177, 186, 187, 211 and 215.)
- [317] A. Gavrilik and Y. Mishchenko, Phys. Lett. A **376**, 1596 (2012). (Cited on page 177.)
- [318] L. de Broglie, Nature **112**, 540 (1923). (Cited on page 178.)
- [319] C. J. Davisson and L. H. Germer, Nature **119**, 558â60 (1927). (Cited on page 178.)
- [320] C. Adams, M. Sigel, and J. Mlynek, Phys. Rep. **240**, 143 (1994). (Cited on page 178.)
- [321] I. Estermann and O. Stern, Z. Phys. **61**, 95â125 (1930). (Cited on page 178.)
- [322] K. Bongs and K. Sengstock, Rep. Prog. Phys. **67**, 907 (2004). (Cited on page 178.)
- [323] M. H. Anderson, J. R. Ensher, M. R. Matthews, C. E. Wieman, and E. A. Cornell, Science **269**, 198 (1995). (Cited on page 178.)

- [324] M. R. Andrews *et al.*, *Science* **275**, 637 (1997). (Cited on page 178.)
- [325] Y. Castin and J. Dalibard, *Phys. Rev. A* **55**, 4330 (1997). (Cited on page 178.)
- [326] B. Lücke *et al.*, *Science* **334**, 773 (2011). (Cited on pages 178 and 213.)
- [327] S. Jochim *et al.*, *Science* **302**, 2101 (2003). (Cited on page 178.)
- [328] F. Serwane *et al.*, *Science* **332**, 336 (2011). (Cited on pages 178 and 214.)
- [329] C. Kohstall *et al.*, *New J. Phys.* **13**, 065027 (2011). (Cited on pages 178 and 202.)
- [330] Y. H. Pong and C. K. Law, *Phys. Rev. A* **75**, 043613 (2007). (Cited on page 182.)
- [331] D. G. Fried *et al.*, *Phys. Rev. Lett.* **81**, 3811 (1998). (Cited on page 182.)
- [332] M. Combescot, X. Leyronas, and C. Tanguy, *Eur. Phys. J. B* **31**, 17 (2003). (Cited on pages 182, 186, 205, 211 and 215.)
- [333] M. Combescot and C. Tanguy, *EPL (Europhys. Lett.)* **55**, 390 (2001). (Cited on page 182.)
- [334] J. Schliemann, J. I. Cirac, M. Kuś, M. Lewenstein, and D. Loss, *Phys. Rev. A* **64**, 022303 (2001). (Cited on pages 186 and 198.)
- [335] M. Combescot, *Europhys. Lett.* **96**, 60002 (2011). (Cited on pages 186, 189, 194 and 211.)
- [336] P. A. Macmahon, *Combinatory Analysis* (Cambridge University Press, Cambridge, England, 1915). (Cited on pages 186, 205 and 222.)
- [337] G. H. Hardy, J. E. Littlewood, and P. G., *Inequalities* (Cambridge University Press, Cambridge, England, 1988). (Cited on pages 186 and 212.)
- [338] J. Klotz, 591, University of Wisconsin Report No. 591, 1979 (unpublished). (Cited on pages 187 and 194.)
- [339] T.-C. Wei *et al.*, *Phys. Rev. A* **67**, 022110 (2003). (Cited on page 188.)
- [340] O. Giraud, *J. Phys. A: Math. Theor.* **40**, F1053 (2007). (Cited on page 191.)
- [341] K. Życzkowski, K. A. Penson, I. Nechita, and B. Collins, *J. Math. Phys.* **52**, 062201 (2011). (Cited on page 191.)
- [342] D. N. Page, *Phys. Rev. Lett.* **71**, 1291 (1993). (Cited on page 191.)
- [343] P. Hayden, D. W. Leung, and A. Winter, *Comm. Math. Phys.* **265**, 95 (2006). (Cited on pages 191 and 194.)
- [344] P. Kurzyński, R. Ramanathan, A. Soeda, T. K. Chuan, and D. Kaszlikowski, *New J. Phys.* **14**, 093047 (2012). (Cited on pages 193 and 195.)

- [345] P. Harremoës and F. Topsøe, *IEEE Trans. Inf. Theor.*, **47**, 2944 (2001). (Cited on page 193.)
- [346] K. Życzkowski, *Op. Sys. & Inf. Dyn.* **10**, 297 (2003). (Cited on page 193.)
- [347] A. G. Munford, *Am. Stat.* **31**, 119 (1977). (Cited on pages 194 and 219.)
- [348] S. Mase, *Ann. Inst. Statist. Math.* **44**, 479 (1992). (Cited on page 194.)
- [349] R. Hanbury Brown and R. Q. Twiss, *Nature (London)* **177**, 27 (1956). (Cited on page 195.)
- [350] T. Jeltes *et al.*, *Nature (London)* **445**, 402 (2007). (Cited on page 195.)
- [351] K. Mølmer *et al.*, *Phys. Rev. A* **77**, 033601 (2008). (Cited on page 195.)
- [352] A. Perrin *et al.*, *Nature Phys.* **8**, 195 (2012). (Cited on page 195.)
- [353] C. K. Hong, Z. Y. Ou, and L. Mandel, *Phys. Rev. Lett.* **59**, 2044 (1987). (Cited on pages 195, 196 and 197.)
- [354] Y. L. Lim and A. Beige, *New J. of Phys.* **7**, 155 (2005). (Cited on page 195.)
- [355] F. Laloë and W. Mullin, *Found. Phys.* **42**, 53 (2012). (Cited on pages 195, 196, 197, 201, 202, 203, 210 and 213.)
- [356] M. C. Tichy, M. Tiersch, F. Mintert, and A. Buchleitner, *New J. Phys.* **14**, 093015 (2012). (Cited on pages 195, 197, 210 and 214.)
- [357] Z. Y. Ou, J. K. Rhee, and L. J. Wang, *Phys. Rev. Lett.* **83**, 959 (1999). (Cited on page 195.)
- [358] M. C. Tichy *et al.*, *Phys. Rev. A* **83**, 062111 (2011). (Cited on pages 195, 197, 206, 208, 210 and 215.)
- [359] Y.-S. Ra *et al.*, *Proc. Nati. Acad. Sci.* **110**, 1227 (2013). (Cited on pages 195, 206 and 215.)
- [360] M. Combescot, F. Dubin, and M. A. Dupertuis, *Phys. Rev. A* **80**, 013612 (2009). (Cited on page 195.)
- [361] M. Girardeau, *J. Math. Phys.* **1**, 516 (1960). (Cited on page 199.)
- [362] M. C. Tichy, *Entanglement and Interference of Identical Particles*, PhD thesis, Albert-Ludwigs-Universität Freiburg im Breisgau, 2011. (Cited on pages 200, 202 and 203.)
- [363] W. J. Mullin and F. Laloë, *Phys. Rev. A* **85**, 023602 (2012). (Cited on page 201.)
- [364] F. Laloë and W. J. Mullin, *Eur. Phys. J. B* **70**, 377 (2009). (Cited on page 202.)
- [365] W. J. Mullin and F. Laloë, *Phys. Rev. A* **82**, 013618 (2010). (Cited on page 202.)

-
- [366] W. J. Mullin and F. Laloë, Phys. Rev. Lett. **104**, 150401 (2010). (Cited on page 202.)
- [367] W. J. Mullin, R. Krotkov, and F. Laloë, Am. J. Phys. **74**, 880 (2006). (Cited on page 202.)
- [368] G. Cennini, C. Geckeler, G. Ritt, and M. Weitz, Phys. Rev. A **77**, 013613 (2008). (Cited on page 202.)
- [369] M. P. Strzys and J. R. Anglin, Phys. Rev. A **81**, 043616 (2010). (Cited on page 204.)
- [370] T. Brougham, S. M. Barnett, and I. Jex, J. Mod. Opt. **57**, 587 (2010). (Cited on page 210.)
- [371] G. Zürn *et al.*, Phys. Rev. Lett. **108**, 075303 (2012). (Cited on page 214.)